TIME-VARIANT ULTIMATE STRENGTH RELIABILITY ASSESSMENT OF SHIP HULLS CONSIDERING CORROSION AND FATIGUE

by

Jianwei Bai

B.S. (Harbin Engineering University) 1997

M.S. (Shanghai Jiao Tong University) 2000

M.S. (University of California, Berkeley) 2003

A dissertation submitted in partial satisfication of the

requirements for the degree of

Doctor of Philosophy

in

Engineering-Ocean Engineering

in the

Graduate Division

of the

University of California, Berkeley

Committee in charge:

Professor Alaa E. Mansour, Chair

Professor Filip C. Filippou

Professor David Brillinger

Fall 2006

INFORMATION TO USERS

The quality of this reproduction is dependent upon the quality of the copy submitted. Broken or indistinct print, colored or poor quality illustrations and photographs, print bleed-through, substandard margins, and improper alignment can adversely affect reproduction.

In the unlikely event that the author did not send a complete manuscript and there are missing pages, these will be noted. Also, if unauthorized copyright material had to be removed, a note will indicate the deletion.

ProQuest Information and Learning Company
300 North Zeeb Road
P.O. Box 1346
Ann Arbor, MI 48106-1346

ABSTRACT

TIME-VARIANT ULTIMATE STRENGTH RELIABILITY ASSESSMENT OF SHIP HULLS CONSIDERING CORROSION AND FATIGUE

by

Jianwei Bai

Doctor of Philosophy

University of California, Berkeley

Professor Alaa E. Mansour, Chair

Ship structures suffer various types of damage while in service. Age-related structural degradations, such as corrosion and fatigue cracks, are considered major types of damage. The purpose of this work is to propose a methodology to assess the time-variant ultimate strength of ship hull girder under the degradation of these damages, to provide a procedure to quickly perform reliability analysis of aging ship hulls, and to develop a more rational renewal and repair schemes that not only consider the maximum allowable corrosion wastage and critical crack size criteria, but also take into account the hull ultimate strength.

Mathematical models for predicting corrosion as a function of ship age are reviewed and compared based on sets of real vessel corrosion measurements. Fatigue cracking mechanism is also analyzed in this work. A crack size prediction model as a function of ship age is presented. Extensive numerical studies are carried out to investigate the ultimate strength reduction of unstiffened plates and stiffened panels that are wasted due

to pit corrosion. The effect of fatigue cracks on tensile and compressive ultimate strength of unstiffened plates and stiffened panels are also analyzed by the finite element method. Empirical equations are developed to estimate the ultimate strength of unstiffened plates and stiffened panels with pit corrosion or fatigue crack damage based on the finite element analysis results. Using these equations, a modified simple formulation is proposed to predict the ultimate strength of the entire ship hull girder considering these age-related degradations.

Time-dependent reliability procedure of a double hull tanker is presented as an example with consideration given to the effects of corrosion and fatigue crack damage on ultimate strength and reliability. It is expected that the methodologies and procedures developed in the present study will provide a useful tool for assessing time-variant ultimate strength and reliability of aging ship hulls.

TABLE OF CONTENTS

LIST OF TABLES

LIST OF FIGURES

1. INTRODUCTION

1.1. INTRODUCTION

Since the beginning of 1980s to the middle of 1990s, over 150 bulk carriers have been reported lost, with a loss of more than 1200 lives (RINA 1996). About 20 of those vessels disappeared without known reasons. Also there are numbers of casualties of oil tankers during 1980s and 1990s. Through survey, people found most of the vessels were over 15 years old, which brings the consideration of various potential problems associated with vessel age, like corrosion and fatigue cracks, into attention. There are always vessels that continue to be operated over 15 or 20 years. The International Maritime Organization (IMO), classification societies and ship owners still need to seek an efficient way to assess the time-variant strength of aging ships and acceptable standards for structural integrity of aging ships without excessive economic penalties with respect to repair and maintenance costs incurred over the ship life cycle.

Corrosion and fatigue cracking are the most pervasive types of structural damages experienced by ship structures, especially old vessels. The ultimate strength of ship hull girders will be slowly reduced due to the degradation effects of corrosion and fatigue cracks. But the ship hull girder strength can be improved by repair. Therefore ship hull girder strength is an alternately changing process between degradation and rapid improvement in its whole lifetime.

Bea et al. (1997) conducted extensive research on the significance of corrosion and fatigue cracks in tankers. However, the impact of corrosion and fatigue cracking on the structural integrity of the ship hull structures is needed to be further studied. Guedes Soares and Garbatov (1996, 1998) developed an advanced time-variant formulation for the reliability of a ship hull considering degradations of corrosion and fatigue cracking and the improvement effect of repair operations. In these studies, the first yield reliability of the midship section modulus was analyzed, and the limit state for global hull girder failure was defined as initial yield strength.

Paik et al. (1998) analyzed the ship hull ultimate strength reliability under the effect of corrosion damage. But the unsteady propagation of fatigue cracks may induce rapid reduction of ultimate strength of ship hulls. Paik et al. (2003) performed a risk assessment of aging ships accounting for corrosion, fatigue cracking and local denting damage. In their study, the fatigue cracking effect on ultimate strength is simplified by reducing the original ultimate strength using ratio of area deducted by cracks to original area. The simplified model either overestimates the ultimate strength or underestimates it. It cannot well capture the nonlinear property of ultimate strength of cracked panels. The degradation effect of fatigue cracks on the ultimate strength of ship hull girder still needs further investigation.

The ultimate strength of the ship hull girder is associated with the compressive and tensile ultimate strength of stiffened panels between bulkheads or web frames and unstiffened plates between stiffeners. For aging ships, the fatigue cracks and corrosion

will degrade the ultimate strength of stiffened panels and unstiffened plates. The residual ultimate strength of unstiffened plates and stiffened panels with corrosion and crack damage should be assessed properly. And the degree of damage due to corrosion and fatigue cracks should be determined first to assess the strength of aging ships

At present general corrosion is usually used to calculate the corrosion damage (Guedes Soares and Garbatov 1998, Paik et al. 2002). Constant rate of corrosion model is usually used to assess the wastage of corrosion. But now, more and more research indicates that non-linear corrosion rate models are more reasonable (Paik et al. 1998, 2003, Qin and Cui 2003). Recently pit corrosion also brought considerable attention. In order to investigate the ultimate strength reduction characteristics of unstiffened plates and stiffened panels due to pit corrosion, extensive numerical studies were carried out in the present work. The mathematical models for predicting general corrosion as a function of ship age were reviewed and compared based on sets of real vessel corrosion measurements.

To consider the effect of fatigue cracks on the structure's ultimate strength, there are only very few comprehensive studies in the literature. In this study, the effects of fatigue cracks on the tensile and compressive ultimate strength of unstiffened plates and stiffened panels were analyzed by the finite element method. Empirical equations were developed to estimate the ultimate strength of unstiffened plates and stiffened panels with fatigue crack damage based on the finite element analysis results.

The present study proposes a methodology to assess the time-variant ultimate strength of ship hull girder under the degradation of these damages, and provides a procedure to quickly perform the reliability analysis of aging ship hulls. A more rational renewal and repair scheme was developed. The procedure not only considers the maximum allowable corrosion wastage and critical crack size criterion, but also takes into account the hull ultimate strength.

Finally, time-dependent strength-based reliability assessment of a double hull tanker is presented as an example accounting for the effects of corrosion and fatigue cracking damage. The procedure developed in this work is illustrated by this example.

1.2. OUTLINE OF PRESENT WORK

The present work focuses on the time-variant ultimate strength reliability assessment of ship hulls considering age-related degradations, such as corrosion and fatigue damages.

Chapter 2 reviews corrosion mechanism and existing corrosion models. Real vessel corrosion measurements are introduced and analyzed. Non-linear corrosion model is proposed and compared with existing corrosion models based on the corrosion measurement data.

In Chapter 3, extensive study on the effect of pit corrosion on ultimate strength of unstiffened plates is performed by finite element method. Empirical equations are proposed based on the numerical results.

Chapter 4 describes the fatigue cracking mechanism. The ultimate tensile and compressive strengths of unstiffened plates and stiffened panels with fatigue cracking damage are thoroughly studied. Empirical formulae are developed based on the finite element results.

A short review of ship hull girder strength and existing methods to evaluate the strength is given in Chapter 5. A modified simple method is proposed to quickly evaluate the ultimate ship hull girder strength considering corrosion and fatigue cracking effects.

Chapter 6 describes probabilistic models of wave loads, including stillwater bending moment, wave-induced bending moment, and dynamic moment. Load combinations according to ship classification societies rules and ship structure committee reports are also presented.

In Chapter 7, structural reliability theory is reviewed, and programs for structural reliability analysis are described. An example is introduced to illustrate the reliability analysis procedure.

Inspections and repair scheme is introduced in Chapter 8, in which corrosion and cracks are considered separately.

Chapter 9 gives an illustrative example of an actual double hull tanker. Time-dependent hull ultimate strength is assessed counting for the effects of corrosion and fatigue cracking damage. Repair and renewal scheme is proposed based on the results.

Summary and conclusions are presented in Chapter 10. Recommendations for future research are also given.

2. TIME-VARIANT CORROSION MODEL

2.1. CORROSION MECHANISM

The mechanism of electrochemical corrosion of metals in aqueous electrolytes is associated with the flow of electric current between anodic and cathodic areas within the system. The anodic region is where the metal atoms are transformed into positive ions and free electrons. The cathodic region is where the free electrons unite with inos of the electrolyte to produce either hydrogen or oxygen. Corrosion occurs in the anodic region, i.e., where the dissolution of the metal causes metal ions to go into solution.

Corrosion of iron (Fe) in an aqueous electrolyte can be described as:

1) Hydrogen Evolution (in the absence of oxygen)

$$Fe + 2H_2O \rightarrow Fe(OH)_2 + H_2 \qquad (2.1)$$

The corroding metal simply supplies ions to replace the hydrogen ions in the electrolyte. This type of reaction usually occurs in acid environments. The anodes are usually large areas while the cathodes are small areas. The electrons freed by the dissolution of the corroding metal flow through the metal to the small cathodic areas, and there the hydrogen gas is given off.

2) Oxygen Absorption (in the presence of oxygen)

$$Fe + \tfrac{1}{2}(O_2) + H_2O \rightarrow Fe(OH)_2 \qquad (2.2)$$

In a neutral (pH=7) aqueous electrolyte, or one that is slightly alkaline, iron corrodes in the presence of oxygen. In this type of attack the electrons freed by the dissolution the metal are intercepted by the oxygen according to

$$2e + \tfrac{1}{2}(O_2) + H_2O \rightarrow 2OH^- \qquad (2.3)$$

Notice that the free electrons are converted into hydroxyl ions. In this case the anodic areas on the surface of the metal are due to cracks in the oxide film coating the metal. Consequently, the anodic areas are very small, whereas almost the entire surrounding surface of the metal constitutes the cathode. The corrosion current is concentrated within a very small area. This concentration causes strong, localized attack.

Since seawater, which is one of the best electrolytes, contains sodium and chlorine ions in solution, the cathodic product of this form of corrosion is sodium hydroxide and the anodic product is ferrous chloride. Both products are readily soluble and will diffuse away from their respective electrodes. As they meet in solution, ferrous hydroxide oxidizes to ferric hydroxide, which precipitates even more quickly. Since the products at both electrodes have tendencies to diffuse away, the corrosion will proceed as long as there is a fresh supply of oxygen. In situations where there is agitation of the solution, as with waves and currents offshore, the rate of corrosion increases as the aeration of the solution increases.

Concentration cell corrosion occurs because of differential aeration, that is, when one part of a metal body is exposed to a different air concentration than another part. A difference in electrical potential is created between the differently aerated areas. The surface of that

part of the body exposed to electrolyte of low-oxygen concentration is anodic; the surface area exposed to electrolyte with a high-oxygen concentration is cathodic. The flow of electrons between the two areas is called a differential aeration current.

This form of corrosion occurs just below the waterline for metals that are partially immersed in seawater. Dissolution of the metal just below the waterline releases electrons that flow through the metal body to the highly aerated region just above the waterline. The electrons are said to flow through the metal circuit, or the external circuit. In the cathodic area oxygen combines with the free electrons to form hydroxyl ions. The internal circuit of the corrosion cell consists of the migration of the metal ions through the electrolyte. The amount of oxygen available controls the magnitude of the corrosion current.

A drop of water on a steel or iron surface constitutes a simple example of concentration cell corrosion. The central portion of the surface covered by the drop of water is farthest from the oxygen of the air and becomes anodic, while the outer periphery of the surface covered by the drop has ready access to oxygen and becomes cathodic. The spot of rust forms at the current of the drop of water. In a moist environment this form of corrosion occurs where some object rests on a metal surface and screens that portion of the surface from oxygen access. For example, steel plate will rust under a block of wood that is left lying for some time. Steel or iron equipment exposed to the weather for a long time will rust because of the stagnant films of water left in recesses on the metal surface. Corrosion from differential aeration leads to pitting of the surface.

When two dissimilar metals are in contact with one another in an electrolyte, Galvanic corrosion which is electrochemical corrosion occurs. If the two dissimilar metals are physically touching, or if they are otherwise electrically connected, the potential difference causes an electron flow between them. The less corrosion resistant metal becomes anodic and corrodes, and the more corrosion resistant metal becomes cathodic. The cathodic metal corrodes very little or not at all in this situation.

The chemical reaction at the cathode may be either hydrogen evolution or oxygen absorption depending on the nature of the corrosive environment. The free electrons resulting from the anodic metal transforming into ions and going into solution flow through the electrical junction between the two metals and are intercepted by positive ions from the solution at the cathode.

To account for environmental conditions met in the practical applications, a series was devised of the more often used industrial metals and alloys listing them from the material most easily corroded to that least likely to corrode. This listing, called the galvanic series, is given in Table 2.1 (Fontana and Greene, 1967).

Anodic, most readily corroded
Magnesium and magnesium alloys
Zinc
Commercially pure aluminum
Cadmiun
Aluminum alloy (4.5%Cu, 1.5%Mg, 0.6%Mn)
Steel or iron
Cast iron
Chromium stainless steel, 13%Cr (active)
High nickel cast iron
18%Cr, 8%Ni steel (active)
18%Cr, 8%Ni, 3%Mo steel (active)
Hastelloy C (active) (62%Ni, 18%Cr, 15%Mo)
Lead-tin solders
Lead
Tin
Nickel (active)
Inconel (active) (80%Ni, 13%Cr, 7%Fe)
Hastelloy A (62%Ni, 20%Mo, 20%Fe)
Hastelloy B (65%Ni, 30%Mo, 5%Fe)
Chorimet 2 (66%Ni, 32%Mo, 1%Fe)
Brasses (Cu-Sn)
Copper
Bronzes (Cu-Sn)
Copper-nickel alloys
Monel (70%Ni, 30%Cu)
Silver solder
Nickel (passive)
Inconel (passive) (80%Ni, 13%Cr, 7%Fe)
Chromium stainless steel, 13%Cr (passive)
18%Cr, 8%NI steel (passive)
18%Cr, 8%Ni, 3%Mo steel (passive)
Hastelloy C (passive) (62%Ni, 18%Cr, 15%Mo)
Chorimet 3 (62%Ni, 18%Cr, 18%Mo)
Silver
Titanium
Graphite
Gold and Platinum
Cathodic, least likely to corrode

Table 2.1 Galvanic Series of Metals and Alloys in Seawater

In general, the relative positions of the materials in the galvanic series agree with the positions of their constituent elements in the series of standard electrode potentials. When those metals and alloys listed in Table 2.1 that are adjacent to one another (or only slightly separated in the listing) are coupled in a practical situation, there is little danger of galvanic corrosion. This situation happens because the relative electrical potential generated between the two materials is not great. The farther apart the two materials in the couple are in the galvanic series, the greater the potential generated by electrically connecting them; hence, the more rapid the corrosion.

2.2. TYPES OF MARINE CORROSION

Depending on the exposure environment, marine corrosion may be divided into four categories (Melchers 1999): (1) immersion; (2) splash/tidal zone; (3) atmospheric; (4) (semi-)enclosed space. These are each of considerable practical importance.

Marine structures operate in a complex environment. Water properties, such as salinity, temperature, oxygen content, pH level can chemical composition can vary according to location and water depth. For the ship structures, the inside faces of plates will also be exposed to aggressive environments existing in cargo tanks. A summary of the environmental factors which are considered to have possible effects on corrosion of milde and low alloy steels is given in Table 2.2 (Melchers 1999).

Factor	Effect on initial corrosion rate	Effect on steady state corrosion rate	Influenced by
Biological			
• Bacterial • Biomass/plant life • Animal life	None	Reduces and probably controls rate	• Temperature of seawater • NaCl concentration • Water velocity • Suspended solids • Pollutant type and level • Percentage wetting
Chemical			
• O_2	Directly proportional	None, if corrosion controlled by O_2 transfer rate	• Seawater temperature • NaCl
• CO_2	Little effect	Little effect	
• NaCl	Inversely proportional	Proportional?	• Unimportant in open oceans • Fresh water inflows • Effect of biological activity
• pH	Little effect?	Little effect?	
• Carbonate solubility	Little effect	Little effect	
• Pollutants	Varies	Varies	• Geographical location
Physical			
• Temperature	Directly proportional	Proportional?	• Geographical location
• Pressure			• Not significant for shallow waters
• Water velocity	Little effect?	Little effect?	• Geographical location
• Suspended solids		Little effect, if any	• Geographical location
• Percentage wetting	Proportional for tidal and splash zones	Proportional for tidal and splash zones	• Location, weather patterns

Table 2.2 Environmental factors in marine corrosion

Corrosion of metals can occur in various forms. Figure 2.1 gives a schematic summary of typical corrosion patterns (Melchers 2003). Uniform general corrosion is reflected in a generalized decrease of plate thickness. No account is taken of limited pitting corrosion, even though it occurs to a greater or lesser degree in all longer term marine corrosion. Thus, uniform corrosion is a convenient but not necessarily accurate description. Although for mild and low-alloy steels, corrosion usually approximates a near-uniform loss (Melchers 2003).

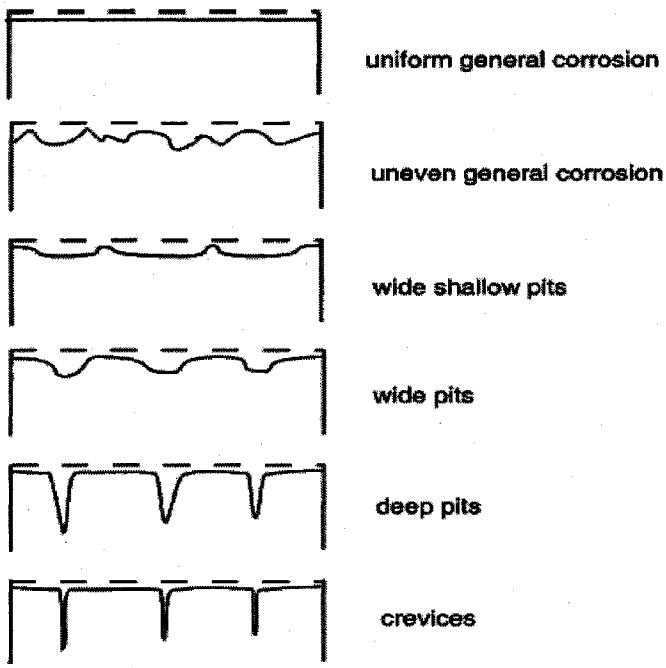

Figure 2.1 Corrosion types

Pitting corrosion is important for containment. Crevice corrosion is relevant mainly to stainless steels at fittings, bolts, etc. Galvanic corrosion caused by differences in material properties around the heat-affected zone (HAZ) of welds may be important for strength considerations of local details and for overall strength of stiffened plates.

Table 2.3 sets out the main types of corrosion, summarizes some characteristics, and indicates where it may be an issue for ships and offshore structures.

Type of corrosion	Material	Feature	Problem areas	Effect
general (or 'uniform')	mild, high tensile steels	roughly uniform over extended areas	plating	reduction in plate thickness, structural capacity
pitting	limited for mild steels, mainly high tensile and stainless steels	highly localized penetration, often with clusters of pits	plating, local details	local reduction in thickness and stress intensification, possibly leakage
crevice	mainly stainless and some high tensile steels	highly localized elongated penetration	at connections, under washers, etc.	localized stress intensifcation, local failure
galvanic	dissimilar metals in contact	localized	different metals in contact, variation in metal composition, HAZs for welds	localized severe material loss

Table 2.3 Main types of corrosion relevant to ships and offshore structures

Because corrosion is a function of many variables, and many of these variables have uncertain nature, a probabilistic model is more appropriate to describe the expected corrosion. Melchers (1997) constructed a probabilistic phenomenological model for corrosion from a mean value expression and an expression picking up random and other uncertainties not modeled in the mean value expression, as follows:

$$c(t,E) = f_n(t,E) + \varepsilon(t,E) \tag{2.4}$$

where c(t,E) is the weight-loss of material, f_n(t,E) is a mean valued function, ε(t,E) is a zero mean error function, t is time, E is a vector of environmental conditions.

Some fundamental studies on the corrosion mechanism of the unprotected steel specimen have been carried out by Melchers (1995a, 1997, 1998, 1999, and 2003a, 2003b). For the unprotected steel structures, the corrosion process can be divided into four stages, which is shown in Figure 2.2:

1) Initial corrosion;

2) Oxygen diffusion controlled by corrosion products and micro-organic growth;

3) Limitations on food supply for aerobic activity;

4) Anaerobic activity.

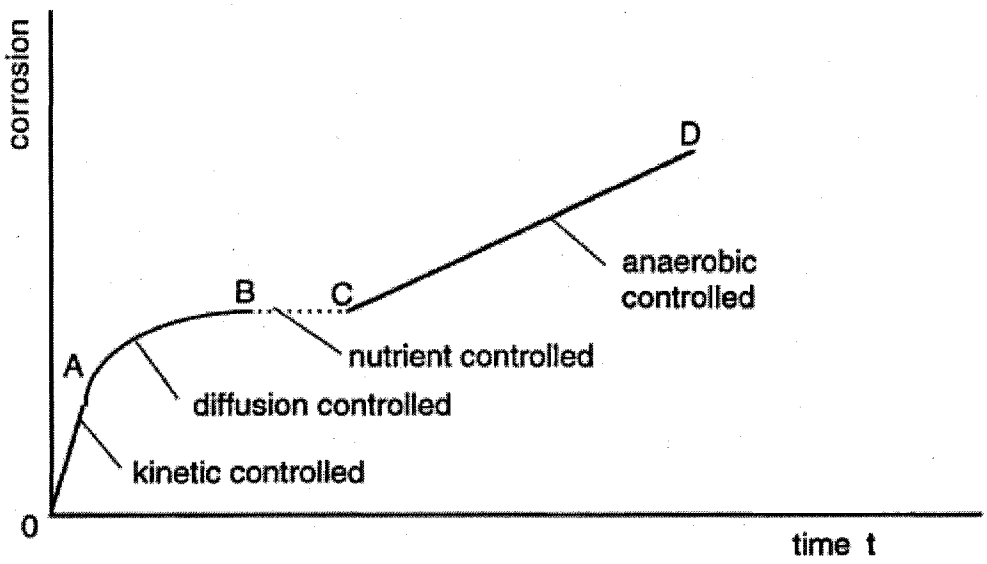

Figure 2.2 Melchers conceptual model for marine corrosion

For some stages, the main environmental parameters, E, have been recognized and quantified. But for other stages, better understanding of the corrosion mechanism is still required. Table 2.2 also indicated this current state-of-the-art where many question marks exist. Therefore, further research is still needed in order to apply the probabilistic phenomenological model.

2.3. EXISTING CORROSION MODELS

Based on empirical models for immersion corrosion conditions, Southwell et al. (1979) proposed a linear model and a bilinear model.

Southwell linear model:

$$d(t) = 0.076 + 0.038t \tag{2.5}$$

Southwell bilinear model:

$$d(t) = \begin{cases} 0.09t & 0 < t < 1.46(years) \\ 0.076 + 0.038t & 1.46 < t < 16(years) \end{cases} \tag{2.6}$$

where d(t) is the thickness of the corrosion wastage at time t.

Also an alternative was attempted to fit a non-linear function to the data, given by Melchers (1995b).

Melchers-Southwell nonlinear model:

$$d(t) = 0.084t^{0.823} \tag{2.7}$$

Melchers (1998) also suggested a trilinear and another power approximation for corrosion wastage thickness, which are given as:

Melchers trilinear model:

$$d(t) = \begin{cases} 0.170t & 0 \le t < 1 \\ 0.152 + 0.0186t & 1 \le t < 8 \\ -0.364 + 0.083t & 8 \le t \le 16 \end{cases} \tag{2.8}$$

Melchers power model:

$$d(t) = 0.1207t^{0.6257} \tag{2.9}$$

Usually, the conventional corrosion models assume a constant corrosion rate, resulting in a linear decrease of plate thickness with time. However, experimental evidence of corrosion reported by various authors shows that a nonlinear model is more appropriate.

Based on some observations reported in the literature, Guedes Soares and Garbatov (1999) proposed a nonlinear model to describe the growth of corrosion. The whole corrosion process was divided into three phases, shown in Figure 2.3.

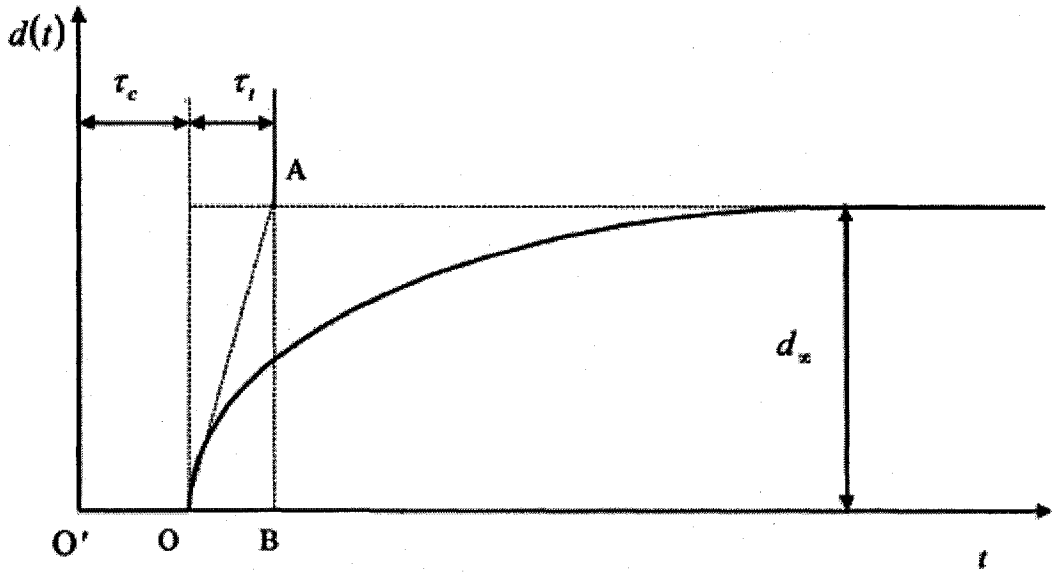

Figure 2.3 Thickness of corrosion wastage as a function of time

In the first phase, $t \in [o', o]$ in Figure 2.3, it is assumed that there is no corrosion because the corrosion protection system (CPS) is effective. The first stage depends on many factors and statistics show that in ships it varies in the range of 1.5-5.5 years (Emi, et al. 1994) or in the range of 5-10 years (Loseth, et al. 1994). The second phase, $t \in [o, B]$ in Figure 2.3, is initiated when the corrosion protection is damaged and corresponds really to the existence of corrosion, which decreases the thickness of plate. This process was observed to last a period around 4-5 years in typical ship plating (Maximadj, et al. 1982). The third phase, $t \in [B, \infty]$ in Figure 2.3, corresponds to a stop in the corrosion process and the corrosion rate becomes zero. The corroded material stays on the plate surface,

protecting it from the contact with the corrosive environment and the corrosion process stops. Cleaning the surface or any involuntary action that removes that surface material originates the new start of the nonlinear corrosion growth process. This removal is not considered in the study by Guedes Soares and Garbatov (1999).

The model proposed by Guedes Soares and Garbatov (1999) is given as

$$d(t) = \begin{cases} 0 & t \le \tau_c \\ d_\infty \left(1 - \exp\left(-\dfrac{t-\tau_c}{\tau_t}\right)\right) & t > \tau_c \end{cases} \tag{2.10}$$

where d(t) is the thickness of the wastage at time t, d_∞ is the long-term thickness of the corrosion wastage, τ_c is the coating life, and τ_t is the transition time. In this model, three parameters, d_∞, τ_c, and τ_t, are used to describe the corrosion process.

Paik and Thayamballi (2003) proposed a corrosion process model for a coated area in a marine steel structure, shown in Figure 2.4. The corrosion behavior in this model is categorized into three phases: (1) durability of coating; (2) transition to visibly obvious corrosion; (3) progress of such corrosion.

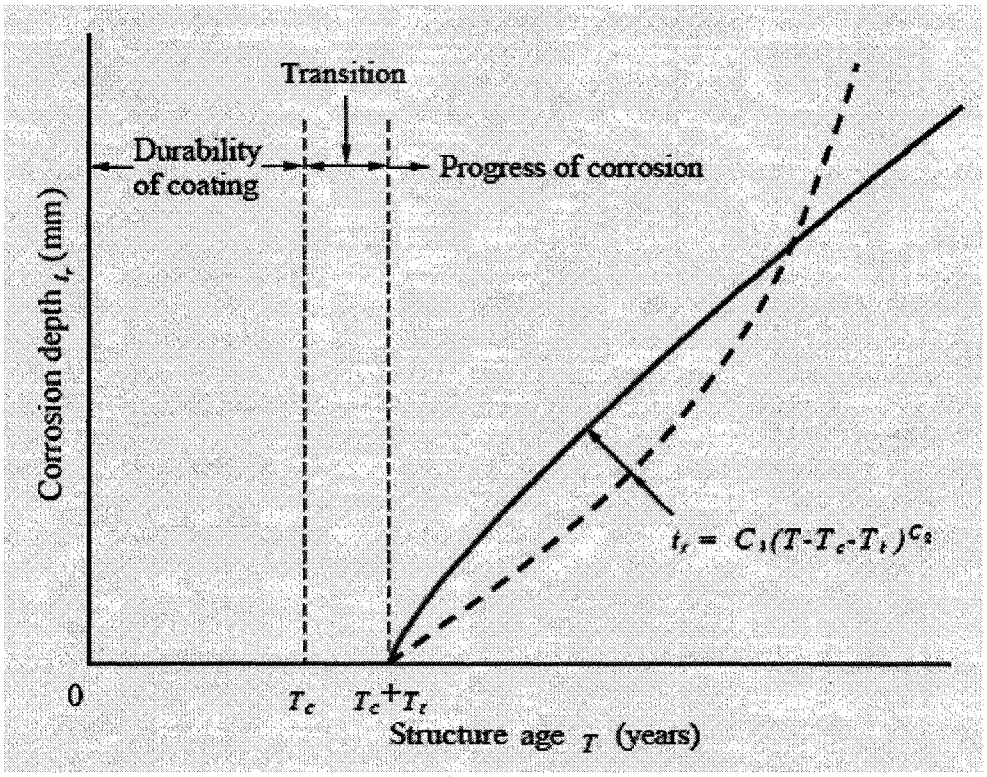

Figure 2.4 A schematic of the corrosion process for marine structures

As shown in Figure 2.4, the curve showing corrosion progression may be convex, as indicated by the solid line, or may in some cases be a concave indicated by the dotted line. The convex curve indicates that the corrosion rate is increasing in the beginning, but is decreasing as the corrosion progress proceeds. This is because corroded material stays on the steel surface, protecting it from contact with the corrosive environment, and the corrosion process stops, which is similar to Guedes Soares and Garbatov (1999) proposed model. This type of corrosion progression may be typical for statically loaded structures so that relatively static corrosion scale at the steel surface can disturb the corrosion progression.

On the other hand, the concave curve (dotted line) in Figure 2.4 represents a case where the corrosion rate is accelerating as the corrosion progress proceeds. This type of corrosion progression may be likely to happen in dynamically loaded structures, such as ship structures where structural flexing due to wave loading continually exposes additional fresh surface to the corrosive attack.

The life of coating depends on the type of coating systems used, details of its application, and relevant maintenance, etc. The coating life to a predefined state of breakdown is often assumed to follow the log-normal distribution (Yamamoto and Ikegami 1998). In corrosion loss measurements, the information of the coating life is normally unclear. In fact, a 5 year coating life is considered to represent undesirable situation, while 10 year or longer will be representative of a relatively more desirable state of affairs.

After the effectiveness of coating is lost, some transition time, that is, duration between the time of coating effectiveness loss and the time of corrosion initiation, may be considered to exist before the corrosion initiate over a large enough and measurable area. The transition time is often considered to be an exponentially distributed random variable (Yamamoto and Ikegami 1998). As an example, the mean value of the transition time for transverse bulkhead structures of bulk carriers is shown to be 3 years for deep tank bulkheads, 2 years for watertight bulkheads, and 1.5 years for stool regions. When the transition time is assumed to be zero, it is implied that the corrosion will start immediately after the coating effectiveness is lost.

Based on the corrosion process model, the depth of corrosion wastage is expressible as a function of time after the corrosion starts, as follows (Paik, et al. 2003)

$$t_r = C_1(T - T_c - T_t)^{C_2} \tag{2.11}$$

where t_r is depth of corrosion wastage in mm, T is age of vessel in years, T_c is life of coating in years, T_t is duration of transition in years. C_1 and C_2 are coefficients determined by the statistical analysis of corrosion measurement data. For corrosion of marine structures, some past studies indicate that the coefficient C_2 for marine structures may be typically in the range of 0.3-1.5. The coefficient C_1 is assumed to follow Weibull distribution (Paik, et al. 2003).

Qin and Cui (2003) assumed the corrosion protection system (CPS) would deteriorate gradually and the corrosion may start as pitting corrosion before the CPS loses its complete effectiveness. For each CPS, two parameters T_{st} and T_{cl} may be used to describe its corrosion protection function. T_{st} is the instant at which the pitting corrosion starts. This quantity can be measured. T_{cl} is the life of the CPS at which general corrosion starts.

By distinguishing the corrosion initiation life T_{st} and the life of the CPS T_{cl}, in the stage of pitting corrosion progress, both the CPS and the environmental parameters will affect the corrosion rate. The corrosion rate can be defined by equating the volume of pitting corrosion to uniform corrosion. This can be regarded as the transition period and the corrosion rate increases. After the CPS loses its complete effectiveness, general corrosion starts and the corrosion rate decreases owing to the increasing thickness of the corrosion product (and the microbial biomass).

The proposed a corrosion model is as follows (Qin and Cui 2003)

$$d(t)=\begin{cases} 0 & 0 \le t \le T_{st} \\ d_{\infty}\left(1-\exp\left(-\dfrac{t-T_{st}}{\eta}\right)^{\beta}\right) & T_{st} \le t \le T_L \end{cases} \tag{2.12}$$

where d(t) is the corrosion wastage at time t, d_∞ is the long-term thickness of the corrosion wastage, T_{st} is the instant at which the pitting corrosion starts, T_L is the life of the structure or the time at which repair and maintenance action takes place. β and η are model parameters determined by corrosion measurement data.

2.4. CORROSION MEASUREMENT DATA ANALYSIS AND CORROSION MODELS COMPARISON

Measured data for the corrosion loss in structural members of seawater ballast tanks and cargo tanks for ocean-going oil tankers have been collected (Wang et al. 2003). It is seen that in the literature there are many existing corrosion models, like the ones reviewed in the preceding section. Therefore it is worthwhile to consider the adequacy of each model by comparing it with full scale measured data.

Two sets of corrosion data, deck plates on ballast and cargo tanks of oil tankers provided by ABS, are analyzed in this study (ABS 2002, Wang et al. 2003, and Garbatov, et al. 2005). The first set includes 1168 corrosion measurements of deck plates from ballast tanks with original nominal thickness varying from 13.5 mm to 35 mm on ships with lengths between perpendiculars in the range of 163.5 m to 401 m, and service years with the range 12-26 years, and 32 years, shown in Figure 2.5.

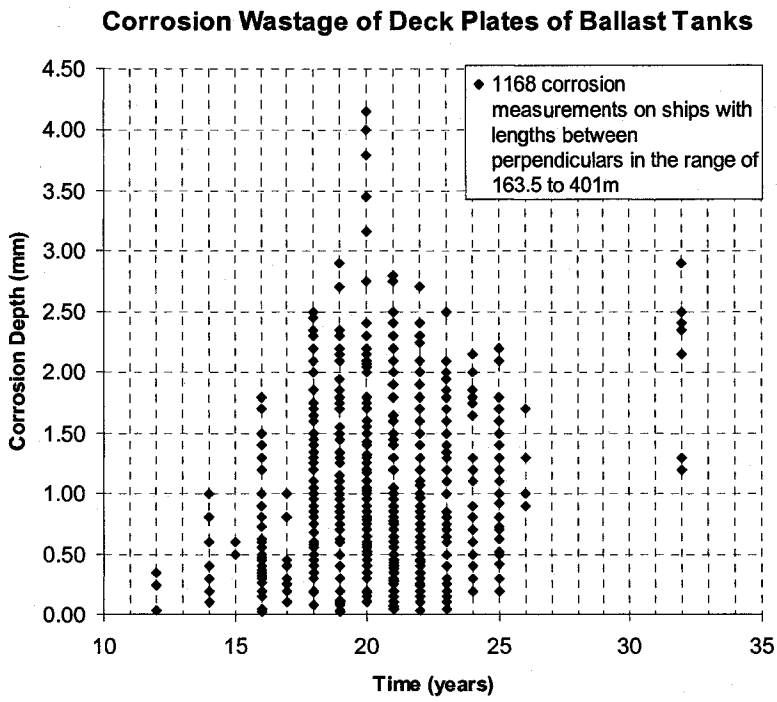

Figure 2.5 Corrosion wastage of deck plates in ballast tanks

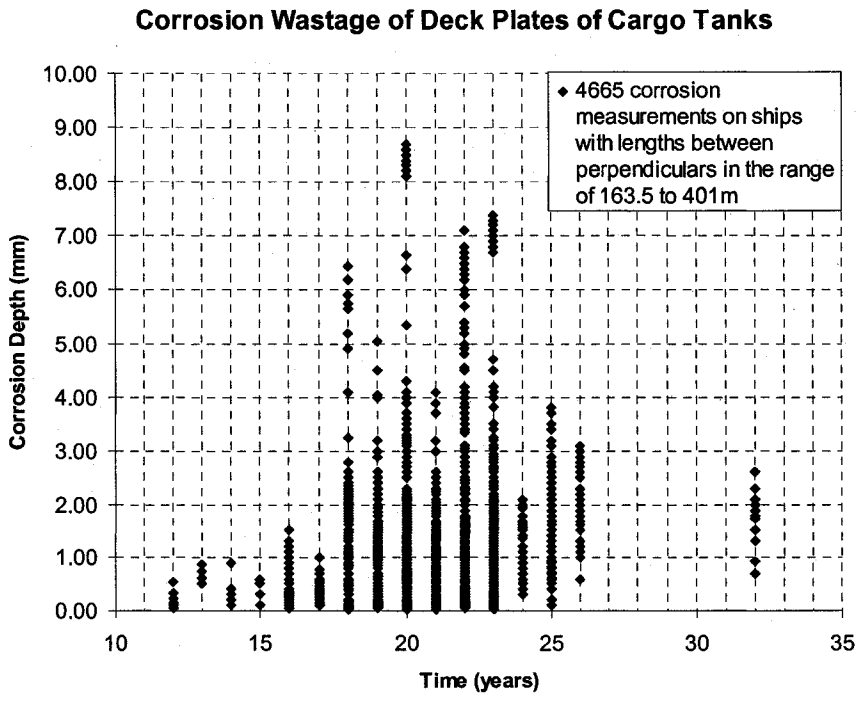

Figure 2.6 Corrosion wastage of deck plates in cargo tanks

The second set of data includes 4665 corrosion measurements of deck plates from cargo tanks with original nominal thickness varying from 12.7 mm to 35 mm on ships with lengths between perpendiculars in the range of 163.5 m to 401 m, and service years with the range 12-26 years, and 32 years, shown in Figure 2.6.

It is seen from Figure 2.5 and Figure 2.6 that the distribution of corrosion wastage is very scattered. The sources of such uncertainty involved are various, such as differences in data collection sties typically visited over the life of the vessel and possibly also differing time between visits. That is, it is normally difficult to track corrosion at a particular site based on the typically available thickness gauging data for ships, which are mostly obtained at periodic inspections of different representative regions of the structure. This is part of the reason for the relatively large scatter of corrosion data in many studies (Paik, et al. 2003). Also the coating life is a factor in such uncertainties. It should be noted that some of the data used in this study may pertain to uncoated spaces, especially in the cargo tanks, while any information about coating life is not available.

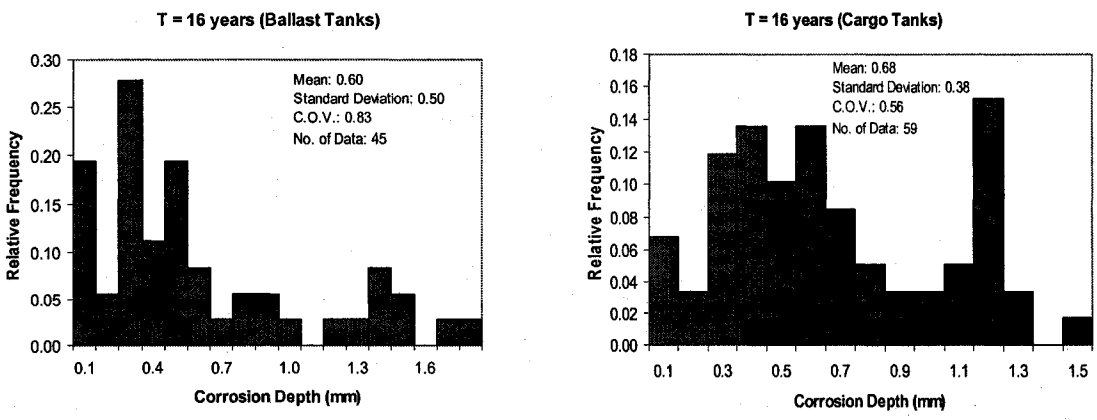

Figure 2.7 Relative frequency of corrosion wastage of deck plates for 16th year in ballast tanks and cargo tanks, respectively

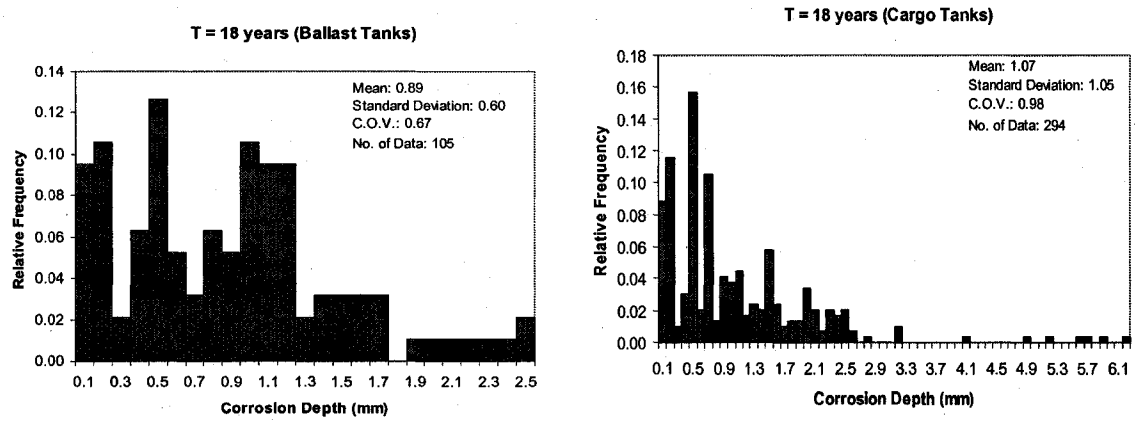

Figure 2.8 Relative frequency of corrosion wastage of deck plates for 18th year in ballast tanks and cargo tanks, respectively

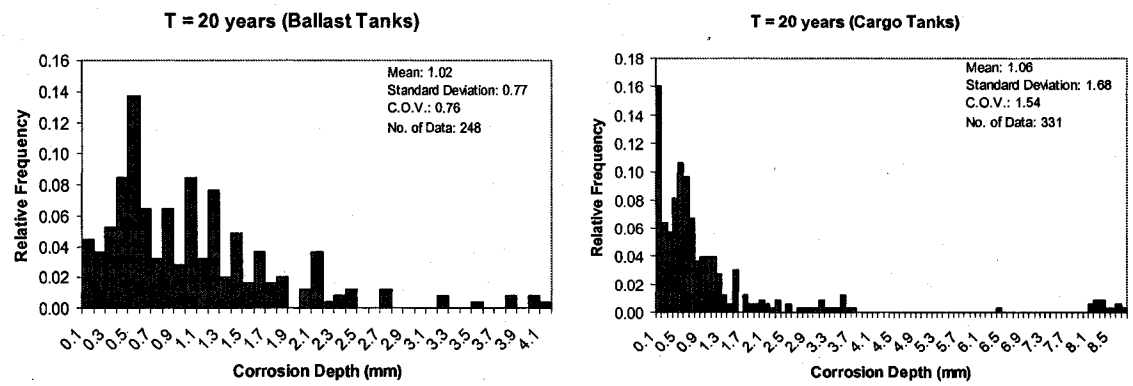

Figure 2.9 Relative frequency of corrosion wastage of deck plates for 20th year in ballast tanks and cargo tanks, respectively

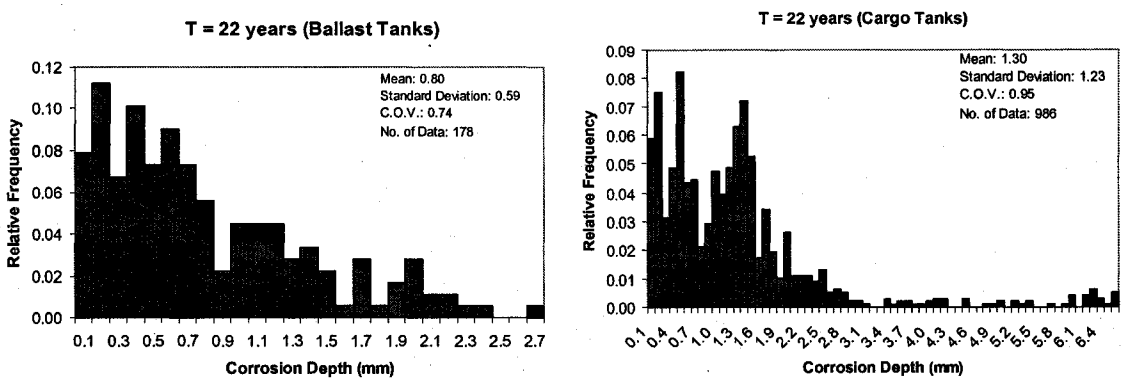

Figure 2.10 Relative frequency of corrosion wastage of deck plates for 22nd year in ballast tanks and cargo tanks, respectively

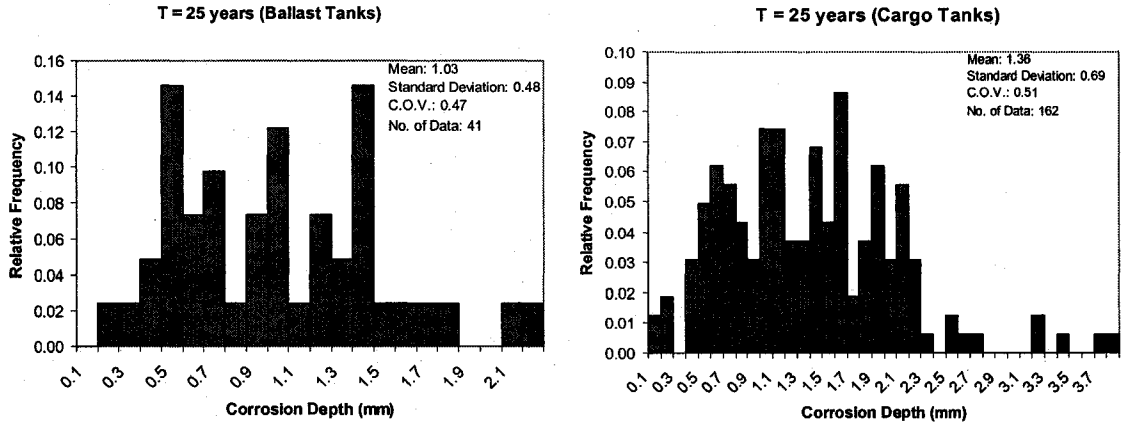

Figure 2.11 Relative frequency of corrosion wastage of deck plates for 25th year in ballast tanks and cargo tanks, respectively

Figures 2.7-2.11 show the relative frequency of corrosion wastage of deck plates for different ship ages in both ballast tanks and cargo tanks. Roughly the frequency distribution of corrosion depth at younger age tends to follow the normal function. As ship gets older, it more likely follows log-normal function, then turns into normal finally.

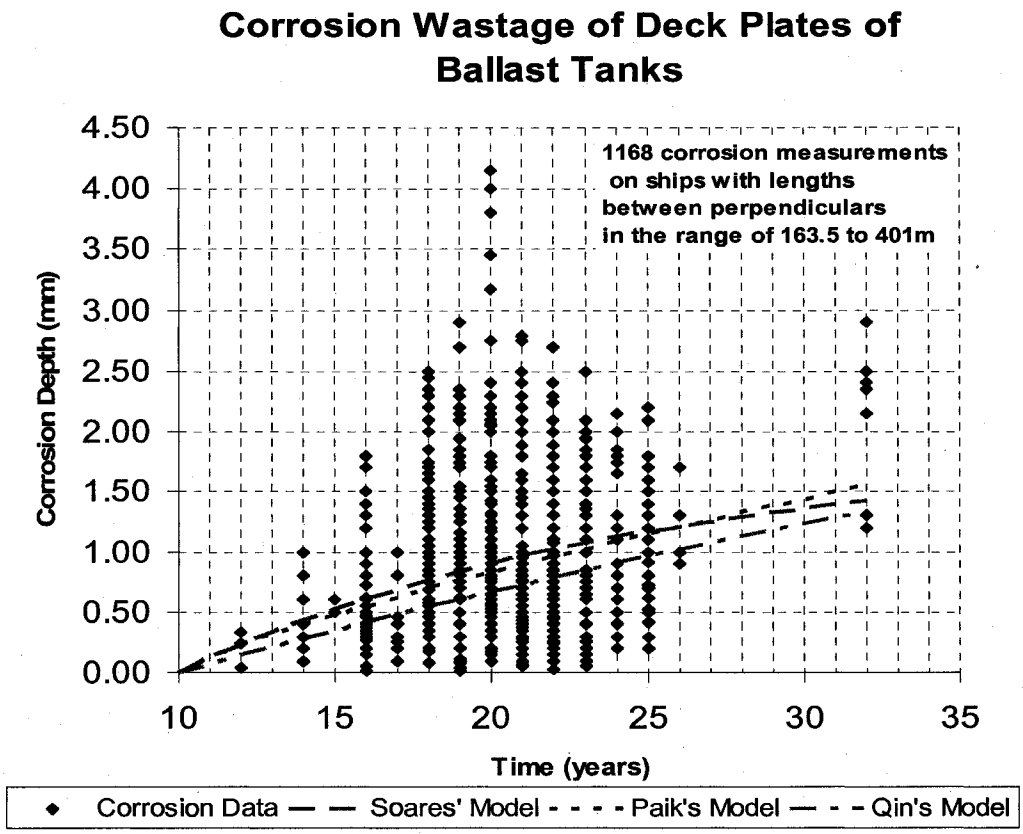

Figure 2.12 Comparison of major corrosion models, together with the measured corrosion data of deck plates in ballast tanks

Figure 2.12 shows the comparison of major existing corrosion models like those described in previous section, together with measured corrosion data of deck plates in ballast tanks. All the parameters of the corrosion models are determined based on the measured data. From the graphs, it is seen that (Guedes) Soares' model and Paik's model are very similar in this circumstance. Qin's model underestimates the corrosion wastage in some respect.

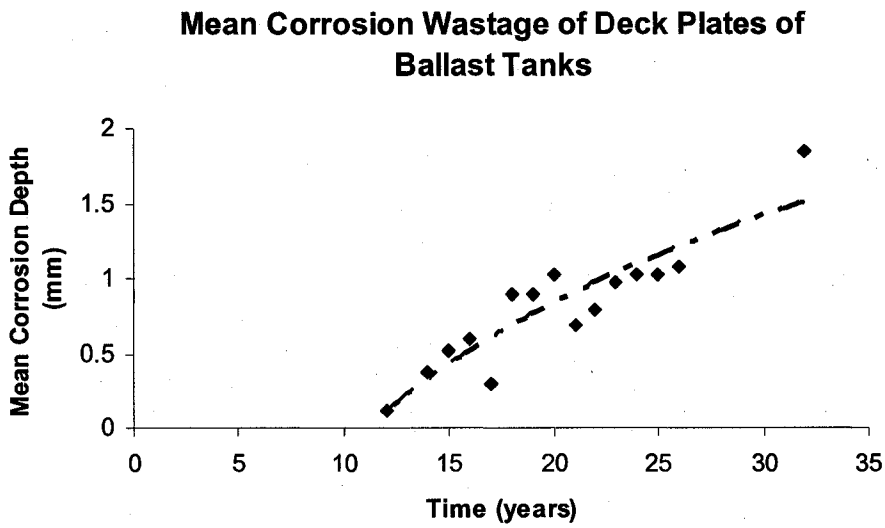

Figure 2.13 Proposed corrosion model (ballast tanks)

Based on the mean corrosion wastage data, a nonlinear time-variant corrosion model is proposed using regression analysis for the deck plates in ballast tanks of oil tankers.

$$d(t) = 1.4283\log(t) - 3.3402 \tag{2.13}$$

Where d(t) is the corrosion wastage at time t in years. The corrosion model is shown in Figure 2.13 together with mean corrosion wastage data, in which the dotted line represents the corrosion model, and the diamond dots stands for corrosion wastage. .

As mentioned before there are many existing corrosion models. It is necessary to verify the proposed model by comparing it with those existing models. For simplicity, only major corrosion models are chosen. They include Southwell's bilinear model, Melchers' power model, Soares' model, Paik's model, and Qin's model. Figure 2.14 shows the comparison results, together with corrosion wastage measurements.

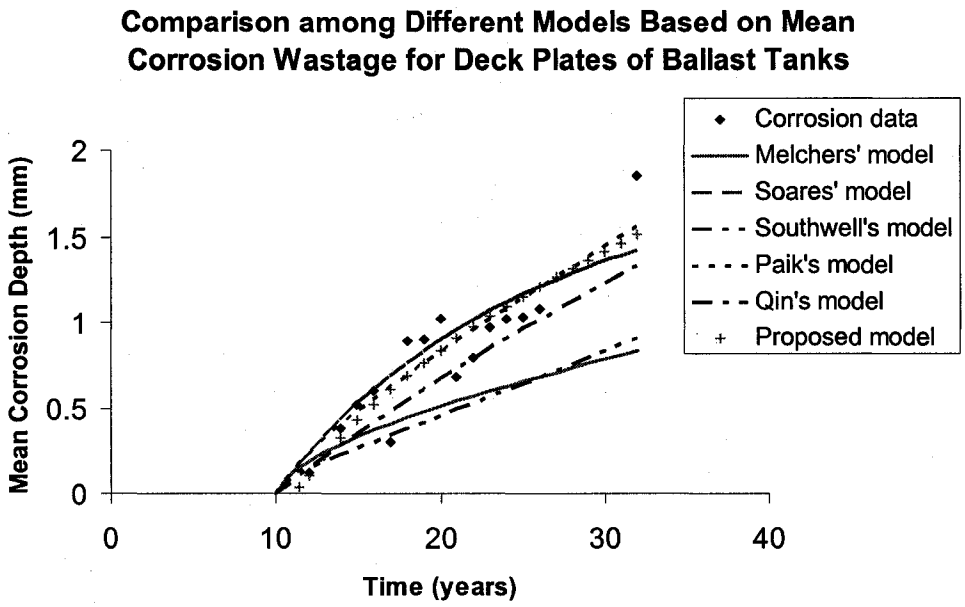

Figure 2.14 Comparison of existing corrosion models (ballast tanks)

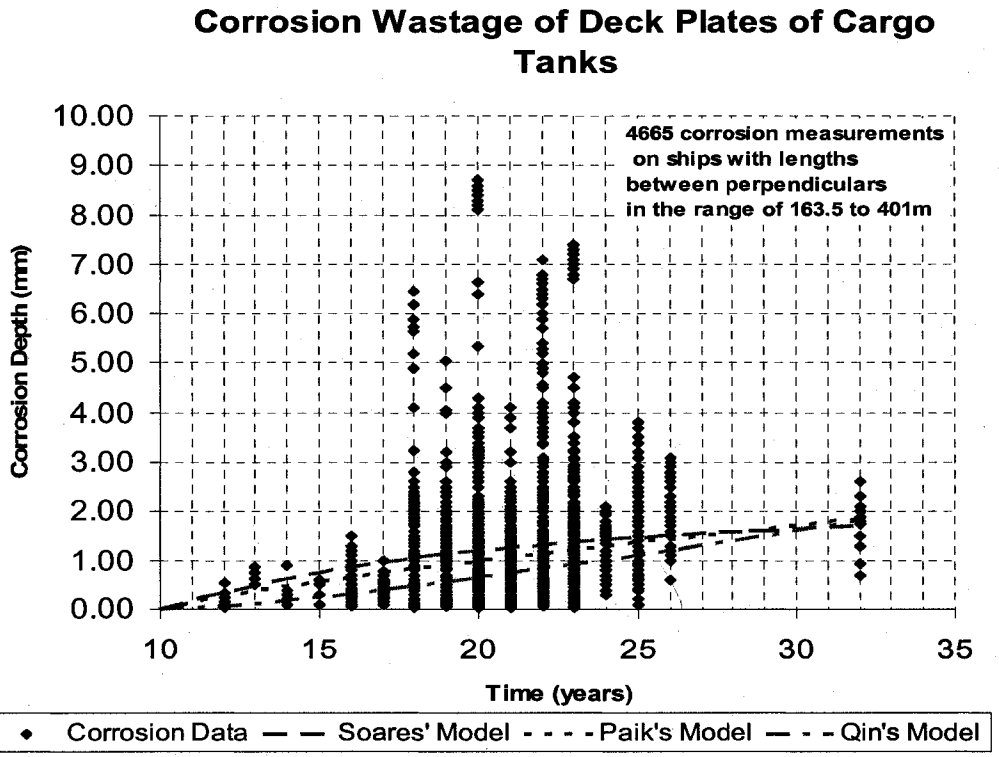

Figure 2.15 Comparison of major corrosion models, together with the measured corrosion data of deck plates in cargo tanks

Figure 2.15 shows the comparison of major existing corrosion models as described in previous section, together with measured corrosion data of deck plates in cargo tanks. All the parameters of the corrosion models are determined based on the measured data. From the graphs, it is seen that Soares' model and Paik's model are very close. Qin's model underestimates the corrosion wastage in this circumstance.

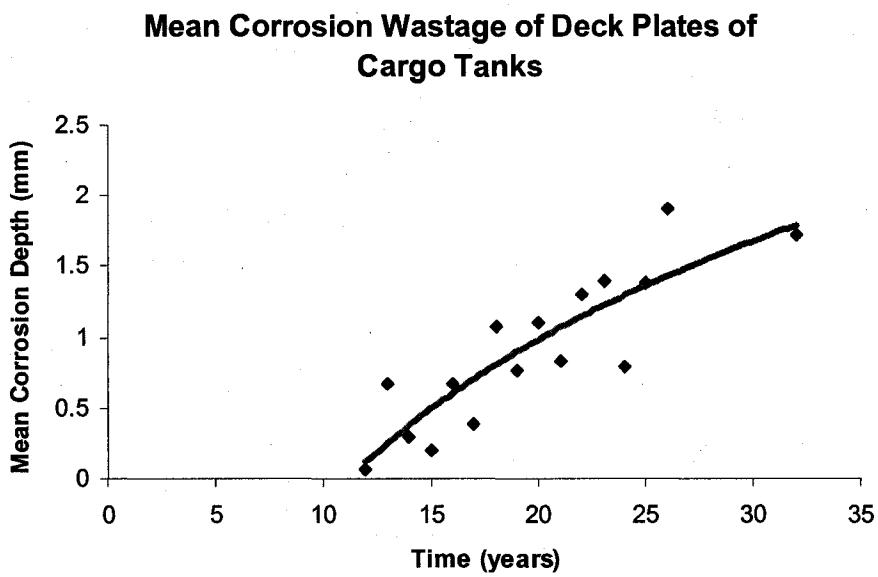

Figure 2.16 Proposed corrosion model (cargo tanks)

Based on the mean corrosion wastage data, a nonlinear time-variant corrosion model is proposed using regression analysis for the deck plates in ballast tanks of oil tankers.

$$d(t) = 1.704\log(t) - 4.0173 \qquad (2.14)$$

Where d(t) is the corrosion wastage at time t in years. The corrosion model is shown in Figure 2.16 together with mean corrosion wastage data, in which the red line represents the corrosion model, and the diamond dots stands for corrosion wastage.

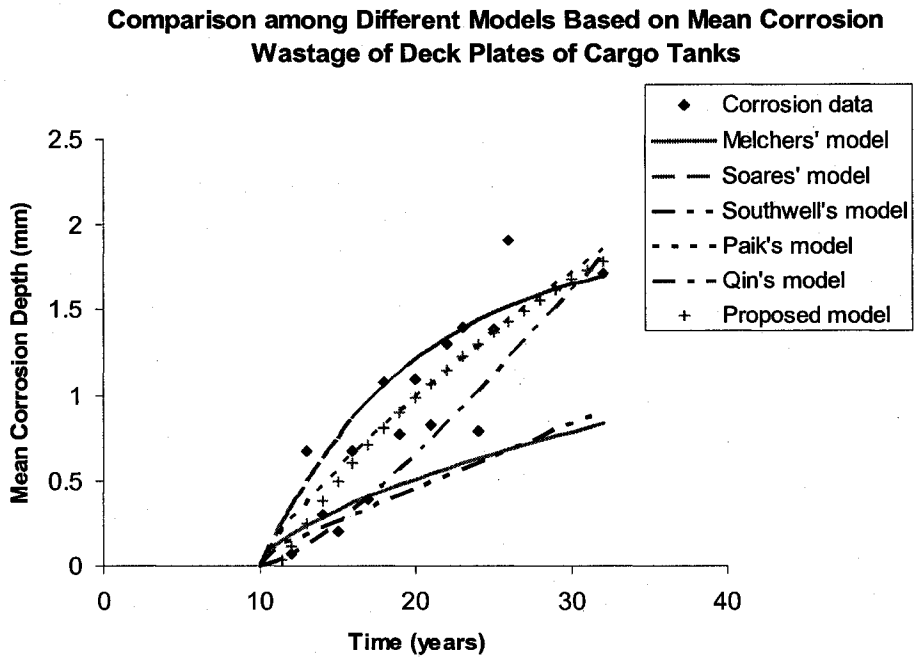

Figure 2.17 Comparison of existing corrosion models (cargo tanks)

Figure 2.17 shows a comparison between existing corrosion models, together with corrosion wastage measurements. Based on these comparisons, it can be concluded:

1. The Southwell's model and Melchers' model are simple and easy to use, but they cannot capture the time-variant corrosion wastage tendency. Generally, they underestimate the corrosion wastage.
2. The Soares' model, Paik's model and Qin's model fit the data much better. Soares' model has a good curve-fitting capability, but the parameters, d_∞ and τ_t, are very crucial. In some circumstances, they are hard to determine.
3. Paik's model has very close results to Soares' model. Once corrosion measurement data are obtained, the parameters in Paik's model can be determined more easily and accurately than those in Soares' model.

4. Qin's model underestimates the time-variant corrosion wastage in both circumstances. Therefore it may not be conservative under some circumstances.
5. The Proposed corrosion model is similar to Paik's model with errors under 2%. But it is faster and easier to estimate the time-variant corrosion wastage in the deck plates both in ballast tanks and cargo tanks.

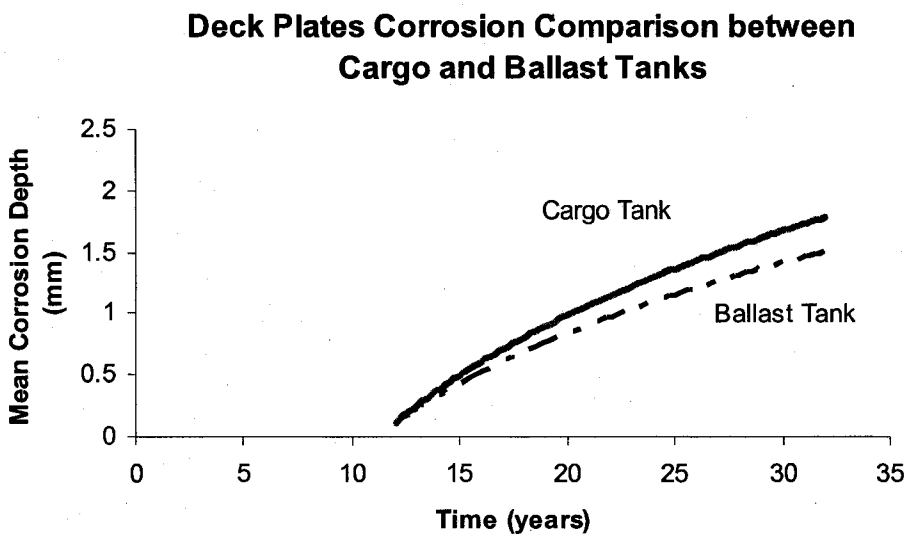

Figure 2.18 Comparison of proposed corrosion models for ballast tanks and cargo tanks

Figure 2.18 shows the comparison between the two proposed corrosion model for ballast tanks and cargo tanks. It is seen that corrosion is slightly more severe in cargo tanks than in ballast tanks based on the measurements taken in deck plates of tankers.

3. ULTIMATE STRENGTH OF UNSTIFFENED PLATES CONSIDERING PIT CORROSION

For general corrosion which uniformly reduces the plate thickness, the ultimate strength for the corroded plates is typically calculated by excluding the thickness loss due to corrosion. For the localized corrosion such as pitting or grooving, the ultimate strength calculation procedure may be more complex. For a simplified pessimistic treatment, the corroded plates can be idealized using an equivalent general corrosion. However, this treatment is not always relevant since it is not straightforward to define the equivalent general corrosion. Therefore, the influence of pit corrosion on the ultimate strength of steel plates needs to be specifically examined.

The aim of the study is to investigate the ultimate strength of unstiffened plates with pit corrosion wastage under axial compressive loads. The nonlinear finite element analysis software ANSYS is utilized. In order to examine the capability of the finite element program, the ultimate strength of intact plates is studied firstly. Effects of boundary conditions, strain hardening, and initial imperfections are also studied. A series of buckling and post-buckling numerical analyses are carried out. The effects of different degrees of pit corrosion wastage on the ultimate compressive strength are examined in the late of the portion

3.1. PHYSICAL GEOMETRY AND MATERIAL PROPERTIES

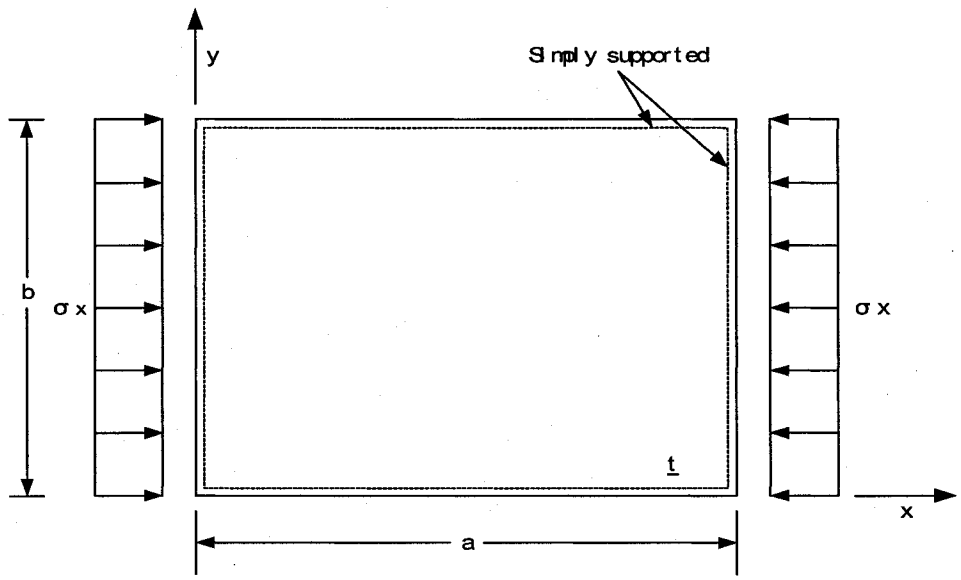

Figure 3.1 A simply supported steel plate under axial compressive loads

Buckling of plates between stiffeners is a basic failure mode in stiffened panels. Figure 3.1 is a typical steel plate between stiffeners from a continuous stiffened structure, which is subjected to axial compressive loads. The plate has length a, breadth b, and thickness t.

Plate elements in steel-plated structures are supported by numerous types of members along the edges, which have finite values of torsional rigidity. Depending on the torsional rigidity of the support members, the rotation along the plate edges will to some extent be restrained. When the rotational restraints are zero, the edge condition is a simply supported case, while the edge condition becomes clamped when the rotational restraints are infinite. For conservation, this study deals with the simply supported boundary condition. Though it is ideal, it is often adequate for practical design purposes.

The material of the plates used is usually mild steel or high tensile steel, with yield strength σ_0 in the range of 230 – 450 MPa. The Young modulus and Poisson's ratio are E and ν respectively. The plate bending rigidity is $D = Et^3/[12(1-\nu^2)]$. The plate reduced slenderness ratio is $\beta = (b/t)[\sigma_0/E]^{1/2}$.

As we know, there are age related degradations. Corrosion is the important one. It is categorized as general corrosion, which uniformly reduces the thickness of structural members, and localized corrosion, which causes degradation in local areas. The corrosion degradation of steel structures is influenced by many factors, like corrosion protection system, operational parameters, etc. Localized corrosion is as important as general corrosion, if not more. TSCF (1993) gave samples of the pit corrosion damage distribution in a plate of oil tankers, shown as figure 3.2. From these pictures, we can see, typically, the shape of pit corrosion on the plate is circular. Therefore circular holes are reasonable for simulating the pit corrosion when we are doing the finite element analysis. Figure 3.3 shows an idealized geometrical model of a steel plate with localized pit corrosion damage under axial compressive loads.

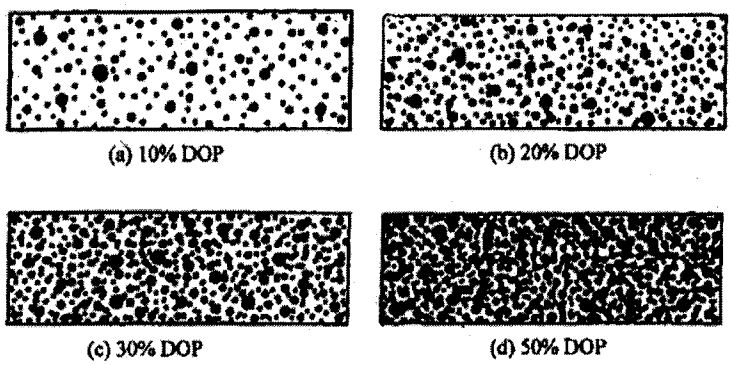

Figure 3.2 Pit corrosion intensity diagrams (DOP = degree of pit corrosion intensity as a ratio of the pitted cross section area to the original plate cross section area)

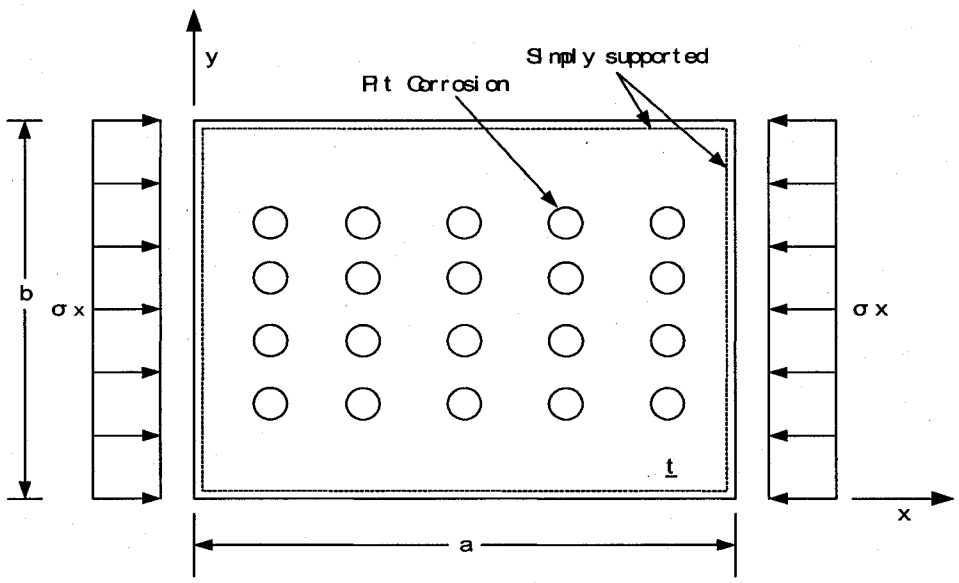

Figure 3.3 A steel plate with localized pit corrosion under axial compression

3.2. ELASTIC BUCKLING OF SIMPLY SUPPORTED PLATES - COMPARISON BETWEEN CLASSICAL THEORETICAL SOLUTION AND FEA SOLUTION

The elastic buckling of simply supported plated has been thoroughly studied through the decades. The elastic buckling stress solutions are widely available from classical works on the theory of elasticity (Bleich 1952, Timoshenko and Gere 1982). Therefore it is a good starting point for us to verify the FEA solutions. The elastic buckling strength of a plate with a/b $\geq$1 is typically given as:

$$\sigma_E = k\frac{\pi^2 E}{12(1-\nu^2)}\left(\frac{t}{b}\right)^2 \tag{3.1}$$

Where

σ_E : Plate elastic buckling strength under a single type of load.

k: Buckling coefficient for the corresponding load.

σ_E and k for various single types of loads are given in the following Table 3.1:

Load type	σ_E	k
σ_x	$\sigma_{xE,1}$	$k_x = [a/(m_0 b)+(m_0 b)/a]^2$ where m_0 is the buckling half-wave number for the plate in the x direction which is the minimum integer satisfying $a/b \le \sqrt{m_0(m_0+1)}$. For practical usage, he half-wave number m may be taken as $m_0 = 1$ for $1 \le a/b \le \sqrt{2}$, $m_0 = 2$ for $\sqrt{2} \le a/b \le \sqrt{6}$ and $m_0 = 3$ for $\sqrt{6} \le a/b \le 3$. If a/b > 3, the buckling coefficient can be approximated to $k_x = 4$.
σ_y	$\sigma_{yE,1}$	$k_y = \left[1+(b/a)^2\right]^2$
τ	$\tau_{E,1}$	$k_\tau \approx 4(b/a)^2 + 5.34$ for a/b ≥ 1 $k_\tau \approx 5.34(b/a)^2 + 4.0$ for a/b < 1
σ_{bx}	$\sigma_{bxE,1}$	$k_{bx} \approx 23.9$
σ_{by}	$\sigma_{byE,1}$	$k_{by} \approx \begin{cases} 23.9 & for \quad 1 \le a/b \le 1.5 \\ 15.87+1.87(a/b)^2+8.6(b/a)^2 & for \quad a/b > 1.5 \end{cases}$

Table 3.1 Buckling coefficients for a simply supported plate (a/b≥1) under single types of loads

Like shown as Figure 3.1, we choose a = 580mm, b = 500mm, t = 4.4mm, E = 197.5GPa, and ν = 0.3. From Equation 3.1 and Table 3.1, plate elastic buckling strength can be computed as σ_E = 56.52 MPa.

The finite element analysis program ANSYS (2005) has been used to analyze the elastic deflection behavior of the structure. A convergence study has been carried out firstly to determine a fine mesh size of the finite elements.

a coarse mesh with 16x14 elements, a regular mesh with 32x28 elements, and a fine mesh with 64x56 elements are chosen. The finite element models are shown as Figure 3.4. Along x direction compressive loads have been applied to both sides. All four sides are simply supported, which means displacements along z direction have been restrained. The boundary conditions and applied loads are shown clearly in Figure 3.5.

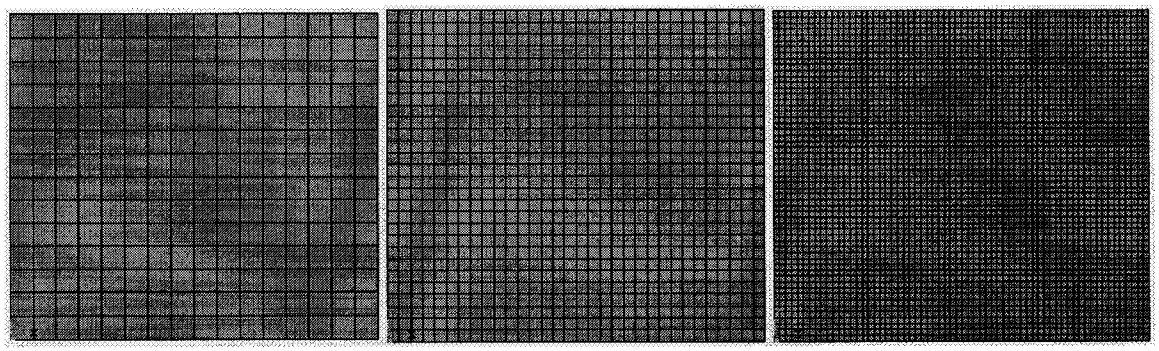

Figure 3.4 Finite element model with 16x14 elements

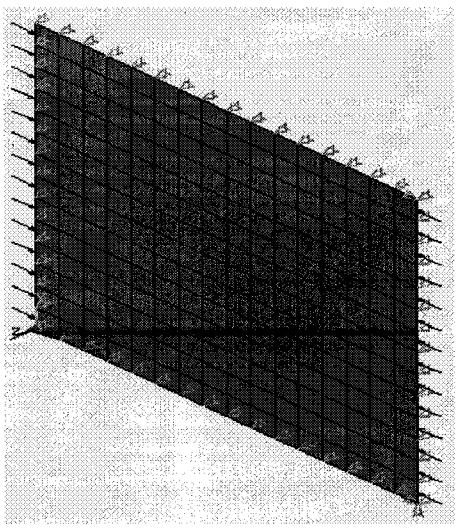

Figure 3.5 Finite element model with applied loads and boundary conditions

Eigen buckling has been carried out. The elastic buckling strength is computed as σ_E = 56.83 MPa from the finite element analysis for the coarse mesh; σ_E = 56.49 MPa for the regular mesh; and σ_E = 56.34 MPa for the fine mesh.

Through the series of comparisons, though three models give very close results, the computing time is much different. The refined model (64x56 elements) costs much more time. Besides it does not create too much different results comparing the regular model (32x28 elements). For the coarse model (16x14 elements), the result is a little away from the classic solution (.σ_E = 56.52 MPa). The regular model (32x28 elements) gets the elastic buckling stress that is very close to the classic solution. It is just a little smaller than that. The reason might be that the finite element program introduces a very small initial lateral deflection when performing the engi buckling analysis.

Buckling modes and contour plots of u_z field (z-displacement) under each mode are shown as Figures 3.6-3.9. The fine mesh is picked up as the demonstration model.

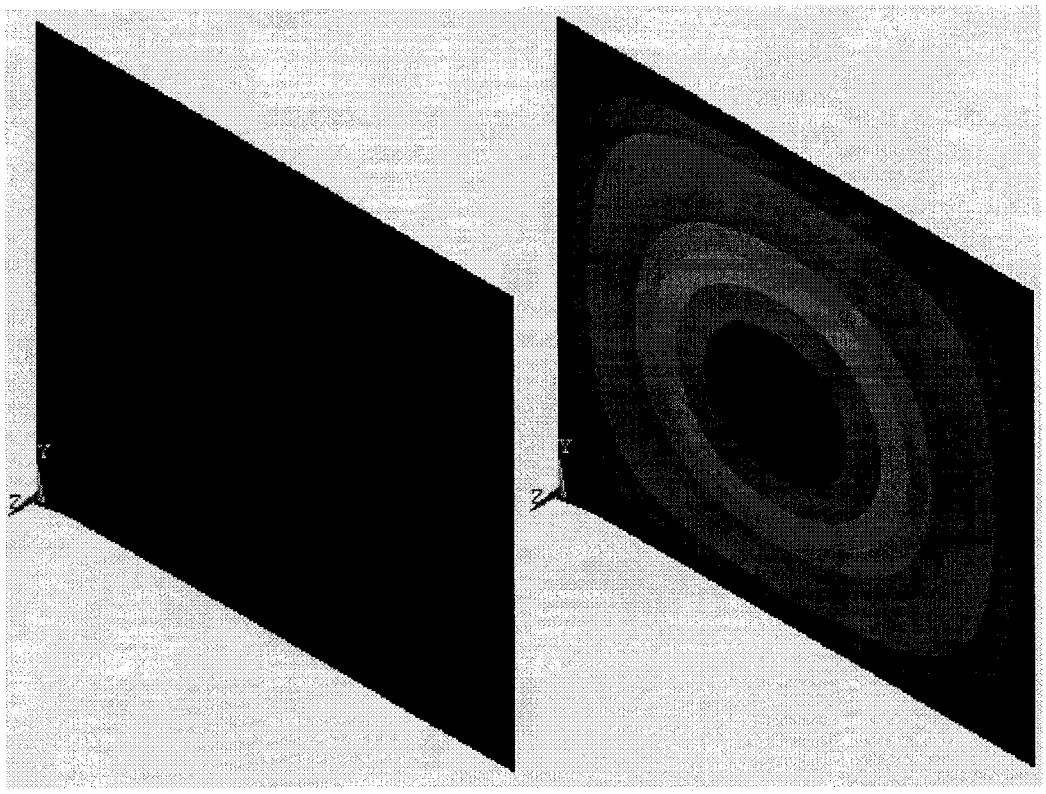

Figure 3.6 Buckling mode 1 and contour plot of u_z field (z-displacement)

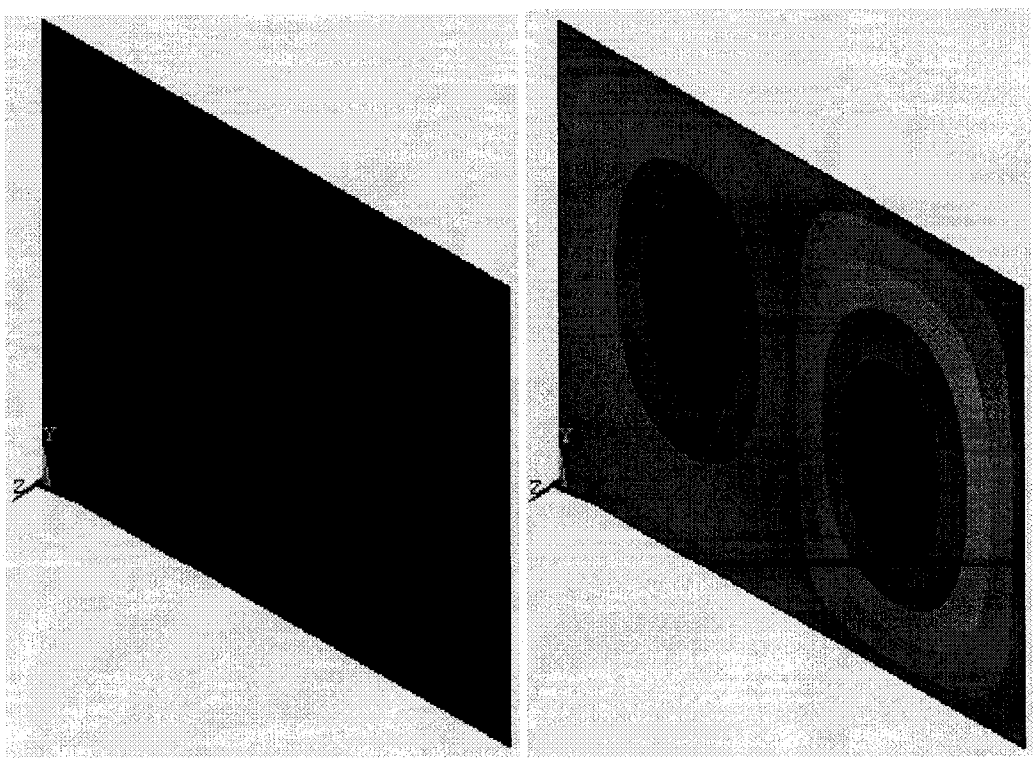

Figure 3.7 Buckling mode 2 and contour plot of u_z field (z-displacement)

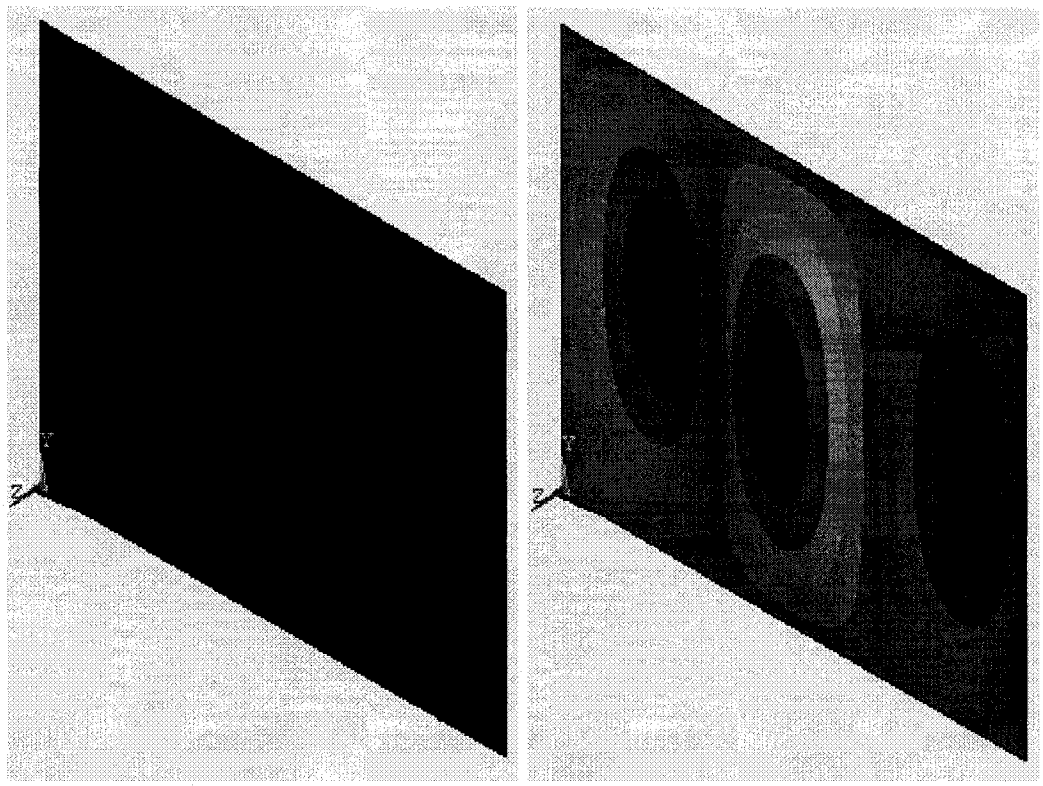

Figure 3.8 Buckling mode 3 and contour plot of u_z field (z-displacement)

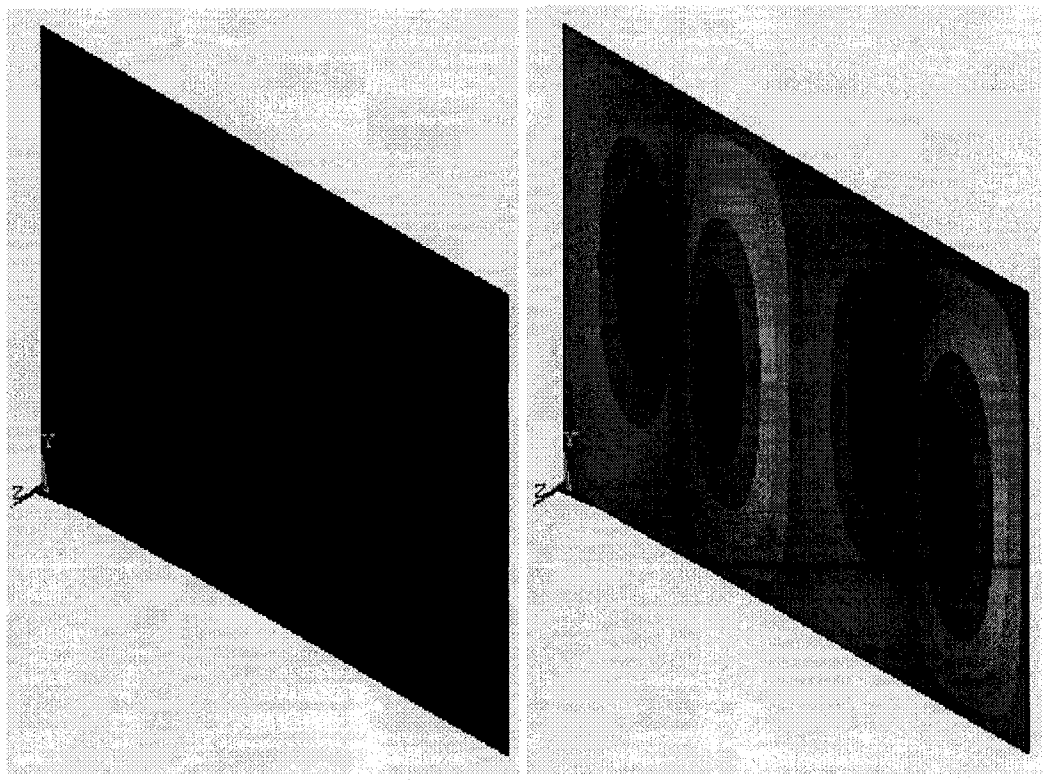

Figure 3.9 Buckling mode 4 and contour plot of u_z field (z-displacement)

3.3. POST BUCKLING AND ULTIMATE COMPRESSIVE STRENGTH OF INTACT PLATES - FURTHER CONVERGENCE STUDY

Using the preceding models, the post buckling and ultimate strength behavior of the plates has been examined. At present, the plate has been treated as a perfect steel plate without any imperfection. An elastic-perfectly plastic material model has been used so that no strain-hardening effect needed to be considered at this stage. Similar as the elastic buckling simulation, three FE models, 16x14 elements, 32x28 elements and 64x56 elements, have been used to carry out the convergence study once more for the post buckling and ultimate strength behavior of the simply supported plates.

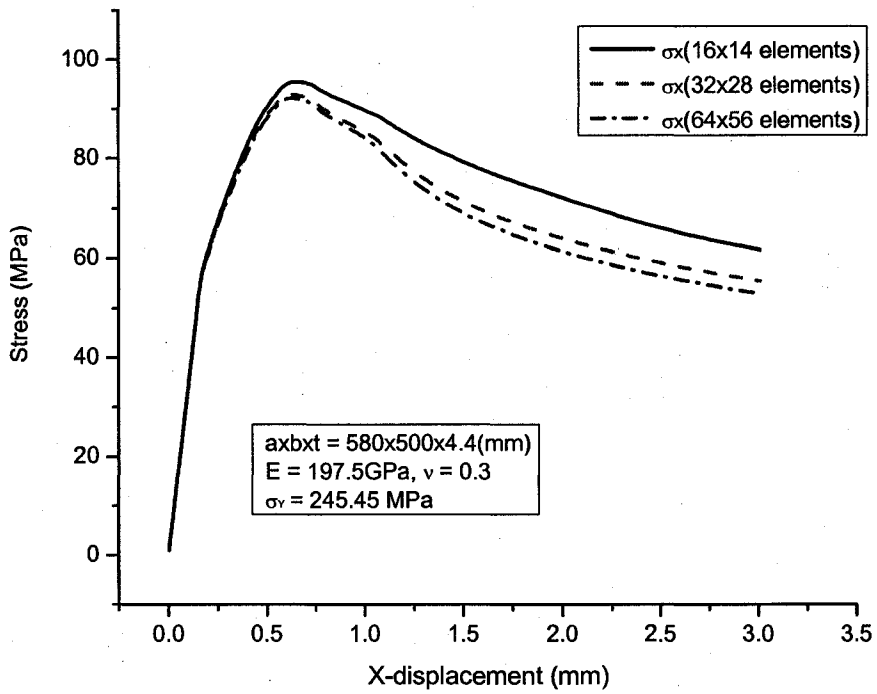

Figure 3.10 Mesh size effect on axial compressive strength versus x-displacement curves

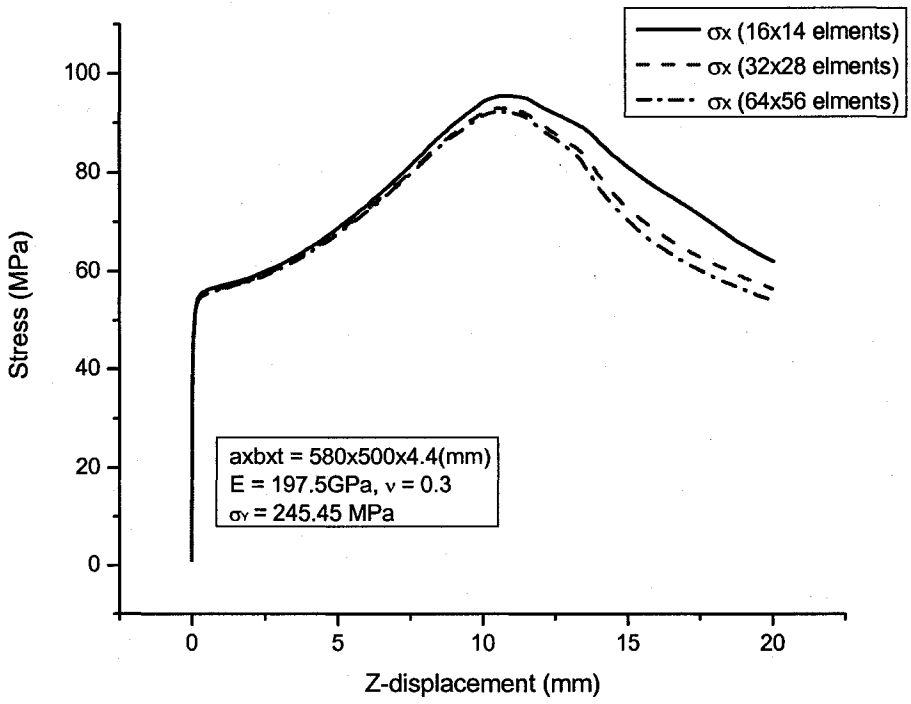

Figure 3.11 Mesh size effect on axial compressive strength versus z-displacement curves

Figures 3.10 and 3.11 show the mesh size effects on axial compressive strength versus displacement curves. Considering ultimate compressive strength, convergence of the mesh has been clearly demonstrated. For the regular mesh model with 32x28 elements and the fine mesh model with 64x56 elements, very close results have been obtained.

Numerically, from the finite element analysis the ultimate compressive strength of the simply supported intact plate is 93.02 MPa. Based on the formula given in Cui & Mansour (1999), the ultimate strength of a perfect plate, which is without any corrosion or unfairness, is presented in the following format:

$$\phi_{up} = \frac{\sigma_{up}}{\sigma_0} = \begin{cases} 1.0 & if \quad \beta < 1.9 \\ 0.08 + \dfrac{1.09}{\beta} + \dfrac{1.26}{\beta^2} & if \quad \beta > 1.9 \end{cases} \tag{3.2}$$

where

ϕ_{up} : Normalized ultimate strength of perfect plate

σ_{up} : Ultimate strength of perfect plate

σ_0 : Yield strength of material

β : Plate reduced slenderness ratio = $(b/t)[\sigma_0/E]^{1/2}$

From the geometry and material property, plate reduced slenderness ratio β equals to 4.006. Therefore, the ultimate strength of the perfect plate can be computed as 105.85 MPa. By comparison, numerical result obtained by the finite element analysis through ANSYS is smaller than the one computed by the formula, which is more conservative in this scenario.

Figures 3.12-3.15 give the contour plots of displacements, stresses and von Mises equivalent stresses.

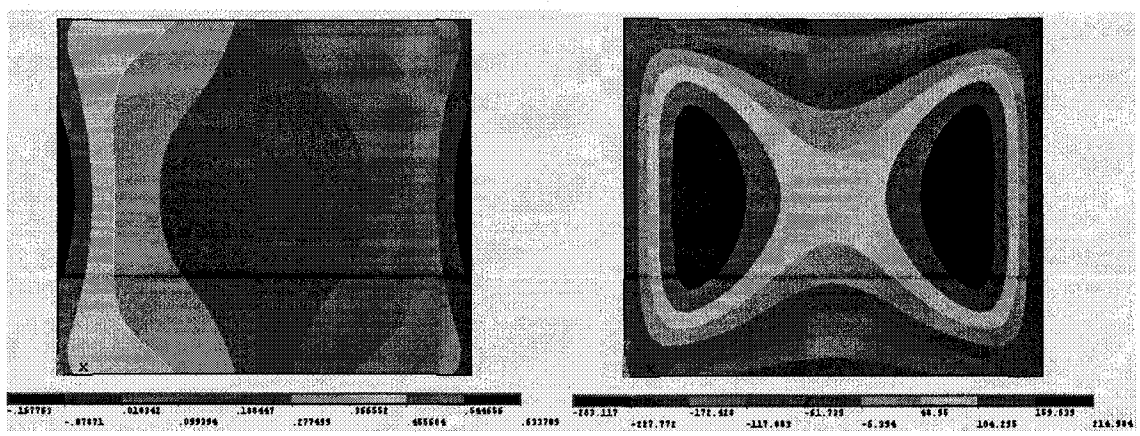

Figure 3.12 Contour plots of u_x field (x-displacement) and the stresses in x-direction

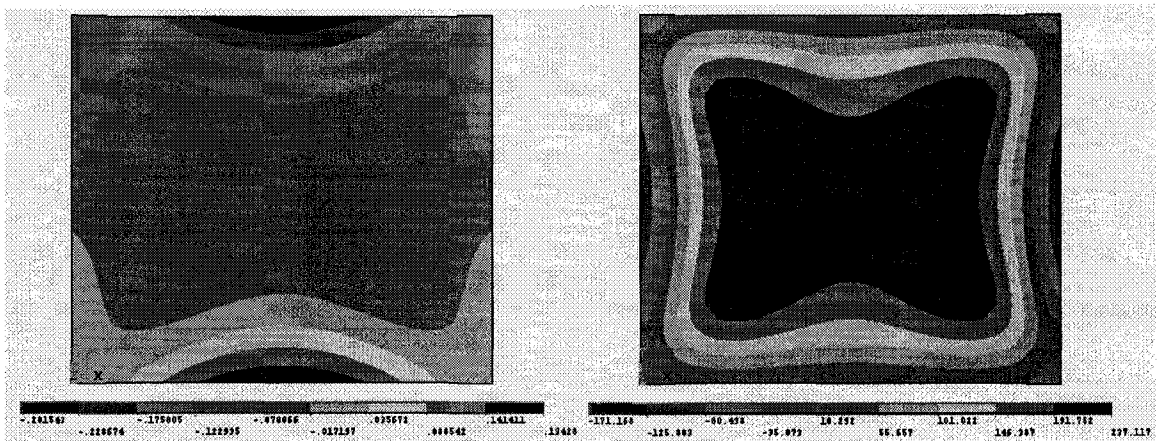

Figure 3.13 Contour plots of u_y field (y-displacement) and the stresses in y-direction

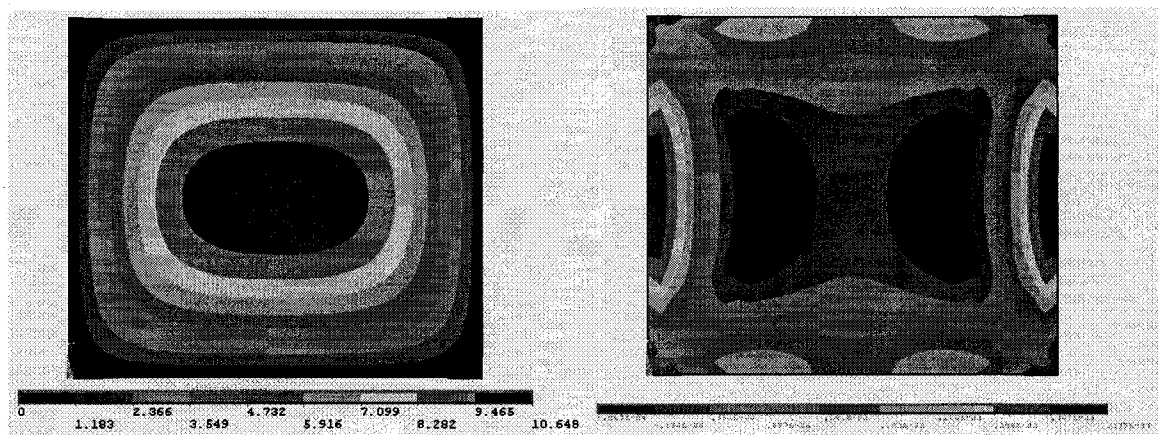

Figure 3.14 Contour plots of u_z field (z-displacement) and the stresses in z-direction

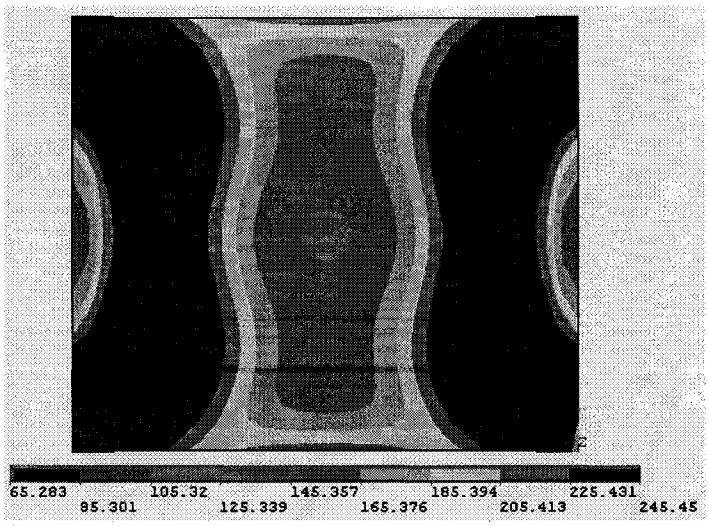

Figure 3.15 Contour plot of von Mises equivalent stresses

Figure 3.16 compares the deformed shapes of the compressed plate at the ultimate limit state and right after it passes the state. Considerable damage has been viewed clearly.

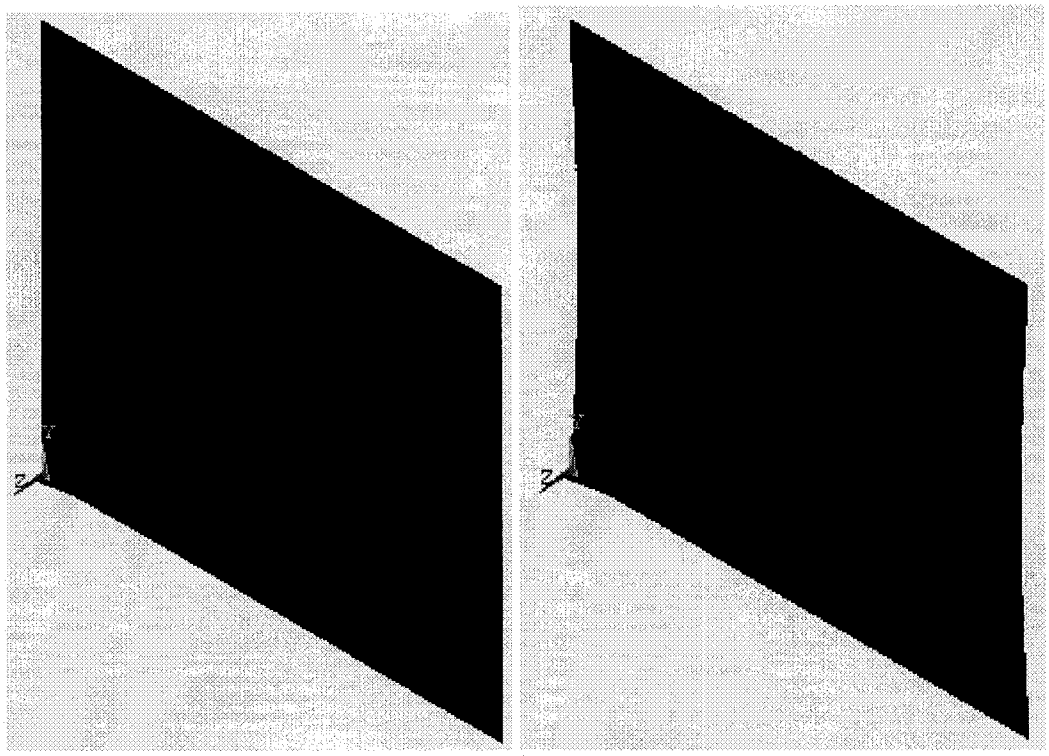

Figure 3.16 Deformed shapes at and right after the ultimate limit state

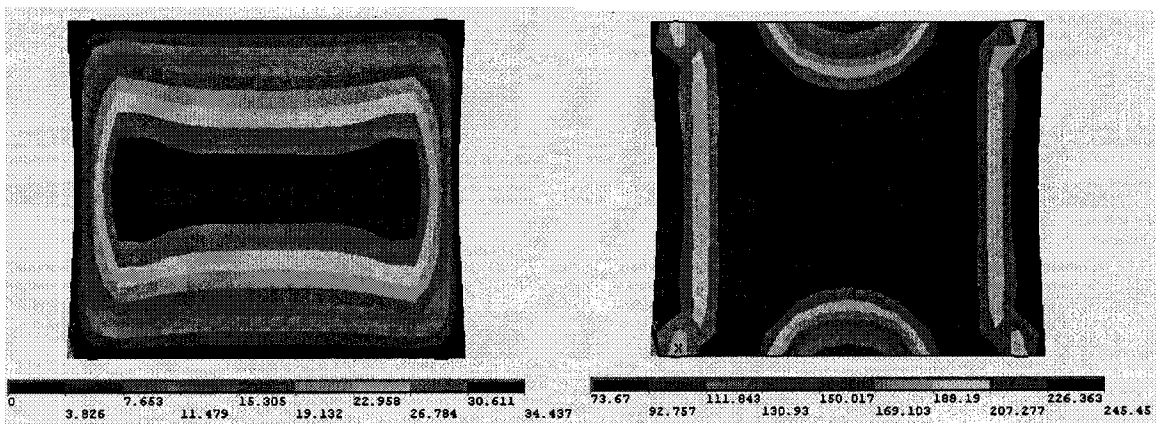

Figure 3.17 Contour plots of u_z field (z-displacement) and von Mises equivalent stresses right after the plate reaches the ultimate state

Figure 3.17 shows the contour plot of u_z field (z-displacement) right after the plate reaches the ultimate state. Large deflections have been created in the middle area. Also, it demonstrates the contour plot of von Mises equivalent stresses right after the plate reaches the ultimate state. The yielding region has been expanded to almost the whole structure. The structure collapses and is about to lose all the capability to bear loads.

3.4. MODEL SIMPLIFICATION USING SYMMETRY CONDITIONS

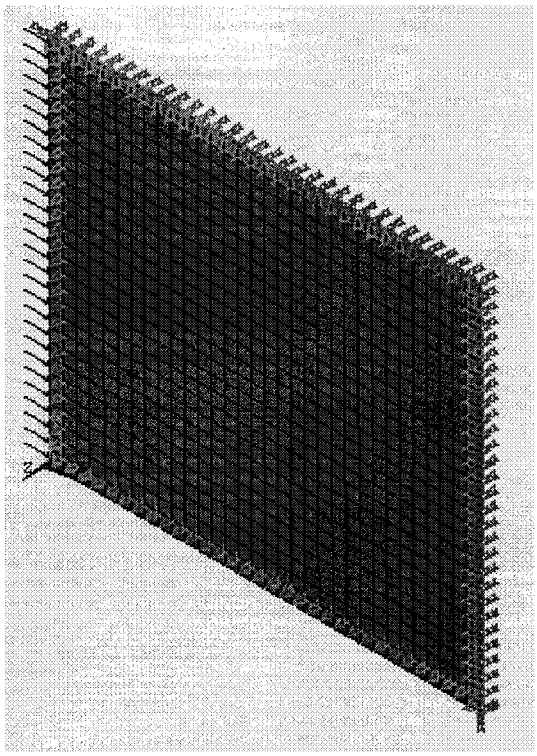

Figure 3.18 One quarter finite element model with applied loads and boundary conditions

From the geometry model and result contour plots, symmetry conditions are observed. Therefore, one quarter of the plate is taken as the extent of the analysis. The validity of the symmetric condition has been checked by comparing it with the eigen buckling

analysis and post buckling analysis for the intact full plate. Figure 3.18 shows the one quarter model with applied loads and boundary conditions. The model has 32x28 elements, which is equivalent to the full plate model with 64x56 elements. Figure 3.19 demonstrates the deformed shape at the ultimate limit state and contour plot of u_z field.

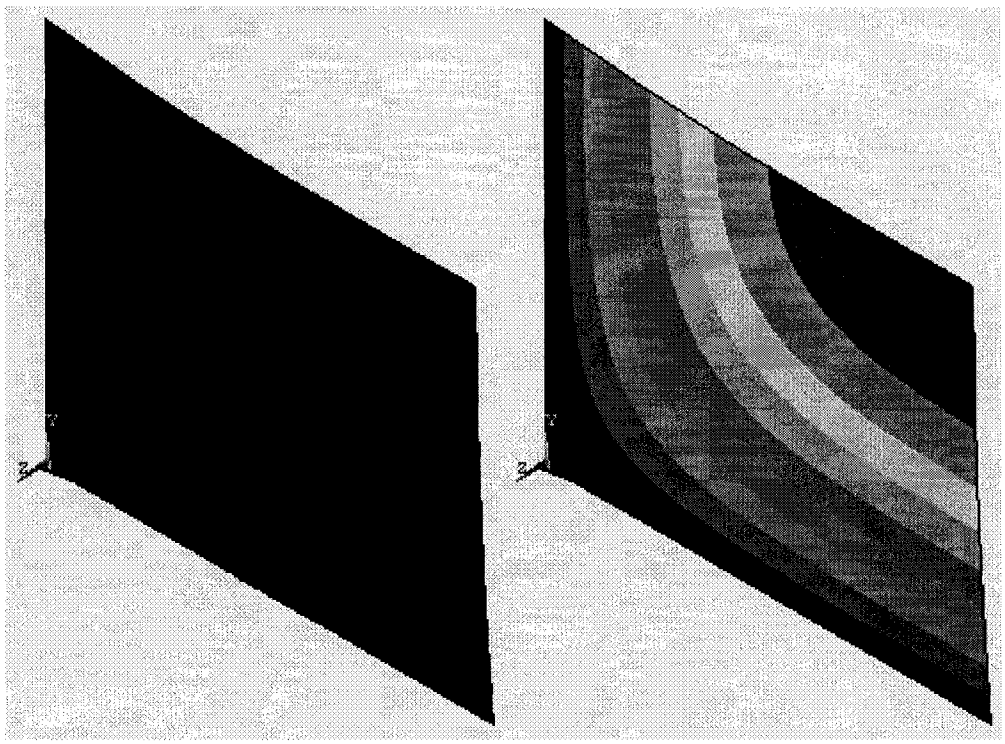

Figure 3.19 Deformed shape at the ultimate limit state and contour plot of u_z field

Through careful computation and analysis by using the one quarter model, same elastic buckling strength and ultimate compressive strength as the full plate model with 64x58 elements have been obtained. The symmetric conditions have been verified. Though the results are same, the one quarter model analysis is using much less time than the full model. Approximately, it has saved about 80% CPU time. Thus one quarter model has been used for the further analyses thereafter.

3.5. THE EFFECT OF STRAIN HARDENING

As mentioned previously an elastic-perfectly plastic material model has been used for the finite element analyses. In the model, no strain-hardening effect needed to be considered. However, for actual steel materials, there is the strain-hardening regime after the steel flows plastically passing the strain-hardening strain. The slope of the stress-strain curve in this regime is defined as the strain-hardening tangent modulus, E_h, which may not be constant, but is typically 5 to 15% of the Young's modulus for structural steels (Paik and Thayamballi 2003).

Figure 3.20 and Figure 3.21 illustrate the effect of strain hardening on the elastic and plastic large deflection behavior of an intact steel plate under axial compression. As shown though strain hardening affects the post-buckling behaviors, the effect on the ultimate strength of the simply supported intact steel plate is very small and could be neglected for conservative strength assessment and structural design.

In order to verify this further, the plate length and breadth ratio, α, is changed into 3 and the plate slenderness ratio, β, is set up at 2. Figure 3.22 shows the results of finite element analysis. Clear to see, the effect is even smaller. Therefore, an elastic-perfectly plastic material model, i.e., without considering strain hardening, is sufficient for practical strength assessment of steel-plated structure.

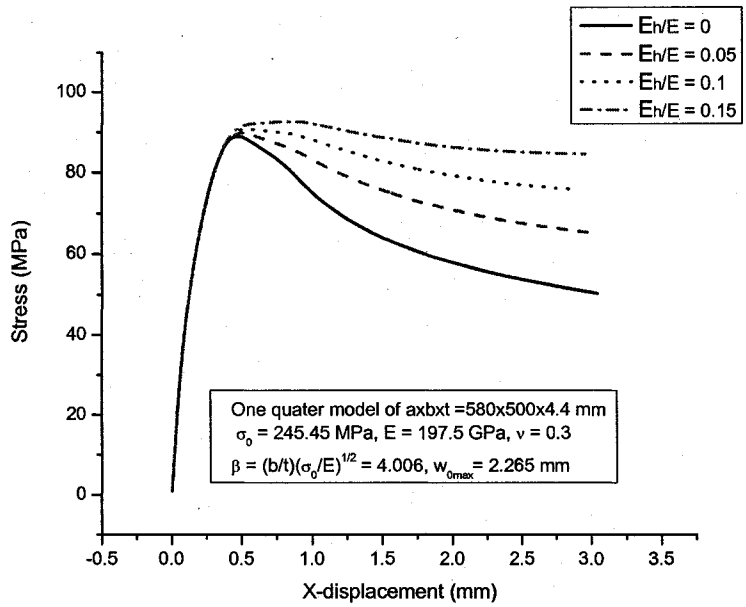

Figure 3.20 The effect of strain hardening on the ultimate strength of an intact steel plate under axial compression – stress vs x displacement curves

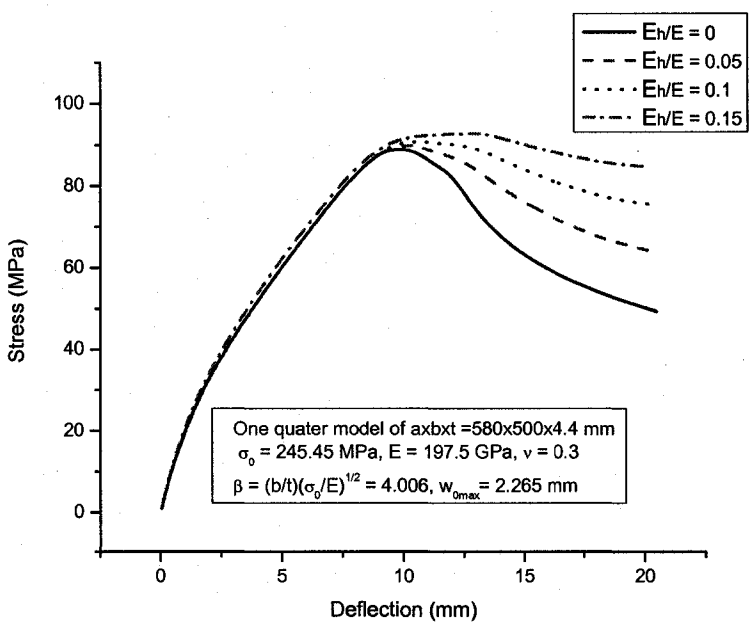

Figure 3.21 The effect of strain hardening on the ultimate strength of an intact steel plate under axial compression – stress vs deflection curves

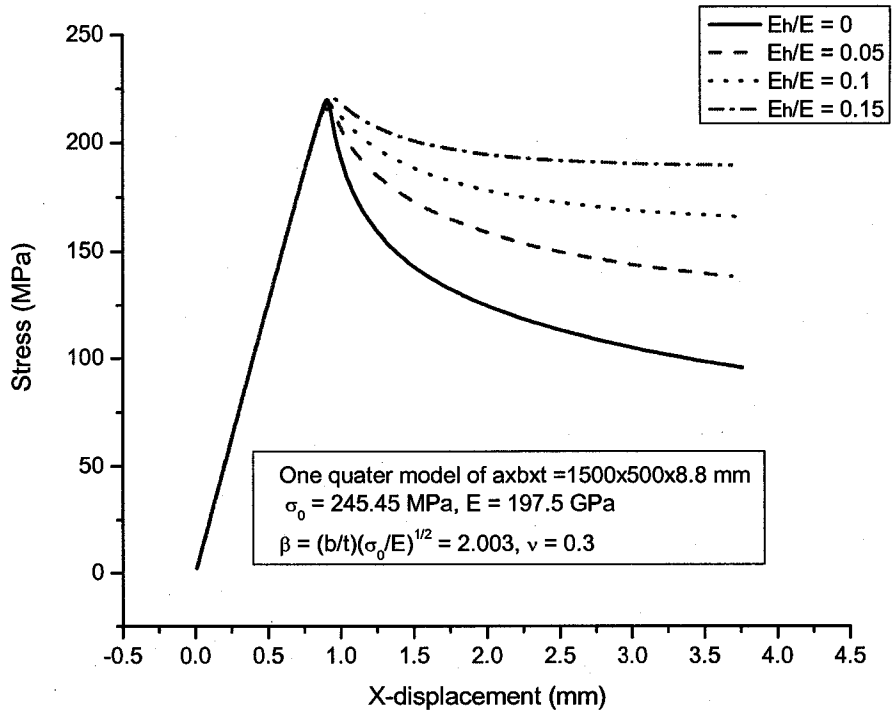

Figure 3.22 The effect of strain hardening on the ultimate strength of an intact steel plate under axial compression – stress vs x displacement curves (β =2)

3.6. THE EFFECT OF INITIAL DEFLECTION

Steel structures are typically fabricated by flame cutting and welding, thus initial imperfections in the form of initial distortions and residual stresses may be developed and will reduce the structural capacity.

According to measured data fro welding-induced initial deflections of plates in merchant steel ship structures (Carlsen and Czujko 1978, Antoniou 1980, Kmiecik et al. 1995), the geometric configuration of such initial deflections is quite complicated. The following

expression for the post-weld initial deflection of steel plating between stiffeners was developed by those measurements.

$$\frac{w_0}{w_{0\max}} = \sum_{i=1}^{M}\sum_{j=1}^{N} B_{0ij} \sin\frac{i\pi x}{a}\sin\frac{j\pi y}{b} \tag{3.3}$$

where

w_0 : Initial deflection function

$w_{0\max}$: Maximum initial deflection

a: Plate length

b: Plate breadth

B_{0ij} : Welding-induced initial deflection amplitude normalized by the maximum initial deflection

The subscripts i and j denote the corresponding half-wave numbers in the x and y directions. M and N can be chosen depending on the complexity of the initial deflection shape.

As we can see, Equation 3.3 is still quite complex. For practical design purposes, further idealization may sometimes be necessary. Figure 3.23 shows a multi-wave shape is predominant in the long direction from the measurements of initial deflection for plate elements in steel plate structures (Paik and Thayamballi, 2003). While Figure 3.24 shows one half wave is often found in the short direction (Paik and Thayamballi, 2003).

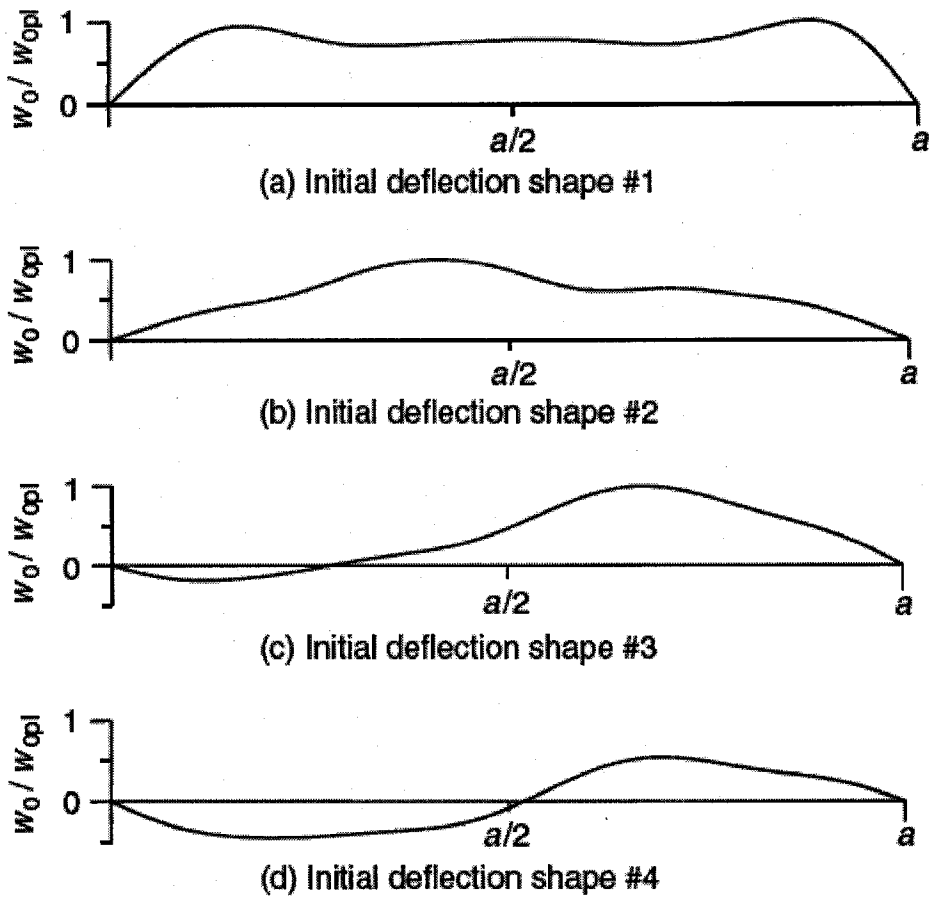

Figure 3.23 Some typical initial defection patterns in steel plating between stiffeners in the long (plate length) direction

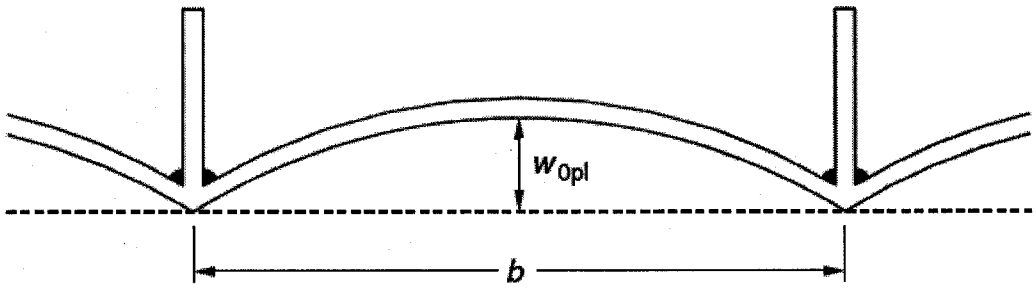

Figure 3.24 A typical initial deflection pattern in steel plating between stiffeners in the short (plate breadth) direction

For a nearly square plate element, Equation (3.3) can be simplified by taking M = N = 1. For a long plate with a multi-wave shape in the x direction and one half wave in the y direction, Equation (3.3) turns into:

$$\frac{w_0}{w_{0\max}} = \sum_{i=1}^{M} B_{0i} \sin\frac{i\pi x}{a} \sin\frac{\pi y}{b} \tag{3.4}$$

The values of B_{0i} for the initial deflection shapes shown in Figure 3.24 are given in Table 3.2, by taking M = 11 (Paik and Thayamballi, 2003).

Initial deflection shape	B_{01}	B_{02}	B_{03}	B_{04}	B_{05}	B_{06}	B_{07}	B_{08}	B_{09}	B_{010}	B_{011}
#1	1.0	−0.0235	0.3837	−0.0259	0.2127	−0.0371	0.0478	−0.0201	0.0010	−0.0090	0.0005
#2	0.8807	0.0643	0.0344	−0.1056	0.0183	0.0480	0.0150	−0.0101	0.0082	0.0001	−0.0103
#3	0.5500	−0.4966	0.0021	0.0213	−0.0600	−0.0403	0.0228	−0.0089	−0.0010	−0.0057	−0.0007
#4	0.0	−0.4966	0.0021	0.0213	−0.0600	−0.0403	0.0228	−0.0089	−0.0010	−0.0057	−0.0007

Table 3.2 Initial deflection amplitudes for initial deflection shapes shown in Figure 3.24

In practice, usually relevant initial deflection measurements are not available. the initial deflection amplitude can be approximately defined by assuming an appropriate initial deflection configuration. In literature there are some empirical formulae to approximate the maximum plate initial deflection of steel plates between stiffeners.

Faulkner (1975):

$$\frac{w_{0\max}}{t} = \begin{cases} k\beta^2(t_w/t) & for \quad t_w < t \\ k\beta^2 & for \quad t_w < t \end{cases} \tag{3.5}$$

where β = plate reduced slenderness ratio = $(b/t)[\sigma_0/E]^{1/2}$, t_w = thickness of stiffener web, k = coefficient which may be in range 0.05 – 0.15 fro marine structures and les than

0.1 for land-based structures. Faulkner (1975) adopted for his sample calculations k =0.12 for $\beta \leq 3$, and k = 0.15 for $\beta > 3$. While Antoniou (1980) suggested k = 0.091 for $t_w < t$ and k = 0.0628 for $t_w \geq t$.

Carlsen & Czujko (1978):

$$\frac{w_{0\max}}{t} = 0.016\frac{b}{t} - 0.36 \quad for \quad \frac{b}{t} > 40 \tag{3.6}$$

Antoniou (1980) (modified Carlsen & Czujko's formula):

$$\frac{w_{0\max}}{t} = \begin{cases} 0.018b/t - 0.55 & for \quad t \leq 14mm \\ 0.014b/t - 0.32 & for \quad t > 14mm \end{cases} \tag{3.7}$$

Antoniou (1984):

$$\frac{w_{0\max}}{t} = 0.238\beta - 0.177 \tag{3.8}$$

ISSC-76:

$$\frac{w_{0\max}}{t} = 0.10\beta^2\left(\frac{t_w}{t}\right) \quad for \quad t_w < t \tag{3.9}$$

ISSC-79:

$$\frac{w_{0\max}}{t} = \begin{cases} 0.091\beta^2\left(\frac{t_w}{t}\right) & t_w < t \\ 0.0628\beta^2\left(\frac{t_w}{t}\right) & t_w > t \end{cases} \tag{3.10}$$

Smith *et al.* (1988):

$$\frac{w_{0\max}}{t} = \begin{cases} 0.025\beta^2 & for\ slight\ level \\ 0.1\beta^2 & for\ average\ level \\ 0.3\beta^2 & for\ severe\ level \end{cases} \tag{3.11}$$

Masaoka (1996):

$$\frac{w_{0\max}}{t} = k\left(\frac{b}{t}\right)^2 \tag{3.12}$$

where k = coefficient which may be taken as $k = 8 \times 10^{-5}$ for merchant ship structures.

Mansour & Elsayed (1999):

$$\frac{w_{0\max}}{t} = 0.073\beta^2 + 0.026\beta - 0.203 \tag{3.13}$$

Classification societies or other regulatory bodies specify the maximum initial deflection with the intention that the initial distortion in the fabricated structure must be less than the corresponding specified values. The following is some examples:

Det Norske Veritas:

$$\frac{w_{0\max}}{b} \leq 0.01$$

Shipbuilding quality standards of Japan and Germany:

$w_{0\max} \leq 7mm$ for bottom plate

$w_{0\max} \leq 6mm$ for deck plate

Steel box girder bridge quality standards of the UK:

$$w_{0\max} \leq \min(\frac{t}{6}+2, \frac{t}{3}) \qquad t \text{ in mm}$$

It has been noticed that the initial deflection might have some effects on the ultimate strength behavior of steel plating. Since the initial deflection shapes are not symmetry, in order to study the effects of theirs, full models have been used in this portion. Smith's equation (1988) has been used since even for the average level in the equation it is much worse than the results computed by the other equations.

Figure 3.25 shows the effect of initial deflection shape on the axial compressive stress-deflection curves. From that the effect of different initial deflection shapes on the ultimate strength of a simply supported steel plate under axial compression can be viewed clearly. It is interesting to notice that shape 1 and shape 2 have very different effects, while shape 3 and shape 4 almost have same influences on the ultimate strength. By comparison, in this scenario, shape 1 has the worst effect on the ultimate compressive strength of the simply supported steel plate. It is easy to understand that from the initial deflection shape which has big deflections along the plate length and reaches the biggest close to both sides subjected to compressive loads.

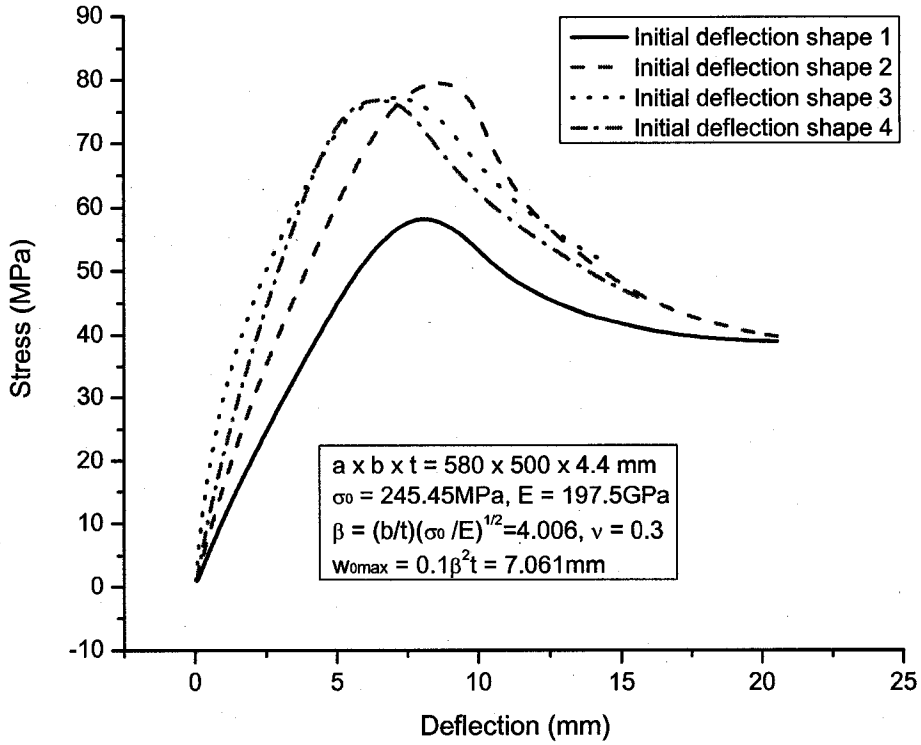

Figure 3.25 Effect of initial deflection shape on the axial compressive stress

Figures 3.26-3.29 show contour plots of u_z field and von Mises equivalent stresses at the ultimate state according to different initial deflection shapes. Collapse patterns and damage zones can be seen clearly. The effects of different initial deflection shapes on the post-buckling of the steel plate are also demonstrated.

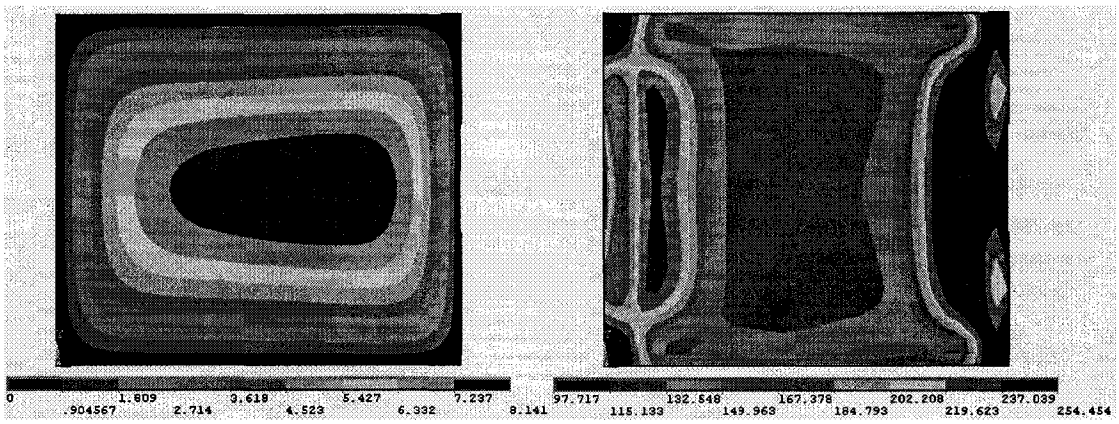

Figure 3.26 Shape 1 contour plots of u_z field and von Mises equivalent stresses at the ultimate state

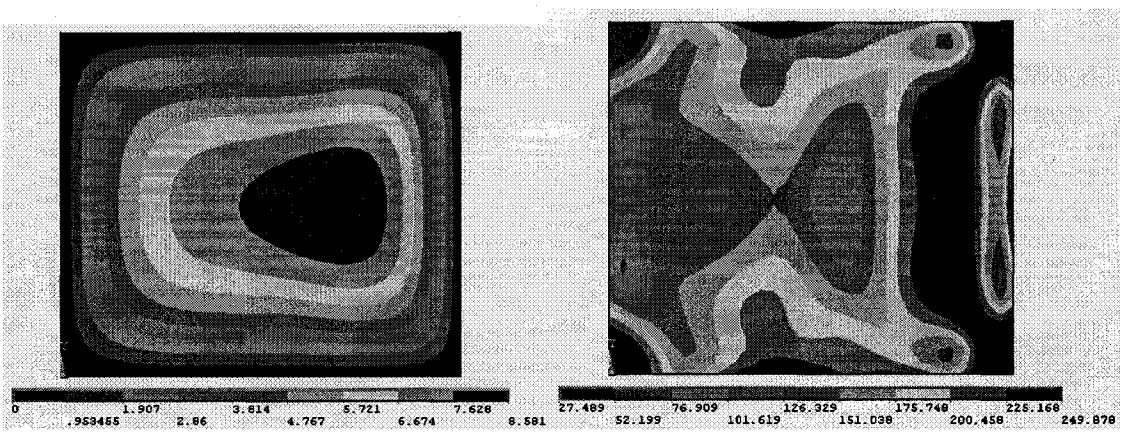

Figure 3.27 Shape 2 contour plots of u_z field and von Mises equivalent stresses at the ultimate state

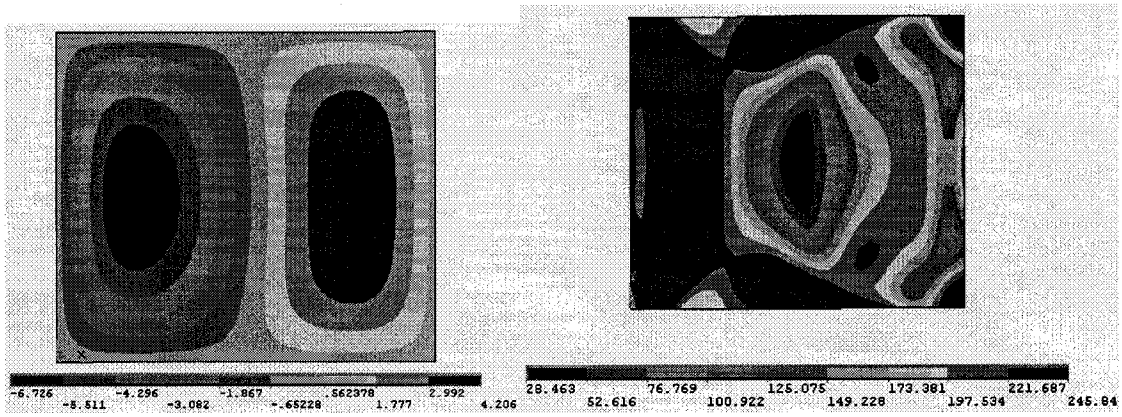

Figure 3.28 Shape 3 contour plots of u_z field and von Mises equivalent stresses at the ultimate state

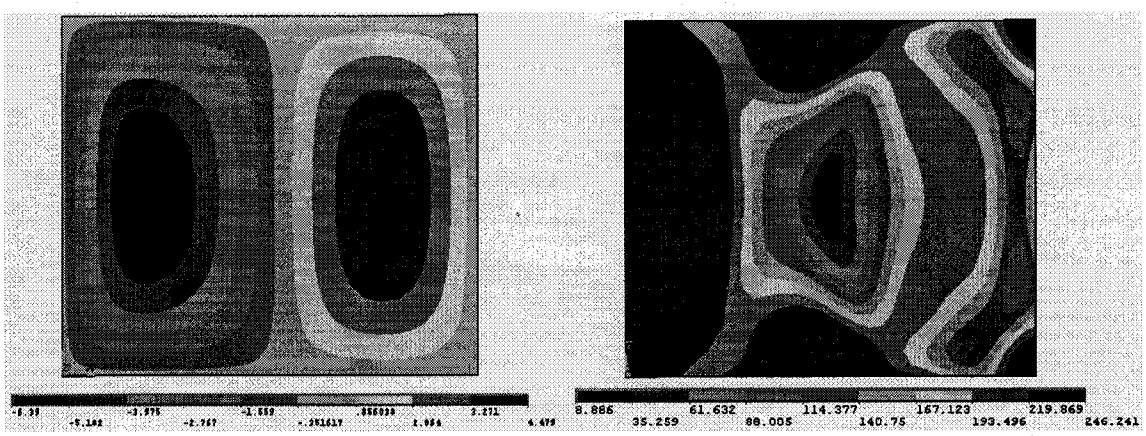

Figure 3.29 Shape 4 contour plots of u_z field and von Mises equivalent stresses at the ultimate state

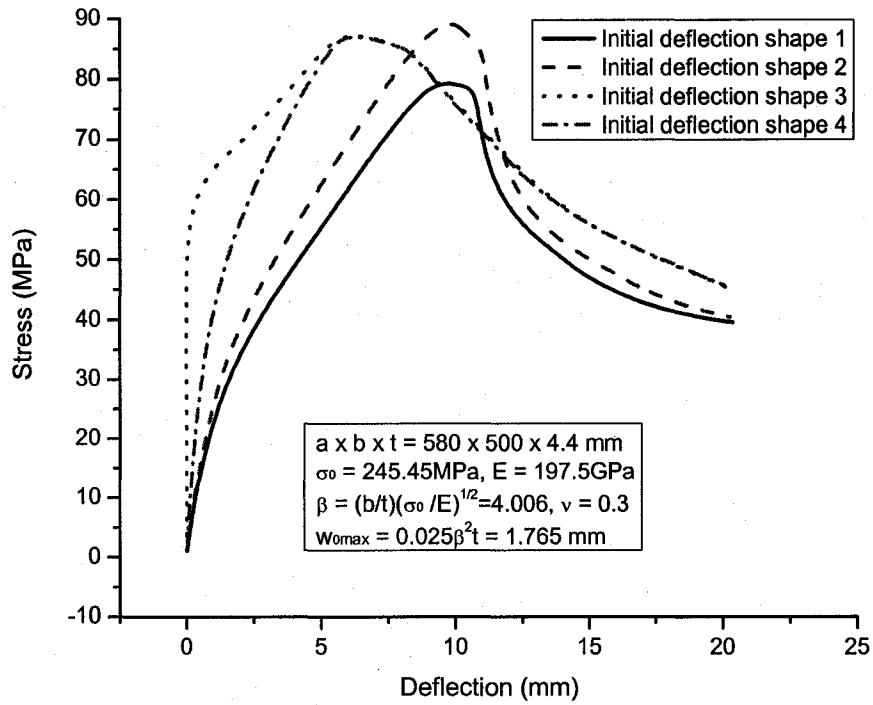

Figure 3.30 Effect of slight level initial deflection shape on the axial compressive stress

Figure 3.30 gives the effect of slight level initial deflection shape on the axial compressive stress-deflection curves. Here Equation 3.11 slight level has been used to approximate the maximum plate initial deflection $w_{0\max} = 0.025\beta^2 t = 1.765mm$. For the slight level initial deflection, various initial deflection shapes have nearly same effects on the ultimate compressive strength of the simply supported steel plate except shape 1 which is still 10% smaller than the others.

As for the current model, according to the ratio of length and breadth, it is nearly square. Therefore Equation 3.3 can be simplified by taking M = N = 1. B_{01} can be taken as 1 for conservation. As noticed, this kind of initial deflection is symmetrical, and the benefit of

symmetry conditions as mentioned before can be utilized. Figure 3.31 graphs the comparison of axial compressive stress-deflection curves between full model and one quarter model using symmetrical boundary conditions. As shown the perfect match is concluded, which again verifies the symmetrical boundary conditions that are applied to the finite element analysis.

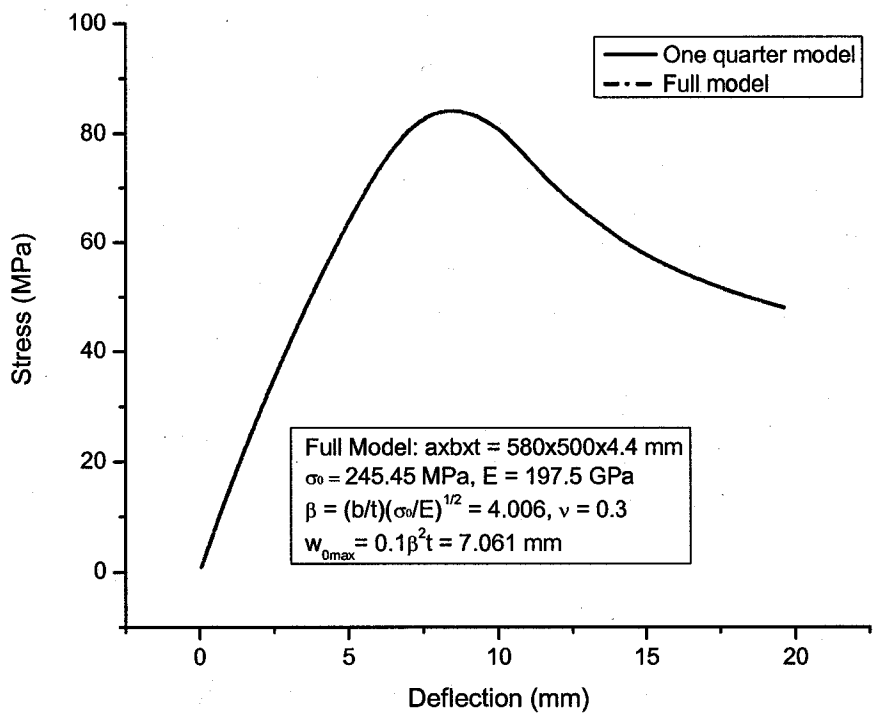

Figure 3.31 Comparison of axial compressive stress-deflection curves between one quarter model and full model

As mentioned before, there are various equations to approximate the maximum plate initial deflection when the actual measurements are not available. Also from Figure 3.35 and Figure 3.30, the effects on the ultimate strength of the different the maximum plate initial deflections computed by different equations are quite different. Therefore the

difference caused by different maximum plate initial deflections is needed to be analyzed further.

Figure 3.32 shows the comparison of axial compressive stress and x-displacement curves due to different maximum plate initial deflections. And Figure 3.33 shows the comparison of axial compressive stress and deflection curves due to different maximum plate initial deflections.

It has been demonstrated that as the maximum plate initial deflection increases, x-displacement also increases at the ultimate state. The curves are shifted right according to Figure 3.32. The post-buckling behaviors are almost same no matter how big the maximum plate initial deflections are. While the deflection (z-displacement) decreases as the maximum plate initial deflection increases. The curves are shifted left according to Figure 3.33.

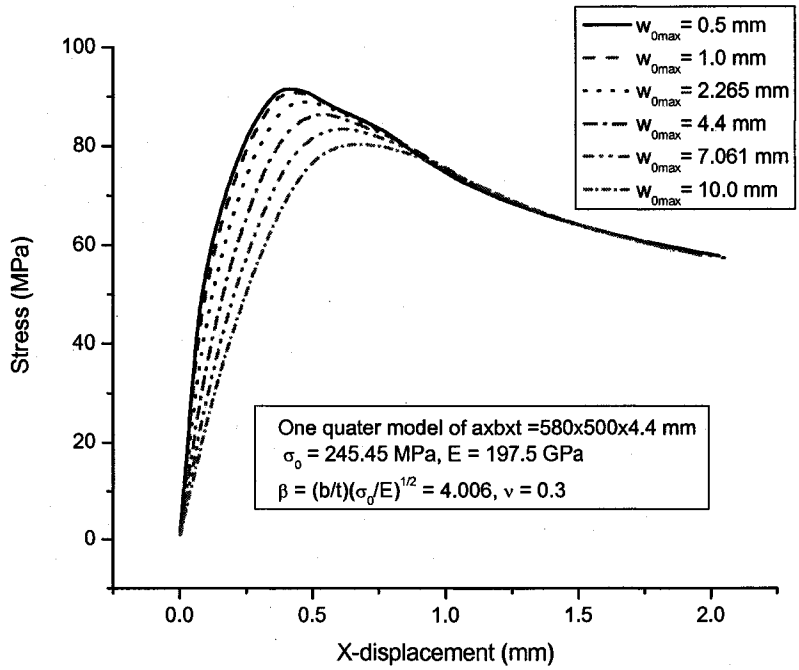

Figure 3.32 Comparison of axial compressive stress and x-displacement curves due to different maximum plate initial deflections

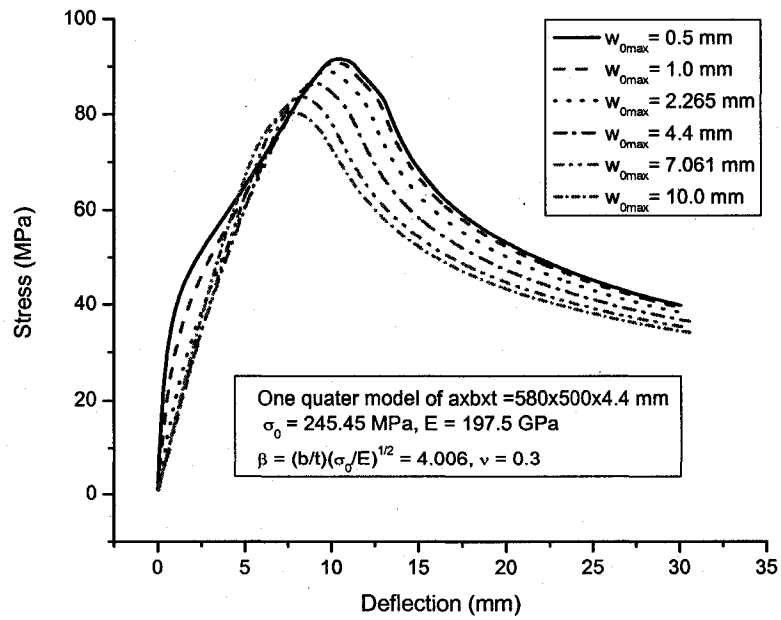

Figure 3.33 Comparison of axial compressive stress and deflection curves

Nonlinear least-square fitting has been used to derive a relationship between the maximum plate initial deflection and the ultimate compressive strength for the simply supported steel plate. This relationship has been found to be:

$$\phi = 0.0025\gamma^2 - 0.0262\gamma + 0.3759 \tag{3.14}$$

where

$\phi = \sigma_u / \sigma_0$ = normalized ultimate strength

$\gamma = (w_{0\max} / t)$ = normalized maximum plate initial deflection

This relationship is shown in Figure 3.34. The limitations of the relationship are $a/b \approx 1$ and $\beta \approx 4$.

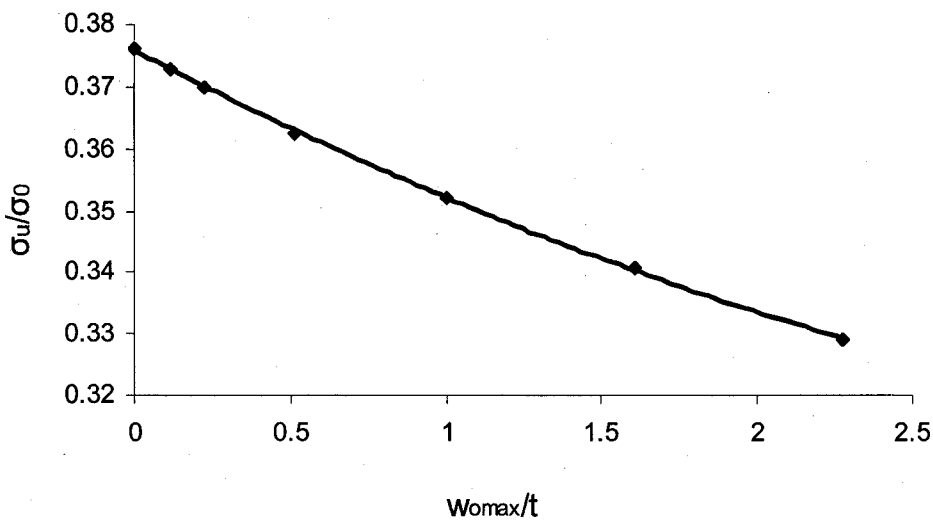

Figure 3.34 Relationship between the maximum plate initial deflection and the ultimate compressive strength for a simply supported steel plate

Figure 3.35 compares the difference when the ratio of length and breadth changes to 2, while the other conditions keep same. Also by using nonlinear least-square fitting, the relationship between the maximum plate initial deflection and the ultimate compressive strength for the simply supported steel plate is following, where $\alpha = a/b = 2$ and $\beta \approx 4$. The other notations are same as Equation 3.14.

$$\phi = 0.0024\gamma^2 - 0.0264\gamma + 0.4117 \tag{3.15}$$

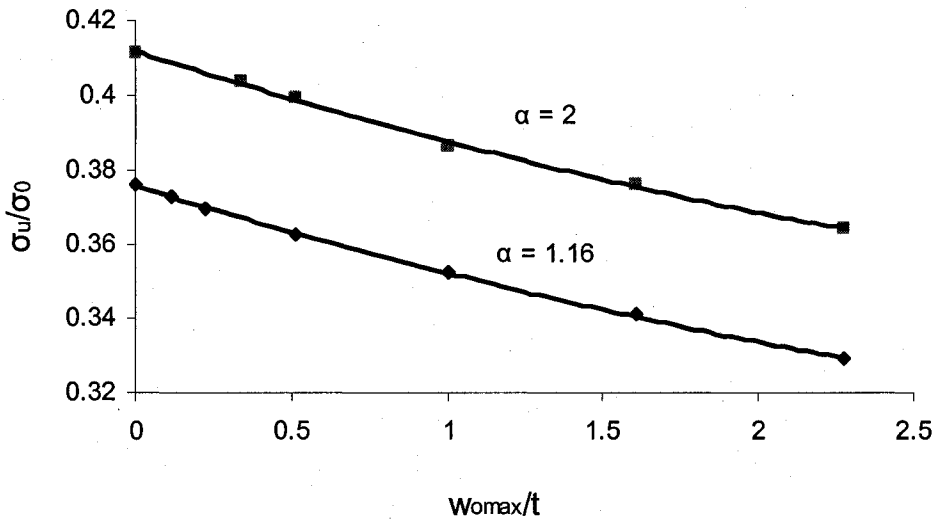

Figure 3.35 Comparisons of relationship between the maximum plate initial deflection and the ultimate compressive strength for a simply supported steel plate

3.7. THE ASPECT RATIO EFFECT

For the ship structures, the length and breadth ratio of the steel plating between stiffeners may change for 1 to 5 according to different portions. Therefore, examining the length

and breadth ratio effect on the ultimate strength of steel plating is important and necessary.

Figure 3.36 gives the effect of different length and breadth ratios on the ultimate compressive strength of steel plating with plate slenderness ratio $\beta = 2.5$. It is clear that when the length and breadth ratio, α, varies from 1 to 5, though the post-buckling behaviors are different, the ultimate compressive strengths are very similar and the difference can be ignored under acceptable error percentage.

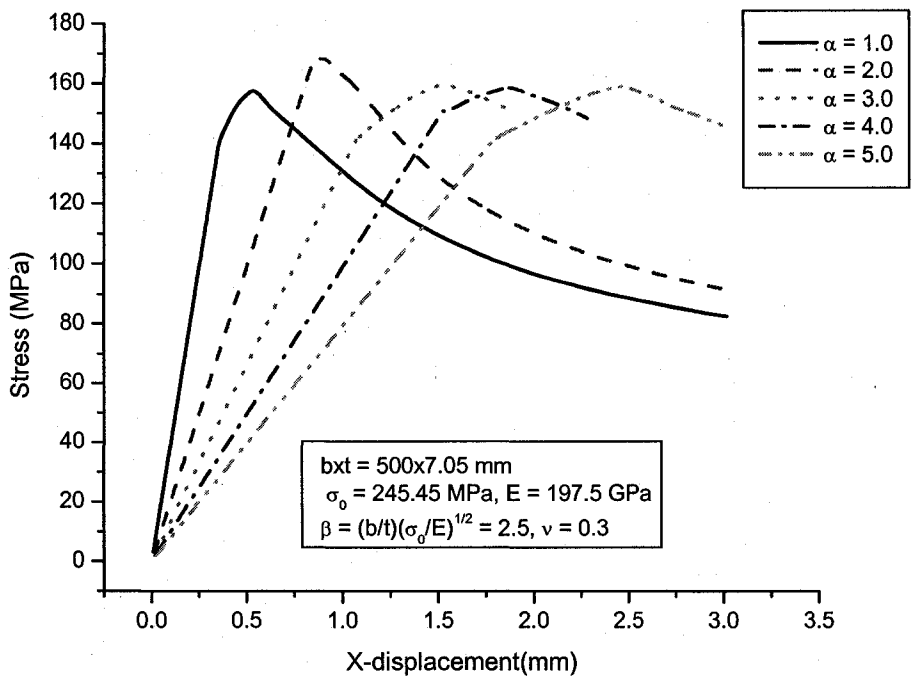

Figure 3.36 Comparison of axial compressive stress and x-displacement curves due to different length and breadth ratios ($\beta = 2.5$)

In order to further study the effects, different plate slenderness ratio, $\beta = 4.5$, is taken. Results are graphed in Figure 3.37. Same conclusions are drawn. Therefore, the effect of plate length and breadth ratio on ultimate strength of plate elements can be ignored in this study. For simplicity, plate length and breadth ratio $\alpha = 1.0$ can be chosen in the finite element analysis thereafter.

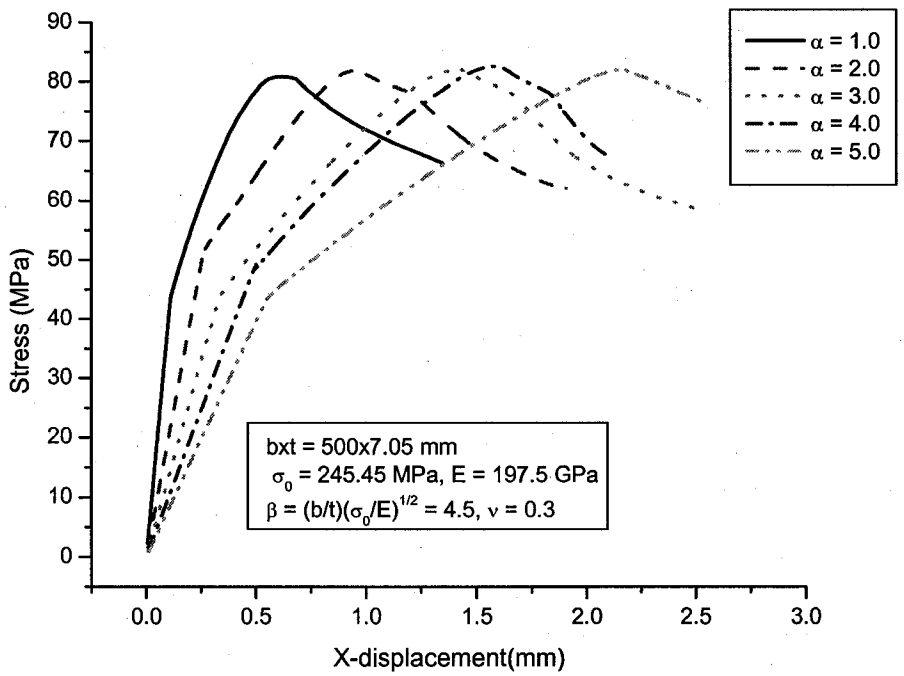

Figure 3.37 Comparison of axial compressive stress and x-displacement curves due to different length and breadth ratios ($\beta = 4.5$)

3.8. THE EFFECT OF BOUNDARY CONDITIONS - CLAMPED BOUNDARY CONDITION

In the preceding sections, ultimate compressive strength has been examined considering simply supported boundary condition with all edges moving freely in plane. In the marine

structures, the rotational restraints along the plate edges depend on the torsional rigidities of the support members. In some circumstance, these are very small, so zero constrains can be assumed like being studied in the preceding sections. In the other circumstance, these are very large, clamped boundary conditions can be applied. In this section, this situation is stated.

Geometry and loading conditions can be shown in Figure 3.1 except the boundary conditions are clamped, which the rotational restraints are infinite. Figure 3.39 shows the finite element (FE) model and boundary conditions of the clamped steel plate subject to axial compressive loads.

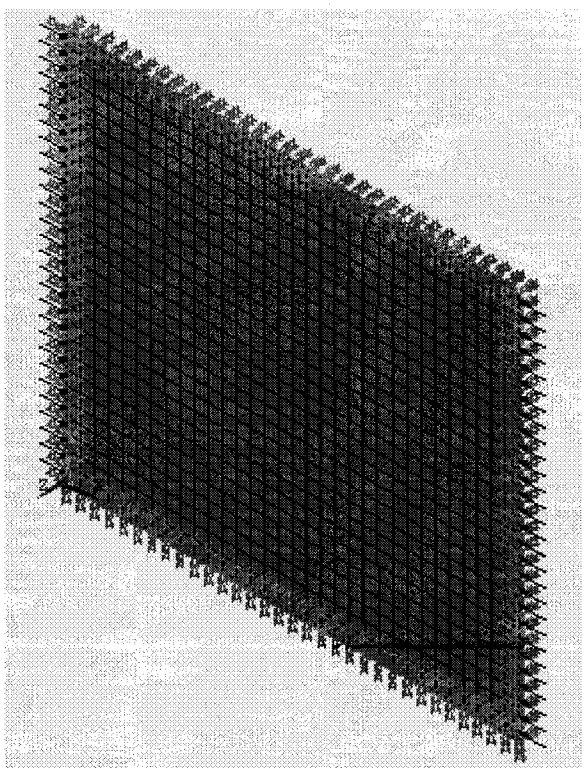

Figure 3.39 FE model and boundary conditions of a clamped steel plate subject to axial compressive loads

Due to the symmetry, one quarter of the model can be used. But before doing that, it is interesting to see the whole picture of the steel plate buckling simulation. Figures 3.40-3.43 show the contour plots of different field and stresses at the ultimate limit state for the intact clamped perfect steel plate subjected to axial compressive loads.

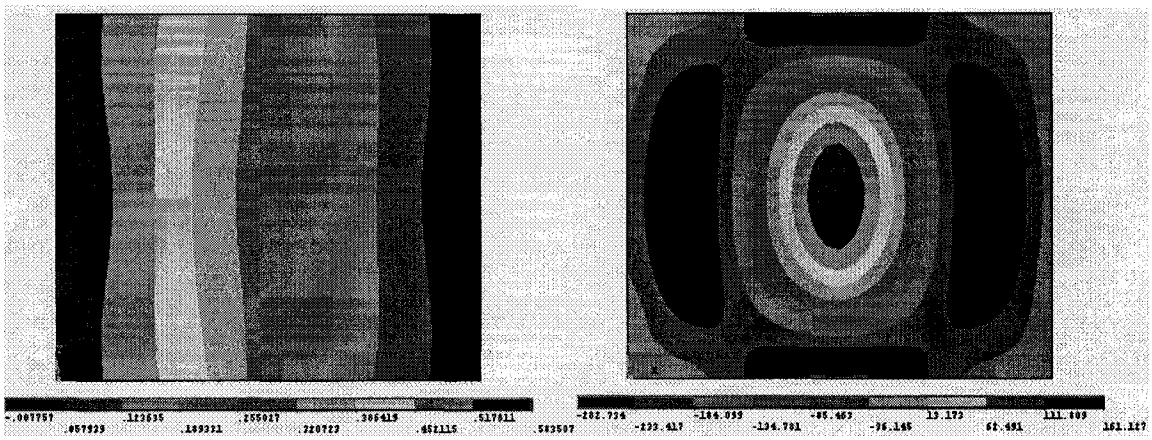

Figure 3.40 Contour plots of u_x field (x-displacement) and the stresses in x-direction

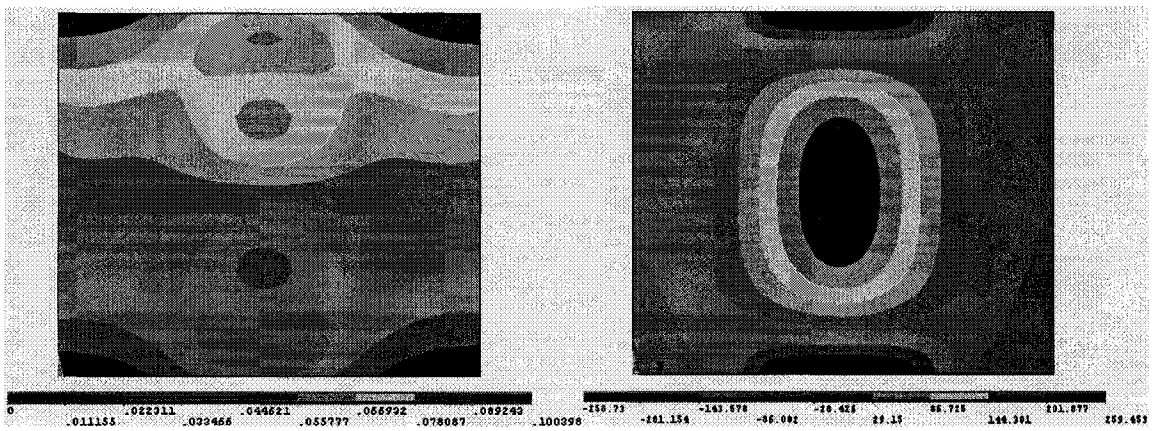

Figure 3.41 Contour plots of u_y field (y-displacement) and the stresses in y-direction

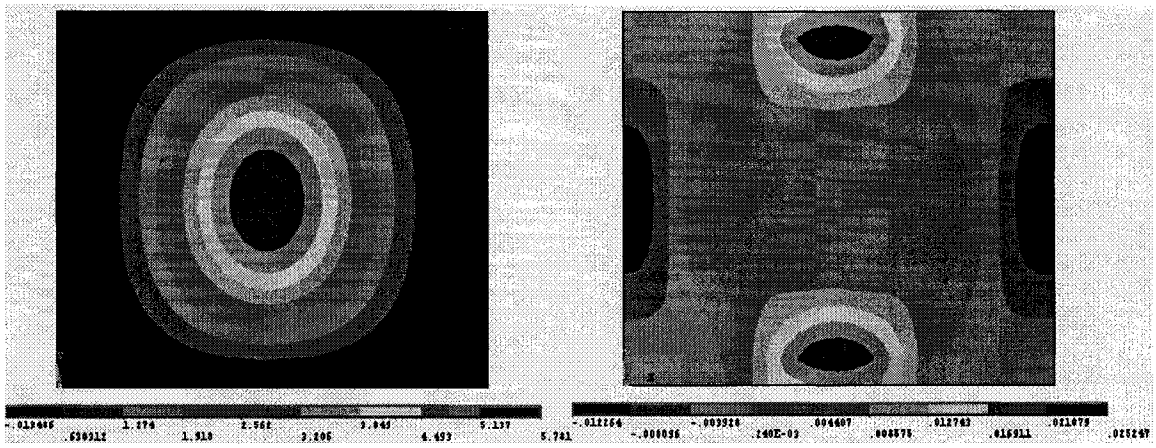

Figure 3.42 Contour plots of u_z field (z-displacement) and the stresses in z-direction

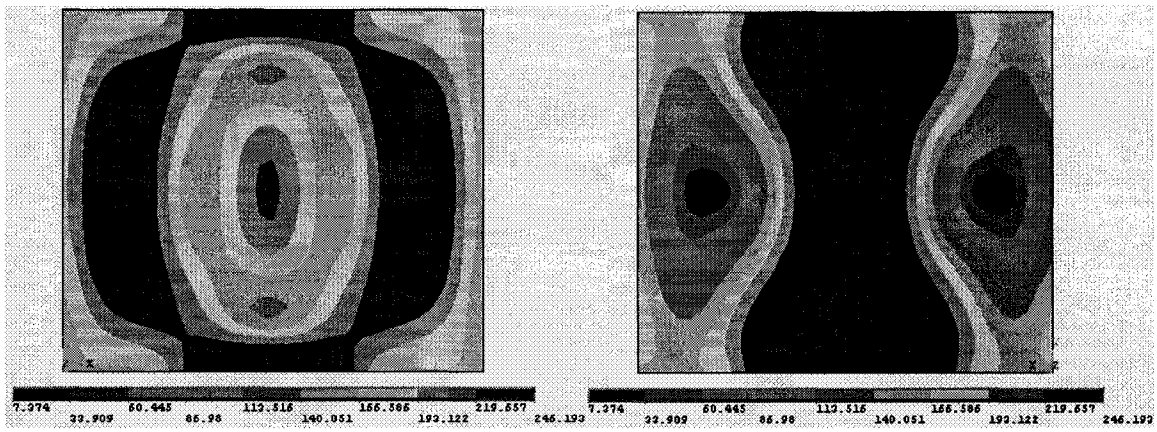

Figure 3.43 Contour plots of von Mises equivalent stresses both top and bottom

Figure 3.44 demonstrates the deformed shape and contour plot of von Mises equivalent stresses right after the ultimate limit state. It shows clearly the damage zone and yielding field after it reaches the ultimate limit state.

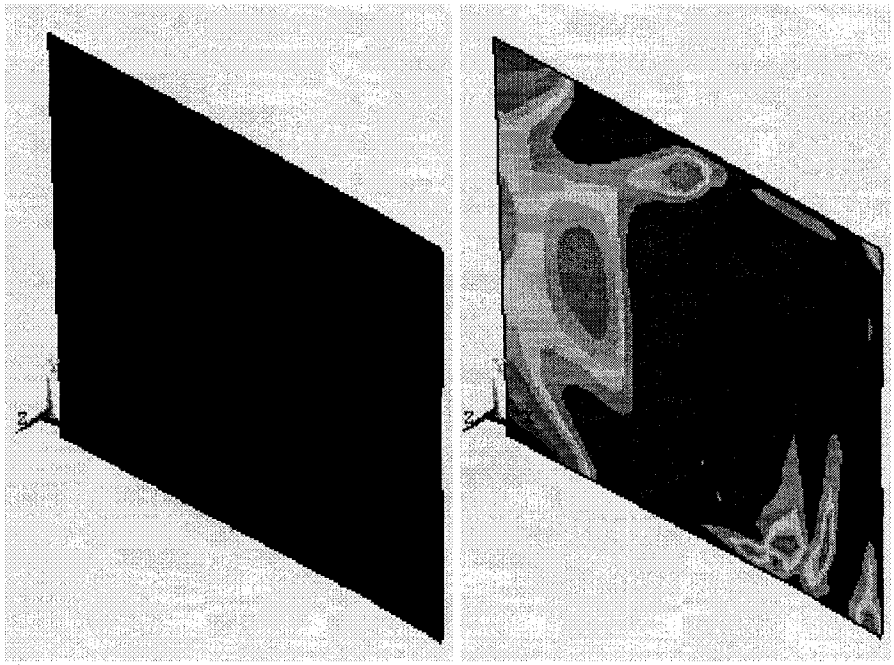

Figure 3.44 Deformed shape and contour plot of von Mises equivalent stresses right after the ultimate limit state

Figure 3.45 shows the comparison of axial compressive stress and x-displacement curves due to different maximum plate initial deflections. And Figure 3.46 shows the comparison of axial compressive stress and deflection curves due to different maximum plate initial deflections. It has been noticed that as the maximum plate initial deflection increases, x-displacement also increases at the ultimate state. The curves are shifted right according to Figure 3.45. Which is same as simply supported boundary conditions. While the deflection (z-displacement) also increases as the maximum plate initial deflection increases. It is different from the situation of simply supported boundary conditions according to Figure 3.42 and Figure 3.46.

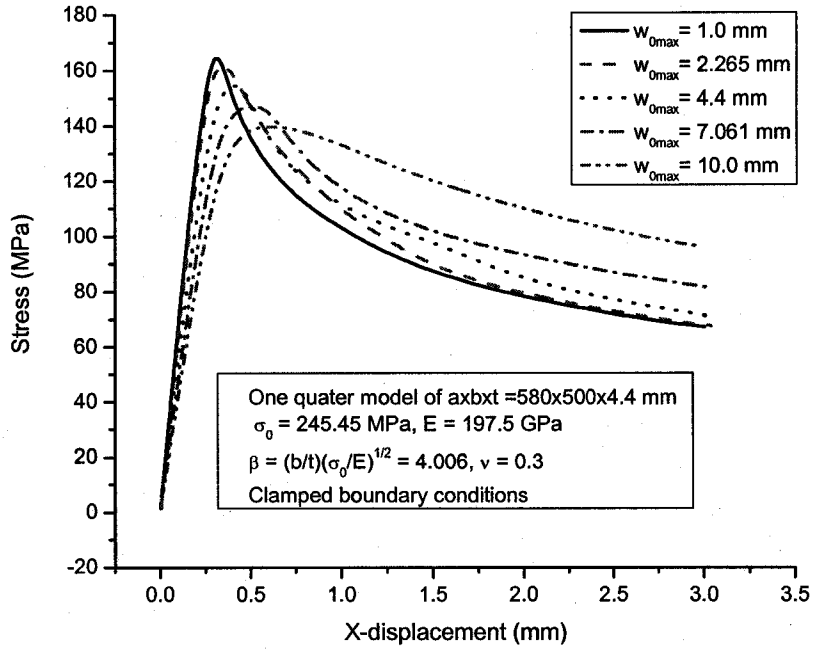

Figure 3.45 Comparison of axial compressive stress and x-displacement curves due to different maximum plate initial deflections

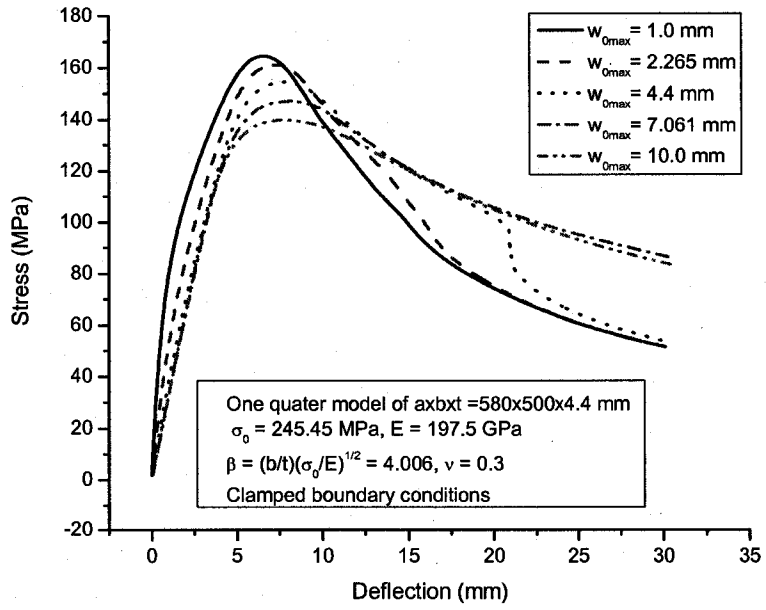

Figure 3.46 Comparison of axial compressive stress-deflection curves due to different maximum plate initial deflections

Nonlinear least-square fitting has been used to derive a relationship between the maximum plate initial deflection and the ultimate compressive strength for the clamped steel plate. This relationship has been found to be:

$$\phi = 0.0011\gamma^2 - 0.0515\gamma + 0.6812 \tag{3.16}$$

where

$\phi = \sigma_u / \sigma_0$ = normalized ultimate strength

$\gamma = (w_{0\max} / t)$ = normalized maximum plate initial deflection

This relationship is shown in Figure 3.47. The limitations of the relationship are $a/b \approx 1$ and $\beta \approx 4$.

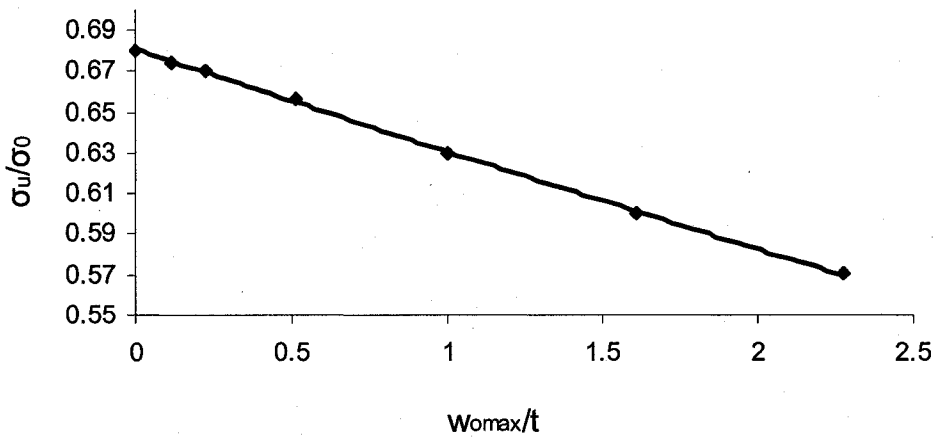

Figure 3.47 Relationship between the maximum plate initial deflection and the ultimate compressive strength for a clamped steel plate

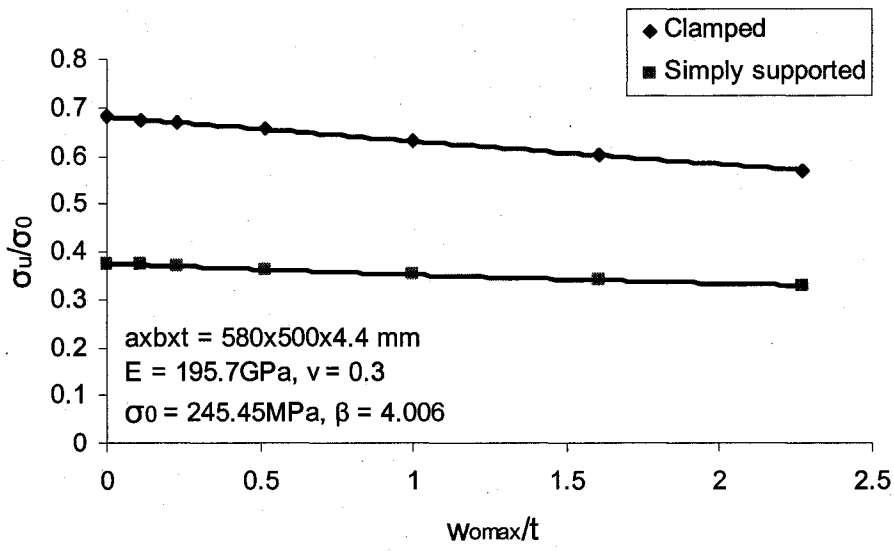

Figure 3.48 Effects of different boundary conditions on ultimate compressive strength with varying maximum initial plate deflections

Figure 3.48 shows the effects of different boundary conditions on ultimate compressive strength with varying maximum initial plate deflections. The discrepancy could be as big as 45%. Actually the real plates of steel structures rarely have zero or infinite rotational restraints, correspondingly simply supported or clamped boundary conditions. They are the lower and upper bounds. Therefore the two ideal conditions are often adequate for practical design purposes.

3.9. PIT CORROSION MODELING AND FINITE ELEMENT ANALYSIS VERIFICATION

Paik et al. (2003) performed a series of collapse tests on box-type plated structures with various amount of pit corrosion damage. Figure 3.49 is the schematic view of the test

structure, which is composed of four same steel plates. The material is mild steel with Young's modulus, E = 197.5GPA, and yield strength, σ_0 = 245.45MPa. Figure 3.50 shows the geometry of the plates and idealization of pit corrosion size and distribution. The initial deflection is measured in the range of 1.15 – 3.38mm. An average value of 2.265mm is used in the following finite element analysis. From Figure 3.2, the samples of the pit corrosion damage distribution in a plate of oil tankers, pit corrosion size 30mm for the test plate is reasonable approximation.

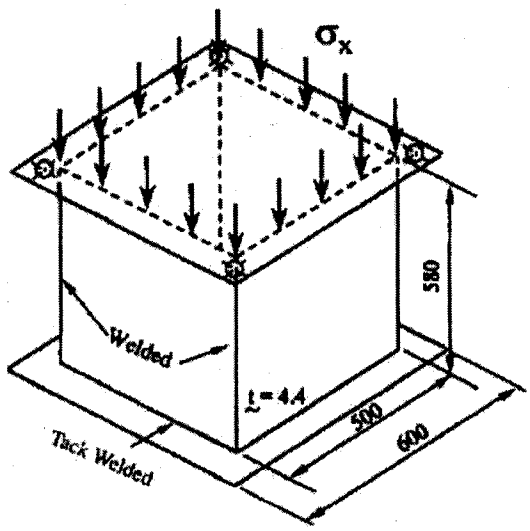

Figure 3.49 A schematic view of the test structure

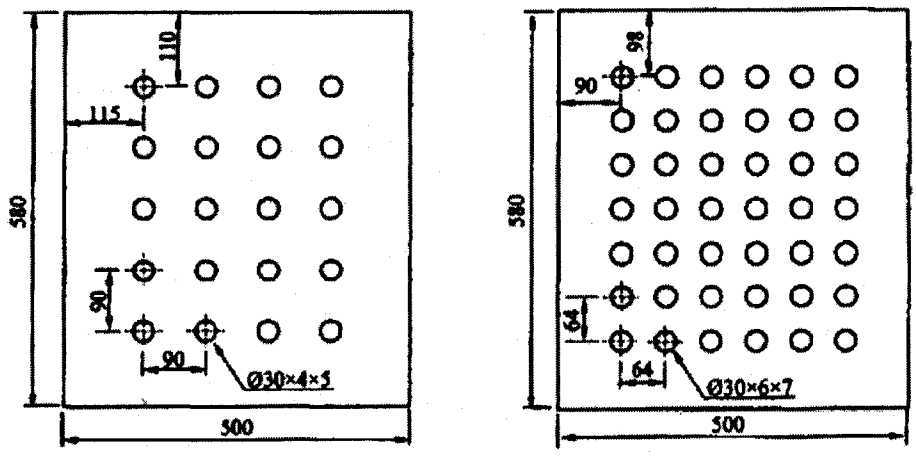

Figure 3.50 Geometry of the plates and idealization of pit corrosion size and distribution

The elastic-plastic large deflection behavior of the test structures has been analyzed by the finite element program ANSYS (2005). It is to confirm whether the finite element analysis is applicable to analysis of the ultimate strength for steel plates with pit corrosion and also to develop a relevant finite element analysis strategy.

To assess scale for breakdown due to pit corrosion, a parameter denoted by DOP (degree of pit corrosion intensity) is often used, where DOP is defined as the ratio percentage of the corroded surface area to the original plate surface area.

Figure 3.51 is the one-quarter finite element models for Figure 3.50 test structures with 4.87 percent DOP and 10.24 percent DOP correspondingly. Figure 3.52 is one more model with 17.55 percent DOP.

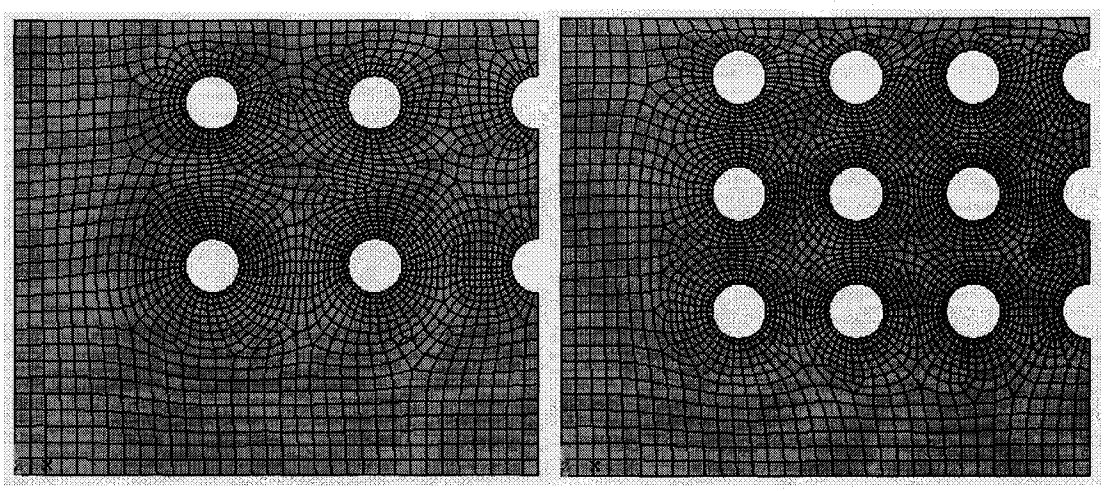

Figure 3.51 Finite element models with 4.87 percent DOP and 10.24 percent DOP

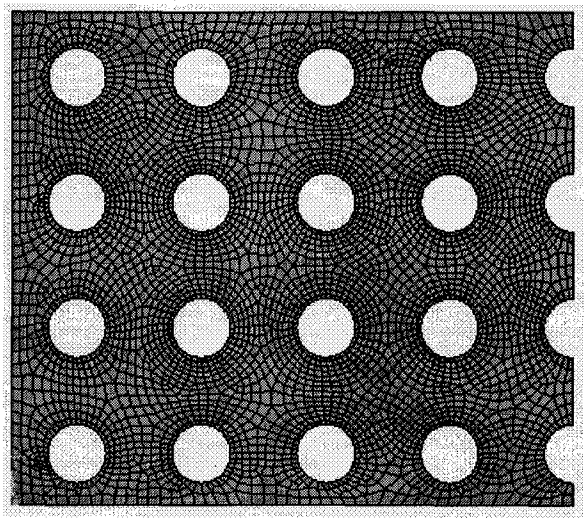

Figure 3.52 A finite element model with 17.55 percent DOP

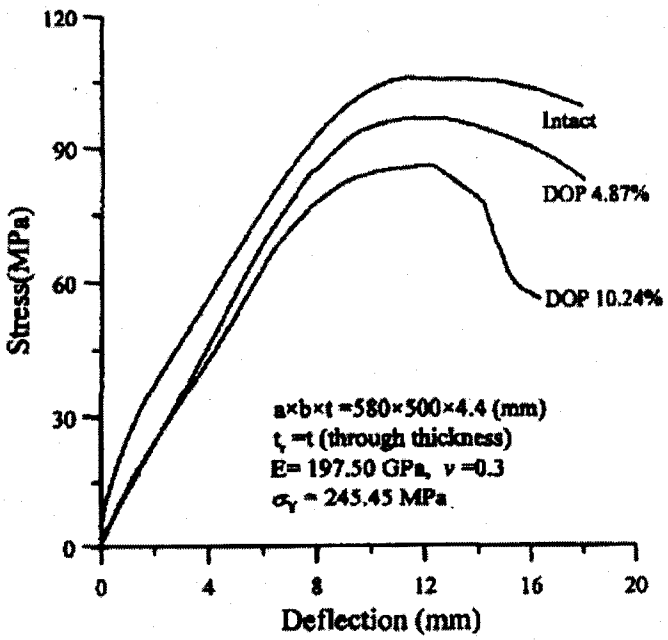

Figure 3.53 Average axial compressive stress-deflection curves for all four test plate elements with pit corrosion under axial compressive loads, varying the level of DOP

Figure 3.53 (Paik et al 2003) shows the experiment results. The finite element analyses are carried out by using the models shown in Figure 3.51 and Figure 3.52. Comparisons are performed also.

Figure 3.54 gives the contour plots of u_z field at the ultimate limit state corresponding to 4.87%, 10.24% and 17.55% DOP steel plates. Figures 3.55-3.57 show the contour plots of von Mises equivalent stresses at the ultimate state for both top and bottom sides. From these figures, damage zones and failure patterns can be viewed.

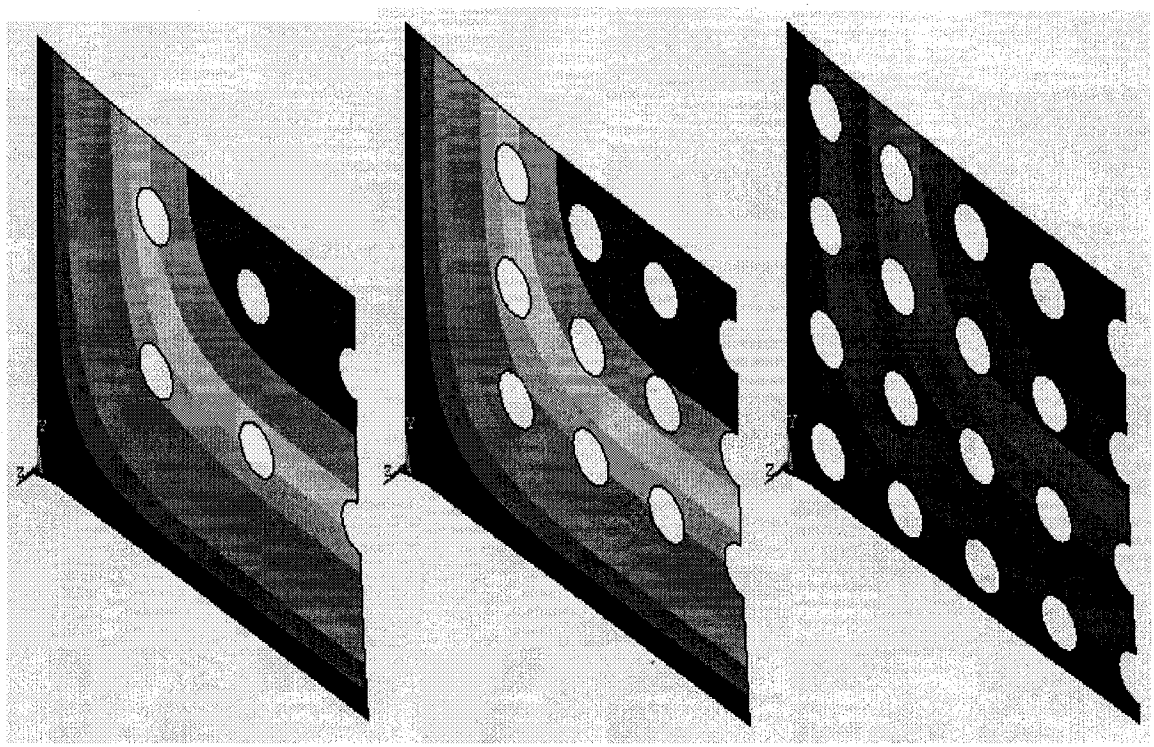

Figure 3.54 Contour plots of u_z field at the ultimate limit state (4.87 percent, 10.24 percent and 17.55 percent DOP correspondingly)

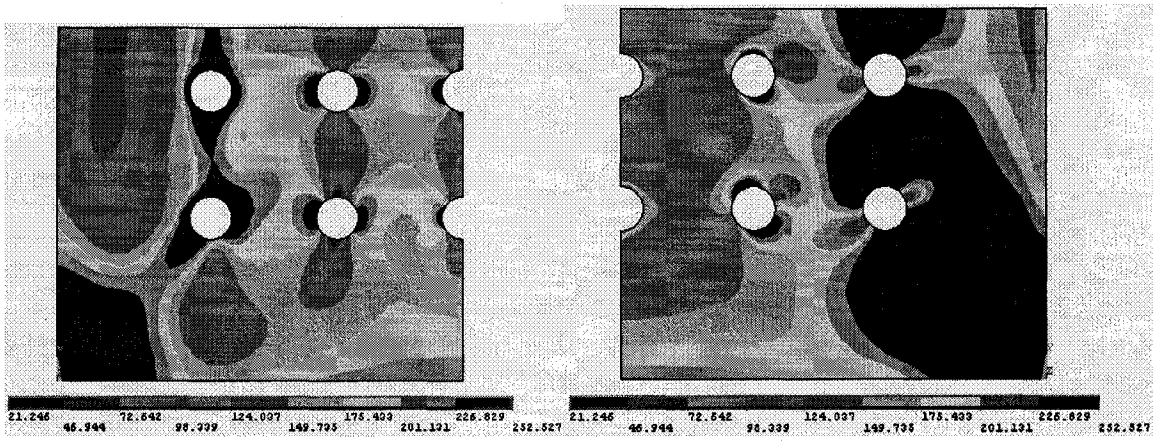

Figure 3.55 Contour plots of von Mises equivalent stresses at the ultimate state for top and bottom (4.87 percent DOP)

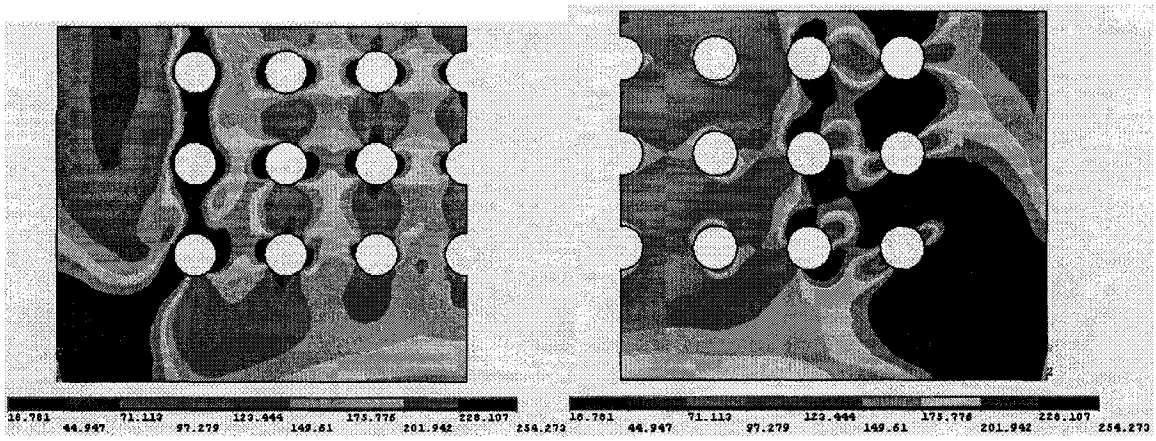

Figure 3.56 Contour plots of von Mises equivalent stresses at the ultimate state for top and bottom (10.24 percent DOP)

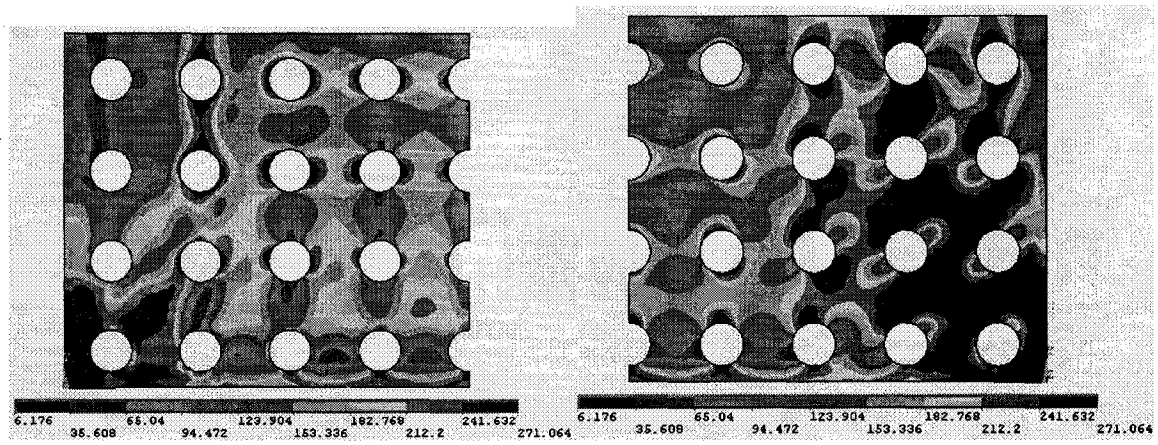

Figure 3.57 Contour plots of von Mises equivalent stresses at the ultimate state for top and bottom (17.55 percent DOP)

Further, interestingly Figure 3.58 shows the deformed shape and contour plot of u_z field right after the ultimate limit state. It has been crashed. From Figure 3.59 it has also been seen clearly almost the whole plate got yielded.

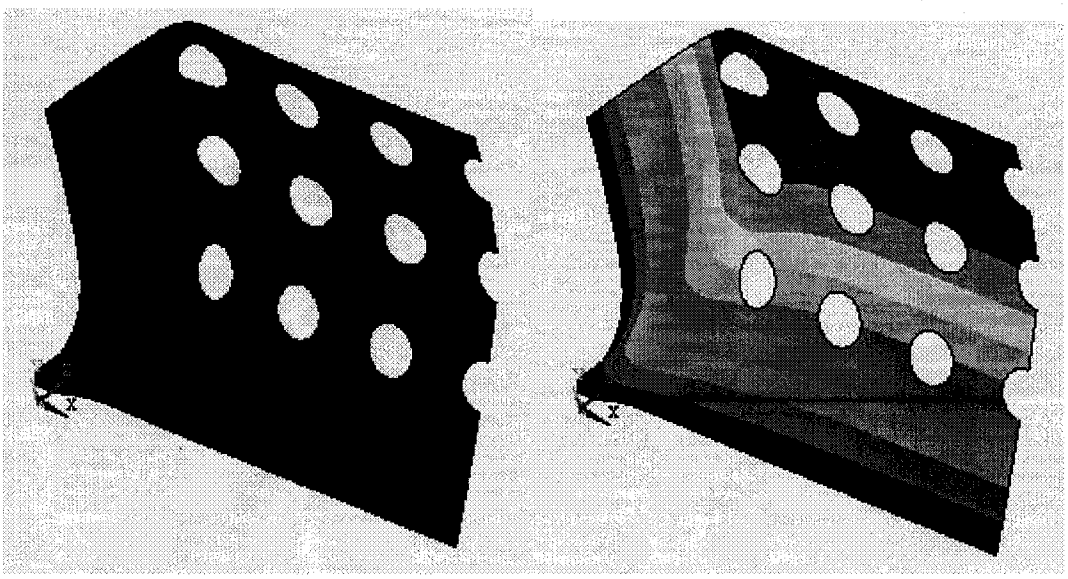

Figure 3.58 Deformed shape and contour plot of u_z field right after the ultimate limit state

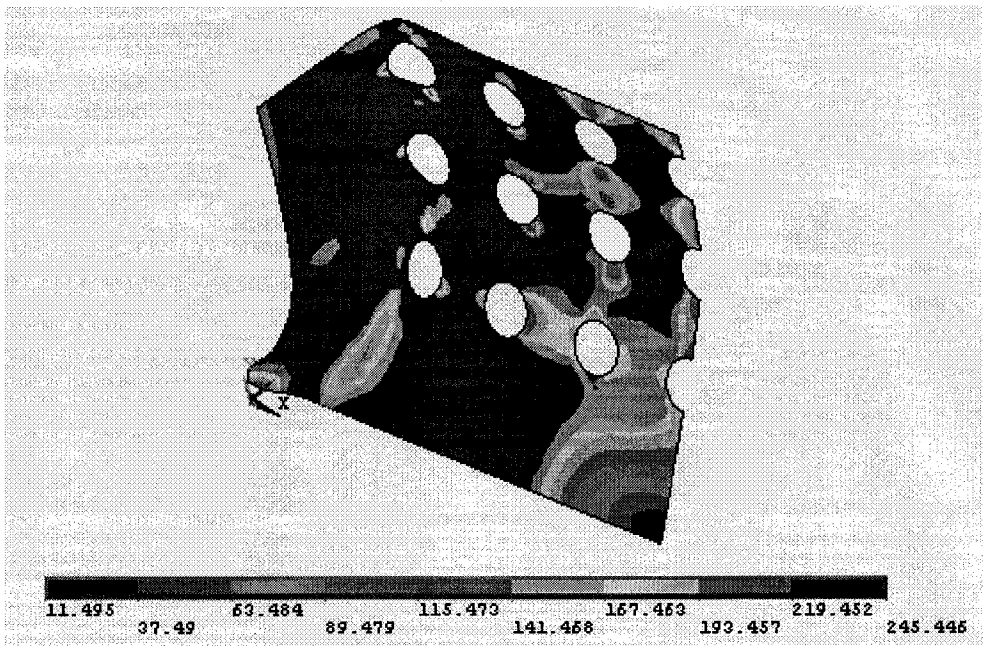

Figure 3.59 Contour plots of von Mises equivalent stresses right after the ultimate state

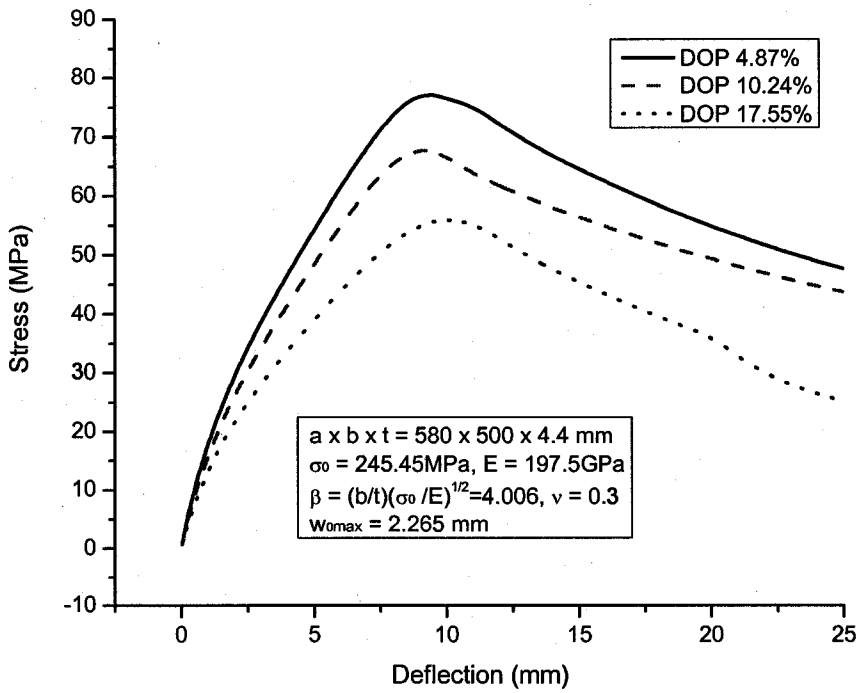

Figure 3.60 Axial compressive stress-deflection curves with varying level of DOP

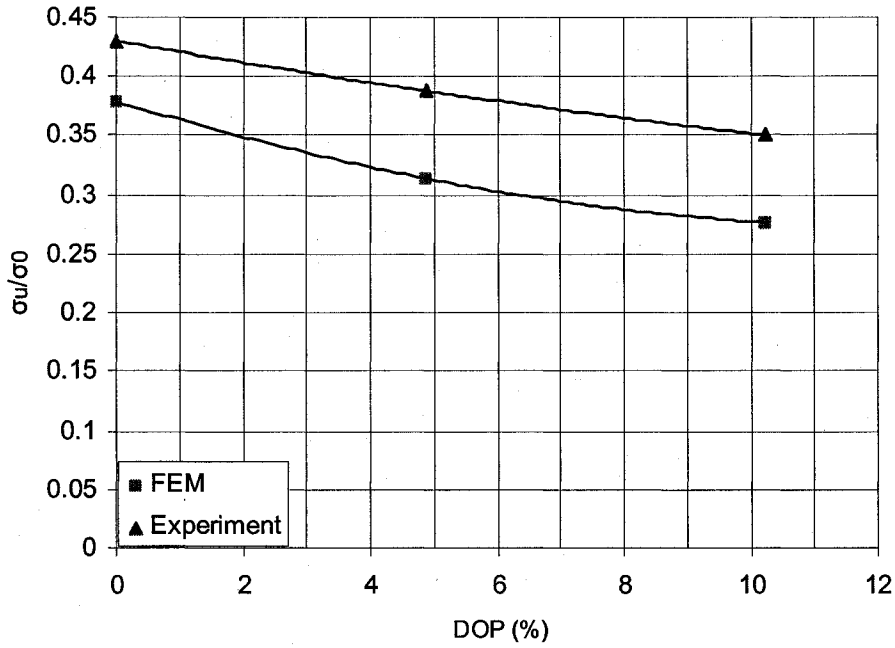

Figure 3.61 Comparison of results between experiment and finite element analysis

Figure 3.60 shows the FE results of compressive stress-deflection curves with different levels of DOP. From Figure 3.61, it demonstrates the comparison for experiment results and FE results. The FE results are averagely 17% below the experiment results. The difference could be caused by the simply supported boundary conditions.

From Figure 3.49 the test structure set-up, it has been simulating the simply supported boundary conditions. The box structure keeps the unloaded edges straight. Actually for simply supported boundary conditions, the unloaded edges can move freely in plane. The difference of the ultimate strength caused by this could be 20% (Paik and Thayamballi 2003). This might explain the discrepancy between FE results and experimental observations.

In order to verify this, a number of simulations which keep unloaded edges remain straight and cannot move freely in plane have been performed. The results are shown in Figure 3.62 with label: FEM2. They match the experiment results very well with errors under 2%. It confirms the above thoughts.

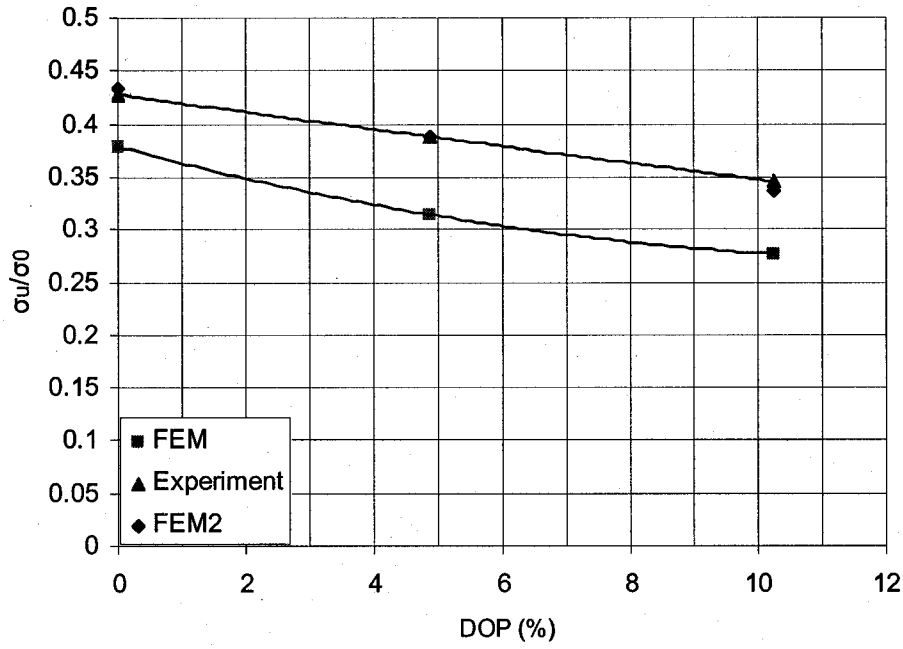

Figure 3.62 Comparison of results between experiment and finite element analysis after modifying the boundary conditions

Therefore the finite element analysis performed by ANSYS is able to capture the ultimate strength behavior of a steel plate with pit corrosion. In the following a series of nonlinear finite element analyses are carried out corresponding to different levels of pit corrosion. The ultimate strength reduction characteristics due to pit corrosion are investigated.

As previous verification, the effect of strain hardening on the ultimate strength of an intact steel plate under axial compression is small could be neglected. Pessimistically an elastic-perfectly plastic material model can be used to carry out the strength assessment. However, simulations still need to be done to verify if it holds for the steel plate with pit corrosion. In the following, the steel plate with 4.87% DOP is taken as example to investigate the effect of strain hardening on the ultimate strength.

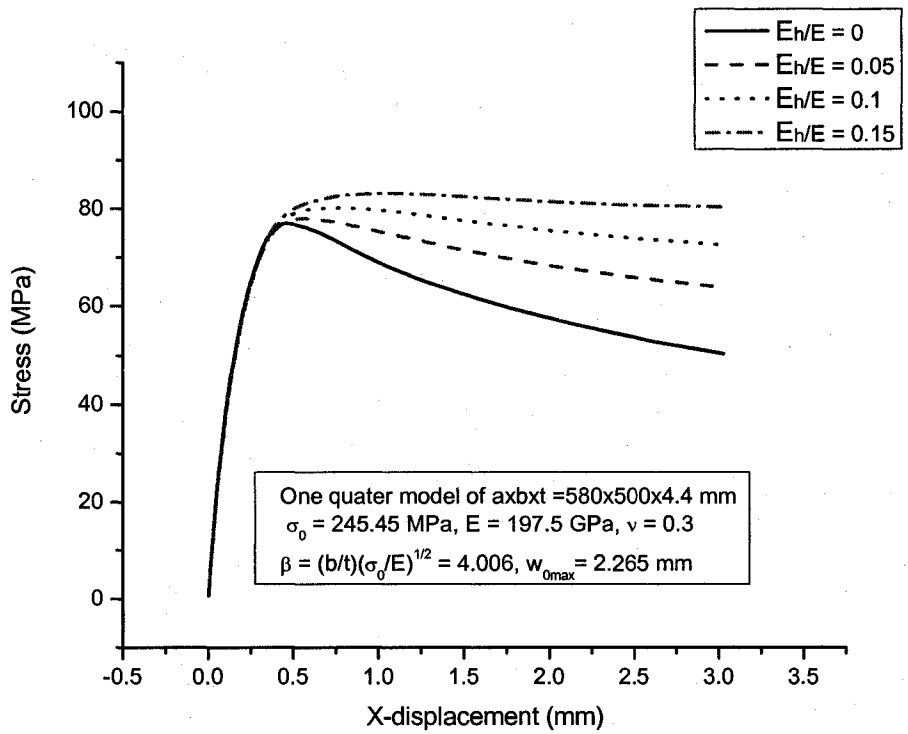

Figure 3.63 The effect of strain hardening on the ultimate strength of a steel plate with pit corrosion under axial compression – stress vs x displacement curves

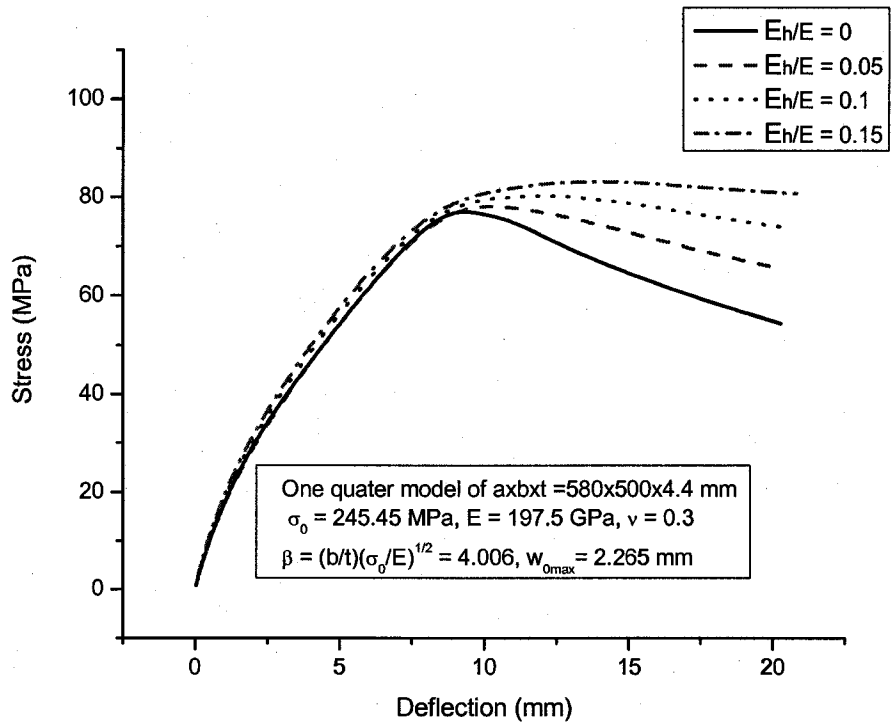

Figure 3.64 The effect of strain hardening on the ultimate strength of a steel plate with pit corrosion under axial compression– stress vs deflection curves

Figures 3.63 and 3.64 illustrate the effect of strain hardening on the elastic and plastic large deflection behavior of a steel plate with pit corrosion (DOP: 4.87%) under axial compression. As shown though strain hardening affects the post-buckling behaviors, the effect on the ultimate strength of the simply supported steel plate with pit corrosion is small and could be neglected for conservative strength assessment and structural design. Therefore, an elastic-perfectly plastic material model, i.e., without considering strain hardening, is sufficient for practical strength assessment of steel-plated structure with pit corrosion.

3.10. PIT CORROSION DISTRIBUTION EFFECTS

In some circumstances, pit corrosion may propagate along some directions. Thus in the following sections these effects are examined. The distributions are divided into three categories according to the pit corrosion directions, names as transverse side, long side, and middle side, respectively.

3.10.1. Pit corrosion on transverse side

Figure 3.65 shows the one quarter models of pit corroded steel plates with different DOP's. The pit corrosion is on the transverse side, and propagates along the long side direction from DOP1 to DOP4, where DOP1 is 4.524% and DOP4 is 18.096%.

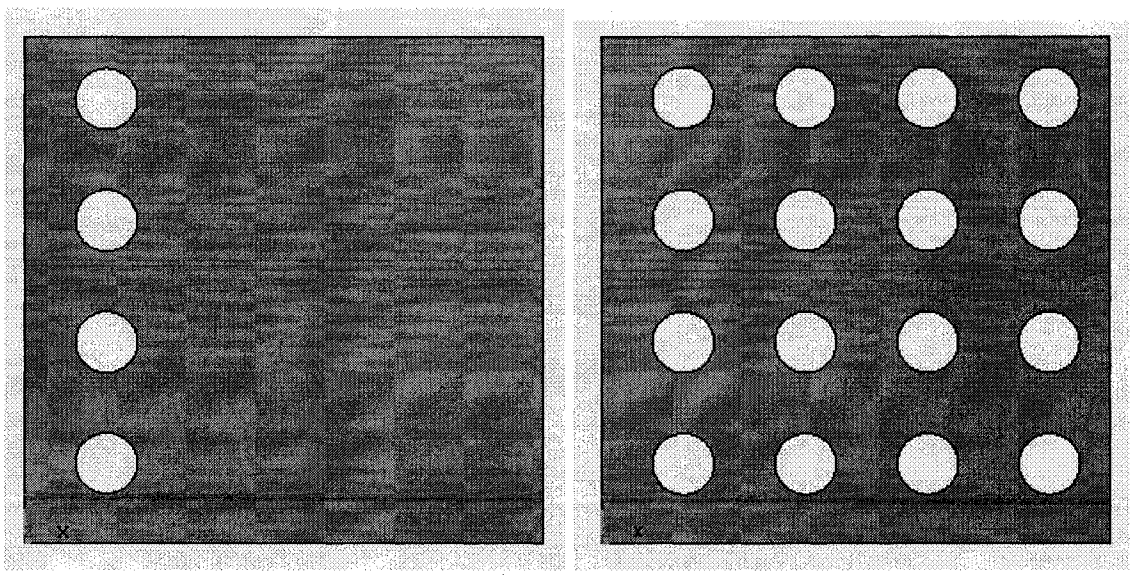

Figure 3.65 One quarter models of pit corroded steel plates (transverse side)

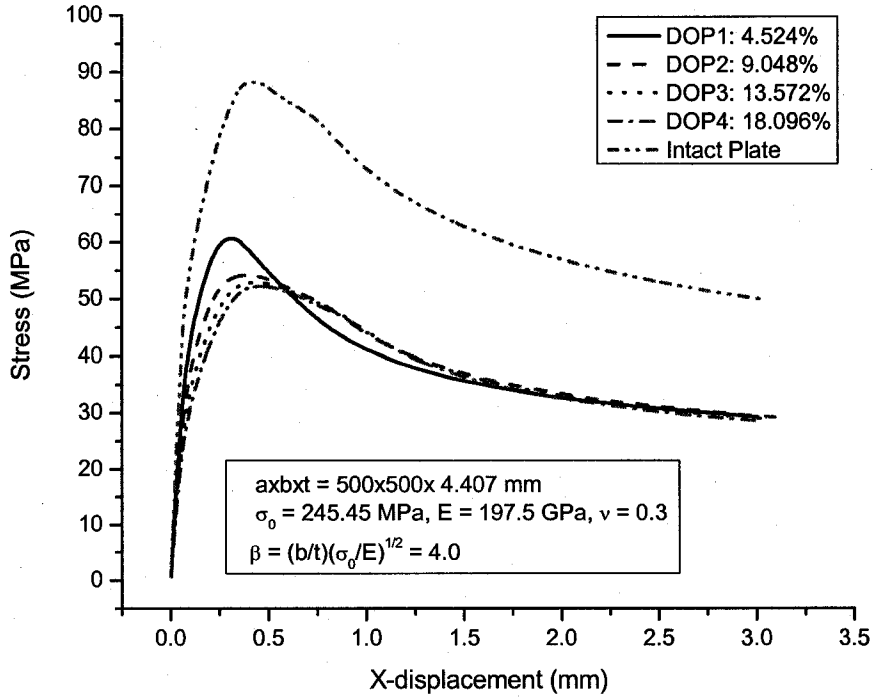

Figure 3.66 Effects of pit corrosion transverse distribution ($\beta = 4.0$)

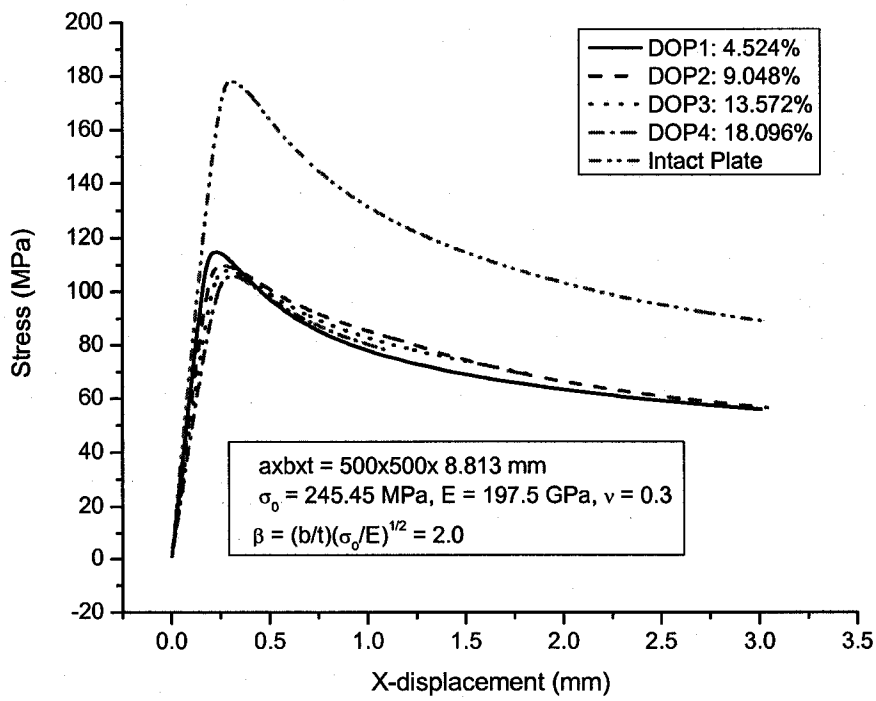

Figure 3.67 Effects of pit corrosion transverse distribution ($\beta = 2.0$)

Figure 3.66 and Figure 3.67 show the effects of pit corrosion transverse distribution with plate slenderness ratio, $\beta = 4.0$ and $\beta = 2.0$, respectively. As shown, the distribution has big effect on the ultimate compressive strength of the pit corroded plate. With only 4.524% DOP, the ultimate compressive strength reduces about 35%, which holds for both $\beta = 4.0$ and $\beta = 2.0$. As the pit corrosion propagates along the long side into middle, the effect diminishes quickly. From 13.572% DOP to 18.096% DOP, there is even no big difference of the ultimate compressive strength for plates with pit corrosion. When plate gets thicker, the tendency becomes more evident.

3.10.2. Pit corrosion on longitudinal side

Figure 3.68 shows the one quarter models of pit corroded steel plates with different DOP's. The pit corrosion is on the longitudinal side, and propagates along the transverse side direction from DOP1 to DOP3, where DOP1 is 4.524% and DOP3 is 13.572%.

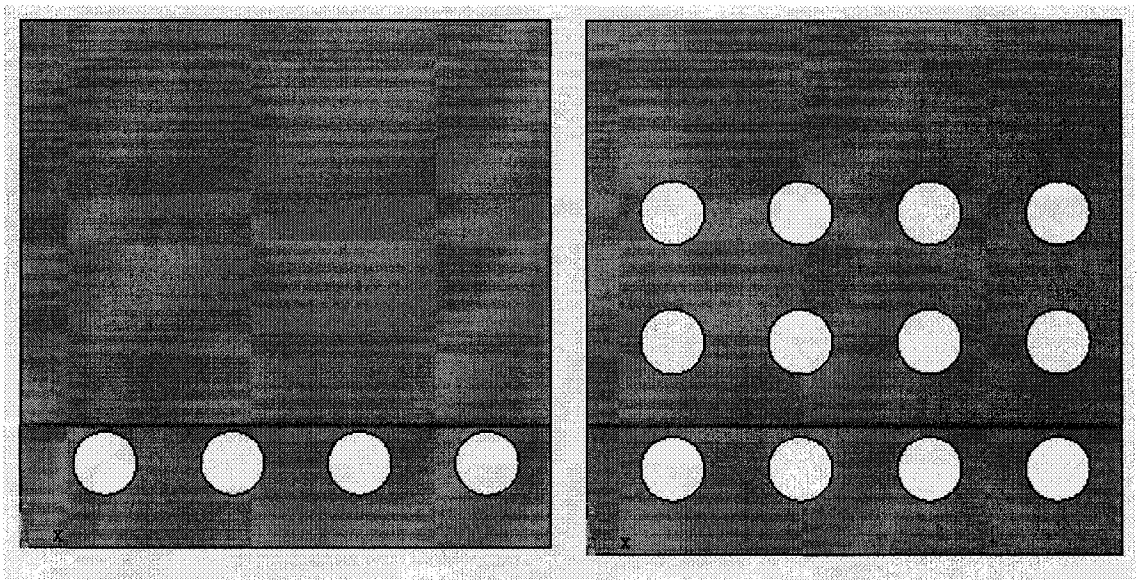

Figure 3.68 One quarter model of pit corroded steel plates (longitudinal side)

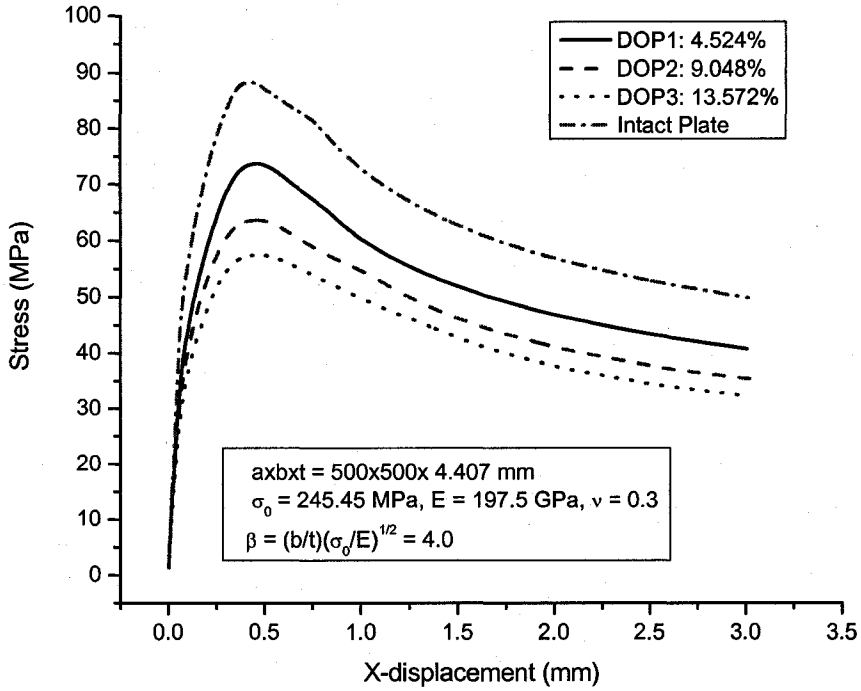

Figure 3.69 Effects of pit corrosion longitudinal distribution (β = 4.0)

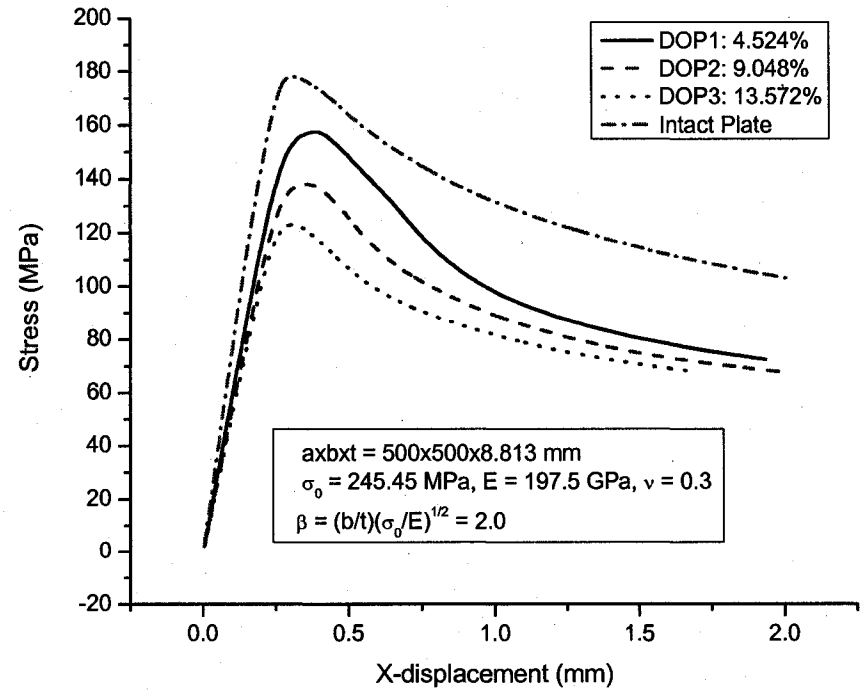

Figure 3.70 Effects of pit corrosion longitudinal distribution (β = 2.0)

Figure 3.69 and Figure 3.70 show the effects of pit corrosion longitudinal distribution with plate slenderness ratio, $\beta = 4.0$ and $\beta = 2.0$, respectively. The ultimate compressive strength of the pit corroded plate is almost changing with DOP's linearly for this distribution. With 4.524% DOP, the ultimate compressive strength reduces about 15%, with 9.048% DOP, the ultimate compressive strength reduces about 25%, and with 13.572% DOP, the ultimate compressive strength reduces about 35%.

3.10.3. Pit corrosion on middle of plate

Figure 3.71 shows the one quarter models of pit corroded steel plates with different DOP's. The pit corrosion is on the middle of plate, and propagates along the longitudinal side direction from DOP1 to DOP3, where DOP1 is 4.524% and DOP3 is 13.572%.

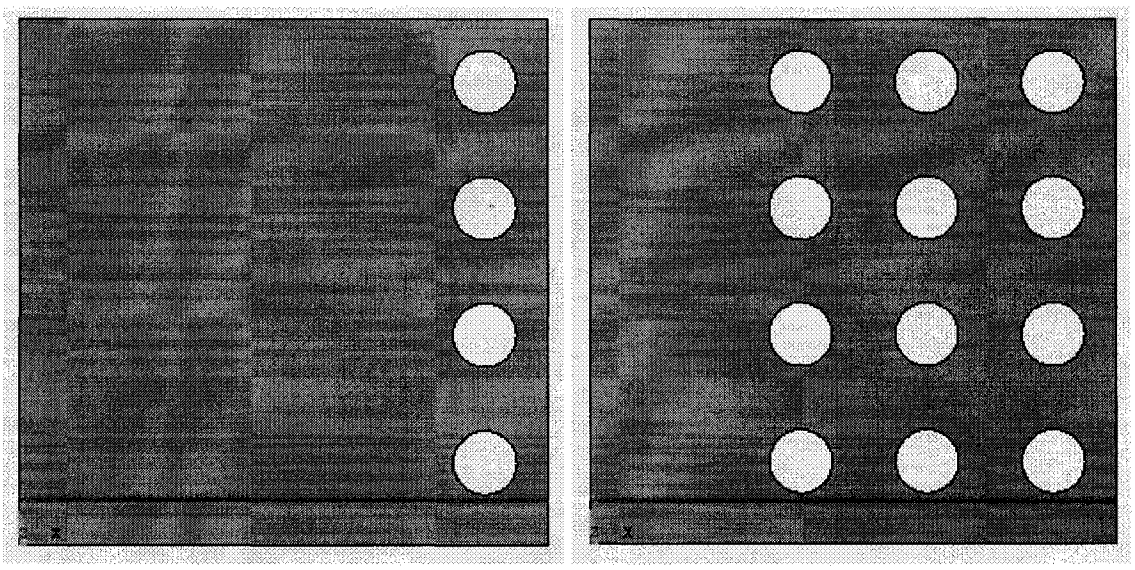

Figure 3.71 One quarter model of pit corroded steel plates (middle of plate)

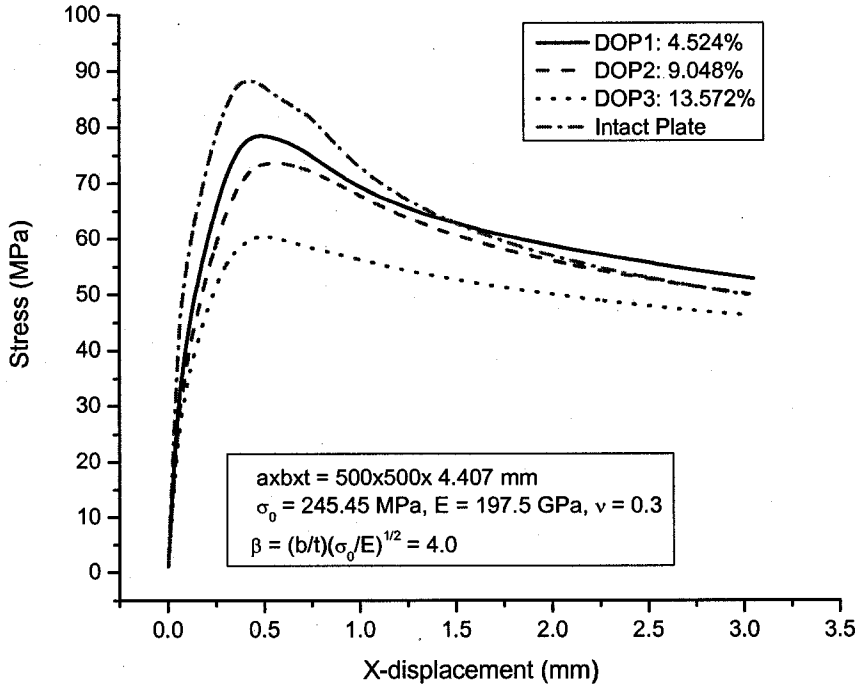

Figure 3.72 Effects of pit corrosion middle distribution (β = 4.0)

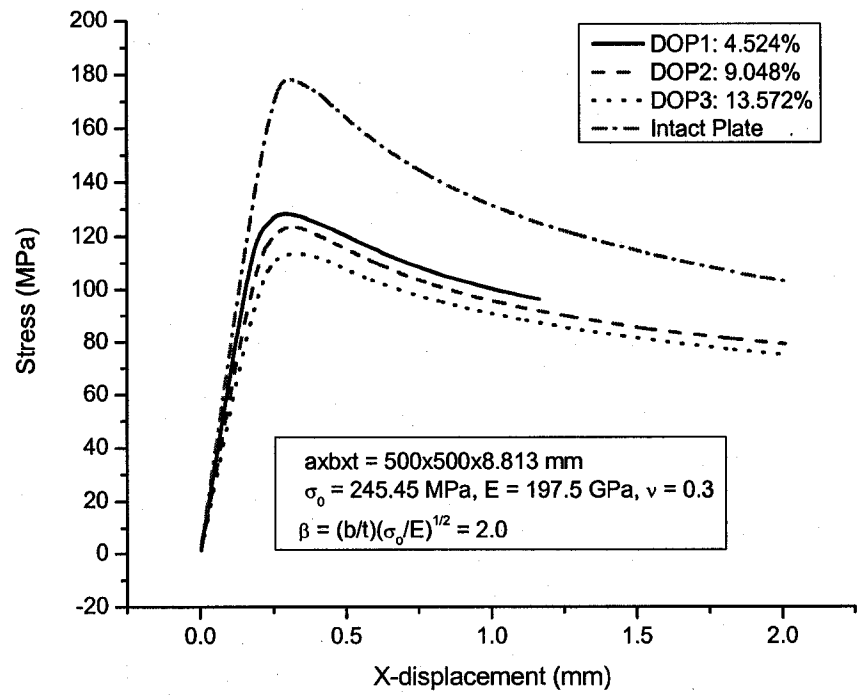

Figure 3.73 Effects of pit corrosion middle distribution (β = 2.0)

Figure 3.72 and Figure 3.73 show the effects of pit corrosion middle distribution with plate slenderness ratio, $\beta = 4.0$ and $\beta = 2.0$, respectively. The ultimate compressive strength of the pit corroded plate changes differently. For $\beta = 4.0$, the ultimate compressive strength reduces rapidly as the pit corrosion propagates along longitudinal side direction and close to edge. For instance, from 4.524% DOP to 9.048% DOP, the ultimate strength only decrease about 6%, while from 9.048% DOP to 13.572% DOP, the ultimate strength decrease about 20%. For $\beta = 2.0$, roughly the ultimate compressive strength decreases linearly.

3.10.4. Comparison of different pit corrosion distributions with same degree of pit corrosion intensity (DOP)

The effects of different pit corrosion distributions have been examined separately with varying degrees of pit corrosion intensity. In some circumstances, different pit corrosion distributions may appear in the different ship structure members at the same time. Therefore, comparison between them with same DOP may give one some insights about which distribution is more severe, and then take correspondent precautions and actions.

Thus, comparisons have been preformed according to different DOP's, i.e. 4.524% DOP first, then 9.048% DOP next, finally 13.572% DOP. Transverse, long, and middle distributions are plotted together. The curve for intact plate has also been added for reference purpose. Figures 3.74 – 3.79 demonstrate the comparison results.

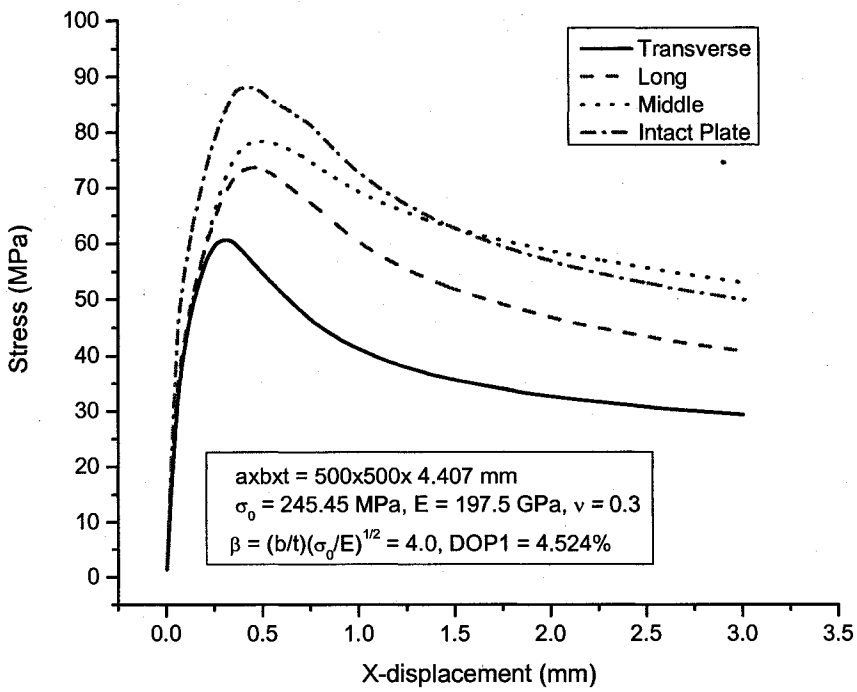

Figure 3.74 Effects of pit corrosion distributions (4.524% DOP, β = 4.0)

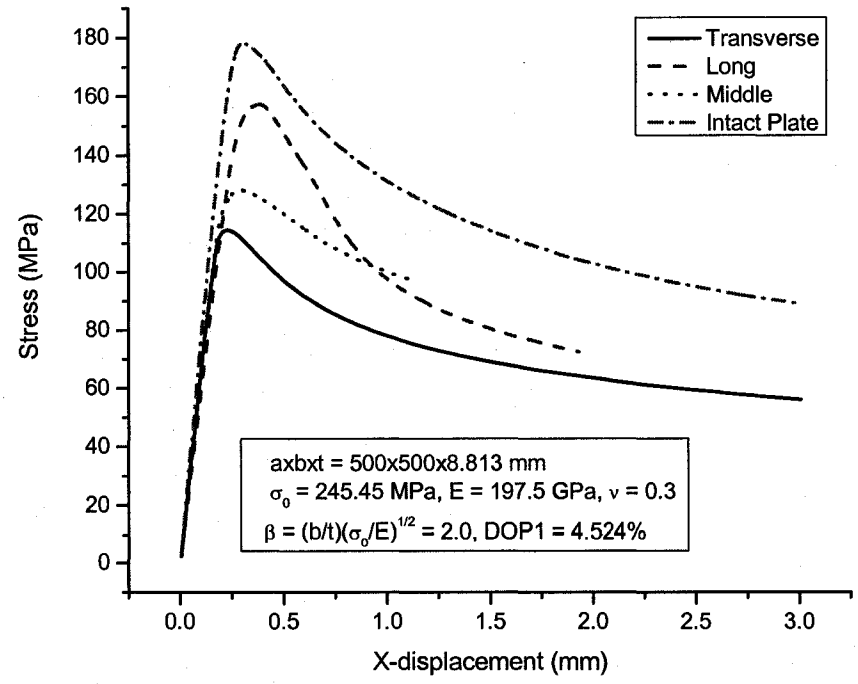

Figure 3.75 Effects of pit corrosion distributions (4.524% DOP, β = 2.0)

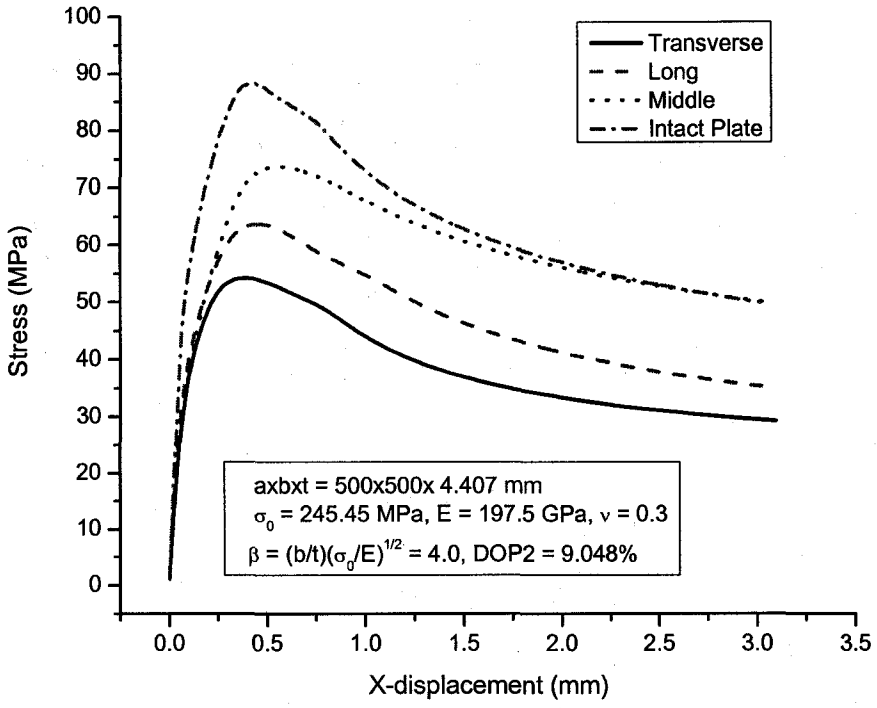

Figure 3.76 Effects of pit corrosion distributions (9.048% DOP, β = 4.0)

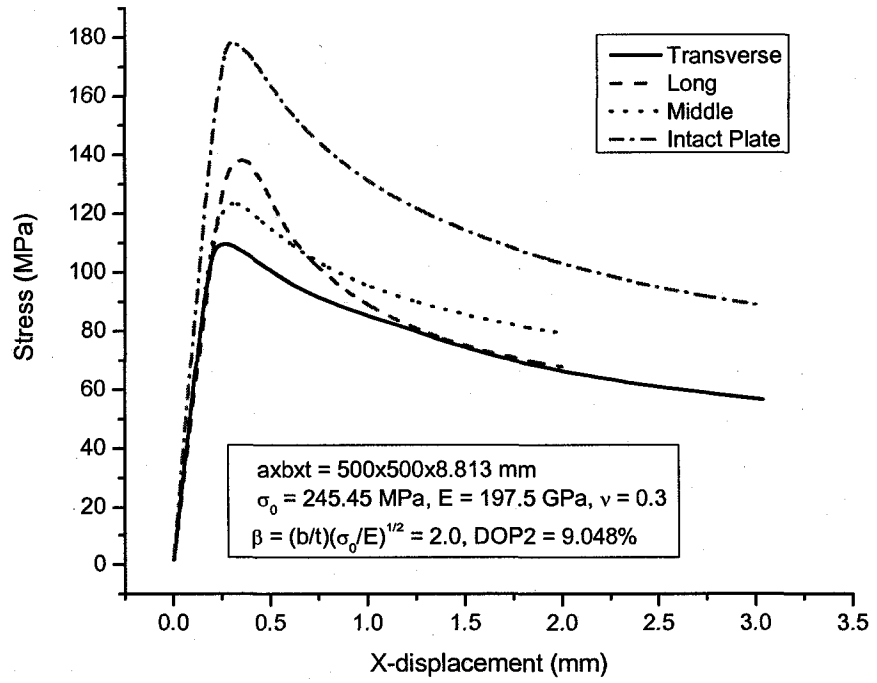

Figure 3.77 Effects of pit corrosion distributions (9.048% DOP, β = 2.0)

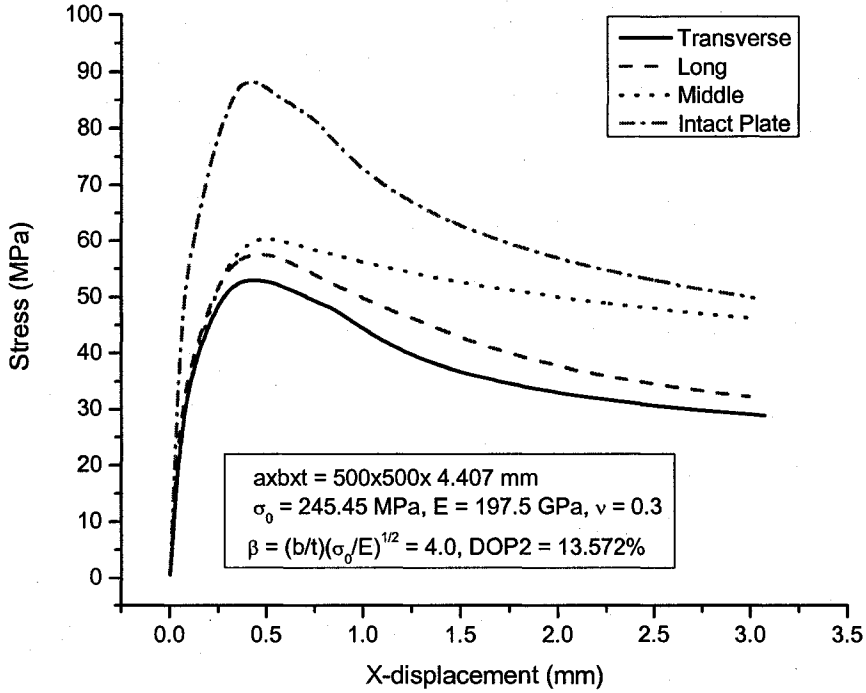

Figure 3.78 Effects of pit corrosion distributions (13.572% DOP, $\beta = 4.0$)

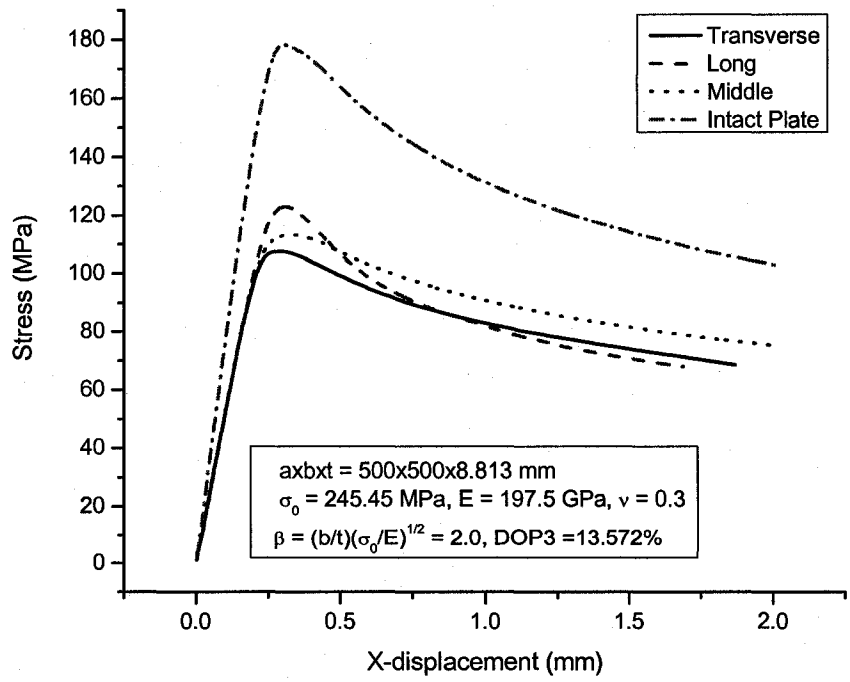

Figure 3.79 Effects of pit corrosion distributions (13.572% DOP, $\beta = 2.0$)

3.10.5. Pit corrosion on transverse side (aspect ratio α = 3.0)

For ship structures, the length and breadth ratios are usually varying according to different portions. Previously it has proven that the length and breadth ratio has a very small effect on ultimate strength of the intact steel plate. In the following this fact is examined for the pit corroded steel plates. Figure 3.80 and Figure 3.81 show the one quarter models of the pit corroded steel plates with different DOP's. The pit corrosion is on the transverse side, and propagates along the long side direction from DOP1 to DOP6, where DOP1 is 1.508% and DOP6 is 9.048%.

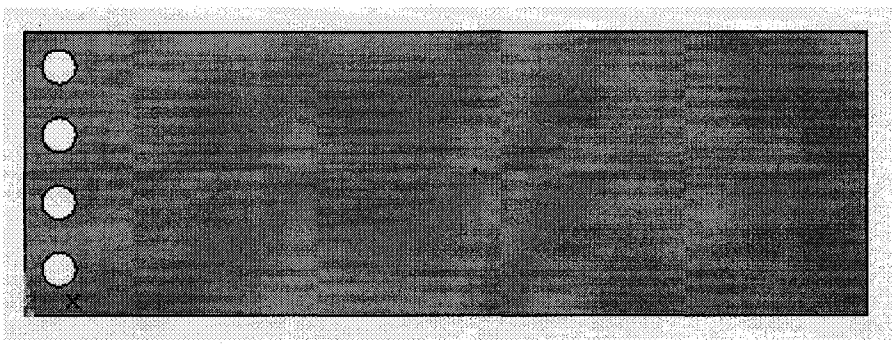

Figure 3.80 One quarter model of pit corroded steel plates (α = 3.0, DOP1)

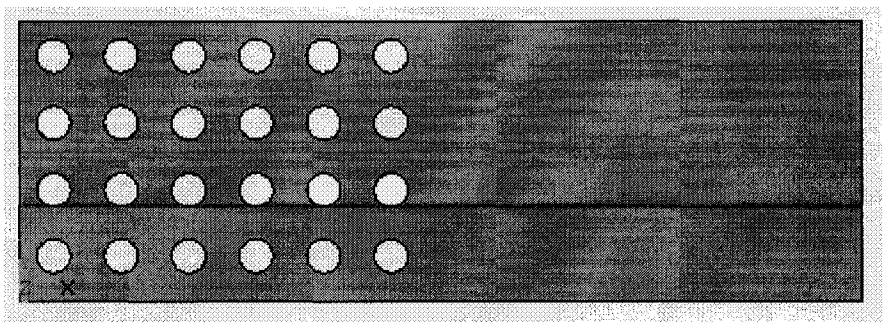

Figure 3.81 One quarter model of pit corroded steel plates (α = 3.0, DOP6)

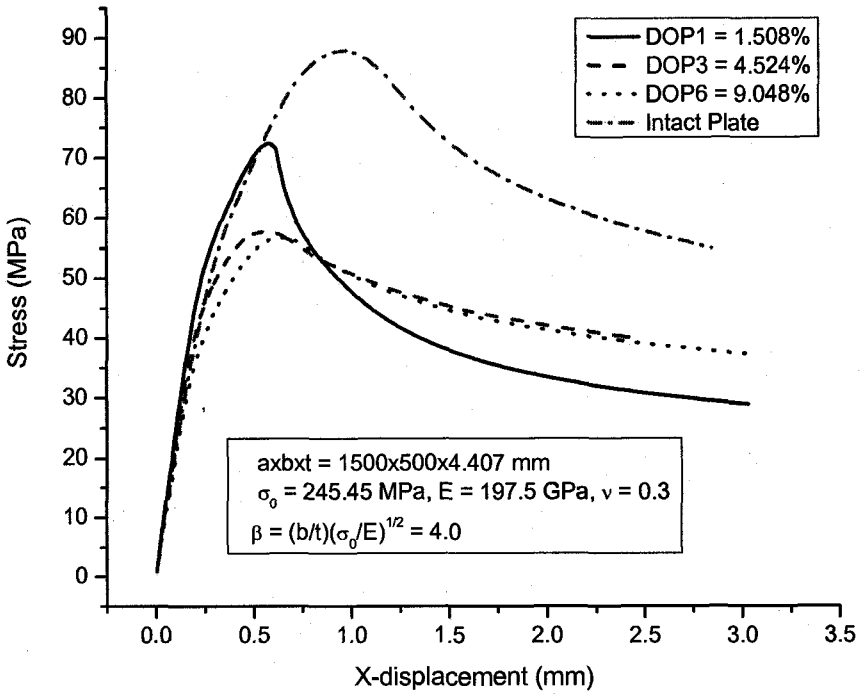

Figure 3.82 Effects of pit corrosion transverse distribution ($\alpha = 3.0$, $\beta = 4.0$)

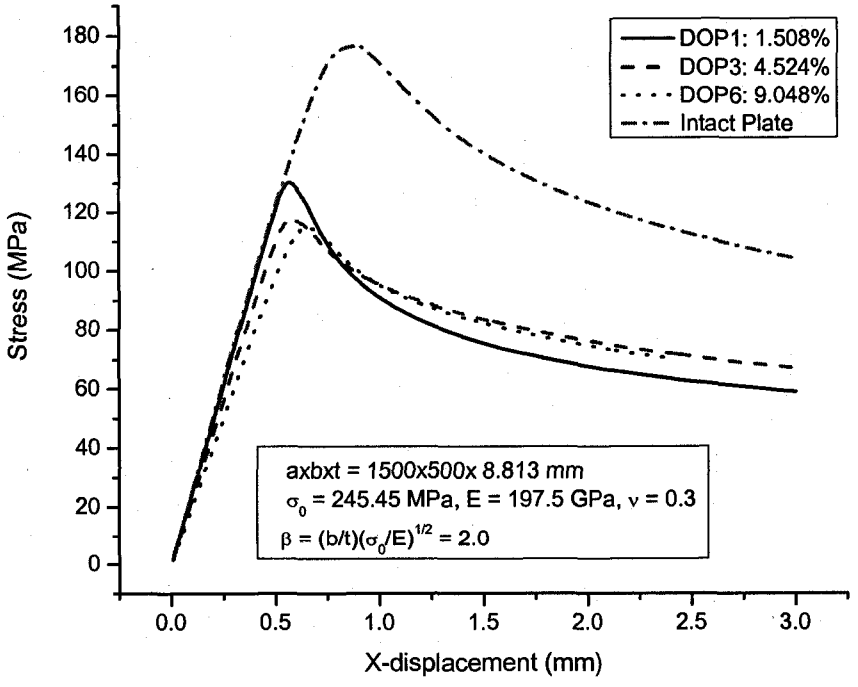

Figure 3.83 Effects of pit corrosion transverse distribution ($\alpha = 3.0$, $\beta = 2.0$)

Figure 3.82 and Figure 3.83 show the effects of pit corrosion transverse distribution with plate slenderness ratio, $\beta = 4.0$ and $\beta = 2.0$, respectively. As shown, the distribution has big effect on the ultimate compressive strength of the pit corroded plate. With only 1.508% DOP, the ultimate compressive strength reduces about 17% for the plate with $\beta = 4.0$ and about 25% for the plate with $\beta = 2.0$. As the pit corrosion propagates along the long side into middle, the effect diminishes quickly. From 4.524% DOP to 9.048% DOP, the differences of the ultimate compressive strength for plates with pit corrosion are very small. When plate gets thicker, the tendency becomes more evident.

3.10.6. Pit corrosion on longitudinal side (aspect ratio $\alpha = 3.0$)

Figure 3.84 and Figure 3.85 show the one quarter models of pit corroded steel plates with different DOP's. The pit corrosion is on the longitudinal side, and propagates along the transverse side direction from DOP1 to DOP3, where DOP1 is 4.524% and DOP3 is 13.572%.

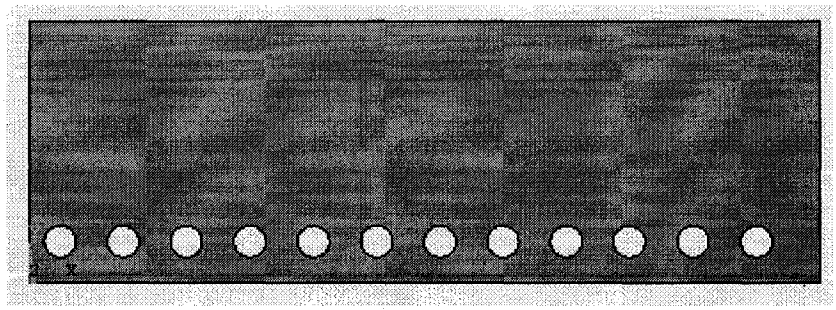

Figure 3.84 One quarter model of pit corroded steel plates ($\alpha = 3.0$, DOP1)

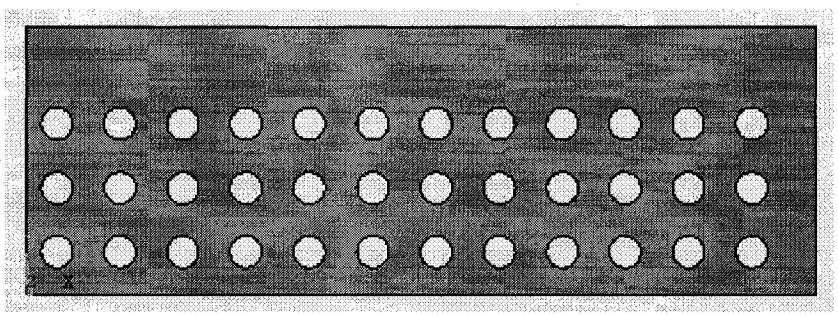

Figure 3.85 One quarter model of pit corroded steel plates ($\alpha = 3.0$, DOP3)

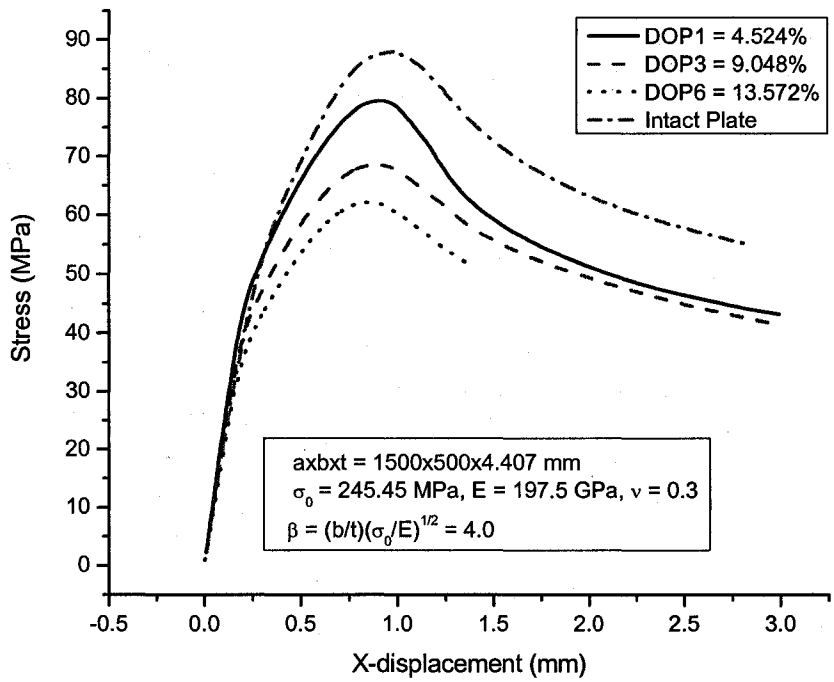

Figure 3.86 Effects of pit corrosion longitudinal distribution ($\alpha = 3.0$, $\beta = 4.0$)

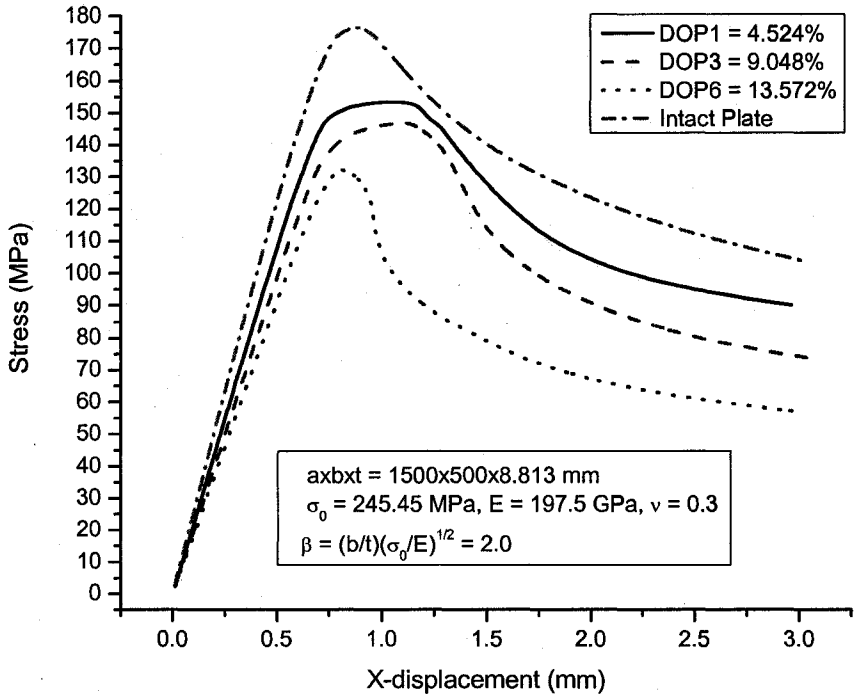

Figure 3.87 Effects of pit corrosion longitudinal distribution ($\alpha = 3.0$, $\beta = 2.0$)

Figure 3.86 and Figure 3.87 show the effects of pit corrosion longitudinal distribution when the plates have aspect ratio $\alpha = 3.0$, and with plate slenderness ratio, $\beta = 4.0$ and $\beta = 2.0$, respectively. The ultimate compressive strength of the pit corroded plate is roughly changing with DOP's linearly for this distribution.

3.10.7. Pit corrosion on the middle of plate (aspect ratio $\alpha = 3.0$)

Figure 3.88 and Figure 3.89 show the one quarter models of pit corroded steel plates with different DOP's. The pit corrosion is on the middle of plate, and propagates along the long side direction from DOP1 to DOP6, where DOP1 is 4.524% and DOP3 is 9.048%.

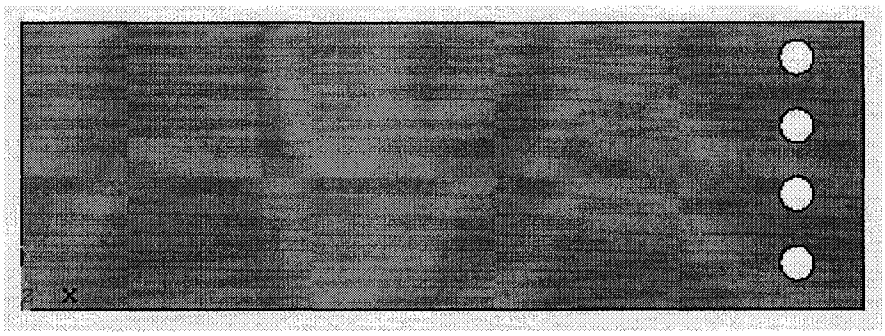

Figure 3.88 One quarter model of pit corroded steel plates (DOP1)

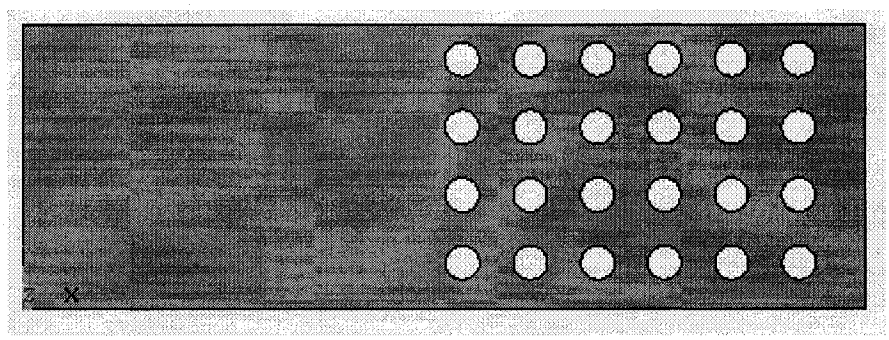

Figure 3.89 One quarter model of pit corroded steel plates (DOP6)

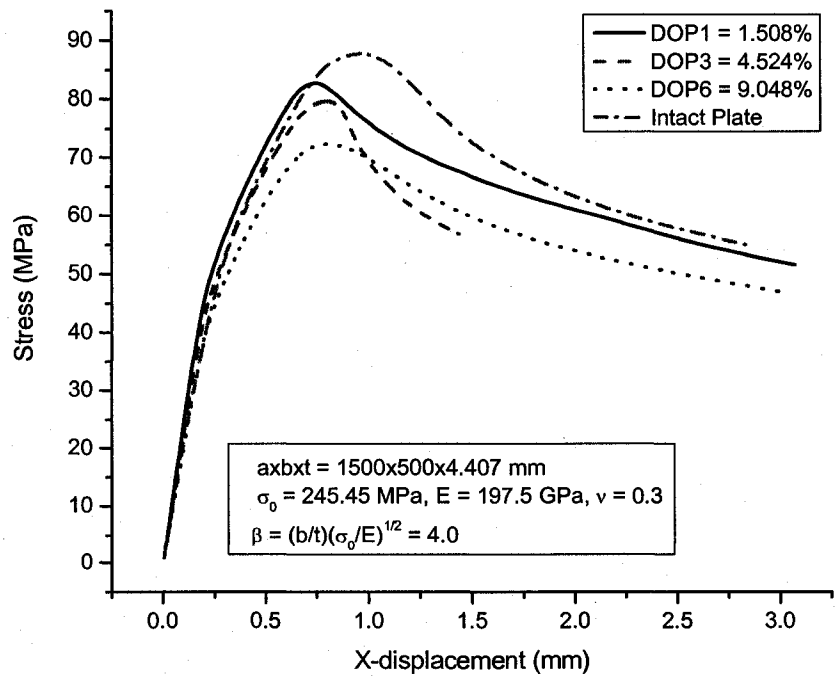

Figure 3.90 Effects of pit corrosion middle distribution ($\alpha = 3.0$, $\beta = 4.0$)

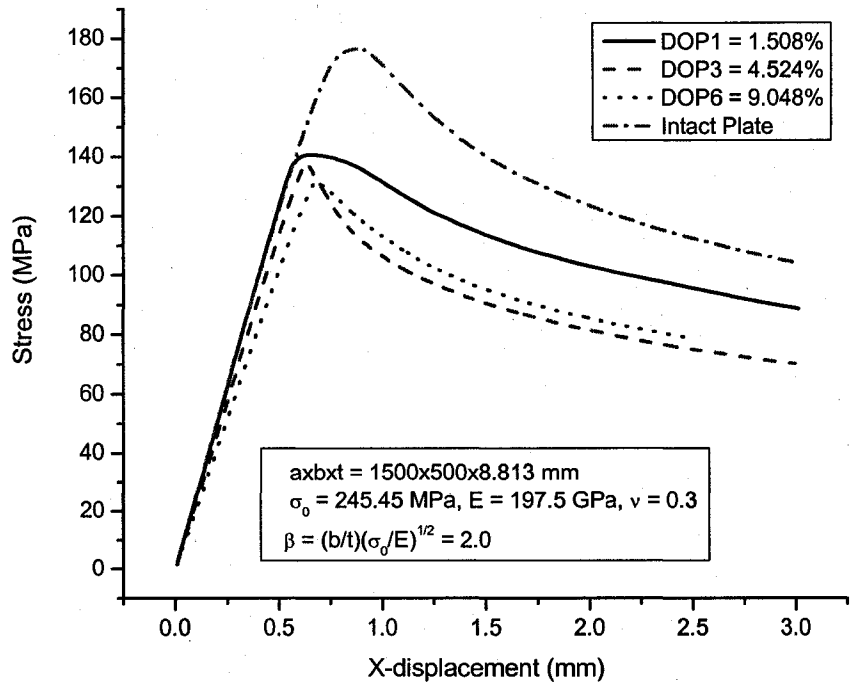

Figure 3.91 Effects of pit corrosion middle distribution ($\alpha = 3.0$, $\beta = 2.0$)

Figure 3.90 and Figure 3.91 show the effects of pit corrosion middle distribution with plate slenderness ratio, $\beta = 4.0$ and $\beta = 2.0$, respectively. As shown, the distribution has not that much effect on the ultimate compressive strength of the pit corroded plate as that of transverse distribution. The reason may be that the pit corroded areas are far away from the loading edges. As expected as the pit corroded areas are closer to these loading edges, the effect on ultimate strength will become more and more important.

3.10.8. Comparison of different pit corrosion distributions with same DOP (aspect ratio $\alpha = 3.0$)

The comparisons have been done for the plates with length and breadth ratio α = 1.0. Same procedures have been followed for plates with length and breadth ratio α = 3.0 in the following.

Similarly, comparisons have been preformed according to different DOP's, i.e. 4.524% DOP first, then 9.048% DOP next. Transverse, long, and middle distributions are plotted together. The curve for intact plate has also been added for reference purpose. Figures 3.92 – 3.95 plot the comparison results. Similarly transverse distribution has the worst effect on the ultimate compressive strength of the steel plate with pit corrosion.

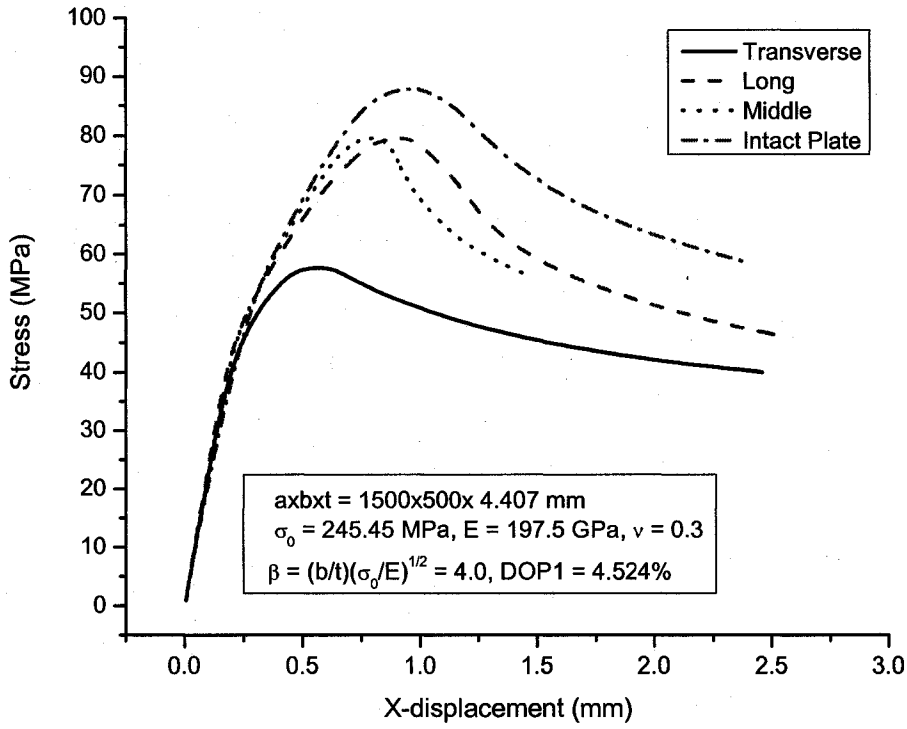

Figure 3.92 Effects of pit corrosion distributions (4.524% DOP, α = 3.0, β = 4.0)

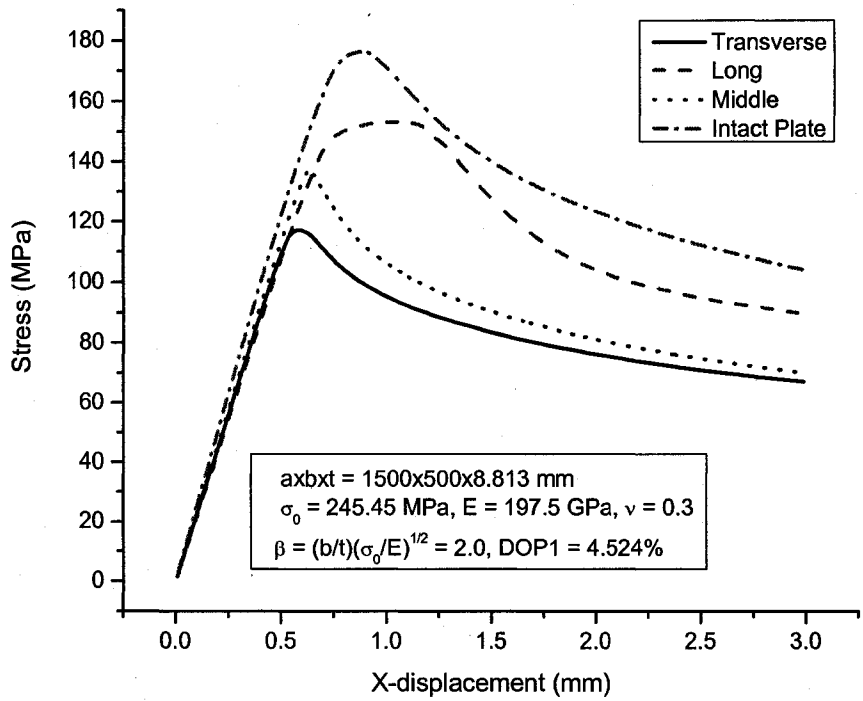

Figure 3.93 Effects of pit corrosion distributions (4.524% DOP, $\alpha = 3.0$, $\beta = 2.0$)

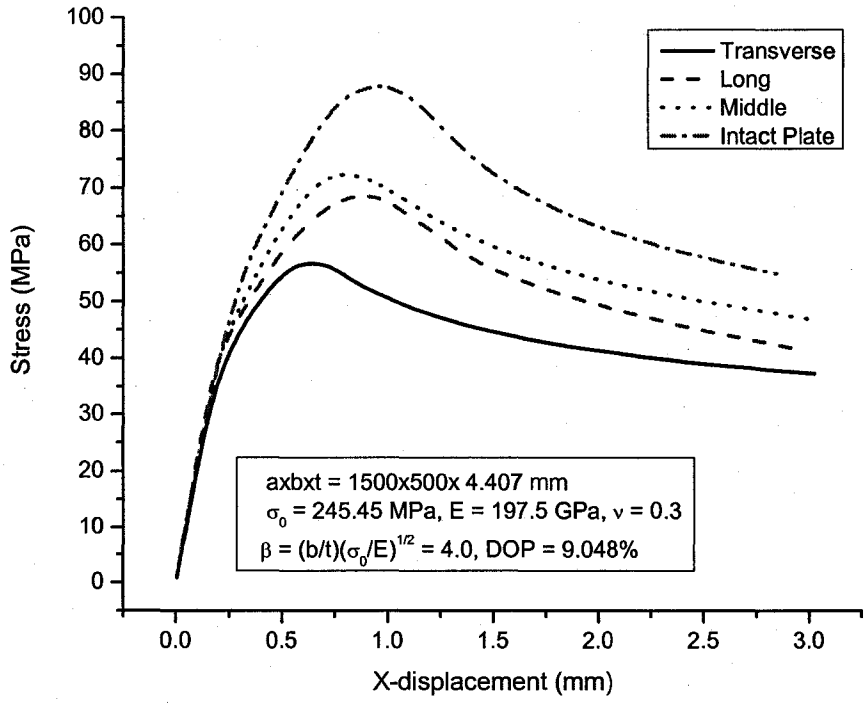

Figure 3.94 Effects of pit corrosion distributions (9.048% DOP, $\alpha = 3.0$, $\beta = 4.0$)

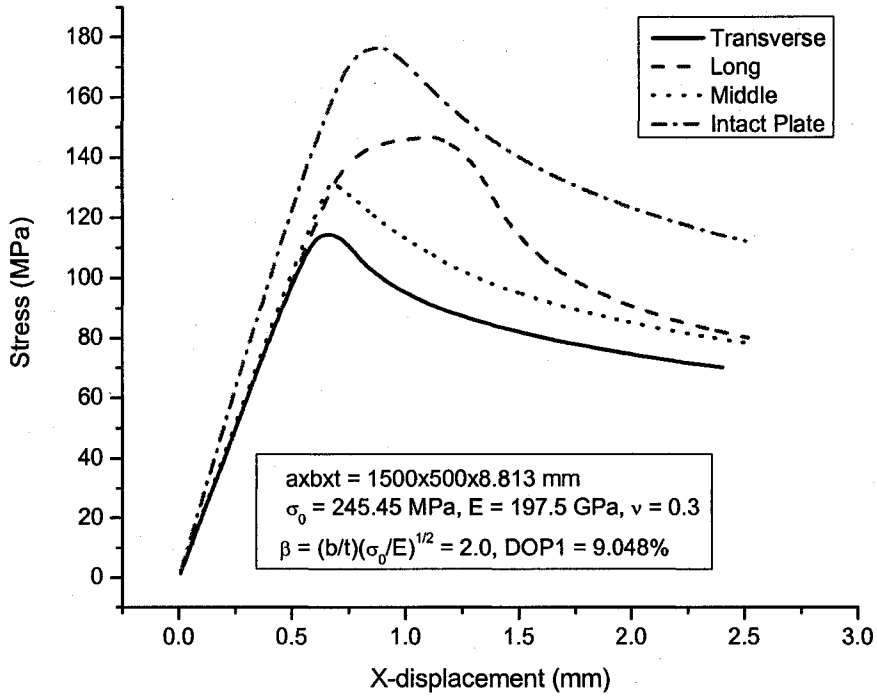

Figure 3.95 Effects of pit corrosion distributions (9.048% DOP, $\alpha = 3.0$, $\beta = 2.0$)

3.10.9. Summary

More comparisons have been made, trying to further confirm that the effect of length and breadth ratio, α, on ultimate compressive strength can be ignored. Two categories, $\beta = 4.0$ and 2.0, have been considered. Transverse, long, and middle distributions have been included, see Figures 3.96 – 3.98 and Figures 3.100 – 3.102. Also Figure 3.99 and Figure 3.103 conclude the comparison results.

(i) $\alpha = 1$ & 3, $\beta = 4.0$, DOP = 4.524%

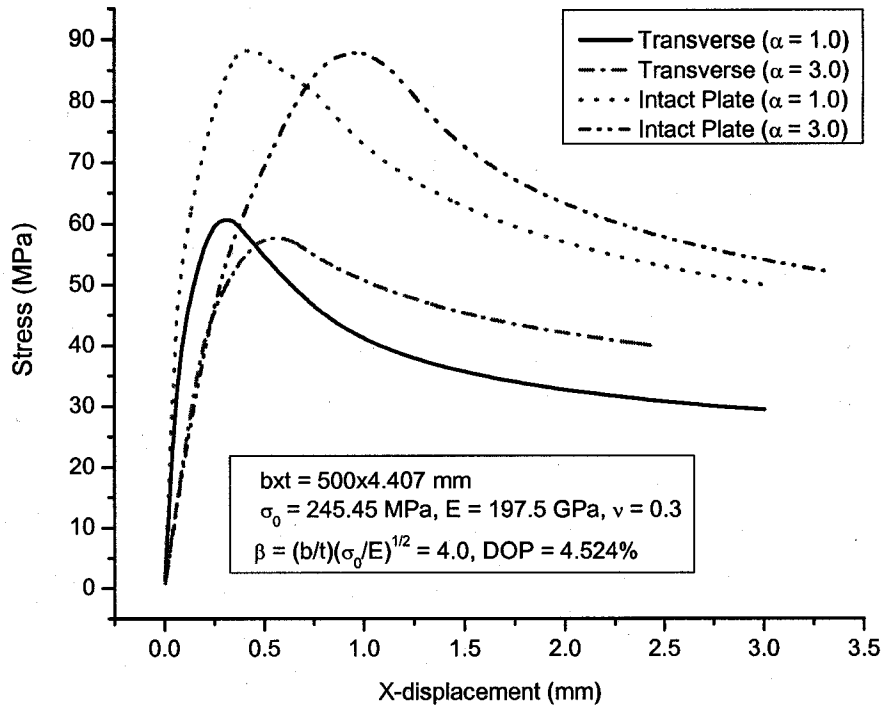

Figure 3.96 Comparison of transverse distribution with different α's (β = 4.0)

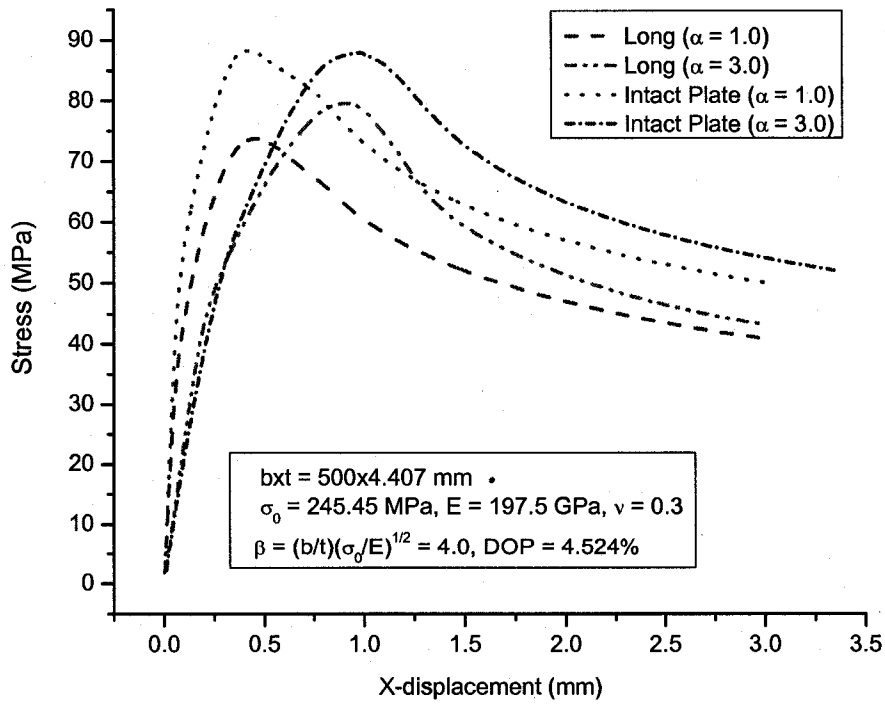

Figure 3.97 Comparison of longitudinal distribution with different α's (β = 4.0)

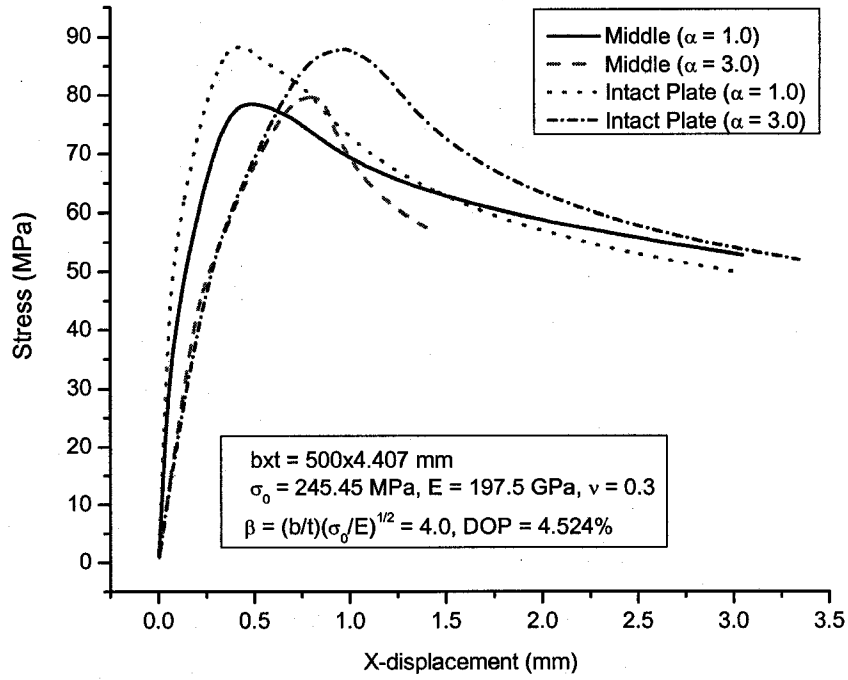

Figure 3.98 Comparison of middle distribution with different α's (β = 4.0)

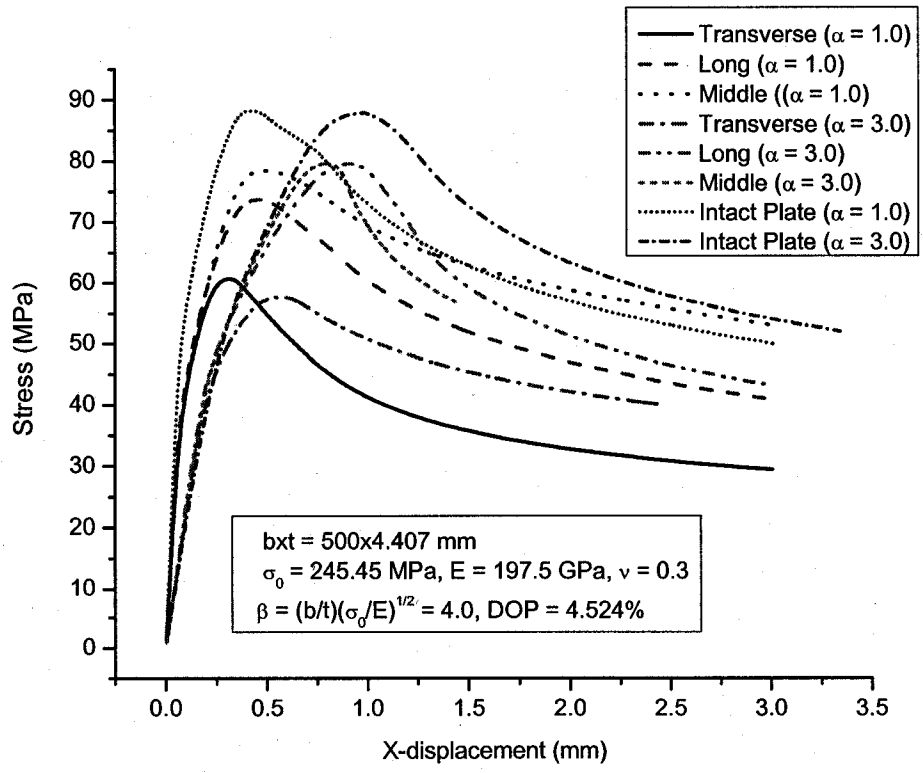

Figure 3.99 Comparison of different distributions with different α's (β = 4.0)

(ii) $\alpha = 1$ & 3, $\beta = 2.0$, DOP = 4.524%

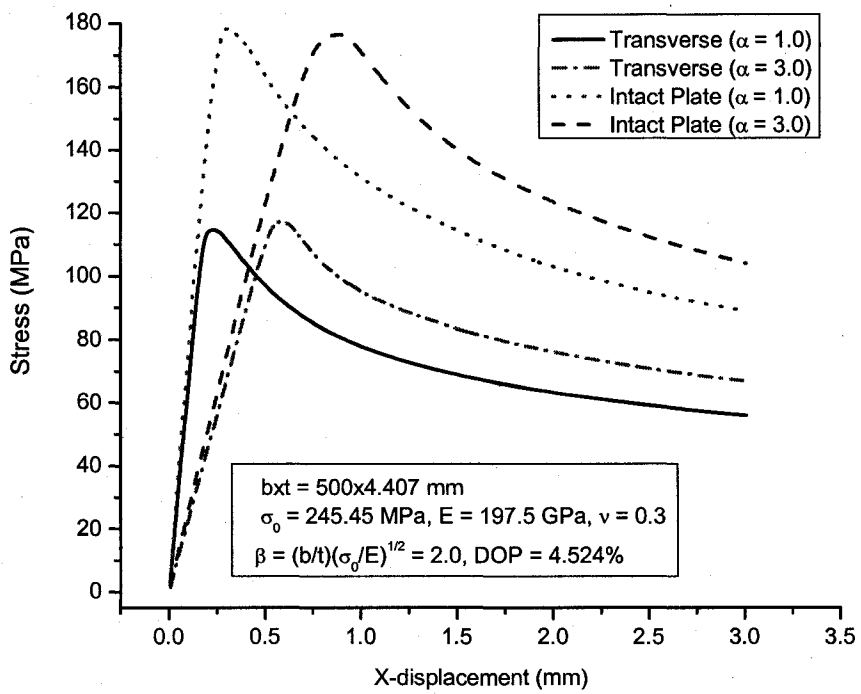

Figure 3.100 Comparison of transverse distribution with different α's ($\beta = 2.0$)

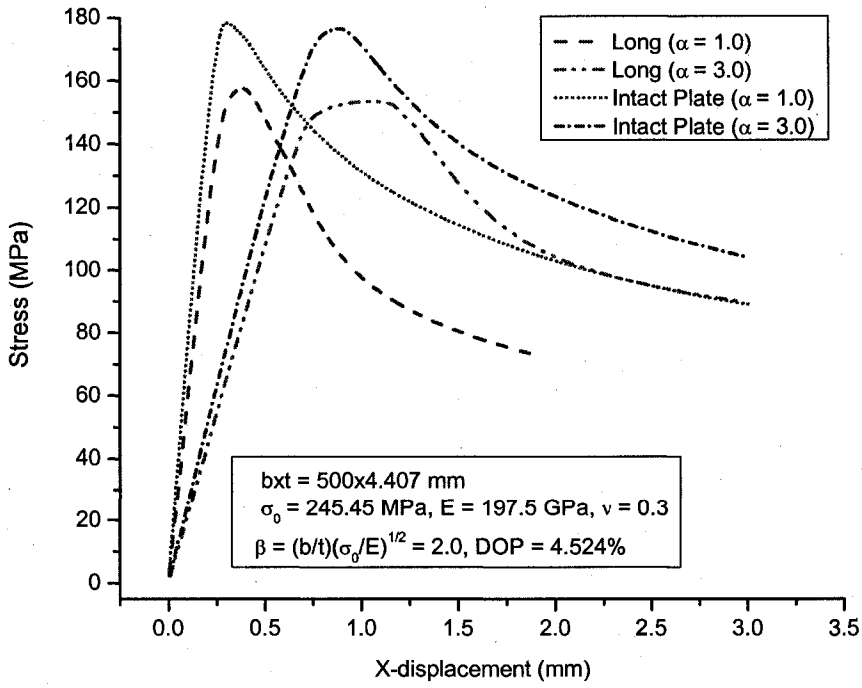

Figure 3.101 Comparison of longitudinal distribution with different α's ($\beta = 2.0$)

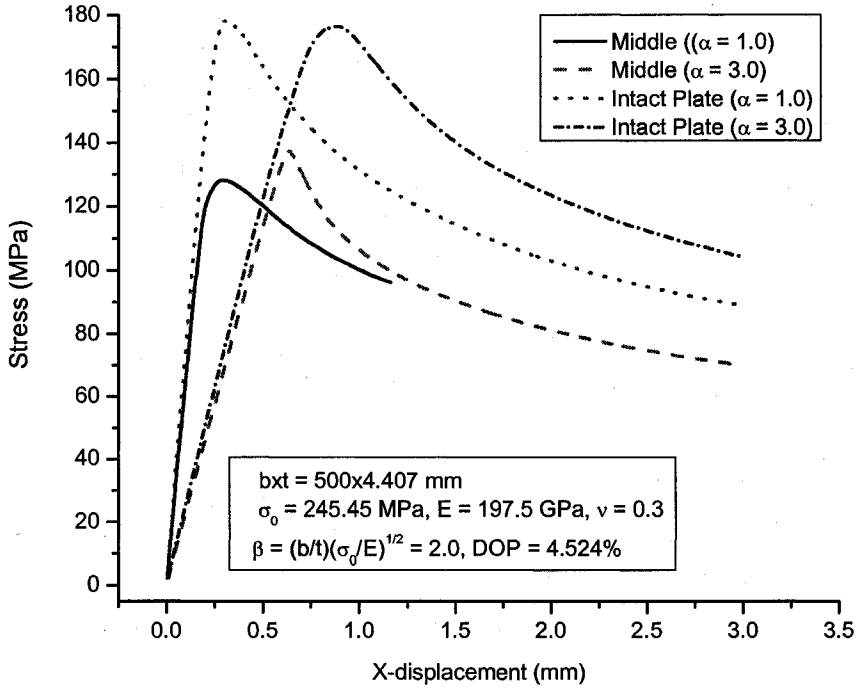

Figure 3.102 Comparison of middle distribution with different α's (β = 2.0)

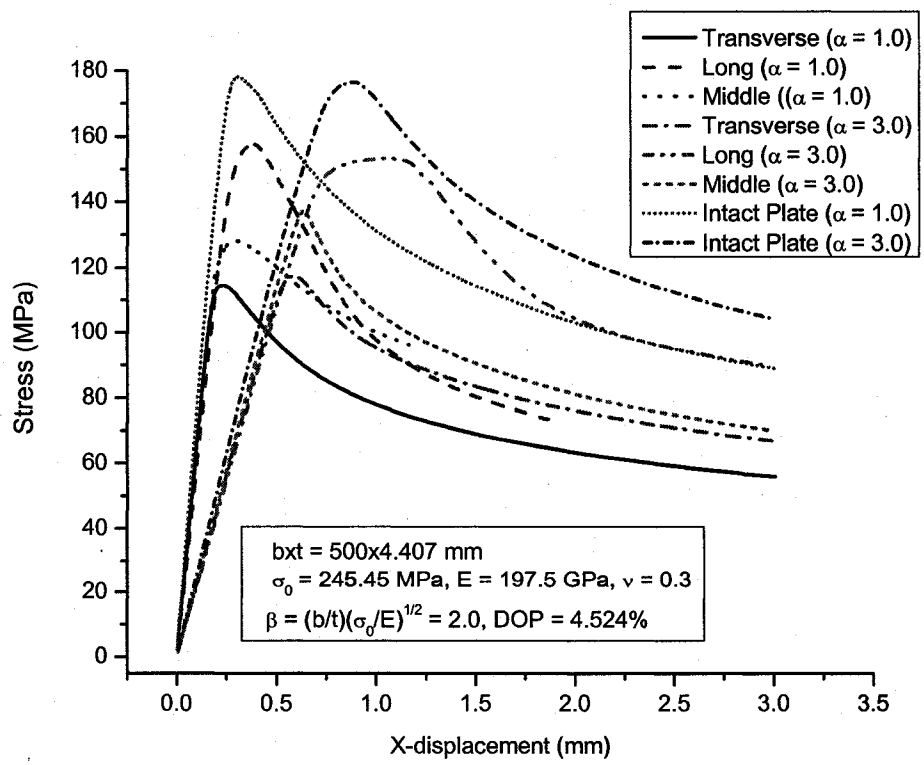

Figure 3.103 Comparison of different distributions with different α's (β = 2.0)

Conclusions:

1. Different pit corrosion distributions have different effects on ultimate compressive strength of steel plates. In the study, it is categorized as transverse, long and middle. Depending on the distributions, for the same DOP (degree of pitting intensity) the influence of the pit distribution can be large.
2. For same DOP, transverse distribution has worst effects on the ultimate compressive strength. According to different slenderness ratio β, longitudinal and middle distributions have different influences. While β is large, the two distributions have very close effects. Longitudinal distribution has slight bigger effect. When β is small, the difference between the two distributions becomes distinct. Middle distribution turns much worse.
3. For the transverse distribution, the initial phase of corrosion has crucial influence on ultimate strength of steel plates. As the pit corrosion propagates along the unload side into middle, the effect of DOP becomes very minor. For the middle distribution, the trend is on the contrary.
4. Length and breadth ratio α has very minor effect on compressive ultimate strength of steel plates. Most circumstances it can be ignored.

3.11. PIT CORROSION DOP EFFECTS

As previously described, DOP (degree of pit corrosion intensity) may be an important parameter when assessing the ultimate compressive strength of steel plates with pit corrosion. Therefore, the effects of DOP are needed to be closely examined.

Figures 3.104 – 3.106 show the finite element models with different DOP's. While Figures 3.107 – 3.110 demonstrate the deformation shapes and von Mises equivalent stress distributions of the plates at and right after the ultimate limit state. Two DOP's, 4.52% and 55.42%, are taken as examples.

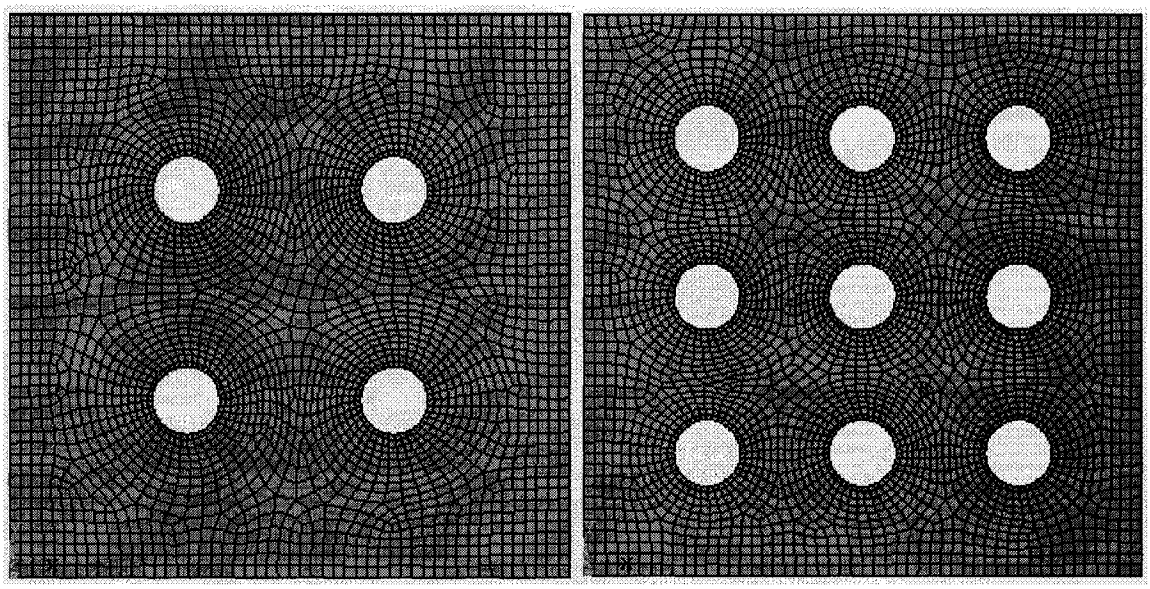

Figure 3.104 FE Models of DOP 4.52% and DOP 10.18%

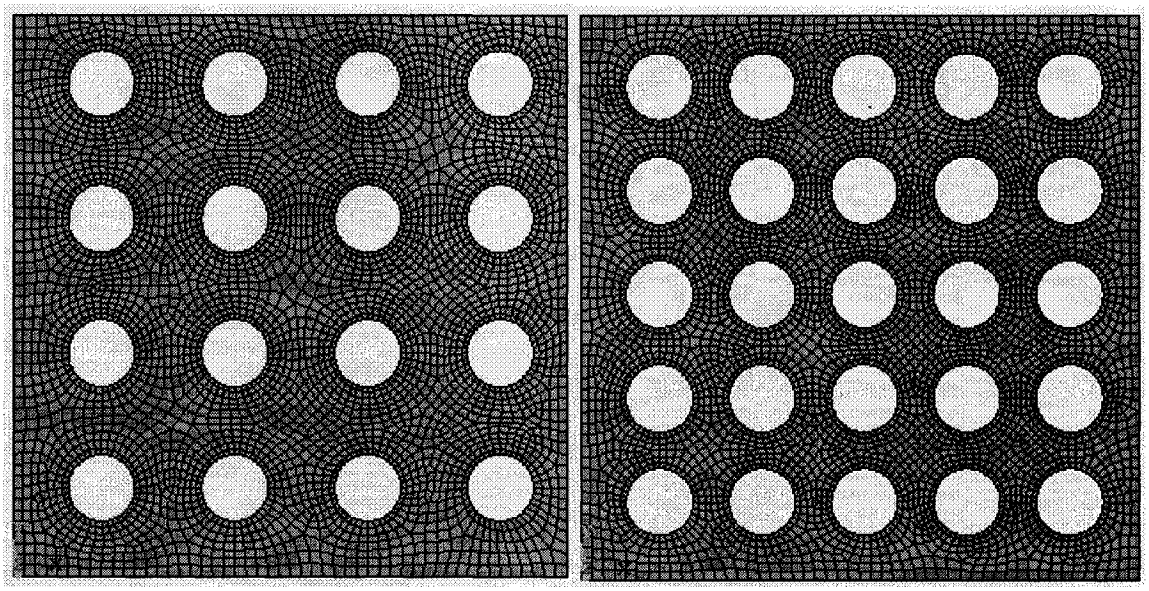

Figure 3.105 FE Models of DOP 18.10% and DOP 28.27%

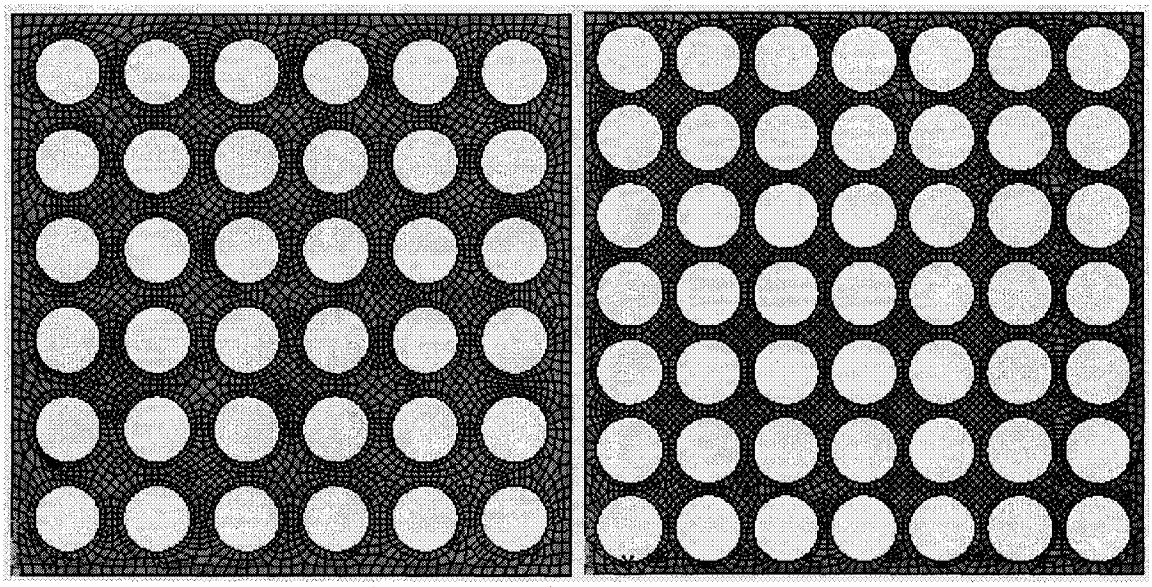

Figure 3.106 FE Models of DOP 40.72% and DOP 55.42%

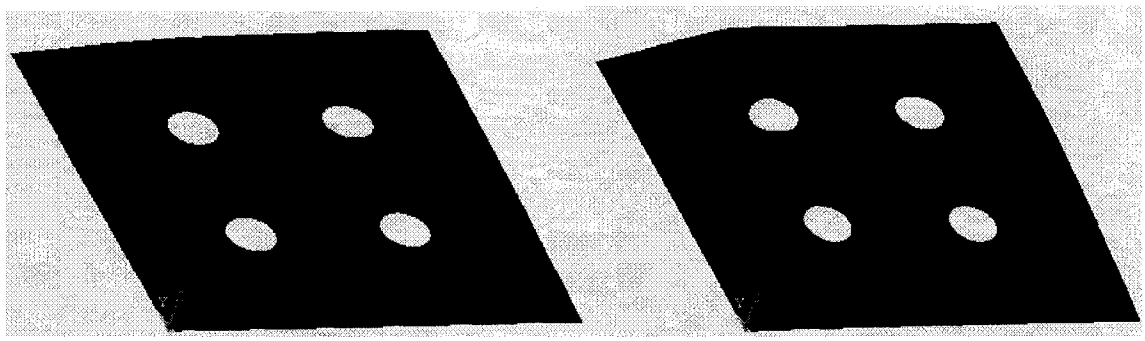

Figure 3.107 The deformation shapes of the plate with 4.52% DOP at and right after it reaches the ultimate limit state

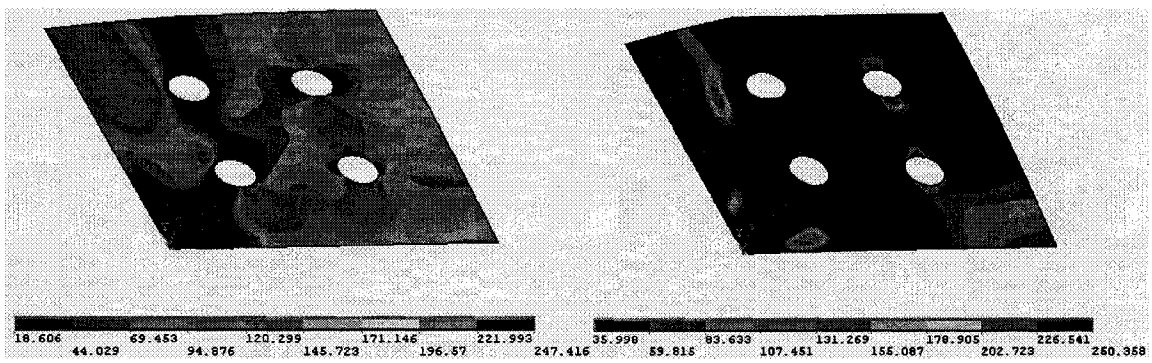

Figure 3.108 The von Mises equivalent stress distributions of the plate with 4.52% DOP at and right after it reaches the ultimate limit state

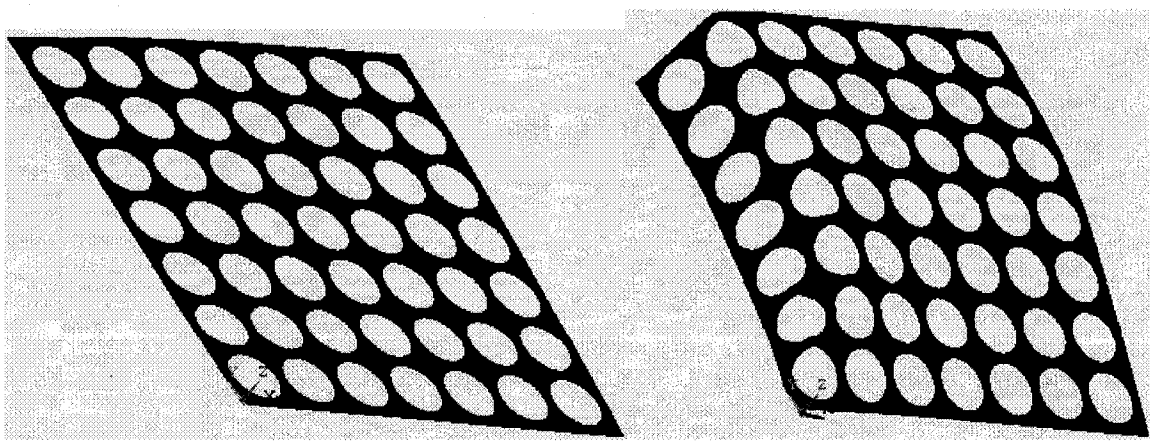

Figure 3.109 The deformation shapes of the plate with 55.42% DOP at and right after it reaches the ultimate limit state

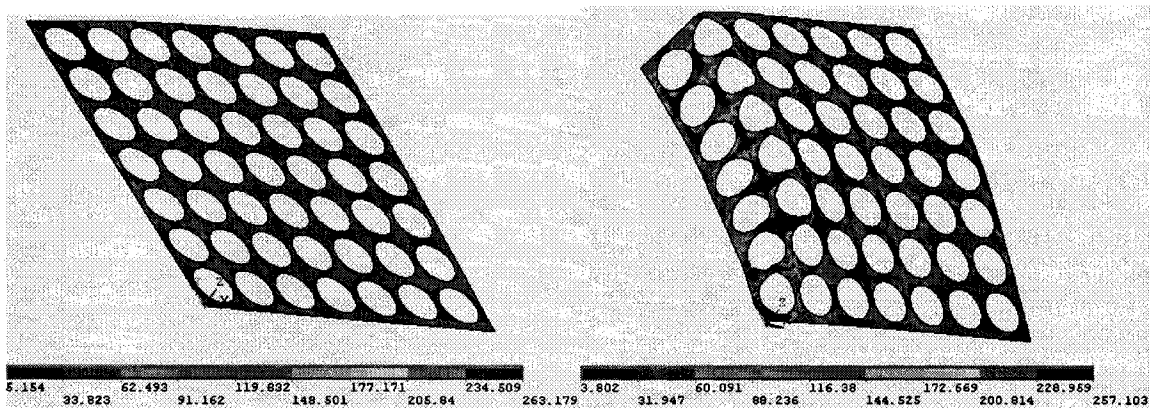

Figure 3.110 The von Mises equivalent stress distributions of the plate with 55.42% DOP at and right after it reaches the ultimate limit state

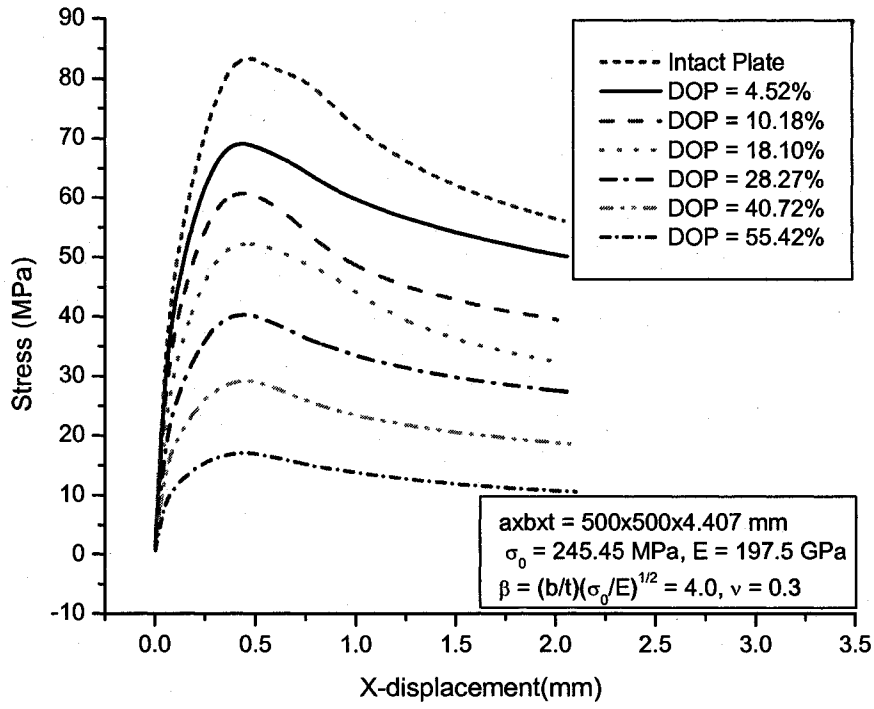

Figure 3.111 Effect of different degrees of pit corrosion intensity on ultimate strength

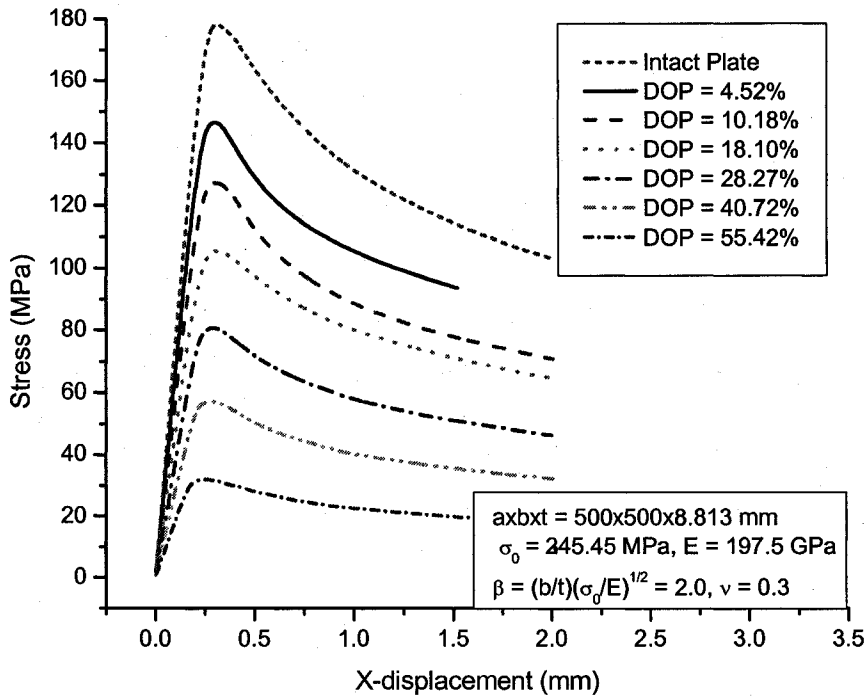

Figure 3.112 Effects of different degrees of pit corrosion intensity for different β

Figure 111 and Figure 112 show the effects of different degrees of pit corrosion intensity considering two different slenderness ratio β scenarios. It demonstrates that when DOP is about 20%, the ultimate compressive strength of the unstiffened plate will drop about 40%. While the DOP reaches 40%, the ultimate compressive strength of the unstiffened plate will drop about 65%.

An ultimate strength reduction factor R_p is introduced as the ratio of the ultimate strength of the plate with pit corrosion to that of the intact plate. Based on the FE results, it can be derived empirically by regression analysis. For the practical usage, the ultimate compressive strength is defined as a function of degree of pit corrosion intensity (DOP),

which is defined as the ratio percentage of the corroded surface area to the intact plate surface area. The resulting formula is given by

$$\phi_u = \frac{\sigma_u}{\sigma_Y} = \phi_{uo} R_p \tag{3.17}$$

where

$$\phi_{uo} = \frac{\sigma_{uo}}{\sigma_Y} = \begin{cases} -0.032\beta^4 + 0.02\beta^2 + 1.0 & for \quad \beta \le 1.5 \\ 1.274/\beta & for \quad 1.5 < \beta \le 3.0 \\ 1.248/\beta^2 + 0.283 & for \quad \beta > 3.0 \end{cases} \tag{3.17a}$$

$$R_p = 0.9796 - 2.9808\varphi + 5.4293\varphi^2 - 4.7375\varphi^3 \tag{3.17b}$$

$$\varphi = \frac{A_{pc}}{A_o}$$

A_{pc}: pit corroded surface area

A_o: intact plate surface area

Paik et al. (2003) proposed an empirical formula based on smallest cross-sectional area:

$$R_p = \frac{\sigma_u}{\sigma_{uo}} = \left(\frac{A_o - A_r}{A_o} \right)^{0.73} \tag{3.18}$$

Figure 3.113 compares the two methods. They are very close except the pit corrosion gets more critical. The equation proposed by this study is more conservative through comparison.

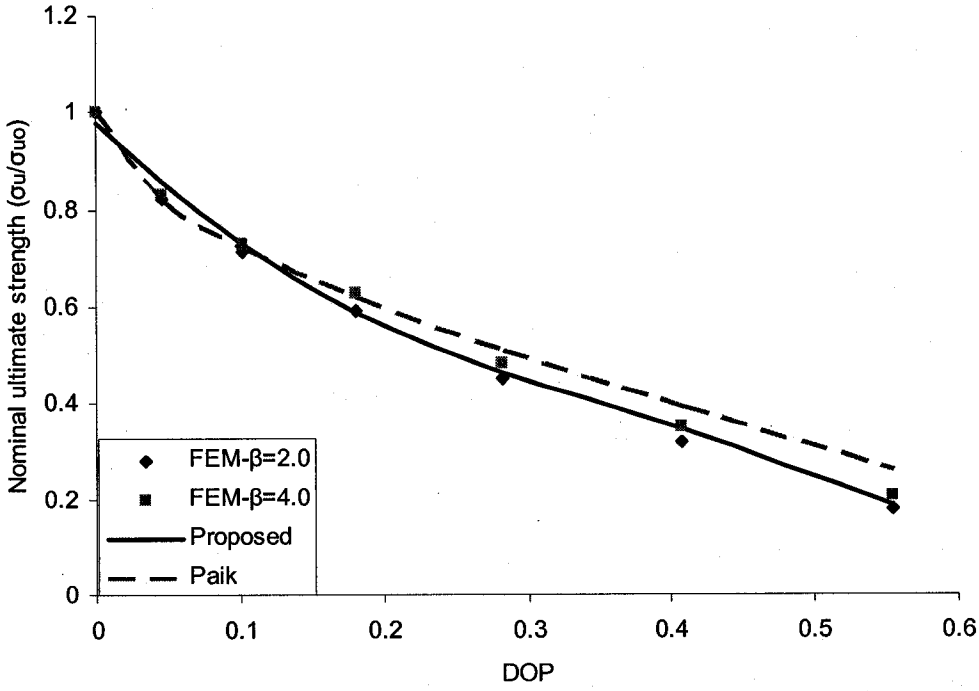

Figure 3.113 Comparison of proposed equation and equation by Paik

4. EFFECT OF FATIGUE CRACK ON ULTIMATE STRENGTH OF PLATES AND STIFFENED PANELS

4.1. FATIGUE CRACKING MECHANISM

The presence of a fatigue crack can lead to loss of effectiveness of a structural element when the crack reaches a critical size. The fatigue cracking damage has been a primary source of costly repair work of aging ships. It has been found in welded joints and local areas of stress concentrations, such as at the weld intersections of longitudinals, frames and girders.

Under a cyclic loading or even monotonic extreme loading, cracking may propagate and become larger with time, eventually cause catastrophic failure of the structure. Therefore, for reliability assessment of aging ship structures under extreme loads, it is necessary to consider the effect of cracks on the ultimate limit state analysis. It is required to develop time-dependent fatigue cracking model which can predict the cracking damage in location and size as the ship get older.

Figure 4.1 shows a schematic of fatigue cracking initiation and propagation for a steel structure with time. The progress is divided as three stages: initiation, propagation, and fracture (failure) stage (Paik, et al 2003).

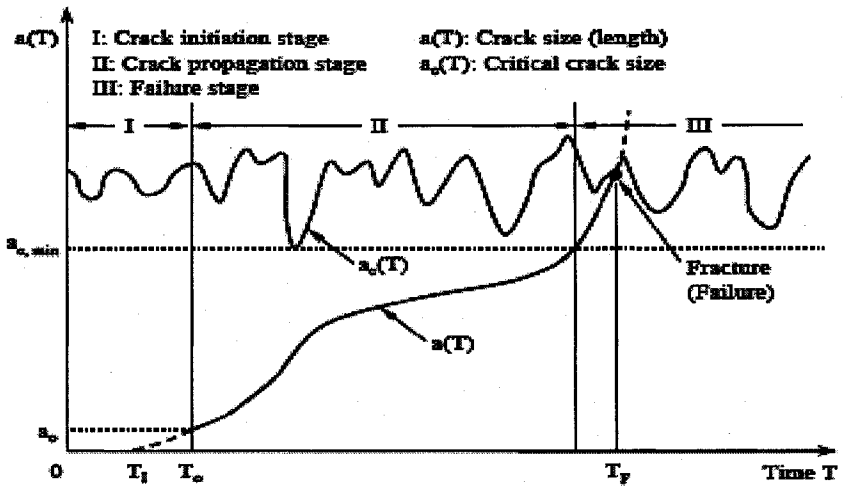

Figure 4.1 A schematic of the crack initiation and propagation for a steel structure

Usually it is assumed that there is no cracking damage until the time T_I. When any crack is detected in an existing structure at time T_o, it has normally a certain amount of crack size, a_o, called the initial crack size, which is detectable. The crack initiation at a critical structural detail can be theoretically predicted by using the S-N curve approach. The Palmgren-Miner cumulative damage rule is applied together with the relevant S-N curve. There are three steps: (1) define the histogram of cyclic stress ranges; (2) select the relevant S-N curve; (3) calculate the cumulative fatigue damage and judge the initiation of crack.

After the fatigue crack initiation, they propagate with time in ductile material, while they may become quite unstable in brittle material. There are many factors affect the crack propagation such as initial crack size, load sequence, stress intensity range, material property, geometry, and so on. The fracture mechanics approach is often used to analyze

the behavior of crack propagation. The most commonly used mechanistic model is the Paris-Erdogan formula, being expressing as follows:

$$\frac{dc}{dN} = C(\Delta K)^m \tag{4.1}$$

$$\Delta K = \Delta\sigma Y(c)\sqrt{\pi c} \tag{4.1a}$$

where

c: the crack size

N: the number of load cycles

ΔK : the stress intensity factor

C, m: material parameters to be determined based on tests

$\Delta\sigma$: the stress range

Y(c): the geometry function

If Y(c) = Y is constant, after substitution of Equation 4.1a into Equation 4.1 and integration of Equation 4.1 it is obtained

$$c(t) = \begin{cases} \left[c_o^{1-\frac{m}{2}} + \left(1-\frac{m}{2}\right) C\left(\Delta\sigma Y\sqrt{\pi}\right)^m \nu_o t \right]^{1/\left(1-\frac{m}{2}\right)} & m \neq 2 \\ c_o \exp\left(C\Delta\sigma^2 Y^2 \pi \nu_o t\right) & m = 2 \end{cases} \tag{4.2}$$

where

c_o: the initial crack size

ν_o : the mean upcrossing rate

t: the time

Roughly it is considered that in ships the expected number of wave load cycles occurs once in every 6-10 seconds, hence $N = v_o t \approx 365 \times 24 \times 60 \times 60/10 \times t$

For m $\neq$ 2, the mean value and variance of the crack propagation length is given by

$$\overline{c(t)} = \left[\overline{c_o}^{1-\frac{m}{2}} + \left(1 - \frac{m}{2}\right) \overline{C} \left(\overline{\Delta\sigma} Y \sqrt{\pi}\right)^m v_o t \right]^{1/\left(1-\frac{m}{2}\right)} \tag{4.3}$$

$$\begin{aligned} D_{c(t)} = & \left[\frac{\overline{c_o}^{\frac{m}{2}} \overline{c(t)}}{\overline{c_o}^{1-\frac{m}{2}} + \left(1 - \frac{m}{2}\right) \overline{C} \left(\overline{\Delta\sigma} Y \sqrt{\pi}\right)^m v_o t} \right]^2 D_{c_o} \\ & + \left[\frac{\left(\overline{\Delta\sigma} Y \sqrt{\pi}\right)^m v_o t \overline{c(t)}}{\overline{c_o}^{1-\frac{m}{2}} + \left(1 - \frac{m}{2}\right) \overline{C} \left(\overline{\Delta\sigma} Y \sqrt{\pi}\right)^m v_o t} \right]^2 D_C \\ & + \left[\frac{\overline{C} \left(\overline{\Delta\sigma} Y \sqrt{\pi}\right)^m}{\overline{c_o}^{1-\frac{m}{2}} + \left(1 - \frac{m}{2}\right) \overline{C} \left(\overline{\Delta\sigma} Y \sqrt{\pi}\right)^m v_o t} \right]^2 D_{\Delta\sigma} \end{aligned} \tag{4.4}$$

Figure 4.2 and Figure 4.3 show a sample application of Equation 4.3 and Equation 4.4. The probabilistic properties of the sample parameters are given in Table 4.1 (Sun and Bai 2003). The crack propagation is depicted in detail. The effect of stress ranges is also emphasized by specifying two stress ranges individually.

Parameter	Definition	Distribution Function	Mean	COV
c_o	Initial crack size	Normal	1.0 mm	0.2
C	Material parameter	Log-Normal	4.349×10^{-12}	0.2
m	Material parameter	Fixed	3.07	-
Y	Geometry function	Fixed	1	-
$\Delta\sigma$ 1	Stress range 1	Exponential	40 MPa	0.1
$\Delta\sigma$ 2	Stress range 2	Exponential	60 MPa	0.1

Table 4.1 The properties of random variables of a sample case

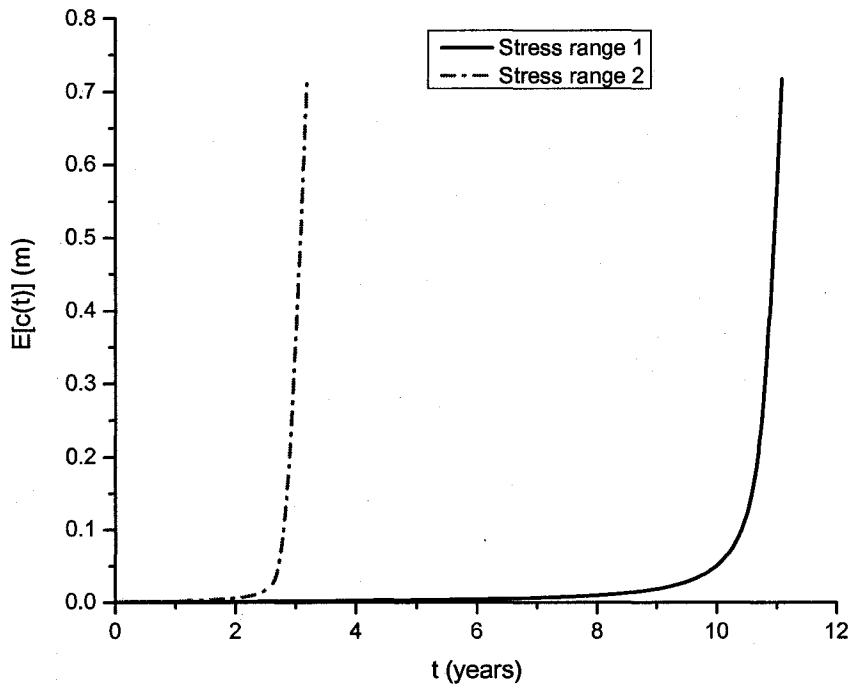

Figure 4.2 Mean value of crack size as a function of time

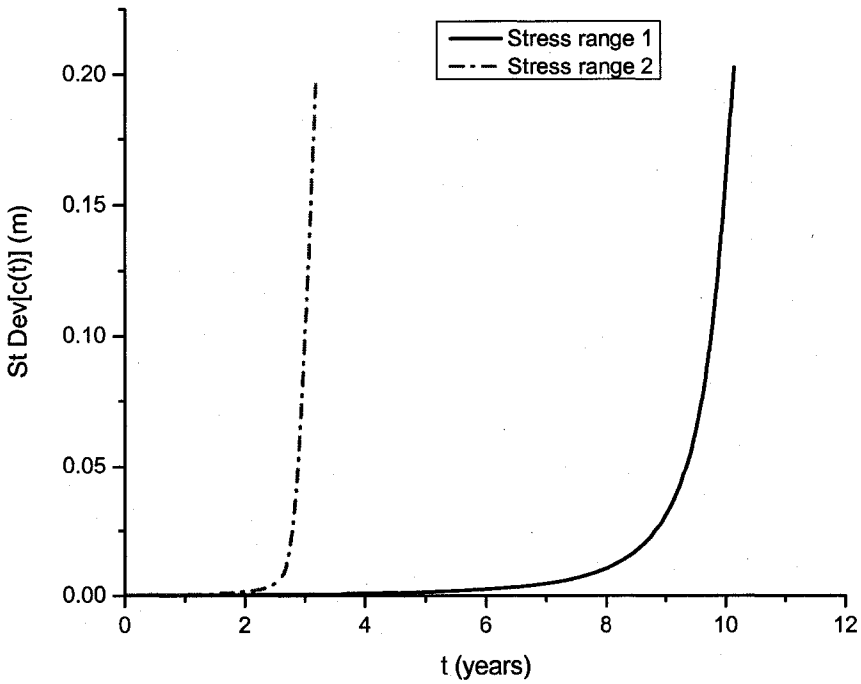

Figure 4.3 Standard deviation of crack size as a function of time

From Figure 4.2, it is concluded that the stress range parameter is very crucial. For different stress ranges, it could get quite different crack growth. Practical estimation of the stress range at the various details and joints is not trivial work. With fatigue loading sequence and amplitude known, Broek (1986) proposed a formulation of the dynamic stress range at the *i*th joint:

$$\Delta\sigma_i = 2 \times k_f \times \sigma_{Xi} \times SCF_i \tag{4.5}$$

$$\sigma_X = \frac{M_w z}{I} \tag{4.5a}$$

where

k_f: the knock-down factor accounting for the dynamic stress cycles

σ_X : cyclic peak stress amplitude

SCF: the stress concentration factor at the critical joint

M_w: wave-induced component of bending moment

I: time-dependent moment of inertia

z: distance from the time-dependent neutral axis to the point of stress calculation

There are two models for possible failure from fatigue after crack initiation in the structure elements. The first one is the loss of effectiveness of the element or the local structure because the crack reaches a size larger than its critical value. The second one is unstable crack growth that can occur when the stress intensity factor reaches the critical value for the specific material. The failure conditions can denoted as:

$$c(t) > c_{cr} \tag{4.6}$$

$$K(t) > K_{cr} \tag{4.7}$$

It needs to be mentioned that the critical crack size is not related to the critical value of the stress intensity factor which is a function of material, while the critical crack size depends also on the geometry of the element (Guedes Soares and Garbatov, 1996).

Due to the fact that the steels used in ships are very ductile and thus the critical crack size is very long, the first model of failure will be the governing one. To calculate the time of crack propagation, let $c(t) = c_{cr}$ in Equation 4.2, for m $\neq$ 2, one obtains

$$T_p = \frac{c_{cr}^{1-\frac{m}{2}} - c_o^{1-\frac{m}{2}}}{\left(1-\frac{m}{2}\right) C\left(\Delta\sigma Y\sqrt{\pi}\right)^m \nu_o} \tag{4.8}$$

For computing the crack propagation time T_p, the critical crack size c_{cr} should be determined first. When the ultimate strength of the unstiffened plate or the stiffened panel is lower than the maximum external load, the crack will propagate unstably, which means the crack length has already reached its critical size. Therefore using the ultimate strength versus crack length equations that will be derived in the following sections the critical crack size c_{cr} can be determined for a given external load.

The complete fatigue life T_f is equal to the sum of the time of crack propagation T_p and the time of crack initiation T_i. There exist some proposals to adopt the Weibull distribution to describe the time to crack initiation. But it is practical and sufficiently accurate to assume that

$$T_i = kT_p \tag{4.9}$$

where k can vary between 0.1 and 0.15 (Guedes Soares and Garbatov, 1996). This simplifying assumption implies that T_i and T_p are fully correlated.

4.2. ULTIMATE TENSILE STRENGTH OF UNSTIFFENED PLATES AND STIFFENED PANELS WITH FATIGUE CRACK

Since fatigue cracking may be one of the most important types of damage in aging structures, it is of crucial importance to estimate the residual strength of cracking damaged structures. In this section, the ultimate strength reduction characteristics of a steel plate with fatigue cracking damage under axial tension is investigated. Theoretical

models for predicting the ultimate strength of unstiffened plates and stiffened panels with fatigue cracking damage under axial tension are developed.

4.2.1. Mechanical tests and finite element analysis of cracked plates

A series of mechanical tests on steel plate elements with premised cracking and under monotonically increasing tensile loads were carried, with varying size and location of the cracks and also the plate thickness (Paik and Thayamballi, 2002). Figure 4.4 shows a schematic of the plate element tested. Figure 4.5 shows the loading setup and a typical pattern of the crack extension immediately before the plate is split into two pieces.

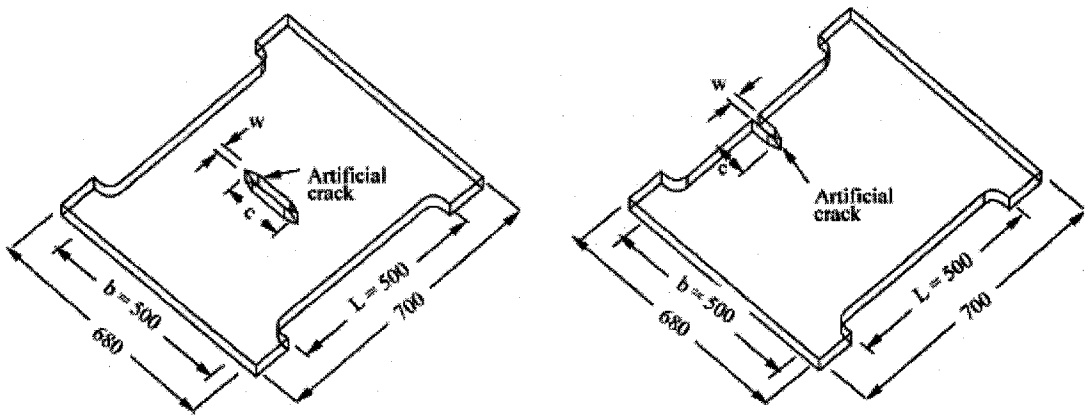

Figure 4.4 A schematic of a plate element with premised fatigue crack at the plate center or at the plate edge

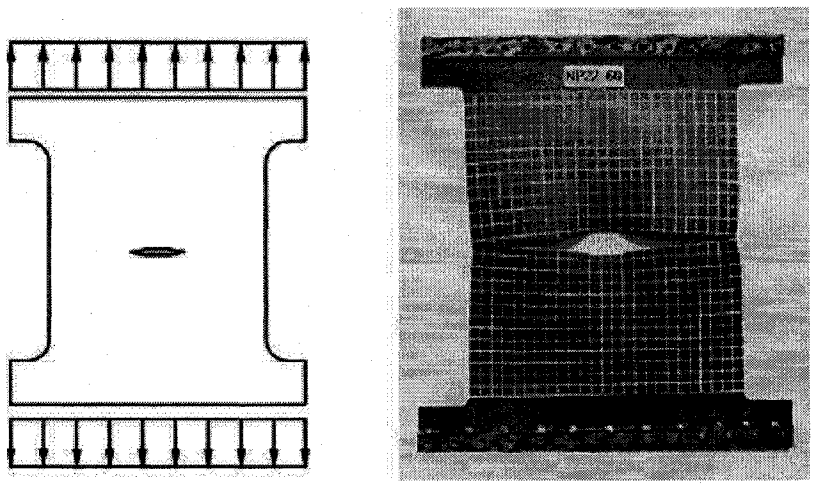

Figure 4.5 A typical pattern of the crack extension immediately before the plate is split into two pieces

Finite element analyses of the test structures are performed in this study. Figures 4.6 – 4.8 show the samples of finite element models for cracked plates. The cracks include edge crack, multiple edge cracks, and center crack.

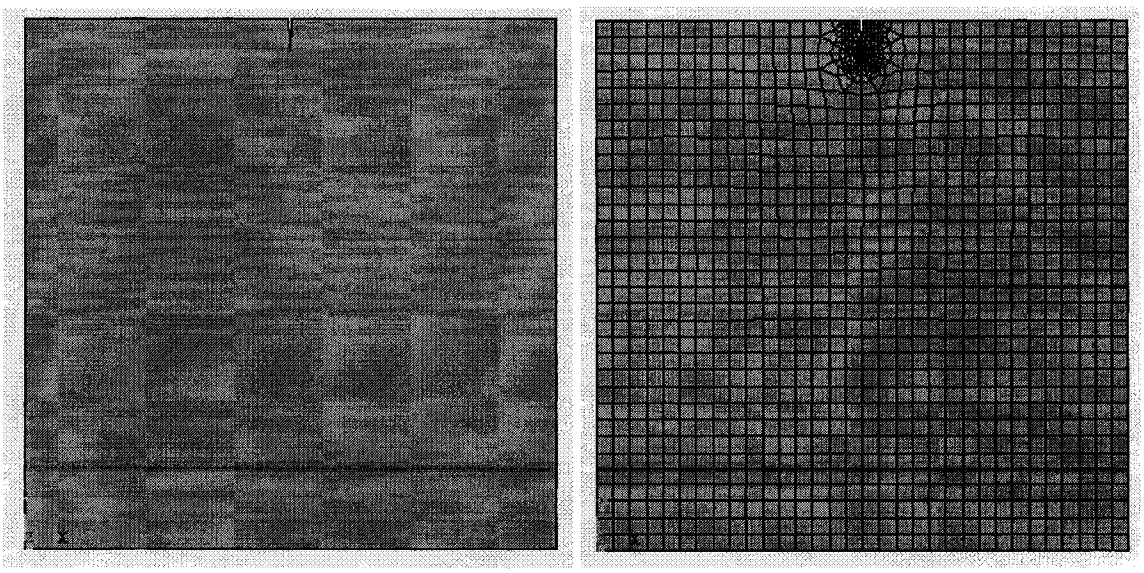

Figure 4.6 Finite element model of a plate with an edge crack

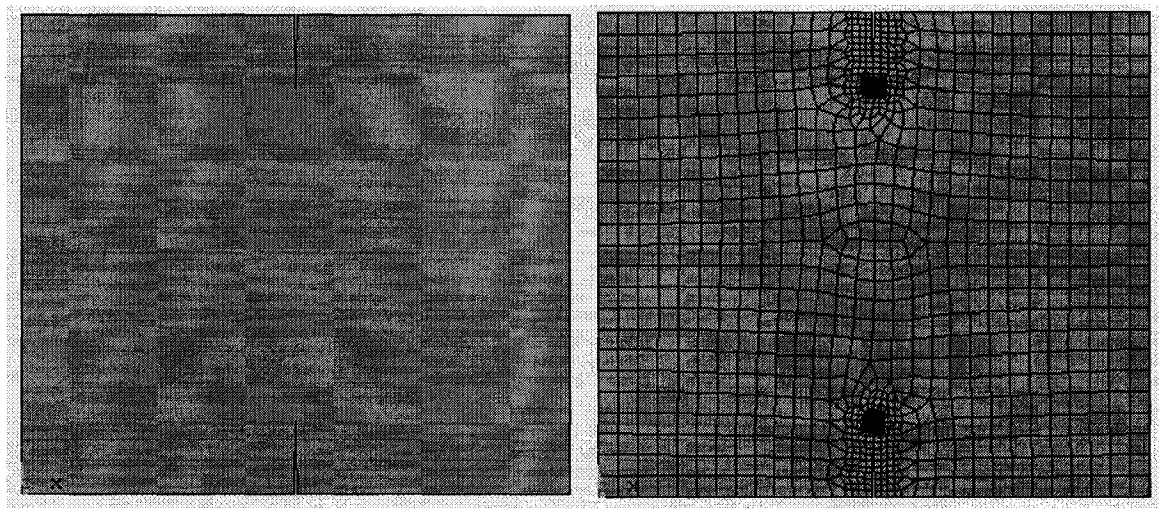

Figure 4.7 Finite element model of a plate with multiple edge cracks

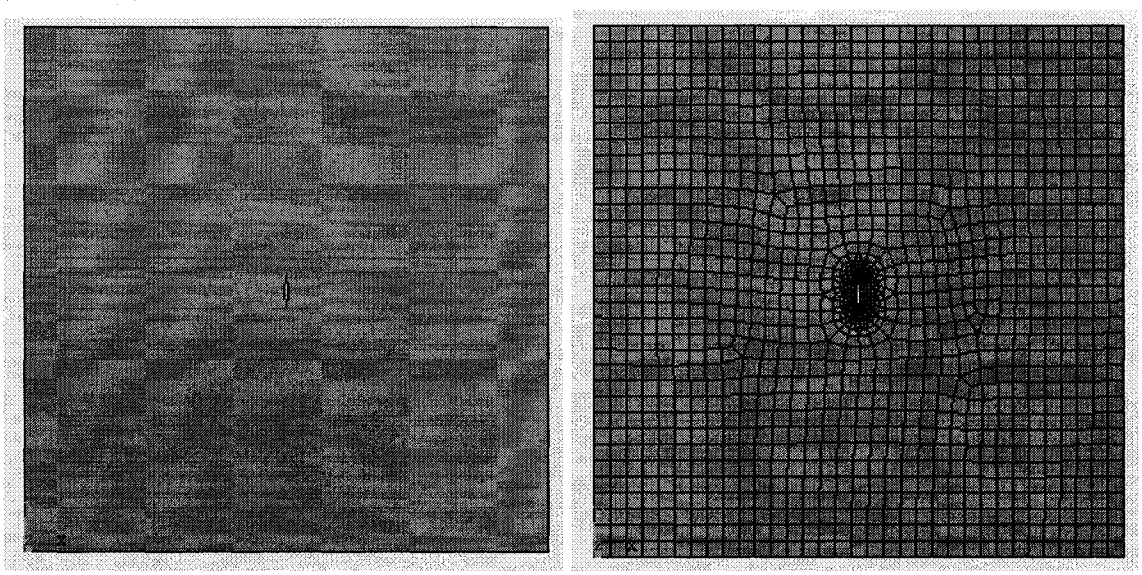

Figure 4.8 Finite element model of a plate with center crack

For the center crack, according to cracking shape, two different finite element models are built up, shown in Figure 4.9 and Figure 4.10. The effects of these two shapes are described in the aftermentioned section.

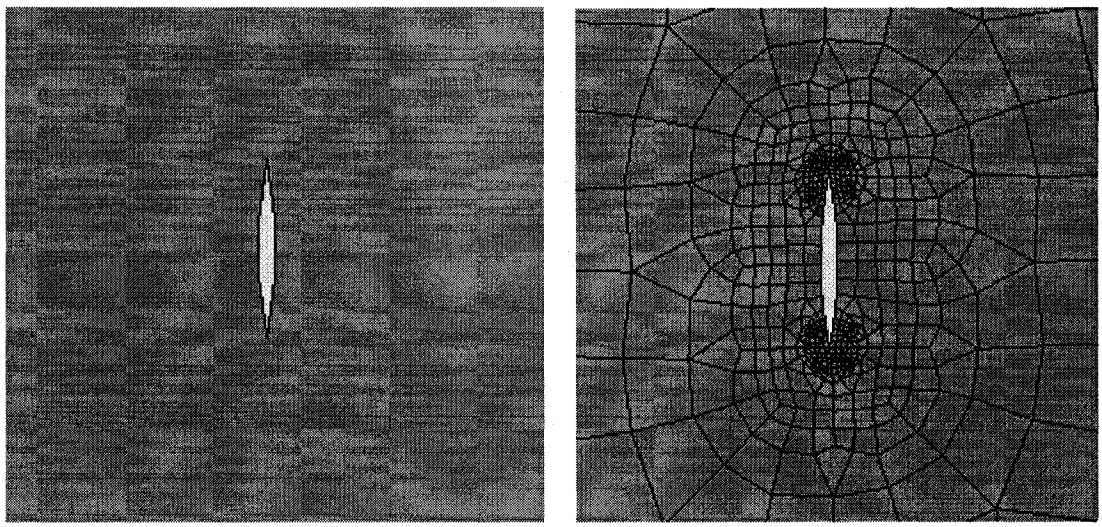

Figure 4.9 Detailed center crack shape I and its finite element model (FEM I)

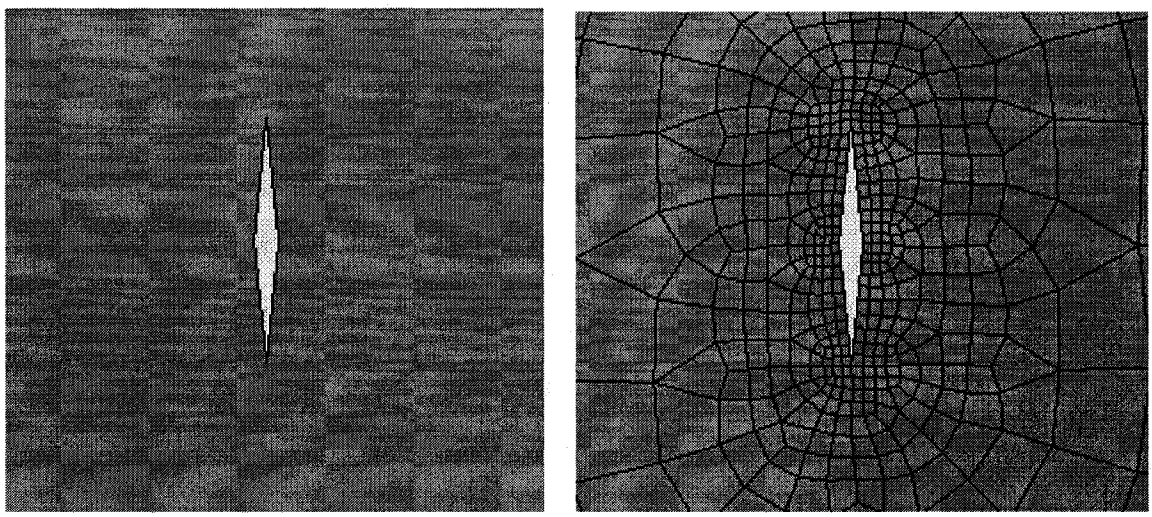

Figure 4.10 Detailed center crack shape II and its finite element model (FEM II)

The finite element analysis results have been compared with the experiment results. Table 4.2 – 4.5 show the conclusions. From these comparisons, we can see that the results by finite element methods are reliable with errors under 4% compared to the test

results. Therefore, the nonlinear finite element method is useful and can be used to analyze the ultimate strength behavior of a steel plate with fatigue cracking damage under axial tension.

Specimen number	Yield stress σ_Y (MPa)	Young's modulus E (GPa)	t (mm)	c (mm)	w (mm)	L (mm)	c/B	Result (σ_u/σ_Y)		Relative error (%)
								Experiment	FEM	
NP16-E	328.8	207.4	1.6	30	3.15	500	0.06	0.9712	0.96	1.15
NP20-E	249.7	202.2	2	30	3.15	500	0.06	1.0012	0.9656	3.56
NP22-E	268.2	206.4	2.2	30	3.15	500	0.06	0.9858	0.9646	2.15

Table 4.2 Comparison I of FEM with test results (edge crack)

Specimen number	Yield stress σ_Y (MPa)	Ultimate stress σ_T (MPa)	t (mm)	c (mm)	w (mm)	L (mm)	c/B	Result (σ_u/σ_T)		Relative error (%)
								Experiment	FEM	
NP16-E	328.8	396.6	1.6	30	3.15	500	0.06	0.8052	0.7959	1.15
NP20-E	249.7	345.4	2	30	3.15	500	0.06	0.7238	0.6981	3.56
NP22-E	268.2	346.5	2.2	30	3.15	500	0.06	0.7630	0.7466	2.15

Table 4.3 Comparison II of FEM with test results (edge crack)

Specimen number	Yield stress σY (MPa)	Young's modulus E (GPa)	t (mm)	c (mm)	w (mm)	c/B	Result (σu/σY)			Relative error I (%)	Relative error II (%)
							Expt.	FEM I	FEM II		
NP16-15	296.1	198.3	1.6	15	3.15	0.03	0.9861	0.989	0.9541	-0.3	3.24
NP16-30	296.1	198.3	1.6	30	3.15	0.06	0.954	0.9515	0.9172	0.26	3.86
NP16-60	296.1	198.3	1.6	60	3.15	0.12	0.912	0.893	0.8467	2.08	7.16

Table 4.4 Comparison I of FEM with test results (center crack)

Specimen number	Yield stress σY (MPa)	Ultimate stress σT (MPa)	t (mm)	c (mm)	w (mm)	c/B	Result (σu/σY)			Relative error I (%)	Relative error II (%)
							Expt.	FEM I	FEM II		
NP16-15	296.1	326.1	1.6	15	3.15	0.03	0.8064	0.8087	0.7802	-0.3	3.24
NP16-30	296.1	326.1	1.6	30	3.15	0.06	0.7801	0.7781	0.7500	0.26	3.86
NP16-60	296.1	326.1	1.6	60	3.15	0.12	0.7458	0.7302	0.6924	2.08	7.16

Table 4.5 Comparison II of FEM with test results (center crack)

From Table 4.4 and Table 4.5, it can also be concluded that the center crack shape I, with errors under 3%, is more related to the test structure than the center crack shape II, with errors greater than 3% and smaller than 8%. Thus, the center crack shape I will be used for the finite element analysis of ultimate strength for steel plates with center cracking damage thereafter.

4.2.2. Simplified methods and finite element method

A simple and intuitive model to predict the ultimate strength of a center or edge-cracked plate under axial tensile loads in the x direction is to predict the tensile strength on the basis of the reduced cross-sectional area associated with the cracking damage (Paik and Thayamballi, 2002). The simplified methods are given by two equations:

Simplified equation 1:

$$\sigma_u = \frac{A_c}{A_0}\sigma_Y \tag{4.10}$$

Simplified equation 2:

$$\sigma_u = \frac{A_c}{A_0}\sigma_T \tag{4.11}$$

Where

σ_u : Ultimate strength of a cracked plate

σ_Y : Yield strength

σ_T : Ultimate tensile strength of an intact plate

A_c : Remaining cross-sectional area of a cracked plate

A_0 : Total cross-sectional area of an intact plate

From the experiments and finite element methods (FEM), the simplified equation 1 has been underestimating the ultimate strength, while the simplified equation 2 has been overestimating the ultimate strength. Therefore, a series of finite element analyses have

been preformed. Through the FEM results, an empirical formula for tensile ultimate strength of a plate with edge crack can be obtained:

$$\phi_{eu} = \frac{\sigma_u}{\sigma_Y} = 1.2925 - 1.8514\left(\frac{c}{b}\right) + 1.1291\left(\frac{c}{b}\right)^2 - 0.5308\left(\frac{c}{b}\right)^3 \quad (4.12)$$

Where

ϕ_{eu} : Nominal ultimate strength of the edge-cracked plate

σ_u : Ultimate strength of the cracked plate

σ_Y : Yield strength of the cracked plate

c: Crack length

b: Plate breadth

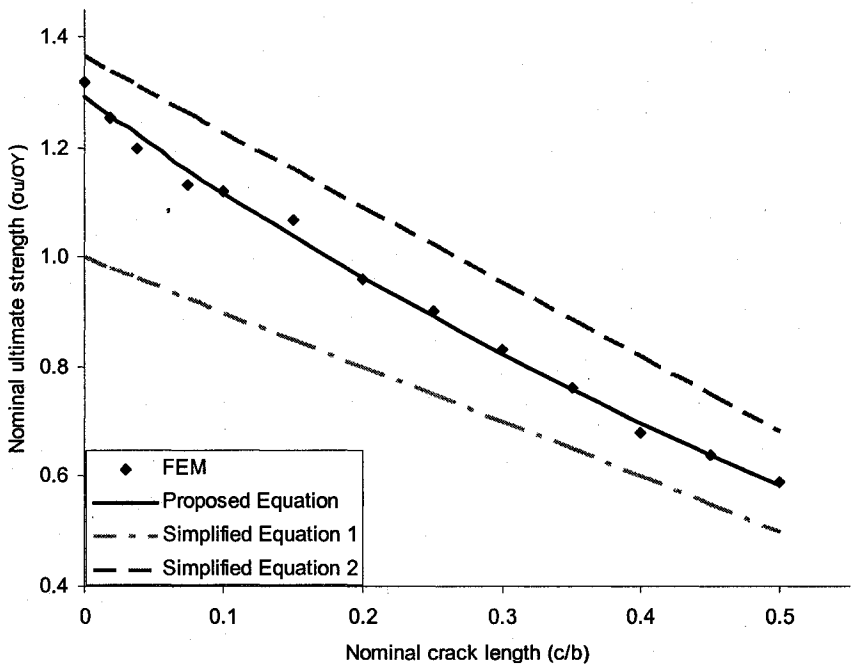

Figure 4.11 Tensile ultimate strength of edge-cracked plates obtained by FEM and simplified methods

Figure 4.11 shows the comparison between the proposed equation and the simplified equations. It is obvious that the simplified equations are providing the lower and upper bounds of the ultimate strength for edge-cracked plates under axial tensile loads, and the proposed equation can capture the ultimate strength behavior of the crack damaged structure more accurately.

Similarly, according to the FE results, an empirical formula for tensile ultimate strength of a plate with a center crack can be obtained:

$$\phi_{cu} = \frac{\sigma_u}{\sigma_Y} = 1.3367 - 2.3320\left(\frac{c}{b}\right) + 3.4013\left(\frac{c}{b}\right)^2 - 2.8880\left(\frac{c}{b}\right)^3 \qquad (4.13)$$

Where

ϕ_{cu} : Nominal ultimate strength of the center-cracked plate

σ_u : Ultimate strength of the cracked plate

σ_Y : Yield strength of the cracked plate

c: Crack length

b: Plate breadth

Figure 4.12 shows the comparison between the proposed equation and the simplified equations. Also the simplified equations are providing the lower and upper bounds of the ultimate strength for center-cracked plates under axial tensile loads. The results by the proposed equation are more close to upper bound comparing to the results of edge-cracked plates.

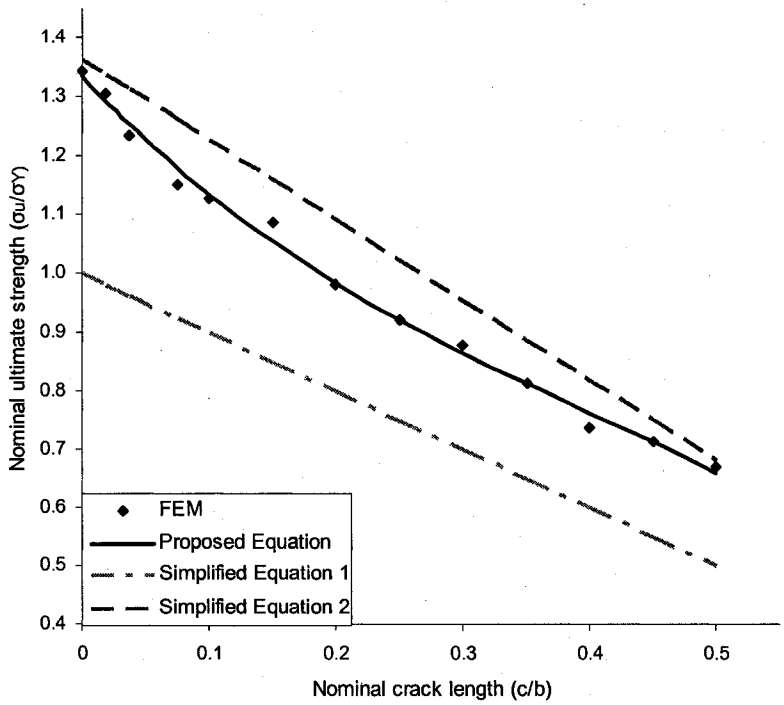

Figure 4.12 Tensile ultimate strength of center-cracked plates obtained by FEM and simplified methods

Figure 4.13 presents the comparison between the proposed equations and the simplified equations, especially demonstrating the difference between the plate with edge crack and the plate with center crack. From the comparison, we can see that the edge crack could cause more severe damage than the center crack under the circumstance of same crack length. The same comparison is also performed using nominal tensile ultimate strength (σ_u/σ_T) instead of (σ_u/σ_Y). It is shown as Figure 4.14.

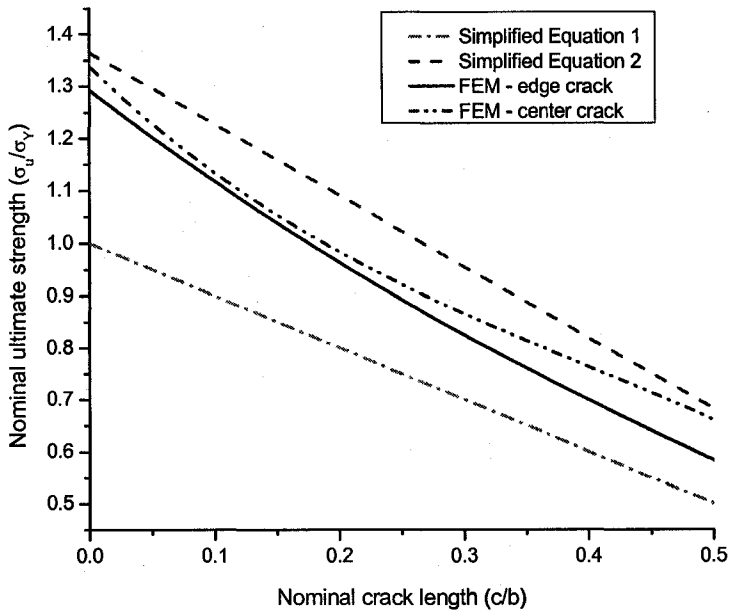

Figure 4.13 Nominal tensile ultimate strength (σ_u/σ_Y) of cracked plates obtained by FEM and simplified methods

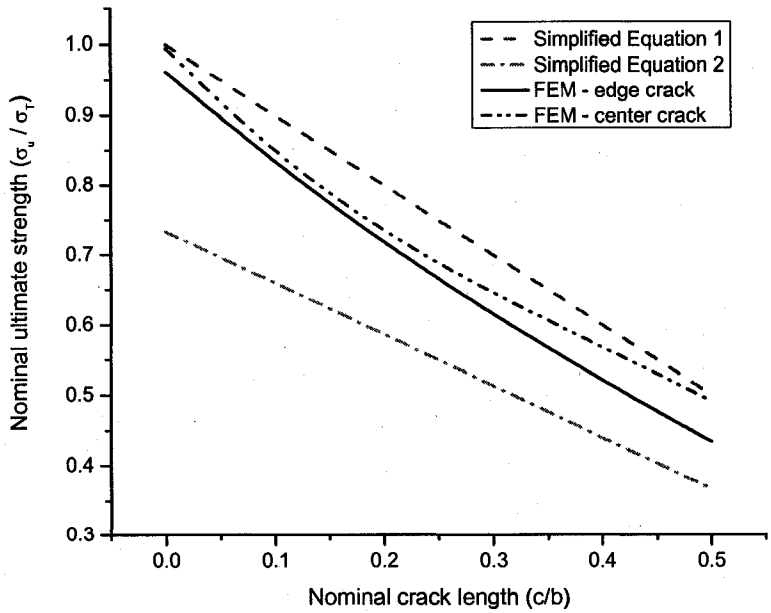

Figure 4.14 Nominal tensile ultimate strength (σ_u/σ_T) of cracked plates obtained by FEM and simplified methods

4.2.3. Ultimate tensile strength of stiffened panels with existing cracks

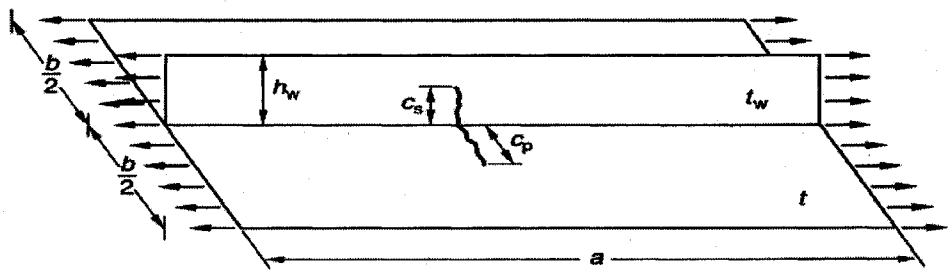

Figure 4.15 A stiffened steel panel with existing cracks

Figure 4.15 shows a stiffened panel with existing crack damage and under monotonically axial tensile loading. The web has an edge crack damage and the plating has a center crack damage. The ultimate strength for this scenario is predicted using a simplified model by Paik and Thayamballi (2003) noted in Equation (4.14) as follows:

$$\sigma_u = \frac{(b - c_p)t\sigma_{Yp} + (h_w - c_s)t_w\sigma_{Ys}}{bt + h_w t_w} \tag{4.14}$$

where

c_p : Crack length for the plating

c_s : Crack length for the stiffener

b: Plating breadth

t: Plating thickness

h_w: Stiffener web height

t_w: Stiffener web thickness

σ_u : Ultimate tensile strength of the stiffened panel

σ_{Yp} : Yield strength of plating

σ_{Ys} : Yield strength of stiffener

In this study, the Equation 4.14 used by Paik and Thayamballi is notified as simplified model 1. Also, in the above equation the ultimate tensile strengths of plate and stiffener could be used, instead of yield strengths, named as simplified model 2.

An empirical model is proposed in this study by using the Equation (4.12) and (4.13):

$$\sigma_u = \frac{\phi_{up}\sigma_{Yp}bt + \phi_{us}\sigma_{Ys}h_w t_w}{bt + h_w t_w} \tag{4.15}$$

where

ϕ_{up} : Nominal ultimate strength of plating, can be obtained by Equation (4.13)

ϕ_{us} : Nominal ultimate strength of stiffener, can be obtained by Equation (4.12)

The other parameters are defined as Equation 4.14.

In the following, a stiffened panel is taken as an example to show the difference between the simplified models and the proposed model. Table 4.6 gives the properties of the stiffened panel. For the cracked panel, the plate crack is treated as double of the stiffener crack.

Category	Breadth	Thickness	Young's Modulus	Yield Stress	Ultimate Tensile Stress
	mm	mm	GPa	MPa	MPa
Plate	200	4.4	197.5	245.45	334.96
Stiffener	70	8	198.3	296.1	362.1

Table 4.6 Properties of the stiffened panel

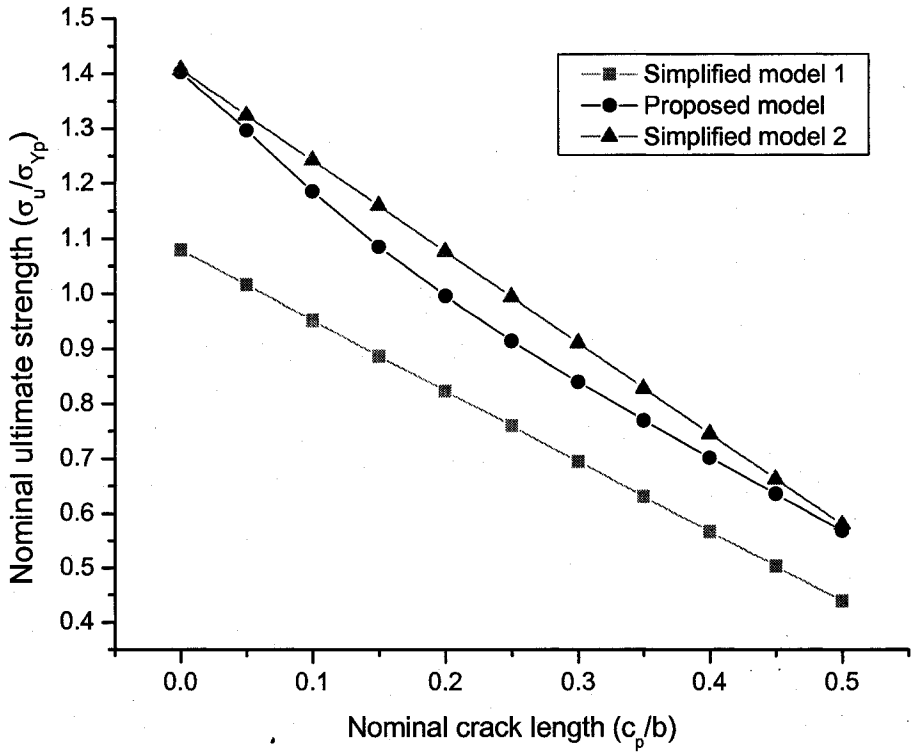

Figure 4.16 Nominal ultimate tensile strength of cracked stiffened panel obtained by proposed model and simplified models

Figure 4.16 shows the comparison of nominal ultimate tensile strengths of cracked stiffened panel obtained by the proposed model and simplified models, where c_p is the plating crack length. Like the unstiffened plate, the simplified model 1 underestimates the ultimate tensile strength, and the simplified model 2 overestimates the ultimate tensile strength. Both of them cannot well catch the nonlinear property of ultimate tensile strength of cracked panels.

4.3. ULTIMATE COMPRESSIVE STRENGTH OF UNSTIFFENED PLATES AND STIFFENED PANELS WITH FATIGUE CRACK

4.3.1. Ultimate tensile strength of stiffened panels with existing cracks

A series of mechanical tests on steel plate elements with premised cracking and under monotonically increasing compressive loads were carried, with varying size and location of the cracks (Paik et al., 2005). The box-type plated structure is used to keep the simply supported unloaded plate edges straight. Axial compressive loads are applied to the test structure in a quasi-static condition. Four plates that built up the structure have same conditions, i.e. same boundary conditions, same crack sizes and locations. The ultimate strength of a plate is taken as an average value of the four plate elements.

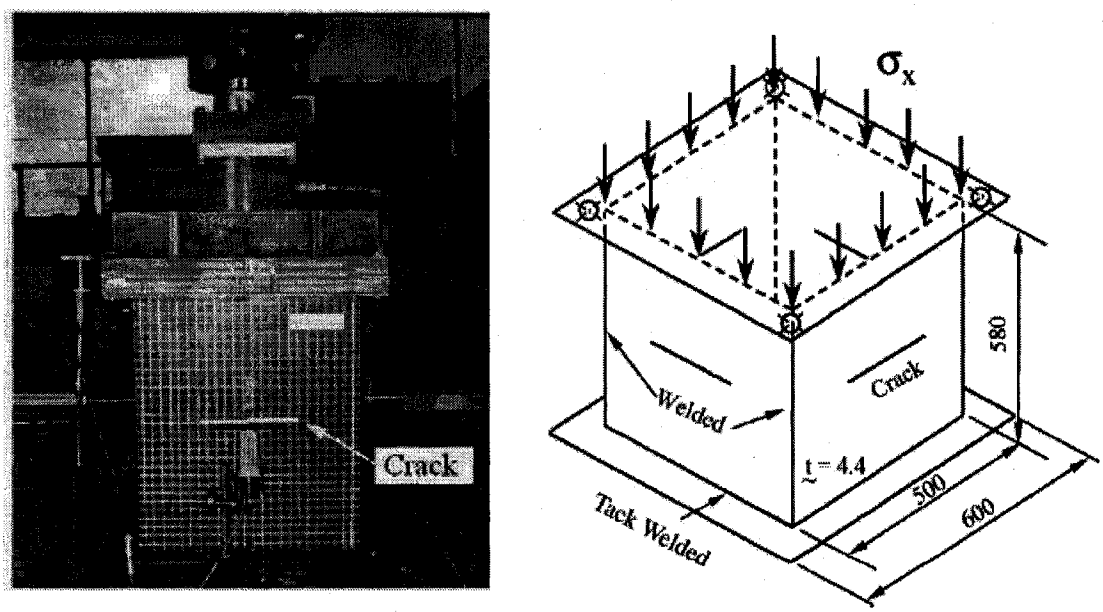

Figure 4.17 The test set-up and the schematic view of the test structure with crack damage under axial compressive loads

Figure 4.18 shows a schematic of the plate elements tested. Various crack locations have been assumed.

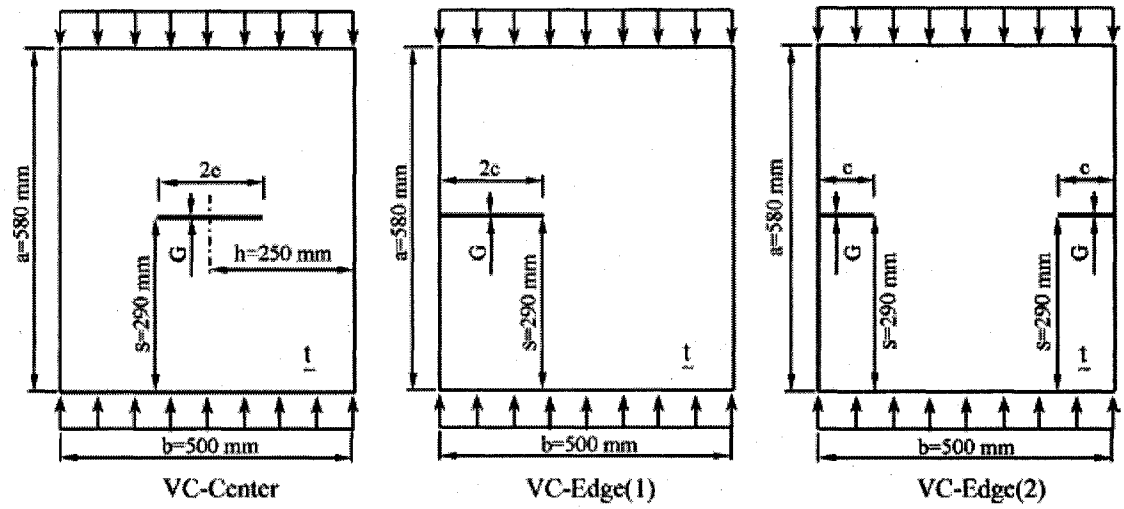

Figure 4.18 Various crack locations in the test structures

Table 4.7 shows the comparison between experiment and finite element method analyses.

Specimen number	Yield stress σY (MPa)	Young's modulus E (GPa)	t (mm)	c (mm)	b (mm)	a (mm)	c/b	Result (σu) (MPa)		Relative error (%)
								Experiment	FEM	
Intact Plate	245.45	197.5	4.4	0	500	580	0	105.3	102.23	2.92
Edge(1)-3.0-15	245.45	197.5	4.4	75	500	580	0.15	93.38	97.05	-3.93
Edge(1)-3.0-30	245.45	197.5	4.4	150	500	580	0.3	90.55	89.44	1.22
Edge(1)-3.0-50	245.45	197.5	4.4	250	500	580	0.5	84.4	78.96	6.45
Edge(2)-3.0-30	245.45	197.5	4.4	150	500	580	0.3	68.6	68.58	0.03
Edge(2)-3.0-50	245.45	197.5	4.4	250	500	580	0.5	53.6	51.83	3.5
Center-0.3-15	245.45	197.5	4.4	75	500	580	0.15	102.27	97.78	4.39
Center-0.3-30	245.45	197.5	4.4	150	500	580	0.3	102.89	96.57	6.14
Center-3.0-50	245.45	197.5	4.4	250	500	580	0.5	92.65	89.44	3.46

Table 4.7 Comparison of experiment results and FEM

From Table 4.7, it is concluded that the results by finite element methods are reliable with errors under 7% compared to the test results. Therefore, the nonlinear finite element method is useful and can be used to analyze the ultimate strength behavior of a steel plate with fatigue cracking damage under axial compressive loads.

4.3.2. Finite element analysis for ultimate compressive strength of plates with center crack

A series of FE simulations have been carried out. The ultimate compressive strengths of plates with different center crack sizes have been first examined. Figures 4.19-4.21 show some FE models of different crack sizes, where c stands for the crack length, b is the plate breadth.

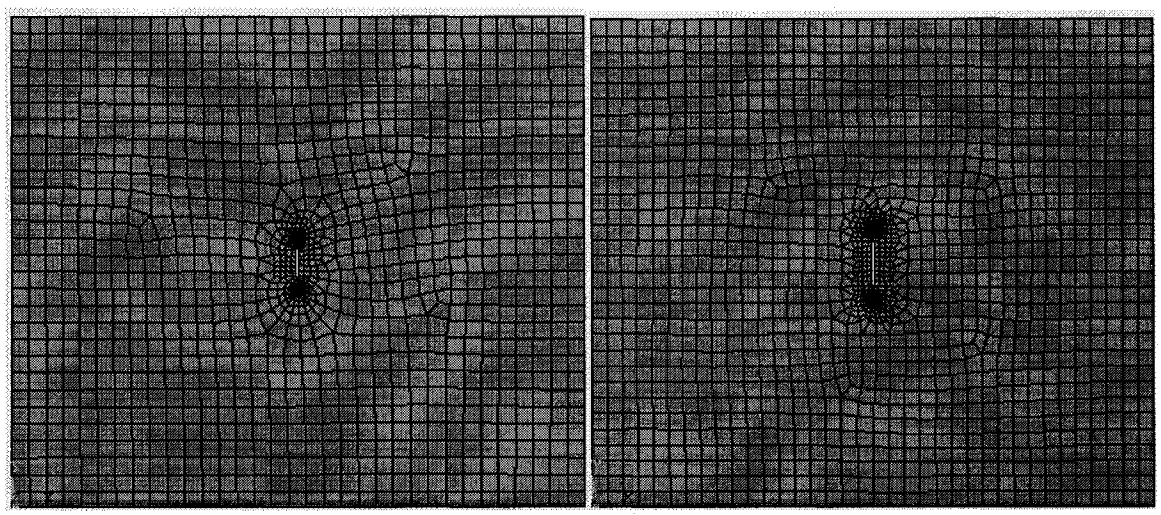

Figure 4.19 FE Models of c/b = 0.1 and c/b = 0.15

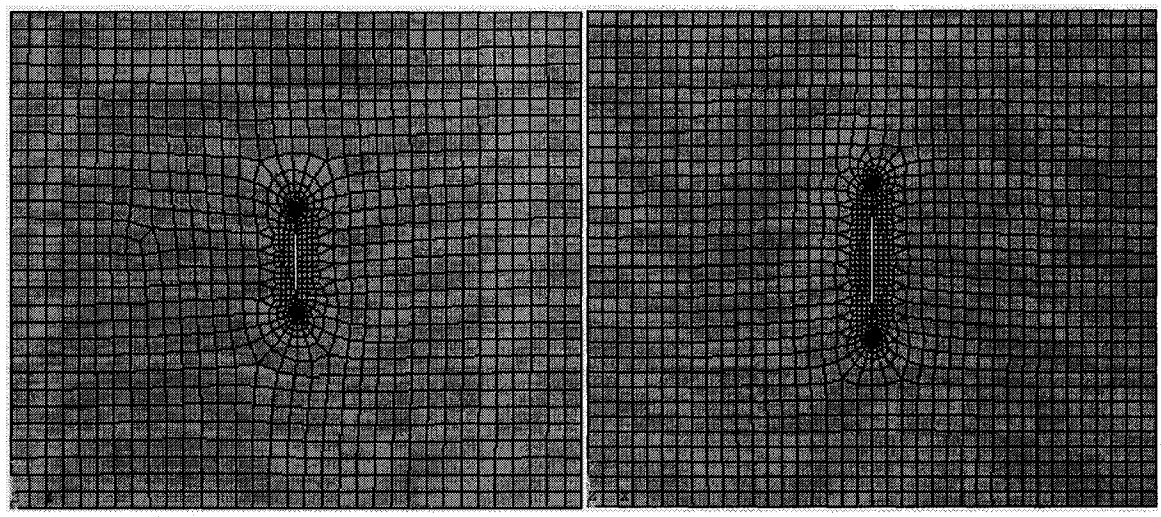

Figure 4.20 FE Models of c/b = 0.2 and c/b = 0.3

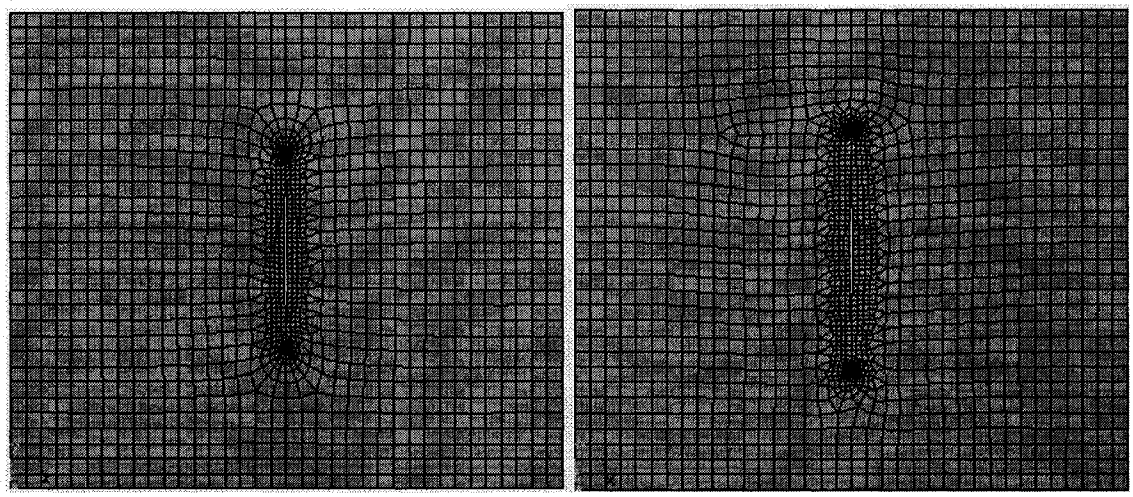

Figure 4.21 FE Models of c/b = 0.4 and c/b = 0.5

Taken as an example, Figure 4.22 and Figure 4.23 show the deformation shape, contour plot of u_z field (z-displacement) and von Mises equivalent stresses right after the plate, with crack size of c/b = 0.3, reaches the ultimate state.

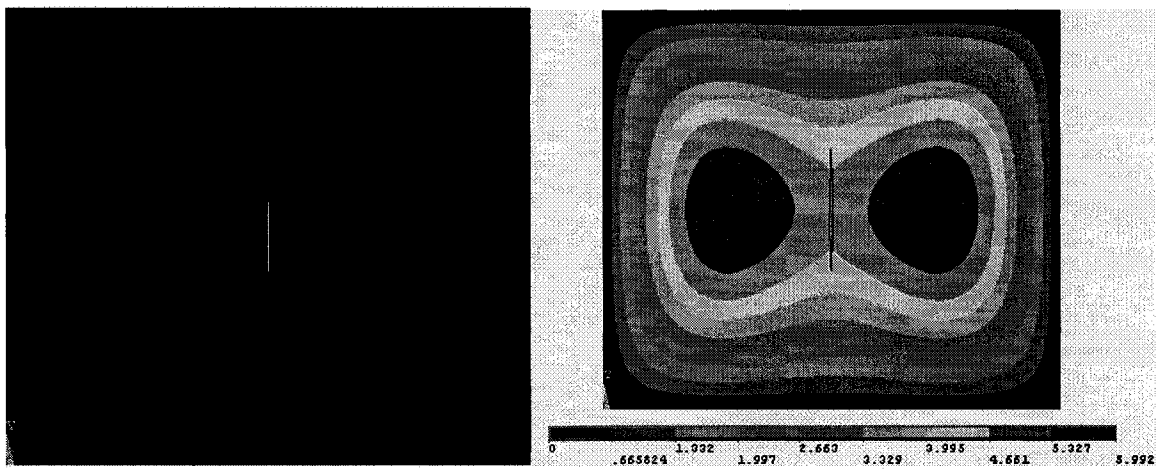

Figure 4.22 Deform shape and contour plot of u_z field (z-displacement) right after the plate reaches the ultimate state

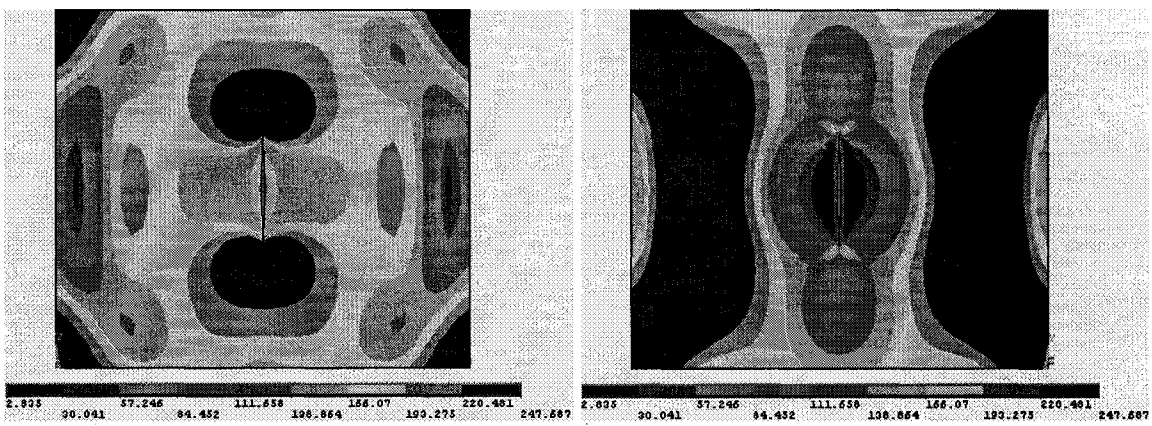

Figure 4.23 Contour plots of von Mises equivalent stresses on the top and bottom

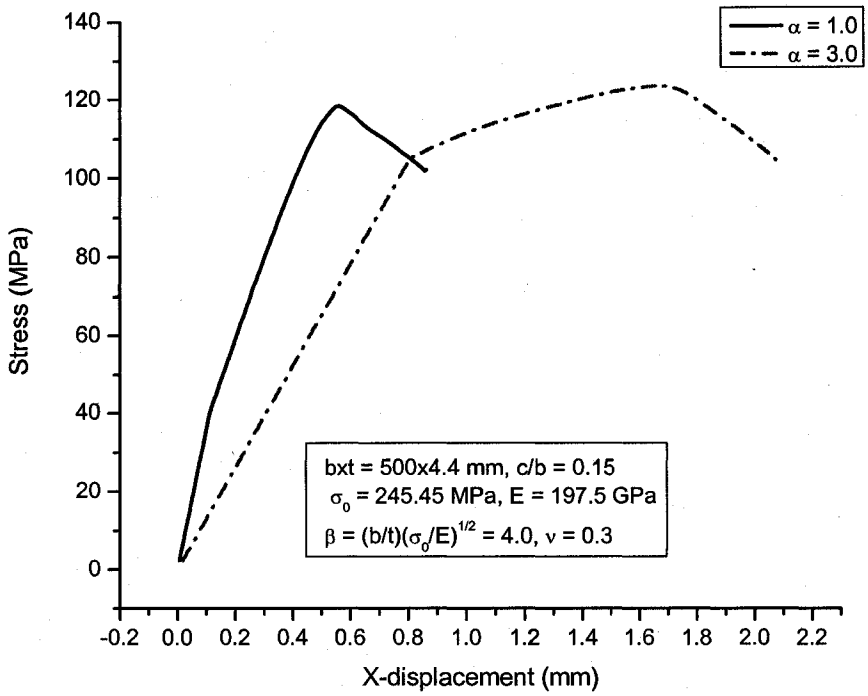

Figure 4.24 Effects of plate length and breadth ratio on ultimate compressive strength

Figure 4.24 shows the effects of plate length and breadth ratio, α = a/b, on ultimate compressive strength of the unstifffened cracked plate. One specific example, c/b = 0.15, is given. The plate length and breadth ratio, α, has some effects on the ultimate strength behavior of the cracked plated under compressive loads, but it does not have major effects on the value of the ultimate strength, which holds for intact plates as well, like described before. Therefore, in the following finite element analysis, the factor α is not considered. Only parameters of plate slenderness ratio, β, and crack length, c, are treated as the major factors that affect the ultimate compressive strength of the unstiffened cracked plates.

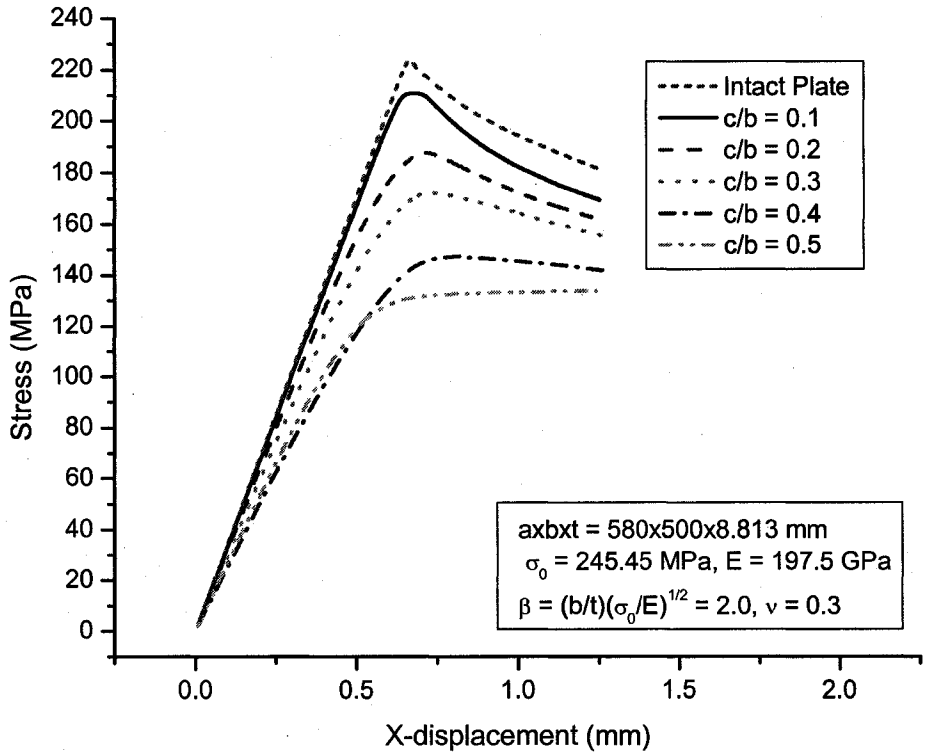

Figure 4.25 Effects of different crack sizes on ultimate compressive strength ($\beta = 2.0$)

Figure 4.25 shows the effects of different central crack sizes on ultimate compress strength of an unstiffened plate with the slenderness ratio $\beta = 2.0$. It demonstrates that when the central crack size is about 20% of the plate breadth, the ultimate compressive strength of the unstiffened plate will drop about 17%. While the central crack size reaches 40% of the plate breadth, the ultimate compressive strength of the unstiffened plate will drop about 35%.

Figure 4.26 shows the effects of different central crack sizes on ultimate compress strength of an unstiffened plate with the slenderness ratio β = 1.0. The similar trend of center edge damage effects has been followed.

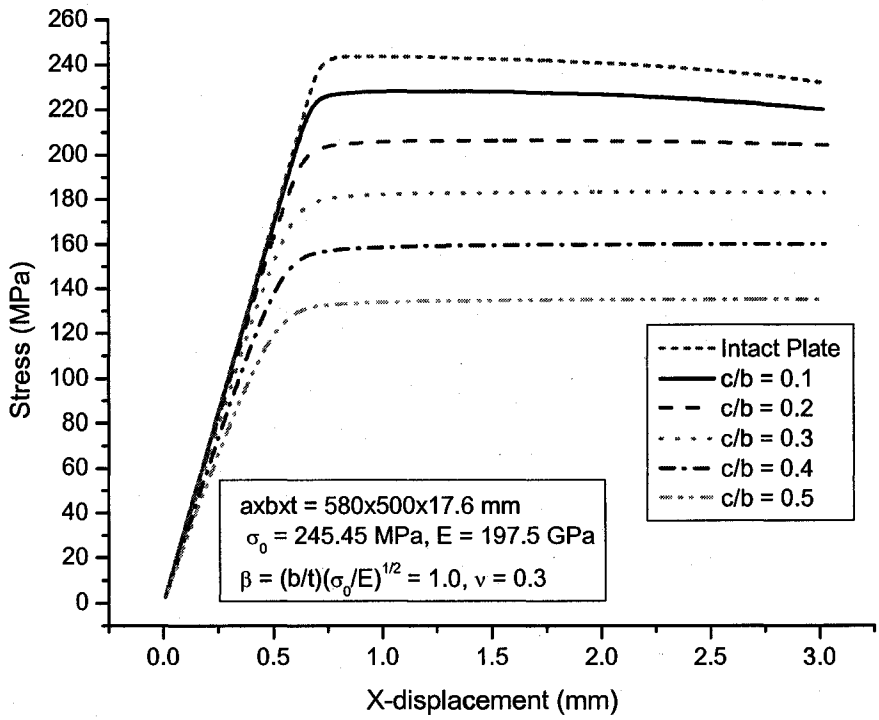

Figure 4.26 Effects of different crack sizes on ultimate compressive strength (β = 1.0)

An ultimate strength reduction factor R_{cc} is introduced as the ratio of the ultimate strength of the plate with center crack to that of the intact plate. Based on the FE results, it can be derived empirically by regression analysis. The resulting formula is given by

$$\phi_u = \frac{\sigma_u}{\sigma_Y} = \phi_{uo} R_{cc} \tag{4.16}$$

where

$$\phi_{uo} = \frac{\sigma_{uo}}{\sigma_Y} = \begin{cases} -0.032\beta^4 + 0.02\beta^2 + 1.0 & for \quad \beta \le 1.5 \\ 1.274/\beta & for \quad 1.5 < \beta \le 3.0 \\ 1.248/\beta^2 + 0.283 & for \quad \beta > 3.0 \end{cases} \tag{4.16a}$$

$$R_{cc} = 1.0031 - 0.7710\left(\frac{c}{b}\right) - 0.1954\left(\frac{c}{b}\right)^2 \tag{4.16b}$$

$$\beta = \frac{b}{t}\sqrt{\frac{\sigma_Y}{E}} \tag{4.16c}$$

c: Crack length

b: Plate breadth

t: Plate thickness

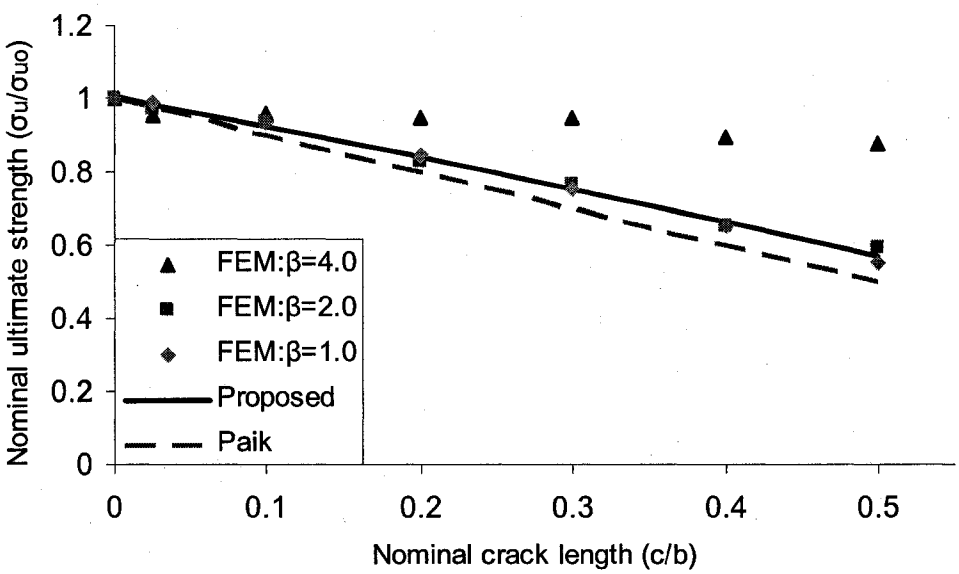

Figure 4.27 Comparison of proposed equation and equation by Paik

Figure 4.27 shows the comparison of equations proposed by author and Paik et al. (2005). It can be seen that Paik's equation underestimates the ultimate compressive strength with small amount in some circumstances. From the experiments and finite element analysis,

the center crack has very minor effect on ultimate compressive strength of the thin plate. As the plate gets thicker, the crack plays more roles on the ultimate compressive strength of the unstiffened plate.

4.3.3. Finite element analysis for ultimate compressive strength of plates with edge crack

With different edge crack lengths, a series of FE simulations have been carried out. The ultimate compressive strengths of the cracked plates have been examined. Figure 4.28 shows the example of a plate with edge crack size of c/b = 0.2. For accurately capturing the nonlinearly large deformation and force behavior of the crack tip, and precisely predicting the ultimate compressive strength, finer meshes are allocated around the crack tip, shown as in Figure 4.28 as well.

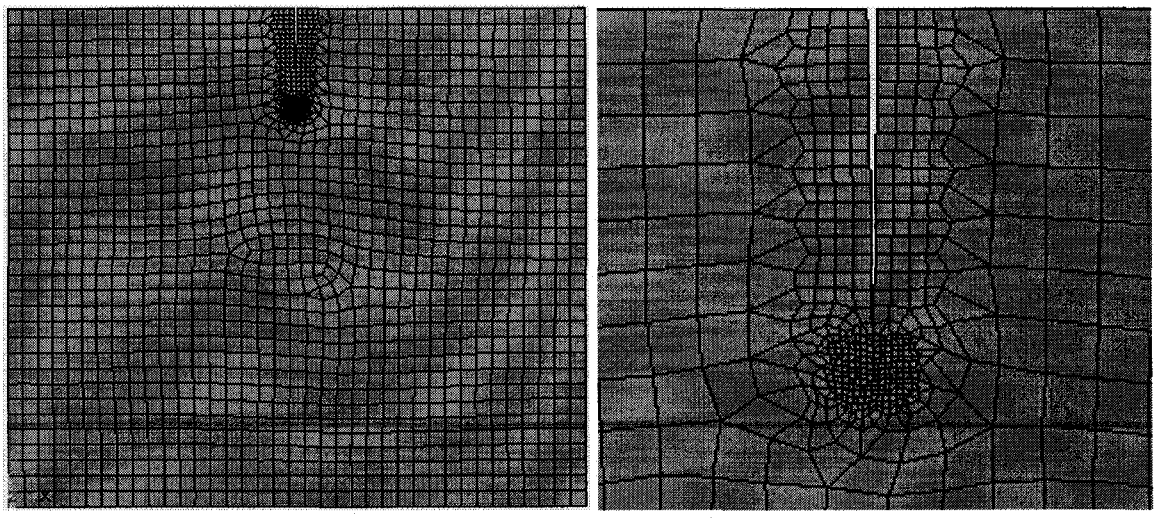

Figure 4.28 Model of c/b = 0.2 and the crack modeling detail

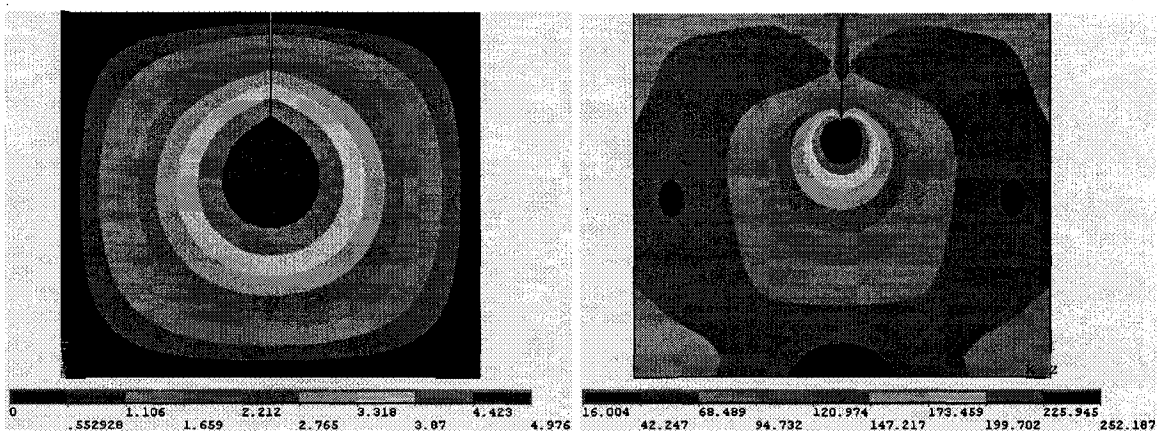

Figure 4.29 Contour plots of u_z field (z-displacement) and von Mises equivalent stresses right after the plate reaches the ultimate state

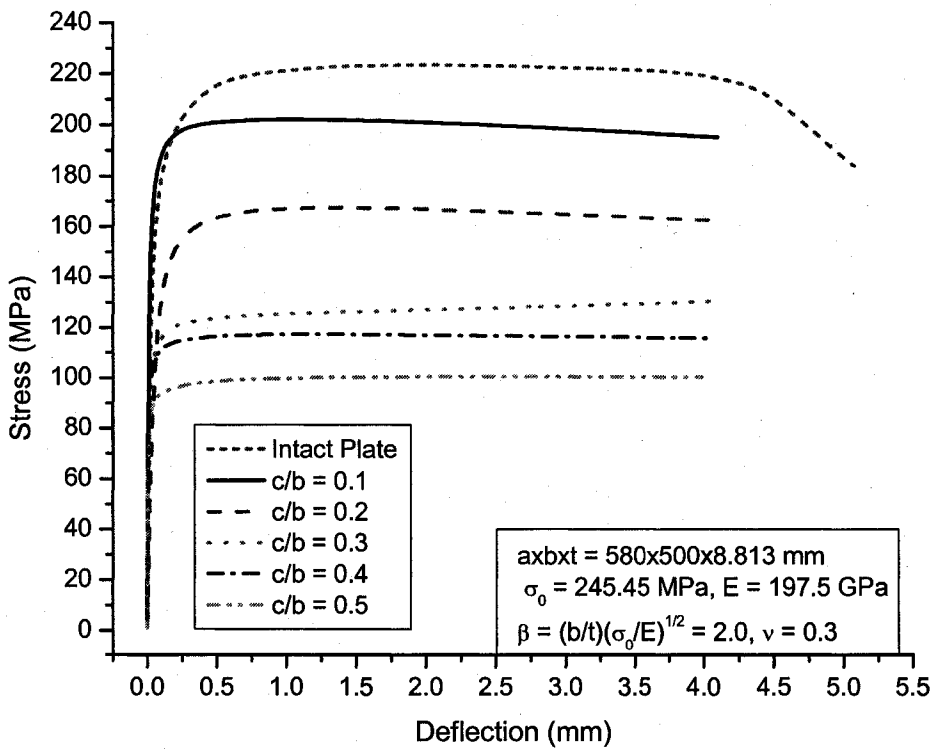

Figure 4.30 Effects of different crack sizes on ultimate compressive strength

Figure 4.29 portraits the contour plots of u_z field (z-displacement) and von Mises equivalent stresses right after the plate, with crack length c/b = 0.3, reaches the ultimate limit state. The effect of the edge crack has been shown clearly.

Figure 4.30 gives an example of the effects of different crack sizes on ultimate compress strength of an unstiffened plate with the slenderness ratio $\beta = 2.0$. It demonstrates that when the edge crack size is about 20% of the breadth, the ultimate compressive strength of the unstiffened plate will drop about 25%. While the edge crack size reaches 40% of the breadth, the ultimate compressive strength of the unstiffened plate will drop about 50%.

An ultimate strength reduction factor R_{ec} is introduced as the ratio of the ultimate strength of the plate with edge crack to that of the intact plate. Based on the FE results, it can be derived empirically by regression analysis. The resulting formula is given by

$$\phi_u = \frac{\sigma_u}{\sigma_Y} = \phi_{uo} R_{ec} \tag{4.17}$$

where

$$\phi_{uo} = \frac{\sigma_{uo}}{\sigma_Y} = \begin{cases} -0.032\beta^4 + 0.02\beta^2 + 1.0 & for \quad \beta \le 1.5 \\ 1.274/\beta & for \quad 1.5 < \beta \le 3.0 \\ 1.248/\beta^2 + 0.283 & for \quad \beta > 3.0 \end{cases} \tag{4.17a}$$

$$R_{ec} = 1.0167 - 1.278\left(\frac{c}{b}\right) + 0.3075\left(\frac{c}{b}\right)^2 \tag{4.17b}$$

The other parameters are defined as Equation 4.16

Figure 4.31 shows the comparison of equations proposed by author and Paik et al. (2005). It can be seen that Paik's equation overestimates the ultimate compressive strength with small amount in some circumstances. From the experiments and finite element analysis, the edge crack has very minor effect on ultimate compressive strength of the thin plate when the crack size is small. As the plate gets thicker, the crack becomes more and more crucial on the ultimate compressive strength of the unstiffened cracked plate.

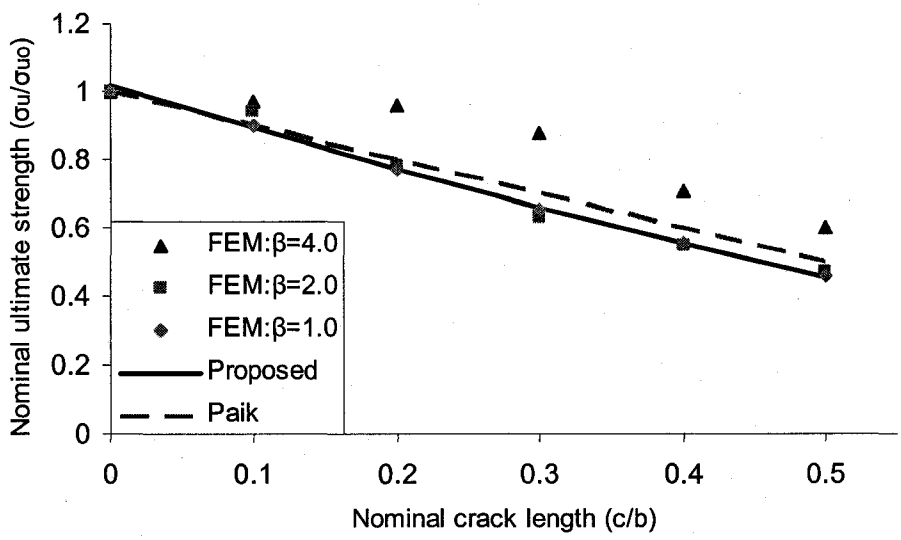

Figure 4.31 Comparison of proposed equation and equation by Paik

4.3.4. Ultimate compressive strength of stiffened panels with existing cracks

Ultimate compressive strength of stiffened panels with existing cracks is a tough topic. So far there are very rare literatures on this subject. However a vast number of empirical formations for the ultimate strength of simple intact I-beams in steel-framed structures have been developed, relevant empirical formulas for plate-beam combination models in steel-plated structures are also available. For instance, Paik & Lee (1996), and Paik &

Thayamballi (1997) developed an empirical formula for predicting the ultimate strength of a plate-stiffener combination under axial compression and with initial imperfections at an average level. Based on this equation, some modifications are made by the author to predict the ultimate compressive strength of a stiffened panel with existing crack damage. It is given by:

$$\frac{\sigma_u}{\sigma_{Yeq}} = \frac{1}{\sqrt{0.995 + 0.936\lambda_m^2 + 0.170\beta^2 + 0.188\lambda_m^2\beta^2 - 0.067\lambda_m^4}} \tag{4.18}$$

Where

$$\sigma_{Yeq} = \frac{bt\sigma_{Yp} + h_w t_w \sigma_{Yw} + b_f t_f \sigma_{Yf}}{bt + h_w t_w + b_f t_f} \tag{4.18a}$$

$$\beta = \frac{b}{t}\sqrt{\frac{\sigma_{Yp}}{E}} \tag{4.18b}$$

$$\lambda_m = \frac{L}{r_m \pi}\sqrt{\frac{\sigma_{Yeq}}{E}} \tag{4.18c}$$

$$r_m = \sqrt{\frac{I_m}{bt + h_w t_w + b_f t_f}} \tag{4.18d}$$

$$I_m = \frac{b_m t^3}{12} + A_{pm}\left(z_m - \frac{t}{2}\right)^2 + \frac{h_{wm}^3 t_w}{12} + A_{wm}\left(z_m - t - \frac{h_{wm}}{2}\right)^2 + \frac{b_{fm} t_f^3}{12} + A_{fm}\left(z_m - t - h_{wm} - \frac{t_f}{2}\right)^2 \tag{4.18e}$$

$$z_m = \frac{0.5 b_m t^2 + A_{wm}(t + 0.5h_{wm}) + A_{fm}(t + h_{wm} + 0.5t_f)}{A_m} \tag{4.18f}$$

$$A_m = A_{pm} + A_{wm} + A_{fm} \tag{4.18g}$$

$$A_{pm} = b_m t \tag{4.18h}$$

$$A_{wm} = h_{wm} t_w \tag{4.18i}$$

$$A_{fm} = b_{fm} t_f \tag{4.18j}$$

$$b_m = R_{cc} b \tag{4.18k}$$

$$h_{wm} = R_{ec} h_w \tag{4.18l}$$

$$b_{fm} = R_{ec} b_f \tag{4.18m}$$

Note:

1. R_{cc} and R_{ec} were derived in the preceding sections, given in Equation 4. 16b and Equation 4.17b, respectively.
2. The usage of R_{cc} or R_{ec} in the above equations depends one the location of the cracks, using R_{cc} in the middle, while using R_{ec} in the edge.
3. The subscript 'm' represents modification.
4. See Figure 32 for more details and definitions of the stiffened bars.

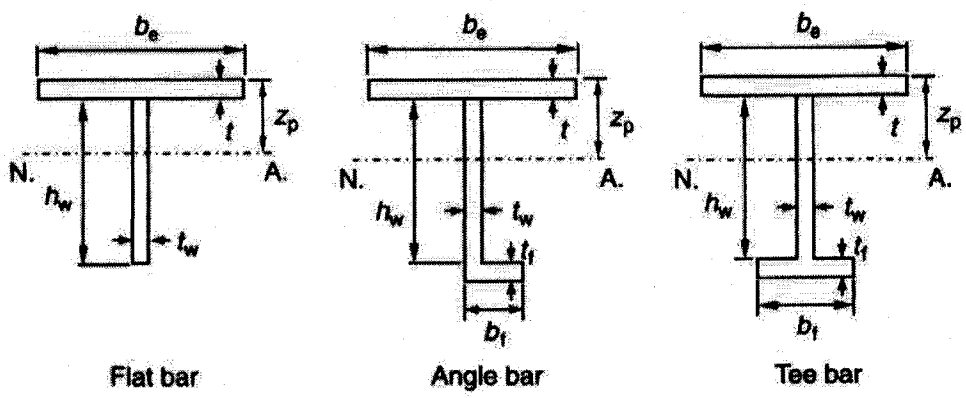

Figure 4.32 Typical types of plate-beam combination models made up of a stiffener and its attached effective plating (N.A. = neural axis)

The cracked panel shown in Figure 4.15 in Section 4.2.3 is taken as an example to demonstrate the results of the proposed modified formula, and the comparisons. The stiffened panel with flat bar has existing crack damage and is under monotonic axial compressive loading. The web has an edge crack damage and the plating has a center crack damage. The web crack length is the half of the plating crack length.

Table 4.8 shows the properties of the stiffened panel. The plate slenderness ratio is computed as $\beta = 1.6$. For generality purpose, plating and stiffener are assumed different materials.

Category	Breadth	Thickness	Young's Modulus	Yield Stress	Ultimate Tensile Stress
	mm	mm	GPa	MPa	MPa
Plate	200	4.4	197.5	245.45	334.96
Stiffener	70	8.0	198.3	296.10	362.10

Table 4.8 Properties of the stiffened panel I

Figure 4.33 graphs the comparison of the ultimate strength for intact stiffened panel and panels with different crack sizes, in which Euler formula is for the elastic column buckling strength, Paik empirical formula is for ultimate compressive strength of the intact stiffened panel, and the modified formula proposed in this study is for ultimate compressive strength of the stiffened panel with existing crack damages. From the

proposed modified formula, the effects of the cracks on the ultimate compressive strength can easily be predicted numerically

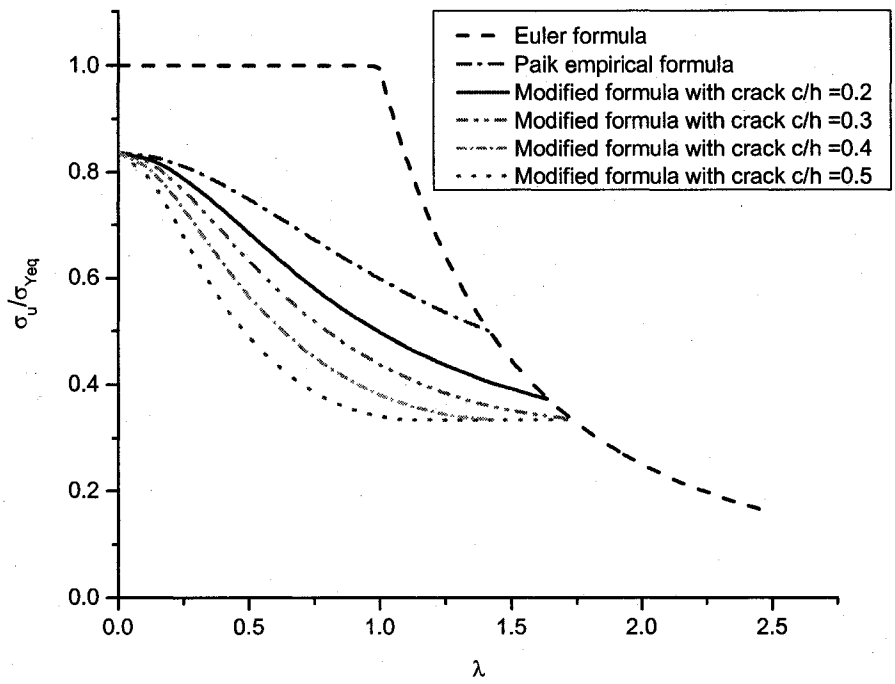

Figure 4.33 A comparison of the ultimate strength for intact stiffened panel and panel with different crack sizes ($\beta = 1.6$)

Category	Breadth	Thickness	Young's Modulus	Yield Stress	Ultimate Tensile Stress
	mm	mm	GPa	MPa	MPa
Plate	400	4.4	197.5	245.45	334.96
Stiffener	70	8.0	198.3	296.10	362.10

Table 4.9 Properties of the stiffened panel II

In order to further demonstrate the effect of plate slenderness ratio according to the modified formula. Another stiffened panel is chosen. Table 4.9 shows the properties of the stiffened panel II. The plate slenderness ratio is computed as $\beta = 3.2$.

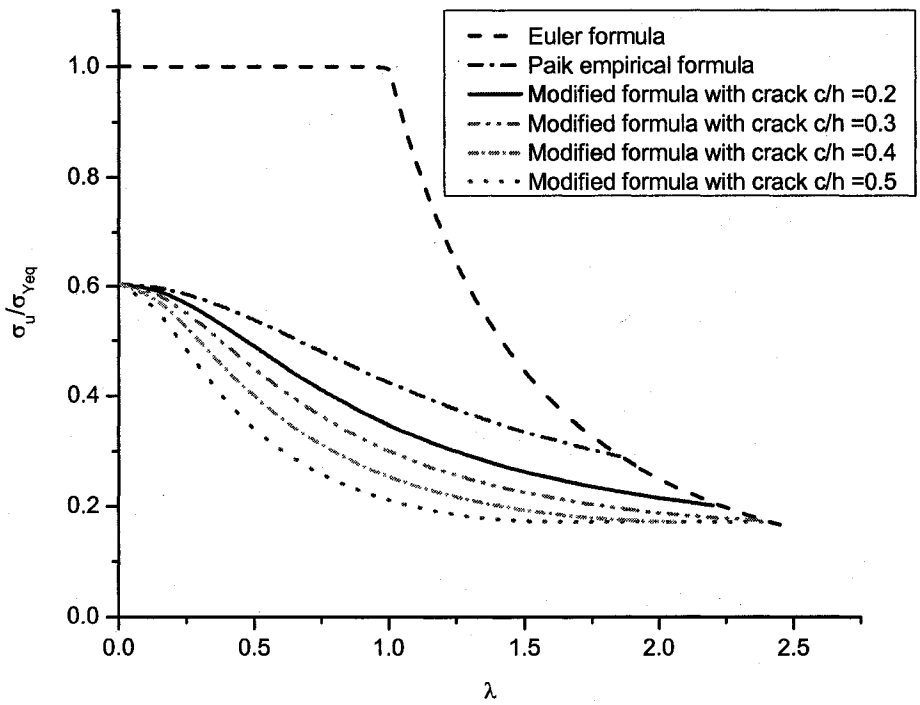

Figure 4.34 Another comparison of the ultimate strength for intact stiffened panel and panel with different crack sizes ($\beta = 3.2$)

Figure 4.34 gives the comparison of the ultimate compressive strength for intact stiffened panel and panel with different crack sizes when the plate slenderness ratio, β, gets doubled comparing to the example, stiffened panel I. Clearly the reduction characteristics of ultimate compressive strength are very similar, except the values are quite smaller as expected.

Typically, for ship structures the column slenderness ratio varies from 0.3 to 1.25, and the plate slenderness ratio may be in the range: 1.0 - 4.0. In these domains, the effects of crack sizes on the ultimate compressive strength are quite big. Therefore, inspections and maintenance are needed to be carefully planed and performed.

5. ULTIMATE STRENGTH OF SHIP HULL GIRDER

5.1. SHIP HULL GIRDER STRENGTH

The most fundamental aspect of the strength of a ship is that longitudinal strength, that is, its ability to withstand longitudinal bending under operational and extreme loads without suffering failure. The assessment of the longitudinal strength involves the evaluation of the capacity of the hull girder under longitudinal bending and also the estimation of the maximum bending moment which may act on it.

Thomas Young, whose name is well known with Young's modulus, was the first to attempt to calculate the longitudinal bending moment of ships. He treated the hull girder as a beam that is subjected to distributed loads due to weight and buoyancy forces that correspond to assumed wave modes (Timoshenko 1953). On the other hand, it was Sir Isambard K. Brunel who was the first to assess hull girder strength under extreme load conditions (Rutherford and Caldwell 1990) in the 1850s. When Sir Isambard designed the Great Eastern, a huge iron ship, he calculated bending stresses in the deck and bottom assuming a grounded condition, and determined the panel thickness so as to prevent breading of the panel.

After Sir Isambard, John (1874) presented a fundamental idea to assess longitudinal strength of a ship's hull. He calculated the bending moment assuming the wave whose

length is equal to the ship length. Based on the results of calculation, he proposed an approximate formula to evaluate the bending moment at a midship section. John calculated the maximum stress in the deck and compared it with breaking strength of the material to determine the panel thickness.

The basic idea proposed by John to assess the longitudinal strength has remained in use until today. However, the methods of analysis that are used to calculate working stress and the wave loading have improved substantially. Furthermore, the criteria to determine the thickness have changed from breaking strength to yield strength and bulking strength. The most recent development is to also take into account the ultimate strength when assessing the hull girder strength.

5.2. EXISTING METHODS OF ANALYSIS TO EVALUATE ULTIMATE HULL GIRDER STRENGTH

There are a number of calculation methods about evaluating the ultimate hull girder strength. Some of important ones are reviewed herein.

5.2.1. Caldwell's method

Caldwell (1965) was the first who tried to theoretically evaluate the ultimate hull girder strength of a ship subject to longitudinal bending. He introduced a so-called Plastic

Design considering the influence of buckling and yielding of structural members composing a ship hull.

He idealized a stiffened cross-section of a ship hull to an unstiffened cross-section with equivalent thickness. If buckling takes place at the compression side of bending, compressive stresses cannot reach the yield stress, and the fully plastic bending moment cannot be attained. Caldwell introduced a tress reduction factor at the compression side of bending, and the bending moment produced by the reduced stress was considered as the ultimate hull girder strength. He performed a series of calculation changing the reduction factors, and discussed the influence of buckling on the ultimate hull girder strength.

In Caldwell's method, reduction in the capacity of structural members beyond their ultimate strength was not taken into account. This caused an overestimation of the ultimate strength in general. In addition to this, at that time the exact values of reduction factors for structural members were not available, and the real ultimate strength itself could not be evaluated. However, Caldwell's original method seems to be rational, and has since been improved with respect to:

1) the derivation of exact reduction factors due to buckling.
2) the introduction of phase lag in collapse of individual structural members.
3) the introduction of load-shedding effect of structural members beyond their ultimate strength.

5.2.2. Improved methods

More than twenty years later, Maestro and Marino (1988) extended the Caldwell's formulation to the case of bi-axial bending, and modified the method to estimate the influence of damage due to grounding and/or collision on the ultimate hull girder strength. Nishihara (1983) applied Caldwell's method to calculate the ultimate strength of a ship hull improving the accuracy of the strength reduction factors. Many researchers proposed similar formulae. Endo et al. (1988) and Mansour et al. (1990) proposed simple calculation methods to evaluate the ultimate hull girder strength using their own formulae. Paik and Mansour (1995) also proposed a simple method to predict the ultimate hull girder strength. Applying this method, Paik et al. (1998) performed reliability analysis considering corrosion damage.

Though these methods described above do not explicitly take into account of strength reduction in the members beyond their ultimate strength, the evaluated ultimate hull girder strength showed good correlation with the measured/calculated results in many cases. For instance, Paik and Mansour (1995) compared the predicted results with those by experiments and ISUM analysis, and the differences were reported to be between -1.9% and +9.1%.

5.2.3. Smith's method

After Caldwell, more exact informations are obtained regarding the strength reduction factor representing the influence of buckling. However, the problem caused by the above-mentioned time lag had not been solved until Smith (1977) proposed a simplified method, which is now commonly called the Smith's method. This method enables to perform progressive collapse analysis on the cross-section of a hull girder subjected to longitudinal bending.

In Smith's method, a cross-section is divided into small elements composed of stiffener(s) and attached plating. At the beginning, the average stress and average strain relationships of individual elements are derived under the axial load considering the influences of yielding and buckling. Then, a progressive collapse analysis is performed assuming that a plane cross-section remains plane and each element behaves according to its average stress and average strain relationships.

After Smith, many research papers have been published, in which new methods are proposed to constitute the average stress and average strain relationship of element composed of stiffener(s) and attached plating.

5.2.4. Finite element method (FEM)

The FEM can also be a powerful method to perform progressive collapse analysis on a hull girder. Chen et al. (1983) presented the first paper to apply the FEM to this collapse analysis. They developed special elements such as orthotropic plate element representing

stiffened plate, and introduced the yielding condition in terms of sectional forces to reduce the number of freedom of the calculated model. The analyses were performed on 1 + 1/2 holds model. DNV group also performed this kind of progressive collapse analysis by the FEM employing specially developed elements (Valsgaard et al. 1991). The analyses were performed on 1/2 + 1/2 holds model and one-frame-space model.

Generally speaking, hull girder is too huge to perform progressive collapse analysis by the ordinary FEM, and some simplified methods are required. However, it has become possible to perform the FEM analysis using ordinary elements, for example, applying the computer code, LSDYNA-3D although it is not common to perform such analysis in the usual design stage. It can be predicted that as the widespread of computer technology and increase of computational power, FEM will become more popular.

5.2.5. Idealised structural unit method (ISUM)

An alternative method to perform progressive collapse analysis may be the ISUM, which was originally proposed by Ueda (1984) to perform progressive collapse analysis on the transverse frame of a ship structure. Then, new elements have been developed to perform progressive collapse analysis of a hull girder under longitudinal bending (Paik et al. 1996). Recently, more sophisticated elements are proposed and still under development. A more thorough historical review is given by Yao (1999).

5.3. A SIMPLE METHOD TO EVALUATE ULTIMATE HULL GIRDER STRENGTH

Through the review, in this study, the simple method proposed by Paik and Mansour (1995) is adopted to evaluate ultimate hull girder strength. Figure 5.1 demonstrates the assumed distribution of longitudinal stresses in a hull cross section at the overall collapse state corresponding sagging and hogging conditions.

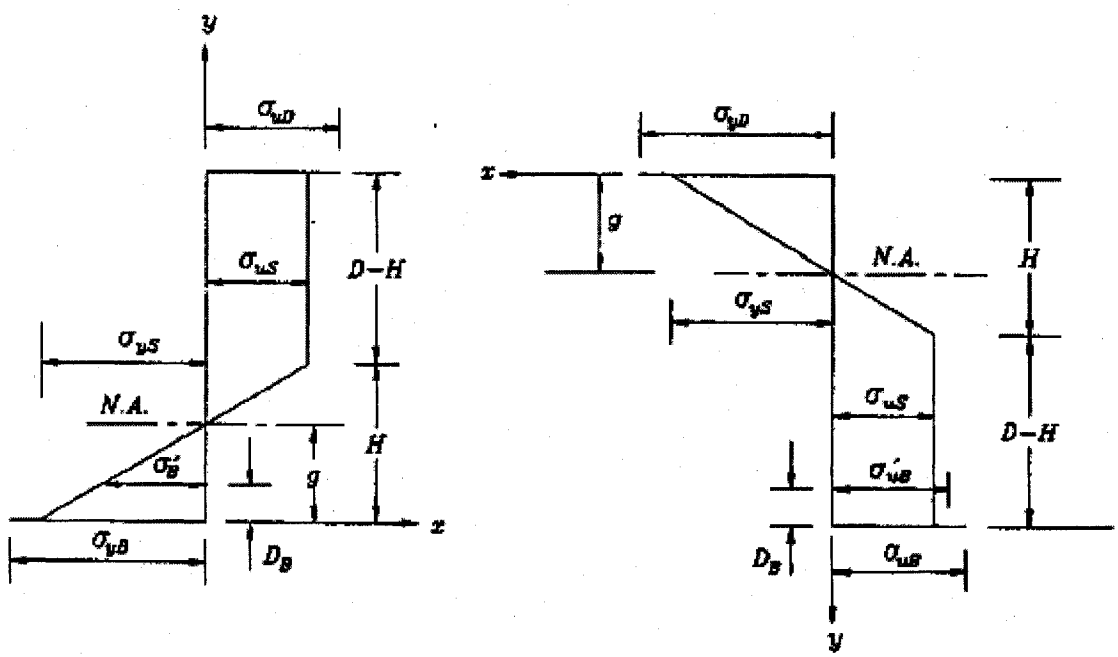

Sagging **Hogging**

Figure 5.1 Assumed distribution of longitudinal stresses in a hull cross section at the overall collapse state

From the distribution, the neutral axis has changed and moved toward the tension flange from its initial position in the intact hull section. In the compressed parts of the section, the flange and a part of sides have reached their ultimate compressive limit state. The ultimate compressive strength of the flange may be different from that of the sides. In the

stretched parts of the section, the full yield strength in tension will have developed in the flange, but the sides are assumed to remain in the elastic state. The yield strength of the tension flange may be different from that of the sides. The stress distribution in the vicinity of the neutral axis is assumed to be linear.

In Figure 5.1, D is the hull depth, D_B is the height of double bottom, H is the depth of hull section in linear elastic state, g is the neutral axis position above the base line in the sagging condition or below the deck in the hogging condition. $\sigma_{yB}, \sigma'_{yB}, \sigma_{yD}, \sigma_{yS}$ are yield strength of outer bottom, inner bottom, deck and side shell, respectively. $\sigma_{uB}, \sigma'_{uB}, \sigma_{uD}, \sigma_{uS}$ are ultimate buckling strength of outer bottom, inner bottom, deck and side shell, respectively. M_{us} and M_{uh} are ultimate bending moment in sagging and hogging, respectively.

According to Figure 5.1, the stress distribution can be expressed by (where compressive stress takes negative sign, while the tensile stress takes positive sign)

In sagging condition

$$\begin{aligned}
\sigma_x(t) &= \sigma_{yB}(t) && \text{at y =0} \\
&= -\frac{1}{H(t)}\left[\left(\sigma_{uS}(t)+\sigma_{yS}(t)\right)y - H(t)\sigma_{yS}(t)\right] && 0 < y < H \\
&= \sigma'_B(t) = -\frac{1}{H(t)}\left\{\left[\sigma_{uS}(t)+\sigma_{yS}(t)\right]D_B - H(t)\sigma_{yS}(t)\right\} && \text{at y = } D_B \\
&= -\sigma_{uS}(t) && H \le y < D \\
&= -\sigma_{uD}(t) && \text{at y = D} \qquad (5.1)
\end{aligned}$$

In hogging condition

$$\sigma_x(t) = \sigma_{yD}(t) \qquad \text{at y =0}$$

$$= -\frac{1}{H(t)}\left[\left(\sigma_{uS}(t) + \sigma_{yS}(t)\right)y - H(t)\sigma_{yS}(t)\right] \qquad 0 < y < H$$

$$= -\sigma_{uS}(t) \qquad H \le y < D$$

$$= -\sigma'_{uB}(t) \qquad \text{at y = D - } D_B$$

$$= -\sigma_{uB}(t) \qquad \text{at y = D} \qquad (5.2)$$

From the condition that no axial force acts on the hull girder, the depth of the collapsed sides, (D-H), can be calculated if H is known such that

$$\int \sigma_x(t)dA(t) = 0 \qquad (5.3)$$

In sagging condition

$$H(t) = \frac{C_1(t)D + \sqrt{C_1^2(t)D^2 + 4C_2(t)D}}{2} \qquad (5.4)$$

where

$$C_1(t) = \frac{A_D(t)\sigma_{uD}(t) + 2A_S(t)\sigma_{uS}(t) - A_B(t)\sigma_{yB}(t) - A'_B(t)\sigma_{yS}(t)}{A_S(t)\left[\sigma_{uS}(t) + \sigma_{yS}(t)\right]} \qquad (5.4a)$$

$$C_2(t) = \frac{A'_B(t)D_B}{A_S(t)} \qquad (5.4b)$$

The position of the neutral axis where the longitudinal stress is zero can be determined from the condition that the stress distribution is linear, namely

$$g(t) = y\big|\sigma_x(t) = 0 \qquad (5.5)$$

Therefore, the location of the neutral axis above the base line in sagging condition is

$$g(t)=\frac{\left[C_1(t)D+\sqrt{C_1^2(t)D^2+4C_2(t)D}\right]\sigma_{yS}(t)}{2\left[\sigma_{uS}(t)+\sigma_{yS}(t)\right]}=\frac{H(t)\sigma_{yS}(t)}{\sigma_{uS}(t)+\sigma_{yS}(t)} \tag{5.6}$$

Similarly, in hogging condition

$$H(t)=D\frac{A_B(t)\sigma_{uB}(t)+A_B'(t)\sigma_{uB}'(t)+2A_S(t)\sigma_{uS}(t)-A_D(t)\sigma_{yD}(t)}{A_S(t)\left[\sigma_{uS}(t)+\sigma_{yS}(t)\right]} \tag{5.7}$$

$$g(t)=D\frac{\left[A_B(t)\sigma_{uB}(t)+A_B'(t)\sigma_{uB}'(t)+2A_S(t)\sigma_{uS}(t)-A_D(t)\sigma_{yD}(t)\right]\sigma_{yS}(t)}{A_S(t)\left[\sigma_{uS}(t)+\sigma_{yS}(t)\right]^2}$$

$$=\frac{H(t)\sigma_{yS}(t)}{\sigma_{uS}(t)+\sigma_{yS}(t)} \tag{5.8}$$

The ultimate moment capacity of the hull under sagging bending moment is

$$\begin{aligned}M_{us}(t)=&-A_D(t)\left[D-g(t)\right]\sigma_{uD}(t)-A_B(t)g(t)\sigma_{yB}(t)\\&-\frac{A_S(t)}{D}\left[D-H(t)\right]\left[D+H(t)-2g(t)\right]\sigma_{uS}(t)\\&+\frac{A_B'}{H}\left[g(t)-D_B\right]\left\{D_B\sigma_{uS}(t)-\left[H(t)-D_B\right]\sigma_{yS}(t)\right\}\\&-\frac{A_S(t)H(t)}{3D}\left\{\left[2H(t)-3g(t)\right]\sigma_{uS}(t)-\left[H(t)-3g(t)\right]\sigma_{yS}(t)\right\}\end{aligned} \tag{5.9}$$

with H(t) and g(t) defined by Equations 5.4 and Equation 5.6, respectively

Similarly, in hogging condition, the ultimate moment capacity of the hull is

$$M_{uh}(t) = A_D(t)g(t)\sigma_{yD}(t) + A_B(t)[D - g(t)]\sigma_{uB}(t)$$
$$+ A_B'(t)[D - g(t) - D_B]\sigma_{uB}'(t)$$
$$+ \frac{A_S(t)}{D}[D - H(t)]\cdot[D + H(t) - 2g(t)]\sigma_{uS}(t)$$
$$+ \frac{A_S(t)H(t)}{3D}\{[2H(t) - 3g(t)]\sigma_{uS}(t) - [H(t) - 3g(t)]\sigma_{yS}(t)\} \qquad (5.10)$$

with H(t) and g(t) defined by Equations 5.7 and Equation 5.8, respectively

To compute the ultimate moment capacity of the hull using Equations 5.9 and Equation 5.10, the ultimate strength of the stiffened panel and unstiffened plate must be known. Calculation of the ultimate strength of them is not an easy task. For practical purpose, a number of simple formulas have been suggested (Moan et al. 1994). On the basis of existing and new collapse test results for a total number of 130 stiffened panels with appropriate values of initial imperfections, Paik and Lee (1996), Paik and Thayamballi (1997) derived an empirical formula for the ultimate compressive strength of a stiffened panel as a function of the plate slenderness ratio β and the column (stiffened) slenderness ratio λ, namely

$$\frac{\sigma_u}{\sigma_{Yeq}} = \frac{1}{\sqrt{0.995 + 0.936\lambda^2 + 0.170\beta^2 + 0.188\lambda^2\beta^2 - 0.067\lambda^4}} \qquad (5.11)$$

Equation 5.11 is not suitable to calculate the ultimate strength of stiffened panel and unstiffened plate with crack damage. Equations 4.12, 4.13, and 4.15 - 4.18 derived in Chapter 4 can be used to predict the ultimate strength of stiffened panel and unstiffened plate with crack damage.

In order to perform reliability analysis, the variance of the ultimate moment capacity of hull girder is also needed. It is calculated as follows. For simplicity, time variable is not shown explicitly in the following formulae.

In sagging condition, the variance of the ultimate moment capacity of the hull is

$$
\begin{aligned}
D_{M_{us}} = & \left[-(D-\bar{g})\overline{\sigma_{uD}}\right]^2 D_{A_D} + (-\overline{g\sigma_{yB}})^2 D_{A_B} \\
& + \left\{-\frac{(D-\overline{H})(D+\overline{H}-2\bar{g})}{D}\overline{\sigma_{uS}} - \frac{\overline{H}}{3D}\left[(2\overline{H}-3\bar{g})\overline{\sigma_{uS}} - (\overline{H}-3\bar{g})\overline{\sigma_{yS}}\right]\right\}^2 D_{A_S} \\
& + \left\{\frac{(\bar{g}-D_B)}{\overline{H}}\left[D_B\overline{\sigma_{uS}} - (\overline{H}-D_B)\overline{\sigma_{yS}}\right]\right\}^2 D_{A_B'} \\
& + \left\{\overline{A_D}D\overline{\sigma_{uD}} + \frac{2\overline{A_S}}{D}(D-\overline{H})\overline{\sigma_{uS}} - \overline{A_B\sigma_{yB}} + \frac{\overline{A_B'}}{\overline{H}}\left[D_B\overline{\sigma_{uS}} - (\overline{H}-D_B)\overline{\sigma_{uS}}\right]\right. \\
& \left. - \frac{\overline{A_S H}}{D}(\overline{\sigma_{yS}} - \overline{\sigma_{uS}})\right\}^2 D_g \\
& + \left\{\frac{\overline{A_S}}{D}(2\overline{H}-2\bar{g})\overline{\sigma_{uS}} - \frac{\overline{A_B'}}{\overline{H}^2}(\bar{g}-D_B)D_B(\overline{\sigma_{uS}}+\overline{\sigma_{yS}})\right. \\
& \left. - \frac{\overline{A_S}}{3D}\left[2\overline{H}(2\overline{\sigma_{uS}} - \overline{\sigma_{yS}}) - 3\bar{g}(\overline{\sigma_{uS}} - \overline{\sigma_{yS}})\right]\right\}^2 D_H \\
& + \left[-\overline{A_D}(D-\bar{g})\right]^2 D_{\sigma_{uD}} + (-\overline{A_B g})^2 D_{\sigma_{yB}} \\
& + \left\{-\frac{A_S}{D}(D-\overline{H})(D+\overline{H}-2\bar{g}) + \frac{\overline{A_B'}}{\overline{H}}(\bar{g}-D_B)D_B - \frac{\overline{A_S H}}{3D}(2\overline{H}-3\bar{g})\right\}^2 D_{\sigma_{uS}}
\end{aligned}
$$

$$+\left\{-\frac{\overline{A_B'}}{\overline{H}}(\overline{g}-D_B)(\overline{H}-D_B)+\frac{\overline{A_S H}}{3D}(\overline{H}-3\overline{g})\right\}^2 D_{\sigma_{yS}} \tag{5.12}$$

where

$$D_H=\left\{\frac{D}{2}+\frac{C_1 D^2}{2\sqrt{\overline{C_1^2}D^2+4\overline{C_2}D}}\right\}^2 D_{C_1}+\left\{\frac{D}{\sqrt{\overline{C_1^2}D^2+4\overline{C_2}D}}\right\}^2 D_{C_2} \tag{5.12a}$$

$$D_g=\left\{\frac{\overline{\sigma_{yS}}}{\overline{\sigma_{uS}}+\overline{\sigma_{yS}}}\right\}^2 D_H+\left\{\frac{\overline{H\sigma_{yS}}}{(\overline{\sigma_{uS}}+\overline{\sigma_{yS}})^2}\right\}^2 D_{\sigma_{uS}}+\left\{\frac{\overline{H\sigma_{uS}}}{(\overline{\sigma_{uS}}+\overline{\sigma_{yS}})^2}\right\}^2 D_{\sigma_{yS}} \tag{5.12b}$$

$$D_{C_1}=\frac{(\overline{\sigma_{uD}})^2 D_{A_D}+(\overline{\sigma_{yB}})^2 D_{A_B}+(\overline{\sigma_{yS}})^2 D_{A_B'}+(\overline{A_D})^2 D_{\sigma_{uD}}+(\overline{A_B})^2 D_{\sigma_{yB}}}{\left[\overline{A_S}(\overline{\sigma_{uS}}+\overline{\sigma_{yS}})\right]^2}$$

$$+\left\{\frac{\overline{A_D\sigma_{uD}}-\overline{A_B\sigma_{yB}}-\overline{A_B'\sigma_{yS}}}{\overline{A_S}^2(\overline{\sigma_{uS}}+\overline{\sigma_{yS}})}\right\}^2 D_{A_S}$$

$$+\left\{\frac{\overline{A_B\sigma_{yB}}+\overline{A_B'\sigma_{yS}}-\overline{A_D\sigma_{uD}}+2\overline{A_S\sigma_{yS}}}{\overline{A_S}(\overline{\sigma_{uS}}+\overline{\sigma_{yS}})^2}\right\}^2 D_{\sigma_{uS}}$$

$$+\left\{\frac{\overline{A_B\sigma_{yB}}-\overline{A_B'\sigma_{uS}}-\overline{A_D\sigma_{uD}}-2\overline{A_S\sigma_{uS}}}{\overline{A_S}(\overline{\sigma_{uS}}+\overline{\sigma_{yS}})^2}\right\}^2 D_{\sigma_{yS}} \tag{5.12c}$$

$$D_{C_2}=\left\{\frac{D_B}{\overline{A_S}}\right\}^2 D_{A_B'}+\left\{\frac{\overline{A_B'}\overline{D_B}}{\overline{A_S^2}}\right\}^2 D_{A_S} \tag{5.12d}$$

In hogging condition, the variance of the ultimate moment capacity of the hull is

$$D_{M_{uh}} = (\overline{g\sigma_{yD}})^2 D_{A_D} + \left[(D-\overline{g})\overline{\sigma_{uB}}\right]^2 D_{A_B} + \left[(D-\overline{g}-D_B)\overline{\sigma'_{uB}}\right]^2 D_{A'_B}$$

$$+\left\{\frac{(D-\overline{H})(D+\overline{H}-2\overline{g})}{D}\overline{\sigma_{uS}} - \frac{\overline{H}}{3D}\left[(2\overline{H}-3\overline{g})\overline{\sigma_{uS}} - (\overline{H}-3\overline{g})\overline{\sigma_{yS}}\right]\right\}^2 D_{A_S}$$

$$+\left\{\overline{A_D\sigma_{yD}} - \overline{A_B\sigma_{uB}} - \overline{A'_B\sigma'_{uB}} - \frac{2\overline{A_S}}{D}(D-\overline{H})\overline{\sigma_{uS}} + \frac{\overline{A_S H}}{D}\left[-\overline{\sigma_{uS}} + \overline{\sigma_{yS}}\right]\right\}^2 D_g$$

$$+\left\{\frac{\overline{A_S}}{D}(2\overline{g}-2\overline{H})\overline{\sigma_{uS}} + \frac{\overline{A_S}}{3D}\left[2\overline{H}(2\overline{\sigma_{uS}} - \overline{\sigma_{yS}}) - 3\overline{g}(\overline{\sigma_{uS}} - \overline{\sigma_{yS}})\right]\right\}^2 D_H$$

$$+(\overline{A_D g})^2 D_{\sigma_{yD}} + \left[\overline{A_B}(D-\overline{g})\right]^2 D_{\sigma_{uB}} + \left[\overline{A'_B}(D-\overline{g}-D_B)\right]^2 D_{\sigma'_{uB}}$$

$$+\left\{\frac{\overline{A_S H}}{3D}(\overline{H}-3\overline{g})\right\}^2 D_{\sigma_{yS}}$$

$$+\left\{\frac{\overline{A_S}}{D}(D-\overline{H})(D+\overline{H}-2\overline{g}) + \frac{\overline{A_S H}}{3D}(2\overline{H}-3\overline{g})\right\}^2 D_{\sigma_{uS}} \qquad (5.13)$$

where

$$D_H = \frac{D^2}{\overline{A_S}^2(\overline{\sigma_{uS}} + \overline{\sigma_{yS}})^2}\left\{\overline{\sigma_{uB}}^2 D_{A_B} + \overline{\sigma'_{uB}}^2 D_{A'_B} + \overline{\sigma_{yD}}^2 D_{A_D}\right.$$

$$\left. + \overline{A_B}^2 D_{\sigma_{uB}} + \overline{A'_B}^2 D_{\sigma'_{uB}} + \overline{A_D}^2 D_{\sigma_{yD}}\right\}$$

$$+ D^2\left\{\frac{\overline{A_D\sigma_{yD}} - \overline{A_B\sigma_{uB}} - \overline{A'_B\sigma'_{uB}}}{\overline{A_S}^2(\overline{\sigma_{uS}} + \overline{\sigma_{yS}})}\right\}^2 D_{A_S}$$

$$+ D^2\left\{\frac{\overline{A_D\sigma_{yD}} - \overline{A_B\sigma_{uB}} - \overline{A'_B\sigma'_{uB}} - 2\overline{A_S\sigma_{uS}}}{\overline{A_S}(\overline{\sigma_{uS}} + \overline{\sigma_{yS}})^2}\right\}^2 D_{\sigma_{yS}}$$

$$+D^2\left\{\frac{\overline{A_D\sigma_{yD}}-\overline{A_B\sigma_{uB}}-\overline{A_B'\sigma_{uB}'}+2\overline{A_S\sigma_{yS}}}{\overline{A_S}(\overline{\sigma_{uS}}+\overline{\sigma_{yS}})^2}\right\}^2 D_{\sigma_{uS}} \tag{5.13a}$$

$$D_g=\left\{\frac{\overline{\sigma_{yS}}}{\overline{\sigma_{uS}}+\overline{\sigma_{yS}}}\right\}^2 D_H+\left\{\frac{\overline{H\sigma_{yS}}}{(\overline{\sigma_{uS}}+\overline{\sigma_{yS}})^2}\right\}^2 D_{\sigma_{uS}}+\left\{\frac{\overline{H\sigma_{uS}}}{(\overline{\sigma_{uS}}+\overline{\sigma_{yS}})^2}\right\}^2 D_{\sigma_{yS}} \tag{5.13b}$$

In order to briefly demonstrate the effect of corrosion and cracks with time, Mansour's box girder model II shown in Figure 5.2 is taken as an example herein. It is assumed that cracking initiates at all stiffeners and plating after 5 years. The initial crack size is considered to be 1.0mm. The previous section's cracking prediction model is taken. Two types of corrosion models are used to simulate the corrosion rates. One is constant corrosion rate model (Model I). The other is nonlinear corrosion rate model (Model II), which is introduced in Chapter 2.

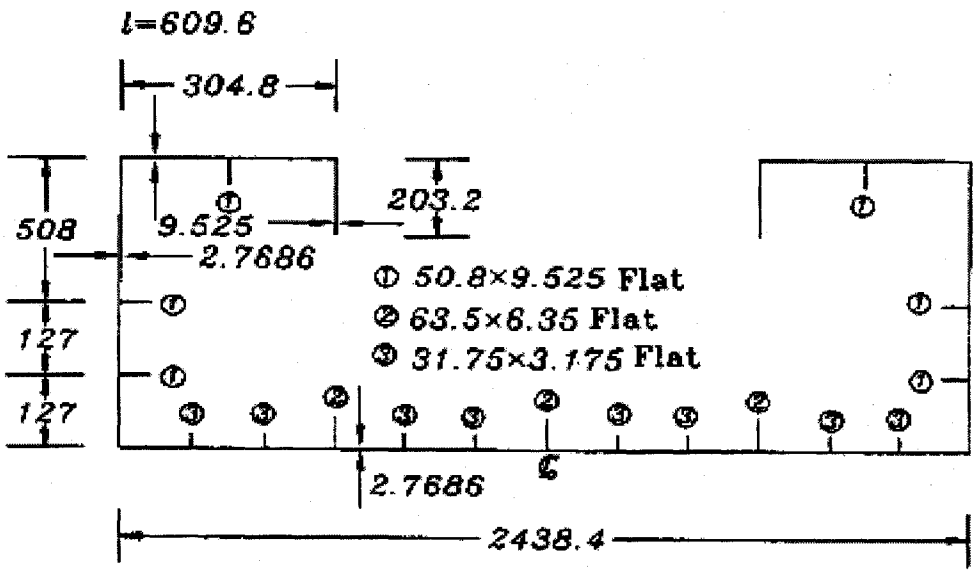

Figure 5.2 Midship section of Mansour's box girder model II tested in the hogging condition (unit: mm)

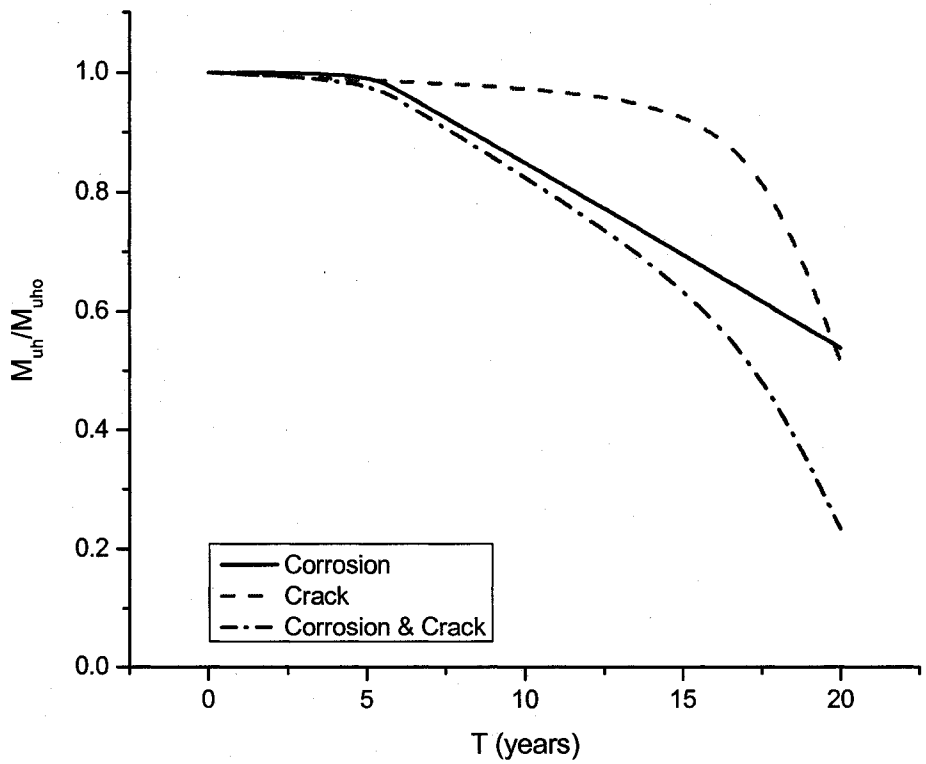

Figure 5.3 Mean value of ultimate moment capacity with time under hogging condition (with constant corrosion rate model)

Figure 5.3 shows the time-dependent ultimate strength of hull girder due to age-related degradations according to Equation 5.10. The age-related degradations include corrosion and fatigue cracking damage. The constant corrosion model (Model I) is applied. The combination of both degradations is also examined. For corrosion damage alone, the ultimate moment of hull girder will decrease to 90% of the initial ultimate moment of intact hull girder after about 8 years; for crack damage alone, it takes about 17 years; while for combination of both, it takes about 7 years. From the comparison, one can see the corrosion damage is more severe. But the fatigue cracking damage is more dangerous

when the cracks approach the critical sizes. It can cause catastrophic collapse of hull girder suddenly even though the cracks have very little effect on the ultimate strength of hull girder before they approach some certain critical sizes.

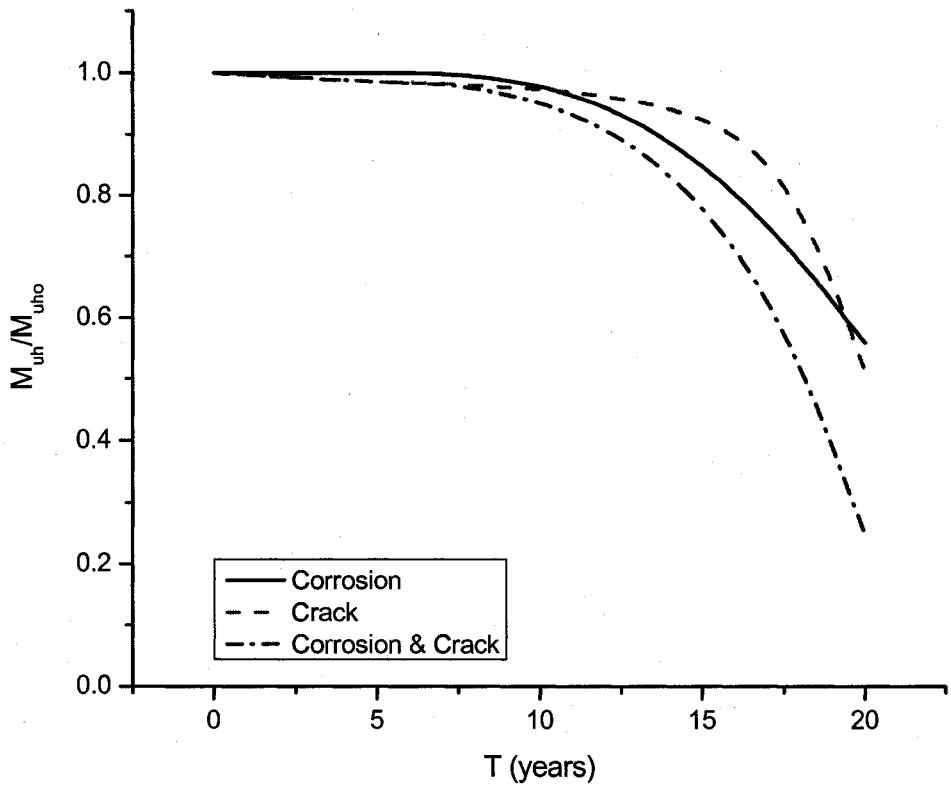

Figure 5.4 Mean value of ultimate moment capacity with time under hogging condition (with nonlinear corrosion rate model)

Figure 5.4 shows the time-dependent ultimate strength of hull girder due to age-related degradations, in which the nonlinear corrosion model (Model II) is assumed. For corrosion damage alone, the ultimate moment of hull girder will decrease to 90% of the initial ultimate moment of intact hull girder after about 14 years; for crack damage alone, it takes about 17 years; while for combination of both, it takes about 12 years.

6. PROBABILISTIC MODELS OF WAVE LOADS AND LOAD COMBINATIONS

Loads come in two flavors. The first, stillwater bending moment (M_{sw}), is determined by the designer and the loading of the ship. Thus, it can be controlled by humans directly. The second, the wave-induced and dynamic bending moments (M_w and M_d), is environmental and can only be influenced by humans indirectly (i.e., by route planning, etc.) (Mansour et al., 1997).

6.1. STILLWATER BENDING MOMENT

The detailed distribution of the stillwater bending moment along the ship's length can be calculated by a double integration of the difference between the weight force and the buoyancy force, using the simple beam theory.

In this study, the detailed load calculation is not the major task. For convenience, the extreme value of the stillwater bending moment resulting from the worst load condition for a ship is often taken from an empirical formula. In this study, the maximum stillwater bending moment is estimated by the IACS design guidance formula (Nitta et al., 1992):

$$M_{sw} = \begin{cases} 0.015CL^2B(8.167 - C_b)(KNm) & for \quad hogging \\ -0.065CL^2B(0.7 + C_b)(KNm) & for \quad sagging \end{cases} \tag{6.1}$$

where

$$C = \begin{cases} 0.0792L & for \quad L \le 90m \\ 10.75 - \left(\frac{300 - L}{100}\right)^{1.5} & for \quad 90 < L \le 300m \\ 10.75 & for \quad 300 < L \le 350m \\ 10.75 - \left(\frac{L - 350}{150}\right)^{1.5} & for \quad 350 < L \le 500m \end{cases} \tag{6.1a}$$

L = ship length (m)

B = ship breadth (m)

C_b = block coefficient at summer load waterline

Since the above values are calculated for either full load or maximum allowable conditions, the mean values (for use in the reliability analysis) have to be reduced by some amount. For the military ships, the mean value is assumed to be 80 percent of the full load calculated value. For the commercial ships, the mean is assumed to be 60 percent of the calculated maximum allowable value (Mansour et al., 1993 and Mansour, A. and Thayamballi, A., 1994)

The stillwater bending moment is assumed to follow a normal distribution with either a coefficient of variation of 0.15 for the military ships or a coefficient of variation of 0.25 for the commercial ships (Mansour et al., 1993). The differences between the two ship types account for the fact that the majority of the weights of a warship are relatively constant, while the weights on commercial ships vary quite a bit (due to different cargo loading conditions).

6.2. WAVE-INDUCED BENDING MOMENT

The IACS design formula estimates the extreme wave induced bending moment as follows:

$$M_w = \begin{cases} 0.19CL^2BC_b(KNm) & for \quad hogging \\ -0.11CL^2B(0.7+C_b)(KNm) & for \quad sagging \end{cases} \tag{6.2}$$

where C, L, B and C_b are as defined in Equation 6.1.

For the safety and reliability assessment of damaged ship structures in particular cases, short-term based response analysis may be used to determine wave-induced bending moment when the ship encounters a storm of specific duration (usually 3 hours) and with certain small encounter probability (Paik et al., 1997 & 2003).

Such a short term analysis can be performed by applying the direct method. The MIT sea-keeping tables developed by Loukakis and Chryssostomidis (1975) are useful for predicting the short-term based wave-induced bending moment of merchant cargo vessels, and time saving can also be achieved. The tables are designed to efficiently determine the root-mean-square value, $\sqrt{\lambda_0}$, of the wave-induced bending moment given the values of effective wave height, L/B ratio, B/d ratio, ship operating speed, C_b, and sea state persistence time.

If the root-mean-square value, $\sqrt{\lambda_0}$, of the wave-induced bending moment is known, the most probable extreme value of the wave-induced bending moment, M_w, i.e., median,

which we may refer to a mean value for convenience and its standard deviation, σ_w, can then be computed by upcrossing analysis, with the probability density function of a random variable following the Type I extreme distribution (Mansour 1990).

$$F_w(M_w) = \exp\left\{-N\exp\left(-\frac{M_w^2}{2\lambda_0}\right)\right\} \tag{6.3}$$

$$M_w = \sqrt{2\lambda_0 \ln N} + \frac{0.5772}{\sqrt{2\lambda_0 \ln N}} \tag{6.3a}$$

$$\sigma_w = \frac{\pi}{\sqrt{6}}\sqrt{\frac{\lambda_0}{2\ln N}} \tag{6.3b}$$

where N is the expected number of the wave bending peaks. It can approximately be given by (Hogben et al., 1986 and Hogben 1990):

$$N = \frac{T_s}{T_z} \tag{6.4}$$

$$T_z = \sqrt{13H_s} \tag{6.4a}$$

where H_s is significant wave height in meters. T_s is the storm duration in seconds, while T_z is the zero-up-crossing wave period in seconds. For 3 hours storm duration with H_s = 11m, for instance, the number of wave peaks then becomes:

$N = 3\times 60\times 60/\sqrt{13\times 11} = 903$.

Paik et al. (2003) compared the wave-induced bending moments, obtained by using the MIT sea-keeping tables, and the values obtained by IACS formula. It is concluded that

the short-term based wave-induced bending moments are smaller than the IACS formula by 10 to 20 percent for the particular scenarios of operational condition and sea states presumed in that study. For convenience, and also for conservative purpose, IACS formula is used in this study.

The extreme wave moment is assumed to follow the extreme value distribution with a coefficient of variation of 0.10 (Mansour and Thayamballi, 1994).

6.3. DYNAMIC MOMENT

When the ship bottom hits the water surface after a series of large heave and pitch motions, an impact is generated. Usually it is called slamming. According to Ochi and Motter (1973), the necessary and sufficient conditions leading to slamming impact are:

- Relative motion must exceed sectional draft (bottom emergence)
- Relative velocity at instant of reentry must exceed a certain magnitude, called the threshold velocity.

Full-scale measurements have shown that the slamming induced stresses at midship can be of the same order magnitude as the bending induced stresses (Ochi and Motter, 1973). Therefore, slamming stresses must be carefully evaluated in the design phase, and be combined suitably with the low-frequency wave-induced bending stresses.

Slamming loads are significant in many types of oceangoing vessels, particularly, those with fine form, low draft, and high speed. The maximum slam loads do not typically occur when the wave induced loads are the largest, and such phasing needs to be considered in the calculation of combined load effects.

The treatment of slamming in ships is semi-empirical, relying on insights gained from in-service data and measurements. It contains large uncertainties related to methods themselves, effect of operational factors, and load combinations.

In order to model the effects of slamming, a dynamic moment, M_d, is introduced into the analysis. Since the slamming-induced moment is a sagging moment, it is included only when the sagging loading condition is considered. Based on work by Sikora and Beach (1989), the results by Mansour and Thayamballi (1994), and Mansour et al. (1997), the dynamic moment can be taken as a fraction of the extreme wave moment. For the fine-hulled warships, the mean extreme dynamic moment is assumed to be 40 percent of the mean extreme wave moment. For the fuller-formed commercial ships, this percentage is taken to be smaller, specifically, a value of 20 percent of M_w is used.

The extreme dynamic moment is assumed to follow the extreme value distribution. A coefficient of variation of 0.30 is used, due to the large uncertainty in modeling the dynamic effects (Mansour and Thayamballi, 1994).

6.4. LOAD COMBINATION FACTORS

Load combination factors are used to account for the correlations between various loads. Two combination factors are needed: one to combine the wave-induced moment and dynamic moment, k_d, and a second to combine the wave-dynamic composite moments with the stillwater moment, k_w.

Based on the work done by Mansour and Thayamballi (1994), Mansour and Jensen (1995), and Mansour et al (1997), values were selected for both load combination factors. Since these factors are semi-empirical, it is prudent to treat each as random variable instead of deterministic constant. In this study, the normal distribution is chosen to model this uncertainty. A coefficient of variation is selected for each of the factors. The mean load combination factors and their coefficients of variation are shown in Table 6.1. The coefficient of variation of k_d is somewhat large because of the higher uncertainty in making a valid judgment about k_d's value.

Factor	Mean	COV
k_w	1	0.05
k_d	0.7	0.15

Table 6.1 Mean and coefficients of variation of load combination factors

7. STRUCTURAL RELIABILITY

7.1. INTRODUCTION

A common method of treating uncertainties in engineering is using reliability methods (Sundararajan 1995). Structural reliability analysis is concerned with evaluating the probability of failure, taking into account the uncertainties involved in the problem. Uncertainties associated with engineering problems have various sources which can be grouped as follows (Der Kiureghian et al., 1989):

1) Inherent variability or randomness, which is the variability naturally inherent to a physical phenomenon, such as that in material properties and loads. This type of uncertainty cannot be affected without changing the phenomenon itself.
2) Statistical uncertainty, which arises in the process of estimating inherent variability and it due to scarcity of data (uncertainty in distribution on parameters $\underline{\theta}_f$ and limit state function parameters $\underline{\theta}_g$). This type of uncertainty can be reduced through accumulation of data.
3) Model error, which is the error inherent in idealized mathematical models used to describe complex physical phenomena, such as a model describing the strength of a structural member. Sources of model error include ignorance and simplification. This type of uncertainty can be reduced by use of more refined models.

4) Measurement error, which is the error in measuring or observing data for statistical analysis. This type of uncertainty can be reduced by improving the precision of measurement.
5) Human error, which is the unavoidable process of making errors in the design, construction, operation, and maintenance of facilities by human beings. This type of uncertainty can be reduced by use of more refined models.

There is a fundamental distinction between inherent variability and the other sources of uncertainty. Namely, inherent variability is irreducible, whereas statistical uncertainty, model error, measurement error and human error are reducible. Due to this distinction, in some applications it has become a tradition to treat the two types of uncertainty separately.

There are lots of structural reliability methods to treat these uncertainties and compute the probability of failure (Table 7.1). In the reliability analysis, as a simplification, it is assumed that all states of the structure with respect to a failure mode can be divided into a failure state or a safe state. A function, g(x), called limit state function or failure function, is defined such that if $g(x) > 0$ the structure is in the safe state, and if $g(x) < 0$ the structure is in the failure state. $g(x) = 0$ defines the limit state surface which separate the failure region from the safe region. Given a limit state function g(x) and a joint probability density function $f_x(x)$ for the random vector X, the probability of failure is computed by the integral

$$P_f = \int_{\Omega} f_X(x)dx \tag{7.1}$$

where

Ω: the failure domain

$f_X(x)$: joint probability density function of random variables X.

ANALYTICAL METHODS
1. Direct evaluation of the probability-of-failure integral
2. Normal and lognormal formats
3. Mean value first-order second-moment (MVFOSM)
4. Hasofer-Lind generalized safety index
5. First-order reliability methods (FORM)
6. Second-order reliability methods (SORM)
7. Advanced mean value (AMV) method
MONTE CARLO SIMULATION
1. Direct Monte Carlo
2. Importance sampling
3. Domain-restricted sampling
4. Adaptive sampling
5. Directional sampling

Table 7.1 A summary of structural reliability methods (Wirsching 2003)

The failure domain Ω is described in terms of continuous and differentiable limit state functions that define its boundary within the outcome space of X. Depending on the nature of the problem, the following definitions apply (Mansour 1990):

Component problem: $$\Omega \equiv \{g(X) \le 0\} \tag{7.2a}$$

Series system problem: $$\Omega \equiv \bigcup_k \{g_k(X) \le 0\} \tag{7.2b}$$

Parallel system problem: $$\Omega \equiv \bigcap_k \{g_k(X) \le 0\} \tag{7.2c}$$

General system problem: $$\Omega \equiv \bigcup_k \bigcap_{j \in c_k} \{g_k(X) \le 0\} \tag{7.2d}$$

This problem is challenging because for most non-trivial selections of $f_x(x)$ and Ω no closed form solution of the integral exists. A lot of methods have been developed for computing the failure probability integral (Table 7.1). These methods have been implemented in reliability analysis programs such as PROBAN, STRUREL, CalREL, OpenSees, and so on.

Structural reliability analysis also provides the sensitivity of the failure probability with respect to the different input parameters. This information can be used in defining the importance of the different random variables in the reliability model, e.g. which random variables should be include in the model, which random variables are crucial and will require more investigation to reduce uncertainties. Such information is essential in optimizing the reliability of the structure in design and within inspection and maintenance planning.

7.2. COMPONENT STRUCTURAL RELIABILITY METHODS

The component problems are defined in terms of a single limit state function, g(X). Depends on different information we have known, we can choose to use different methods to do the reliability analysis.

7.2.1. Mean value first-order second-moment (MVFOSM) method

If you have incomplete probability information, e.g. we only have the second moments and do not know the detailed distributions, we can choose to use this method (Cornell 1969). Assume a structural reliability problem is characterized by an n-vector of basic random variables $X = \{x_1, x_2, \Lambda, x_n\}^T$ and $\Omega \equiv \{g(X) \le 0\}$, which defines the failure event. The information we have is the mean vector M and covariance matrix Σ. Meanwhile we know

$$P_f = F_Z(0) = F_U(-\beta) \tag{7.3}$$

where

$$\beta = \frac{\mu_Z}{\sigma_Z} \tag{7.3a}$$

Apply for the first order approximation, we have

$$g(X) = g(M) + \nabla_x g(X - M) \tag{7.4}$$

where

$$\nabla_x g = \left[\frac{\partial g}{\partial x}, \Lambda, \frac{\partial g}{\partial x_n}\right]_{X=M} \tag{7.4a}$$

Finally, we can obtain

$$\mu_Z \approx g(M) \tag{7.5}$$

$$\sigma_Z^2 \approx \nabla_x g \sum \nabla_x g^T \tag{7.6}$$

The safety index is given by

$$\beta_{MVFOSM} = \frac{g(M)}{\sqrt{\nabla_x g \sum \nabla_x g^T}} \tag{7.7}$$

Then, the probability of failure is approximated by

$$P_f \approx \Phi(-\beta_{MVFOSM}) \tag{7.8}$$

The advantage of this method is that it is very simple, and easy to compute. But the disadvantage is the method lack of invariance. The safety index depends on the limit state equation. For different limit state equations, very different safety indexes might be obtained. Which is obviously not good for engineers to use. Thus in engineering first order reliability method or second order reliability method is often used.

7.2.2. First order reliability method (FORM) and second order reliability method (SORM)

The FORM and SORM are methods to compute the multi-dimensional integral given by equation (1). As a first step, the vector of basic random variables $X = \{x_1, x_2, \Lambda, x_n\}^T$ is transformed into an independent standard normal (zero mean and unit standard deviation) vector $U = \{U_1, U_2, \Lambda, U_n\}$. If the random variables x_i are statistically independent and

$F(x_i)$ is a continually and strictly increasing function, the transformation can be done directly, see Figure 7.1.

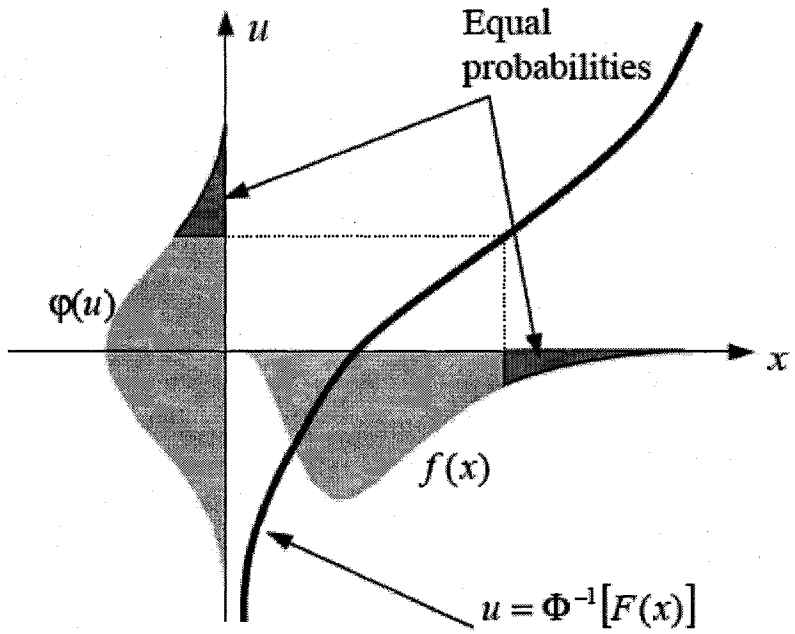

Figure 7.1 Transformation to the standard normal space for a single random variable

If the variables are generally dependent and non-normal, a probability preserving transformation usually referred to as the Rosenblatt transformation is used, see Figure 2 (Bjerager 1989). This mapping uses successively the conditional cumulative distribution functions $F_{X_i|X_x,\Lambda,X_{i-1}}(x_i|x_1,\Lambda,x_{i-1})$ corresponding to the random variable X to describe the independent standard normal vector U. In many cases only the marginal probability distributions and the correlation coefficients between the variables are available. In such cases the Nataf model can be used (Der Kiureghian and Liu 1986).

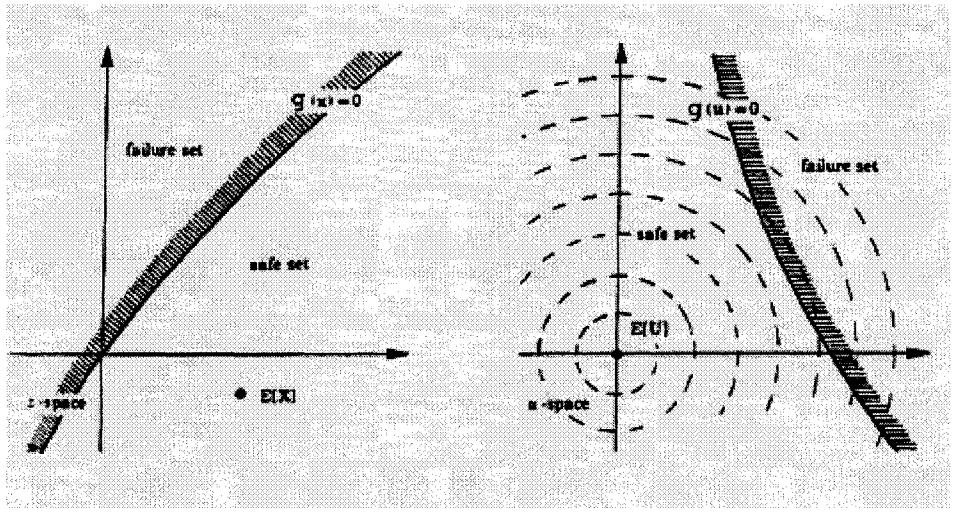

Figure 7.2 Transformation from space of stochastic basic variables X to space of standard normal variables U

In the next step, using FORM, the failure surface in the u-space is approximated by a linear hyper-surface at its point of maximum likelihood, called the design point u^*. For SORM a quadratic approximation is used. Since the density function in the u-space decreases exponentially with the square of the distance from the origin, the main contribution to the probability integral comes from the region near the design point. Due to the rational symmetry of the independent standard multi-normal density function, the design point is the point on the failure surface closest to the origin. This point can be located by solving a constrained optimization problem.

As a final step, the probability of failure is computed. The FORM approximation to the failure probability P_f is equal to (Madsen, et al 1986):

$$P_f \approx P_{f_{FORM}} = \Phi(-\beta_{FORM}) \tag{7.9}$$

where β_{FORM} is called the first order reliability index, and is equal to the minimum distance from origin to failure surface in the u-space, i.e. $\beta_{FORM} = |u^*|$. The FORM approximation is thus the probability content outside the tangent hyperplane. The most likely failure point or design point, is conveniently expressed in terms of β and a unit directional vector α as $u^* = \beta\alpha$, where α is the unit normal vector directed towards the failure set. The second order approximation (SORM) to the failure probability P_f is given as the probability content outside the second order failure surface. The comparison between FORM and SORM approximations is shown in Figure 7.3.

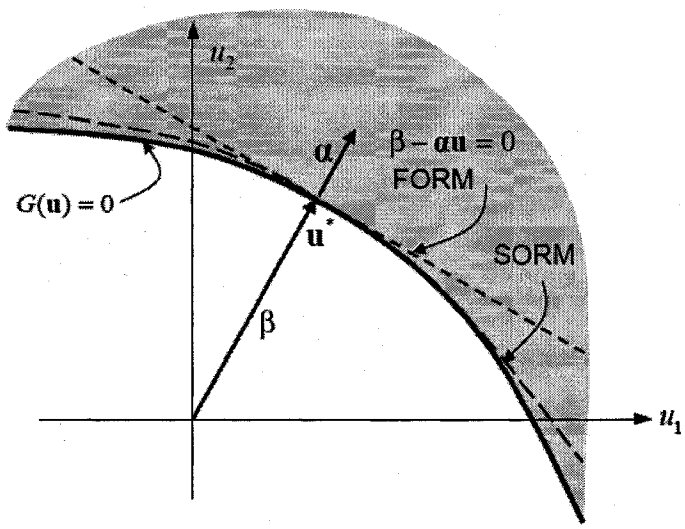

Figure 7.3 FORM and SORM approximations for a component problem

7.2.3. Advanced mean value (AMV) method

A practical limitation on FORM and SORM is that the limit state function must have an explicit closed form. But there are many cases where a reliability analysis is required and the variables are related only through a numerical algorithm, e.g., finite element analysis.

A very efficient numerical algorithm has been developed by Wu (1990) for dealing with these complex problems. The AMV method is the 'heart' of a probabilistic finite element code (NESSUS) developed for NASA to solve complicated design problems associated with space propulsion systems.

7.3. STRUCTURAL SYSTEM RELIABILITY METHODS

The system failure probability is defined as the probability for a structure or a part of a structure to fail in one or several possible failure modes. While a component failure is defined by a single limit state function, a system failure is defined by several limit state functions. The main difference between a system and a component reliability problem is in the complexity of their failure surface. In structural reliability theory, the notions of components and systems do not necessarily correspond to physical components (e.g. beams, braces, etc.) and systems (structures). The component reliability deals with failures involving a single mode defined by a single limit state function. If the failure of an entire structure can be described by a single equation, the problem is one of component reliability. On the other hand, a structural element may fail in flexure or shear or buckling, or combinations thereof, and is to be considered a system for reliability analysis (De 1990).

7.3.1. Parallel system

A parallel system is the system that fails if all of its components fail. The probability of failure of a parallel system with n components described by the limit state functions $g_i(u)$, is given by

$$P_{f_P} = P(\bigcap_{i=1}^{n} g_i(u) \leq 0) \tag{7.10}$$

For a parallel system, an approximation to the failure surface is obtained by linearizing the components at the most likely failure point. The most likely failure point on the parallel system failure surface is u^*, see Figure 7.4. The g-functions that are equal to zero at this point are referred to as the active constraints. The components which are not active, are denoted as inactive. To further improve the approximation to the failure surface, the non-active g-function may be linearized in succession. The linearization point of an inactive component is the point of maximum likelihood on the part of the component boundary that intersects the system surface defined by the previous linearizations, see point u^*_h in Figure 7.4 (Bjerager 1989).

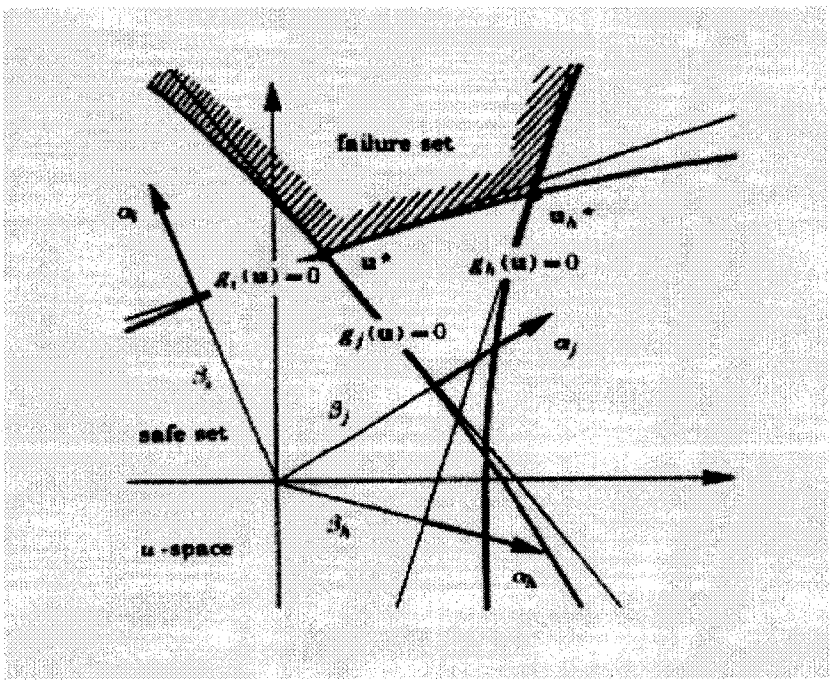

Figure 7.4 Parallel systems of n = 3 components

A FORM approximation to the failure probability is obtained by taking the probability content in the failure area limited by the linearized tangent hyperplanes for the components. The components can be linearized as

$$g_i(u) \approx \beta_i + \alpha_i^T u \tag{7.11}$$

Defining $Z_i = \alpha_i^T u$, then Z_i is a standard normal variable with correlation ρ_{ij} to Z_j and P_{f_P} can be approximated as

$$P_{f_P} \approx P(\bigcap_{i=1}^{n} Z_i \le -\beta_i) = \Phi_n(-\beta, R) \tag{7.12}$$

where

Φ_n : the n-dimensional standard cumulative distribution function.

β: the vector of β_i for the components.

R: the matrix of correlation coefficients defined by $R = \rho_{ij} = \alpha_i^T \alpha_j$.

The evaluation of failure probability is then reduced to evaluation of the cumulative probability of the multi-normal integral (Madsen, et al 1986).

7.3.2. Series system

A series system is the system that fails if any of its components fails. The probability of failure of a series system with n components described by the limit state functions $g_i(u)$, is given by

$$P_{f_S} = P(\bigcup_{i=1}^{n} g_i(u) \le 0) \tag{7.13a}$$

An example of n = 3 of a series system is shown in Figure 7.5 (Bjerager 1989), in which each partial failure surface corresponding to the components of the series system is approximated individually. The probability of the union of n components is expressed in terms of the intersection of the complementary events as

$$P_{fs} = 1 - P(\bigcap_{i=1}^{n} g_i(u) > 0) \tag{7.13b}$$

Each failure surface $g_i(u)$ is approximated by a hyperplane and the P_{fs} is then computed by using the multi-normal cumulative distribution function

$$P_{fs} = 1 - \Phi_n(\beta, R) \tag{7.13c}$$

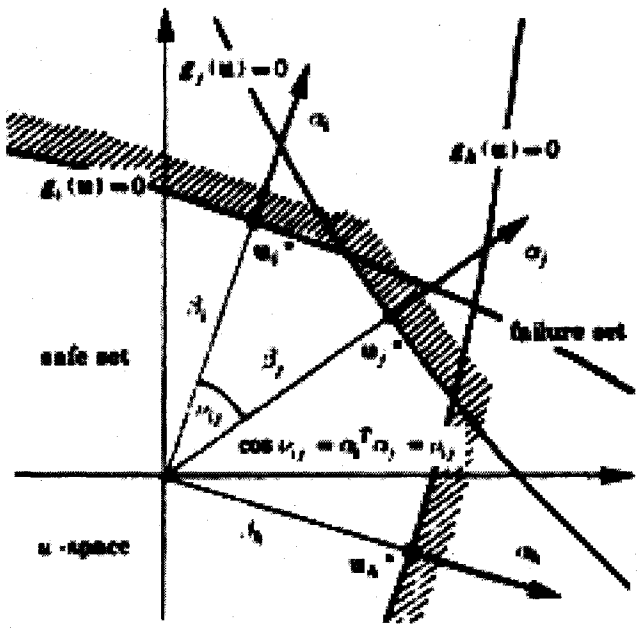

Figure 7.5 Series systems of n = 3 components

Alternatively, for series systems the probability of failure can be calculated by second order probability bounds (Ditlevsen 1979).

7.3.3. General system

A general system is the system that fails if certain subsets of components fail. The probability of failure of a general system with n components described by the limit state functions $g_i(u)$, is given by

$$P_{f_G} = P(\bigcup_{k} \bigcap_{j \in c_k} g_k(u) \leq 0) \tag{7.14}$$

where

C_k: the k-th cut set of components whose joint failure constitutes failure of the system.

For a parallel system, all components form a single cut set.

For a series system, each component is a cut set.

7.4. MONTE CARLO SIMULATION (MCS)

The conceptually simplest way to estimate the probability of failure P_f is to use Monte Carlo simulation (Rubinstein 1981). The simulation is carried out by generating n independent outcomes from the joint probability density function $f_X(x)$. For each outcome x_i, $g(x_i)$ is evaluated and if $g(x_i) <= 0$ it is counted as a "hit". The ratio of the number of hits to the total number of outcomes is used as an estimate of P_f, i.e. the failure probability can be written as

$$\begin{aligned} P_f &= \int_{g(x)\leq 0} f_X(x)dx = \int_{allx} I\{g(x) \leq 0\} f_X(x)dx \\ &= E[I\{g(x) \leq 0\}] = \lim_{n\to\infty} \frac{1}{n} \sum_{i=1}^{n} I\{g(x_i) \leq 0\} \end{aligned} \tag{7.15}$$

where

$$I\{g(x_i) \le 0\} = \begin{cases} 0 & g(x_i) > 0 \\ 1 & g(x_i) \le 0 \end{cases}$$

The estimator for the failure probability is defined by

$$\hat{P}_f = \frac{1}{n}\sum_{i=1}^{n} I\{g(x_i) \le 0\} \tag{7.16}$$

An estimator for the variance to this estimator is given by (if P_f is small)

$$Var(\hat{P}_f) = \frac{P_f(1-P_f)}{n} = \frac{P_f}{n} \tag{7.17}$$

Since the failure probability for structural problems is generally small, a large number of outcomes have to be generated to get a sufficient number of outcomes in the failure region. For example, if the failure probability is 10^{-4}, and the coefficient of variation of the estimated failure probability is required to be less than 10%, n = 10^6 outcomes are needed.

7.5. PROGRAMS FOR STRUCTURAL RELIABILITY ANALYSIS

Mansour et al. (1997) did a literature search, and identified algorithms, of various levels of sophistication, that would be appropriate for ship structure reliability analysis.

CalREL

This is a general purpose structural reliability analysis program. Its capabilities include: (a) probability of failure estimates for component reliability problems, (b) probability of failure estimates for system reliability problem, (c) FORM and SORM analysis, (d) direct Monte Carlo analysis and directional simulation, (e) sensitivity analysis.

PROBAN

It is general structural reliability analysis code, developed and marketed by Det norske Veritas. It is more sophisticated than CALREL, and it is also much more expensive.

COMPASS

This code is developed, maintained, and marketed by Martec Limited, Canada. It is also a general purposed software reliability analysis program.

RELACS

It is developed and distributed by Risk Engineering, Inc. This program, also sophisticated and expensive, is intended to be a competitor to PROBAN.

University of Arizona Software

There are a number of small programs that are likely to be useful in performing reliability analysis. These include: (a) DISTS: determines which of several competing statistical distributions best fits a set of data; (b) POFAIL: produces exact probability of failure calculations for a limit state with only two random variables; (c) RACA: computes safety index and probability of failure using the Hasofer-Lind, Chen-Lind, or Rackwitz-Fiessler algorithms; (d) Wu/FPI: computes the safety index and probability of failure using second order reliability analysis. The Wu/FPI can be conveniently combined with a limit state analysis program (e.g. finite element program) to execute the Advanced Mean Value Method.

ABS

This is a general-purpose structural reliability program. Its capabilities include computation of probabilities of failure for components based on first order reliability method (FORM).

NESSUS

The NESSUS code is developed at Southwest Research Institute under contact with NASA/Lewis to produce a probabilistic structural analysis code having both nonolinear structural behavior and dynamic response capacities. This code, having all of the reliability features of CalREL, is linked to a structural analysis (finite element) program. The core of the NESSUS code is the Advanced Mean Value (AMV) reliability algorithm that allows fast reliability analysis of complicated structural systems. It has a simulation capability using adaptive sampling.

CalREL has been used for the advanced reliability analysis required in this work. CalREL incorporates four general techniques for computing the probability (Liu, et al., 1989):

1) First-order reliability method (FORM), where the limit-state surfaces are replaced by tangent hyper-planes at design points in a transformed standard normal space;
2) Second-order reliability method (SORM), where the limit-state surfaces are replaced by hyper-paraboloids by either curvature fitting or point fitting in the standard normal space;
3) Directional simulation with exact or approximate surfaces:
4) Monte Carlo simulation

In addition to the above, CalREL has routines for computing reliability sensitivity measures with respect to parameters defining probability distribution functions or limit-state functions.

FORM and SORM are applicable to component reliability analysis, FORM is applicable to series system reliability, directional simulation in conjunction with FORM or SORM is applicable to component or system reliability analysis, and Monte Carlo simulation is applicable to all classes of problems.

CalREL has a modular structure with each group of analysis routines contained in a separate module. To run CalREL, it is necessary to compile the user-defined subroutines UGFUN, UGDX and UDD (and other user-provided routines called by these subroutines), and link them with the object modules of CalREL.

CalREL has a large library of probability distributions that can be used for independent as well as dependent random variables. Table 7.2 lists the probability distributions that are currently available. Table 7.3 lists the mean and standard deviation of CalREL library distributions. These distributions can be used both as marginal and conditional. Additional distributions can be included through a user-defined subroutine, UDD.

distribution name	id	PDF, $f_x(x)$	CDF $F_x(x)$	Parameters				Note
				p_1	p_2	p_3	p_4	
Normal	1	$\frac{1}{\sqrt{2\pi}\sigma}\exp\left[-\frac{1}{2}(\frac{x-\mu}{\sigma})^2\right]$	$\Phi\left[\frac{x-\mu}{\sigma}\right]$	μ	$0<\sigma$			1
lognormal	2	$\frac{1}{\sqrt{2\pi}\zeta x}\exp\left[-\frac{1}{2}(\frac{\ln x-\lambda}{\zeta})^2\right]$	$\Phi\left[\frac{\ln x-\lambda}{\zeta}\right]$	$0<\lambda$				1
Gamma	3	$\frac{\lambda(\lambda x)^{k-1}}{\Gamma(k)}\exp(-\lambda x),\quad 0\le x$	$\frac{\Gamma(k,\lambda x)}{\Gamma(k)}$	$0<\lambda$				2,3
Shited exponential	4	$\lambda\exp[-\lambda(x-x_0)],\quad x_0\le x$	$1-\exp(-\lambda(x-x_0))$	$0<\lambda$				
Shited Rayleigh	5	$\frac{(x-x_0)}{\alpha^2}\exp\left[-\frac{1}{2}(\frac{x-x_0}{\alpha})^2\right]$	$1-\exp\left[-\frac{1}{2}(\frac{x-x_0}{\alpha})^2\right]$	$0<\alpha$				
Uniform	6	$\frac{1}{b-a},\quad a\le x\le b$	$\frac{x-a}{b-a}$	a	b			
Beta	7	$\frac{(x-a)^{q-1}(b-x)^{r-1}}{B(q,r)(b-a)^{q+r-1}},\quad a\le x\le b$		$0<q$	$0<r$	a	b	4
Type I largest value	11	$\alpha_0\exp[-\alpha_0(x-u_0)-\exp(-\alpha_0(x-u_0))]$	$\exp[-\exp(-\alpha_0(x-u_0))]$	u_0	$0<\alpha_0$			5
Type I smallest value	12	$\alpha_1\exp[\alpha_1(x-u_1)-\exp(-\alpha_1(x-u_1))]$	$1-\exp[-\exp(-\alpha_1(x-u_1))]$	u_1	$0<\alpha_1$			
Type II largest value	13	$\frac{k}{u_0}\left(\frac{u_0}{x}\right)^{k-1}\exp\left[-\left(\frac{u_0}{x}\right)^k\right],\quad 0<x$	$\exp\left[-\left(\frac{u_0}{x}\right)^k\right]$	u_0	$0<k$			
Type III smallest value	14	$\frac{k}{u_1-\varepsilon}\left(\frac{x-\varepsilon}{u_1-\varepsilon}\right)^{k-1}\exp\left[-\left(\frac{x-\varepsilon}{u_1-\varepsilon}\right)^k\right],\ \varepsilon\le x$	$1-\exp\left[-\left(\frac{x-\varepsilon}{u_1-\varepsilon}\right)^k\right]$	u_1	$0<k$			

Note 1. $\Phi(x)=\frac{1}{2\pi}\int_{-\infty}^{x}\exp\left(-\frac{u^2}{2}\right)du$ is the standard normal cumulative probability.

2. $\Gamma(k)=\int_0^\infty e^{-u}u^{k-1}du$ is the gamma function. For integer k, $\Gamma(k)=(k-1)!$.

3. $\Gamma(k,x)=\int_0^x e^{-u}u^{k-1}du$ is the incomplete gamma function with $\Gamma(k,\infty)=\Gamma(k)$.

4. $B(q,r)=\Gamma(q)\Gamma(r)/\Gamma(q+r)$ is the beta function

5. This distribution is also know as the *Gumbel* distribution.

6. For $\varepsilon=0$, this distribution is known as the *Weibull* distribution.

Table 7.2 CalREL Probability Distribution Library

distribution name	mean	standard deviation
normal	μ	μ
lognormal	$\exp\left(\lambda+\frac{\zeta^2}{2}\right)$	$\exp\left(\lambda+\frac{\zeta^2}{2}\right)\left[\exp(\zeta^2)-1\right]^{1/2}$
gamma	$\frac{k}{\lambda}$	$\frac{\sqrt{k}}{\lambda}$
shifted exponential	$x_0+\frac{1}{\lambda}$	$\frac{1}{\lambda}$
shifted Rayleigh	$x_0+\left(\frac{\pi}{2}\right)^{1/2}\alpha$	$\left(2-\frac{\pi}{2}\right)^{1/2}\alpha$
uniform	$\frac{a+b}{2}$	$\frac{b-a}{2\sqrt{3}}$
beta	$a+\frac{q(b-a)}{q+r}$	$\frac{b-a}{q+r}\left(\frac{qr}{q+r+1}\right)^{1/2}$
type I largest value	$u_n+\frac{0.5772}{\alpha_n}$	$\frac{\pi}{\sqrt{6}\alpha_n}$
type I smallest value	$u_1-\frac{0.5772}{\alpha_1}$	$\frac{\pi}{\sqrt{6}\alpha_1}$
type II largest value	$u_n\Gamma\left(1-\frac{1}{k}\right)$	$u_n\left[\Gamma\left(1-\frac{2}{k}\right)-\Gamma^2\left(1-\frac{2}{k}\right)\right]^{1/2}$
type III smallest value	$\varepsilon+(u_1-\varepsilon)\Gamma\left(1+\frac{1}{k}\right)$	$(u_1-\varepsilon)\left[\Gamma\left(1-\frac{2}{k}\right)-\Gamma^2\left(1-\frac{2}{k}\right)\right]^{1/2}$

Table 7.3 Mean and Standard Deviation of CalREL Library Distributions

7.6. ULTIMATE LIMIT STATE

For hull girder collapse, the vertical bending moment is a primary load component. A limit state function for the ultimate collapse of the hull girder under vertical bending moment (considering yielding and buckling) is now formulated taking into account

corrosion and fatigue cracking damage effects on structural properties of primary members.

$$g(X) = M_u - [M_{sw} + k_w(M_w + k_d M_d)] \tag{7.18}$$

where M_u is ultimate strength of hull girder, which is introduced in Chapter 5 in details. M_{sw}, M_w and M_d are stillwater bending moment, wave-induced bending moment and dynamic moment, respectively. k_w is the combination factor between wave-dynamic composite moments and stillwater moment. k_d is the combination factor between wave-induced moment and dynamic moment.

The Mansour's box girder model II that has been used in Chapter 5 is utilized herein to present the time-dependent reliability assessment. It is needed to mention that the example presented here is only for demonstration purpose. All the load values are assumed, not from the real measurements. A real vessel illustration example will be presented in Chapter 9.

Variable	Mu	Msw	Mw	Md	kw	kd
Distribution	Lognormal	Normal	Ext. Value	Ext. Value	Normal	Normal
Mean	141.12	14.50	46.12	9.22	1.00	0.70
Std. Dev.	14.112	2.18	4.612	2.77	0.05	0.105
Note: All bending moment values are in units of 10^4 Nm						

Table 7.4 Statistics of the input variables for the sample case

Table 7.4 shows the statistics of the input variables for the sample case, where M_u is the ultimate moment capacity without any degradation. Figure 7.6 and Figure 7.7 show the time-dependent safety indexes and probabilities of failure of the Mansour's box girder model II. Age related degradations, i.e., corrosion and fatigue crack, are considered. Meanwhile, no degradation case is also computed for comparison purpose.

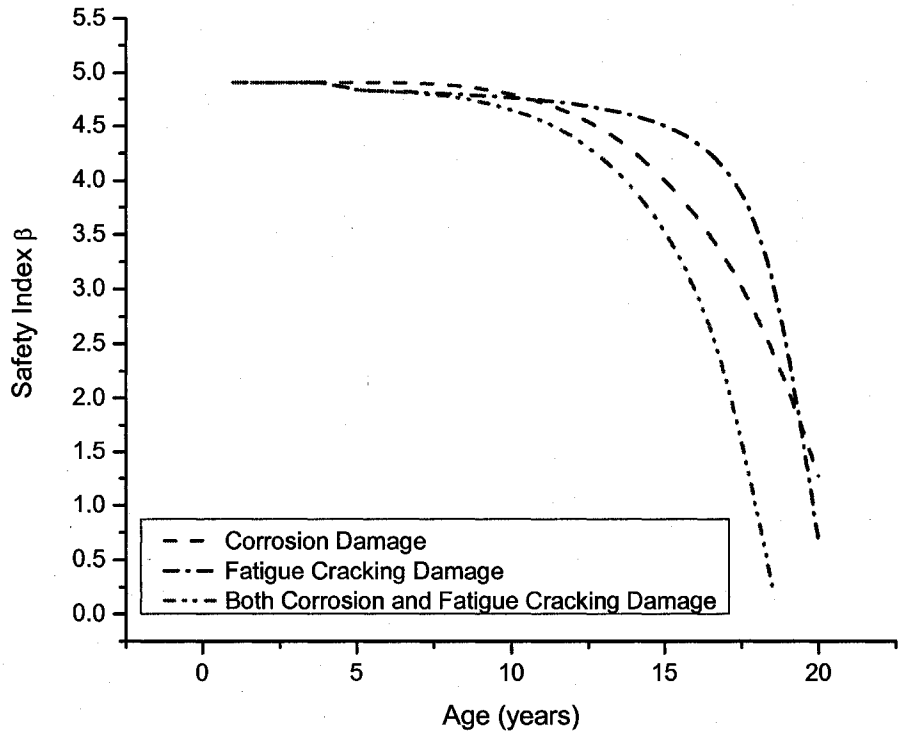

Figure 7.6 Time-dependent reliability of Mansour's box girder model II against hull girder collapse in hogging condition

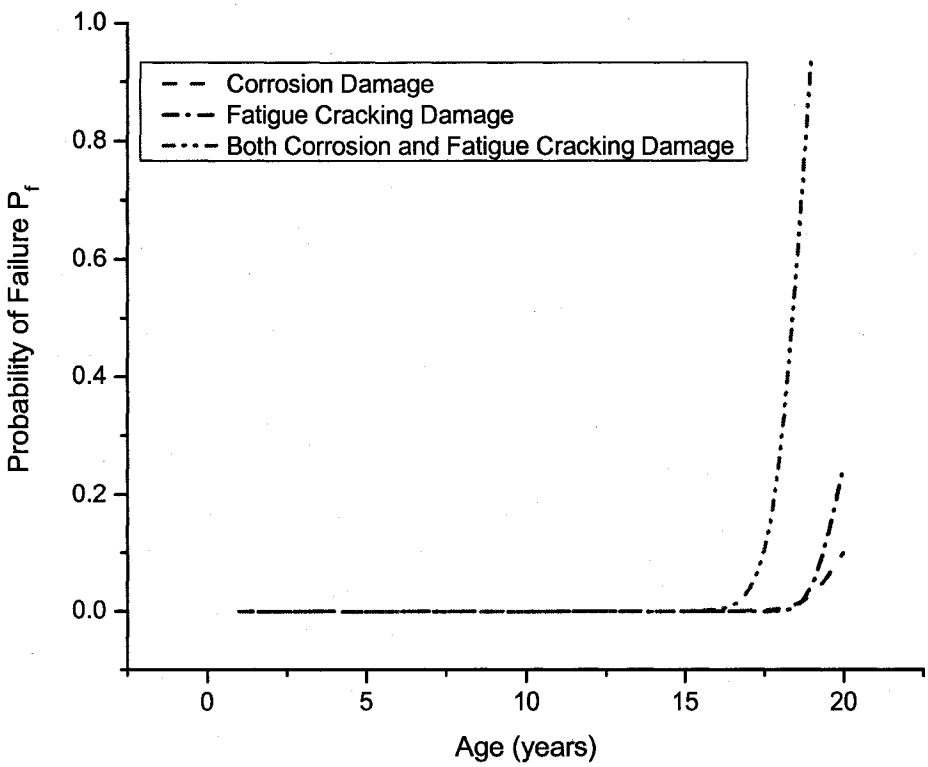

Figure 7.7 Time-dependent risk (probability of failure) of Mansour's box girder model II against hull girder collapse in hogging condition

7.7. SENSITIVITY ANALYSIS

Sensitivity analysis is an important part of structural reliability assessment. One benefit of sensitivity analysis is to identify the model parameters that have the most effect on the calculated safety index. The other benefit is to be able to identify those parameters that can be taken as fixed values need not be considered as random variables.

Basically, there are four important sensitivity measures for each random variable defined in Table 7.5. In these equations, $\mathbf{x}^*$ and $\mathbf{u}^*$ are the coordinates of the design point in the original and standard-normal (transformed) spaces, respectively. β is the safety index. μ and σ are mean and standard deviation for each random variable, respectively.

$\alpha_i = \frac{\partial \beta}{\partial u_i^*}$	$\gamma_i = \frac{\partial \beta}{\partial x_i^*}$	$\delta_i = \sigma_i \frac{\partial \beta}{\partial \mu_i}$	$\eta_i = \sigma_i \frac{\partial \beta}{\partial \sigma_i}$

Table 7.5 Sensitivity factors

The first two parameters, α and γ, known as "important factors" are a measure of the relative importance of each of the random variables, i.e., how much weight each has in the determination of the safety index. These two parameters are always numerically equal, so either one can be used for analysis. The other two parameters, δ and η, are measures of the sensitivity of the safety index to changes in the mean value and standard deviation of the random variable, respectively. A more in-depth treatment of sensitivity factors can be found in Mansour and Wirsching (1995).

CalREL provides the four important sensitivity measures in the output file. For the internally defined distributions, all four sensitivity factors (α, γ, δ and η) are tabulated for each variable. For user-defined distributions, only α and γ are provided in CalREL. But it can instruct CalREL to perform a separate sensitivity analysis in order to determine δ and η (Liu et al. 1989 and Mansour et al. 1997)

Variable	x*	u*	α	γ	δ	η
M_u	107.5	-2.68	-0.5442	-0.5442	0.6959	-1.5039
M_s	15.69	0.55	0.1106	0.1106	-0.1106	-0.0603
M_w	79.44	3.88	0.7903	0.7903	-0.2468	-1.7828
M_d	10.46	0.61	0.1215	0.1215	-0.1083	-0.0487
k_w	1.05	1.09	0.221	0.221	-0.221	-0.2401
k_d	0.73	0.29	0.0588	0.0588	-0.0588	-0.0173

Table 7.6 Sensitivity measures for the sample case

The sample case of the Mansour's box girder model II is used again herein to present the sensitivity analysis. Table 7.6 shows the sensitivity data for the sample case for time equals to zero. The absolute values of the importance factors (α) for each of the different variables provides some insight into the relative weight that each one has in determining the final reliability of the structure. For this sample case, the most critical variable is the wave-induced bending moment, M_w, with an important factor $\alpha = 0.7903$. Right behind this is the ultimate strength, M_u, with an important factor $\alpha = 0.5442$. It is clear that the remaining variables are much less important. Thus, the ultimate strength and the wave loads will dominate this failure mode. From Table 7.6, it is also confirmed that two parameters, α and γ, are numerically equal, so either one can be used for analysis.

Another way to look at the relative impact of the different variables is by examining the sensitivity to the coefficient of variation (η). If a variable has a small value of η, then

assuming that it is a deterministic constant will have a small impact on the probability of failure estimate. By looking for variables with small values of η, one can determine which, if any, of the random variables in the system can be taken as deterministic. In this way, complexity of the mathematical reliability problem can be greatly simplified. It is especially useful for large system reliability problems. For the sample case, the stillwater bending moment and dynamic moment have very small values, which implies that no much accuracy would be lost in assuming that they are deterministic.

8. INSPECTIONS AND REPAIR SCHEME

To avoid total loss caused by any potential hull girder collapse, and to efficiently keep the ship's safety and reliability higher than a critical level, a proper and cost-effective scheme of inspections and repair must be established (TSCF 1997).

Inspections are routinely made for structures in service. In practice, if any member is corroded and/or cracked more than specific amount, it would be normally renewed to maintain the structural safety and reliability at an acceptable level.

It is assumed that the initial thickness of ship structures is the sum of minimum net thickness and the maximum allowable corrosion wastage

$$t = t_{\min} + t_{\max,c} \tag{8.1}$$

where

t: initially intact thickness

t_{min}: minimum net thickness

$t_{max,c}$: maximum allowable corrosion wastage

Through routine inspections, t_{min} is the criteria that whether repair should be performed. If the plate thickness is found to be less than t_{min}, or the corrosion wastage is going to be greater than $t_{max,c}$ at the next inspection time, the plate should be replaced by new one with a thickness equal to its original value.

It is also assumed that when the crack length has propagated to a maximum allowable crack size, it will be repaired.

$$c(t) \geq c_{max,c} \tag{8.2}$$

where

c(t): crack length

$c_{max,c}$: maximum allowable crack size

After repair, the dimensions of the structure element will be restored to the original state.

8.1. CORROSION INSPECTION AND REPAIR

From Equation 8.1, we can see the maximum allowable corrosion wastage, $t_{max,c}$ is very important, which determines not only the repair time, but also the repair cost to some extent. The parameter is needed to be determined carefully, and this is not trivial work. In this study, two strength-base criteria are used, namely, global strength-based criteria and local strength-based criteria (Paik et al., 2003).

Globally, the ultimate moment capacity of hull girder has a minimum allowable value, M_{Ua}, to resist the external bending moment (i.e. stillwater bending moment, wave-induced bending moment, and dynamic moment). Locally, the ultimate strength of each element has a minimum allowable ultimate strength, σ_{ua}, to resist the local loads. When the ultimate moment of hull girder has degraded to the minimum allowable value, M_{Ua}, or the ultimate strength for each element has degraded to the minimum allowable ultimate

strength, σ_{ua}, the ship hull should be repaired. The level of repair depends on many issues. Basically, it includes:

1) How much the strength has been degraded, in the other word, how much the strength should be improved.
2) How long the repaired ship can be used before the ultimate strength degrades to the minimum allowable values, globally or locally.
3) The repair cost.

In practice, the best scheme is to use the least money to get the longest period before the ship needs to be repaired again. Therefore, there are some related important repair indicators. The repair area, A_r, can be treated as one of the factors that determine the repair cost. The time period, T_r, is defined from repair instant to the instant that the ultimate moment degrades to M_{Ua} again. So the goal is to repair a small area, A_r, and to obtain a longer period, T_r. Thus, A_r/T_r is one of the important repair indicators.

Meanwhile, the minimum allowable ultimate moment, M_{Ua}, and the minimum allowable local ultimate strength, σ_{ua}, are the other two important repair indicators. The IACS requires to keep the longitudinal strength of an aging ship at the level of higher than 90% of the initial state of the new-build ship. While the IACS requirement is in fact based on the ship's section modulus, it is in the present study applied for establishing the repair schemes so that the minimum allowable ultimate moment, M_{Ua}, is 90% of the ultimate moment of the original hull girder. The minimum allowable local ultimate strength, σ_{ua}, is simply assumed as 80% of initial local ultimate strength.

8.2. CRACK INSPECTION AND REPAIR

The purpose of periodic inspections is also to detect the fatigue cracks. The inspection quality depends on detecting the crack and quantifying its size. From the preceding crack effect analysis, we can see that crack can cause the ultimate strength decrease dramatically when its size reaches the critical value, which could lead to catastrophic aftermath. This effect is more dangerous than corrosion in some circumstances. Because when the crack size is small the critical size, the ultimate strength degrades very slowing along the crack size increasing. However, when the crack size is get close to the critical size, even a very small amount increase of crack size could cause a big drop of the ultimate strength. Therefore the crack repair criteria should be generated with caution. In this study, there is a reduction factor applied to the critical crack size to calculate the maximum allowable crack size for conservativeness.

$$c_{\max,c} = Rc_{cr} \tag{8.3}$$

where

$c_{max,c}$: maximum allowable crack size

c_{cr}: critical crack length

R: reduction factor

In which c_{cr} can be determined according to Chapter 4. R is assumed to be 0.8 in this study. When the crack length propagates to be equal to or greater than the maximum allowable crack size, the element will be repaired, and restored to the original state.

9. APPLICATION

9.1. SHIP DATA

A double-hull tanker of 307,000 dwt is used to demonstrate the proposed ultimate strength reliability assessment methodology. The vessel is classed by American Bureau of Shipping. Figure 9.1 shows the scheme of the example vessel and frame arrangement. Table 9.1 gives the ship dimensions.

Item	Distance From AP(m)	Frame Location
0.3L From AP	133.054 m	#75 + 0.254 m
Midship	195.35 m	#87 + 3.15 m
0.7L From AP	257.646 m	#100 + 1.096 m
0.125L From FP	312.155 m	#143 + 0.455 m
FP	351.09 m	#192 + 0.19 m

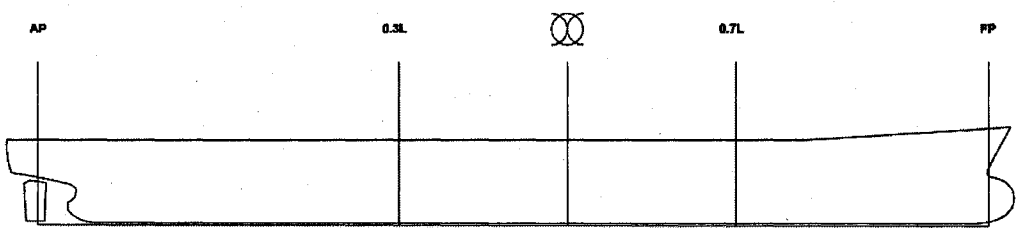

Figure 9.1 Scheme of the example ship and frame arrangement

Length between Perpendiculars (LBP):	351.09 (m)
Scantling Length (Ls):	311.48 (m)
Breadth (B):	58 (m)
Depth (D):	31.8 (m)
Draft (d):	22.85 (m)
Speed (Vd):	15.3 (knots)
Block Coefficient (Cb):	0.83

Table 9.1 Example ship dimensions

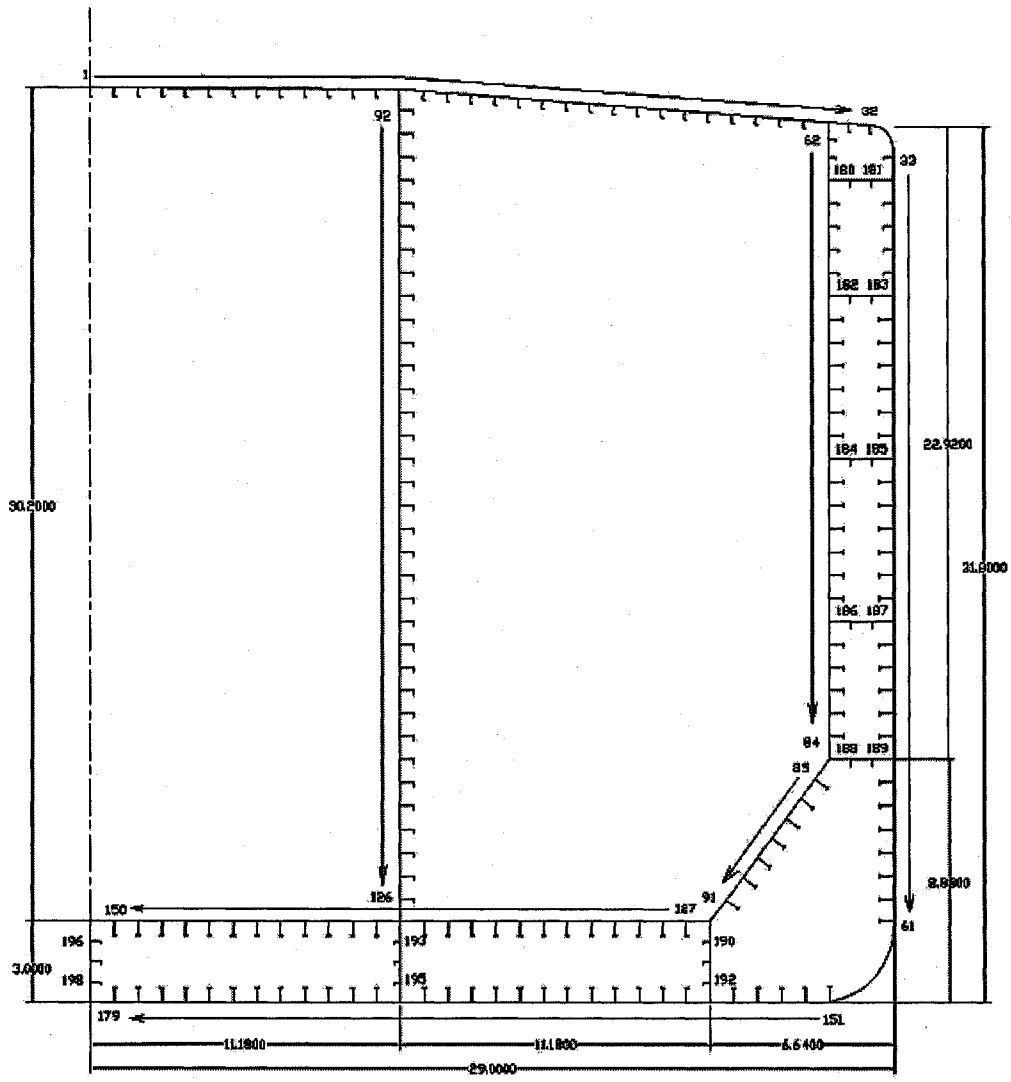

Figure 9.2 Half of midship section of a double-hull tanker with element group members

The midship section of the ship is divided into 392 stiffened panels. Figure 9.2 shows the half of the midship section with element group numbers on it. The dimensions of each element are shown in Table 9.2. The distance between transversal frames is 4950 mm.

Element	Plating			Stiffener				
No.	b_p(mm)	t_p(mm)	σ_Y(MPa)	h_w(mm)	t_w(mm)	b_f(mm)	t_f(mm)	σ_Y(MPa)
1-19	860	17.5	315	300	13	90	17	315
20-30	860	17.5	315	350	12	100	17	315
31-32	780	18.5	315	300	13	90	17	315
33-37	840	18	315	350	12	100	17	315
38-43	840	20	235	450	11	150	14	235
44-49	840	20	235	500	11	150	19	235
50-54	840	20	235	500	11	150	25	235
55-58	840	20	235	450	11	150	28	315
59-61	840	20	235	500	11.5	150	25	315
62-63	630	17	315	250	12	90	16	315
64-67	840	15.5	315	350	12	100	17	315
68-73	840	15	235	450	11	150	14	235
74-79	840	16.5	235	500	11	150	19	235
80-84	840	19	235	500	11	150	25	235
85-86	880	23	235	450	11	150	28	315
87-91	880	23.5	315	500	11.5	150	25	315
92-97	840	16	315	350	12	100	17	315
98-102	840	14.5	235	450	11	150	12	235
103-113	840	15.5	235	500	11	150	19	235
114-122	840	18	235	500	11	150	28	235
123-126	840	18	315	500	11.5	150	25	315
127-150	860	20	315	550	12	150	34	315
151-179	860	19	315	550	12	150	27	315
180-189	780	14	235	250	12.5	0	0	235
190-195	750	14	315	250	12	90	16	315
196-198	750	17	315	350	12	100	17	315

Table 9.2 Element dimensions and material properties

9.2. AGE-RELATED DEGRADATIONS

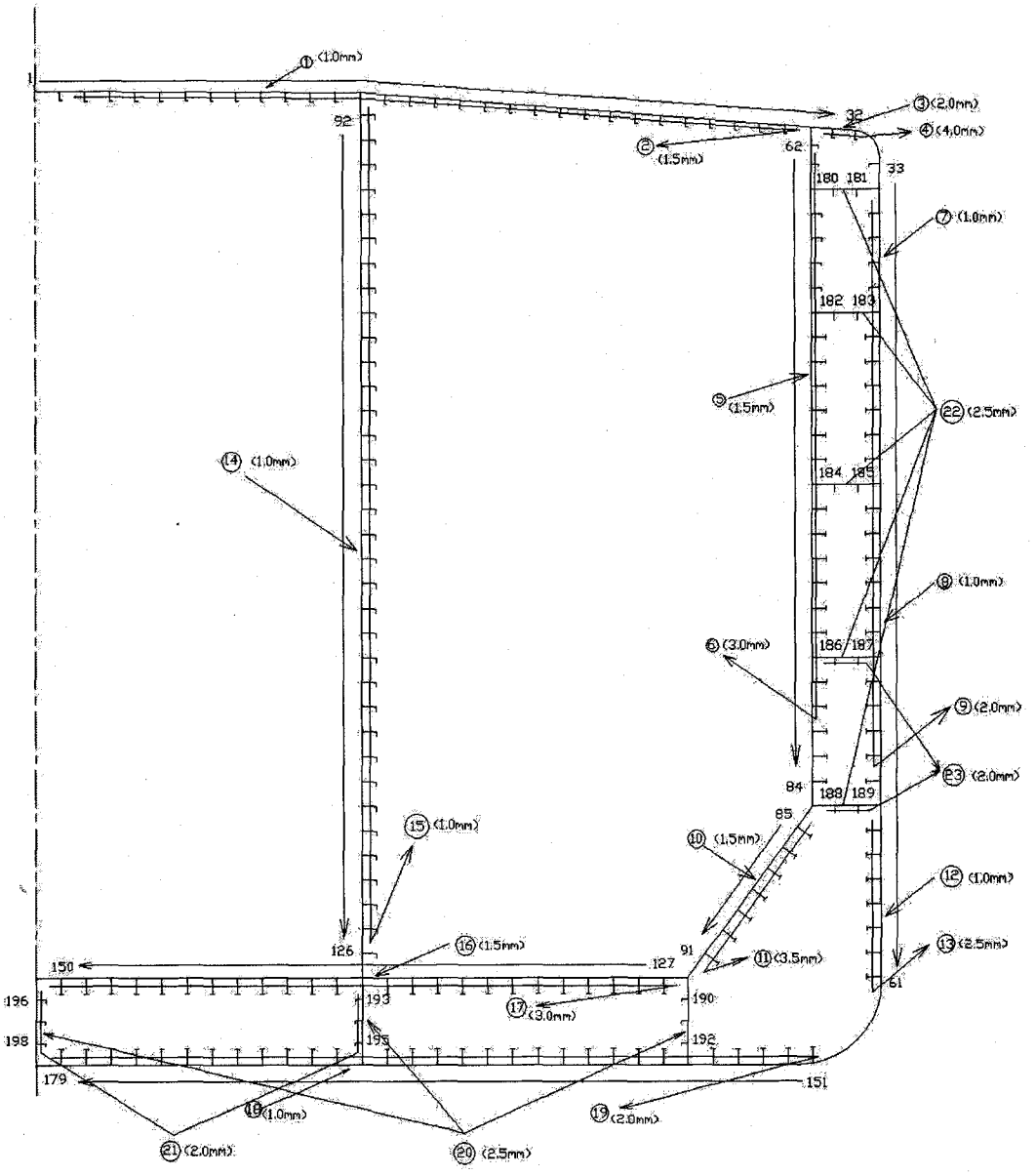

Figure 9.3 Half of midship section of a double-hull tanker with corrosion group numbers

For the ship hull, in different locations the elements are exposed to different environments, therefore the corrosion rates might be different. In this study, the midship section is divided into 23 corrosion groups according to different locations and different element members. The scheme is shown in Figure 9.3. The values in the parentheses after each corrosion group are the maximum allowable corrosion thicknesses. For one element the corrosion rates for plating and stiffener are different. But for one stiffener, the web and flange are usually exposed to a similar environment and the corrosion rates are very close, for simplicity, in this study the corrosion rates of web and flange are treated as same. Non-linear corrosion model is used to simulate the corrosion rate. The depth of corrosion wastage is assumed to follow Equations 2.11 proposed by Paik, et al (2003).

$$t_r = C_1(T - T_c - T_t)^{C_2}$$

For simplicity, the duration of transition time T_t is assumed to be zero, which means the corrosion starts right after the coating life is over, and parameter C_2 is proposed to be 0.8. The other corrosion model parameters for different corrosion groups are shown in Table 9.3 (Paik et al. 2003, ABS 2005).

It is assumed that all of the elements will be inspected properly. If the plate thickness is found to be less than minimum net thickness t_{min}, or the corrosion wastage is going to be greater than the maximum allowable corrosion wastage $t_{max,c}$ at the next inspection time, the plate should be replaced by new one with a thickness equal to its original value.

The amount and location of fatigue cracking damage at any point of time for a ship is generally unknown. It is in fact difficult to predict such damage in any particular case,

even with the benefit of fatigue life assessments, because of variability in both loading and fatigue capacity (Paik and Thayamballi, 2002).

Corrosion group	T_c		C_1	
	Mean	COV	Mean	COV
1	5	0.2	0.1326	0.3
2	5	0.2	0.1102	0.3
3	5	0.3	0.1132	0.5
4	5	0.3	0.3210	0.5
5	7.5	0.2	0.1735	0.2
6	7.5	0.2	0.3241	0.3
7	5	0.2	0.1043	0.3
8	7.5	0.2	0.1090	0.3
9	7.5	0.2	0.2127	0.3
10	7.5	0.3	0.1740	0.5
11	7.5	0.3	0.3310	0.5
12	7.5	0.2	0.1082	0.4
13	7.5	0.2	0.2206	0.5
14	7.5	0.2	0.1025	0.3
15	7.5	0.2	0.1010	0.3
16	5	0.2	0.1725	0.3
17	7.5	0.2	0.3182	0.3
18	10	0.2	0.1862	0.2
19	10	0.2	0.2837	0.2
20	7.5	0.2	0.2496	0.3
21	7.5	0.2	0.1985	0.3
22	7.5	0.2	0.2485	0.3
23	7.5	0.2	0.1976	0.3

Table 9.3 Corrosion model parameters for each corrosion group

In this study, it is assumed that cracking initiates at all stiffeners and plating after 5 years of the ship age. The initial crack size is considered to be 1.0 mm. While this presumed fatigue cracking damage scenario may not be very realistic, it is not completely meaningless for a preliminary investigation of the effect of cracking damage on the ultimate strength of ageing ships. If the crack length is found to propagate to be equal to or greater than the maximum allowable crack size $c_{max,c}$ at the next inspection time, the element will be repaired, and restored to the original state.

9.3. ULTIMATE STRENGTH OF SHIP HULL GIRDER

The developed equations in Chapter 5 have been used here to compute the time-dependent ultimate hull girder strength considering the age-related degradations, like corrosion or/and fatigue cracking damages. Figure 9.4 and Figure 9.5 show the time-dependent ultimate hull girder strength under hogging condition and sagging condition respectively.

In Figures 9.4 and 9.5, the IACS requirement is also pointed out. In this example, the renewal and repair criterion is based on the ultimate strength. The heavily degraded or damaged members are renewed or repaired to their original state immediately before the ultimate hull girder strength of the aged ship becomes a value smaller than 90% of that of the original ship.

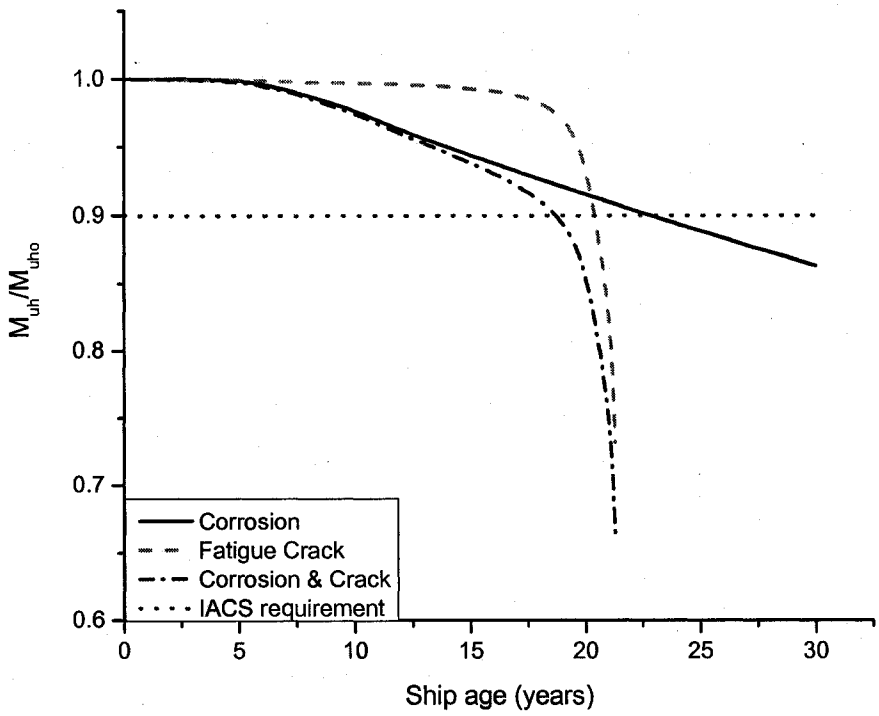

Figure 9.4 Time-dependent ultimate hull girder strength under hogging condition

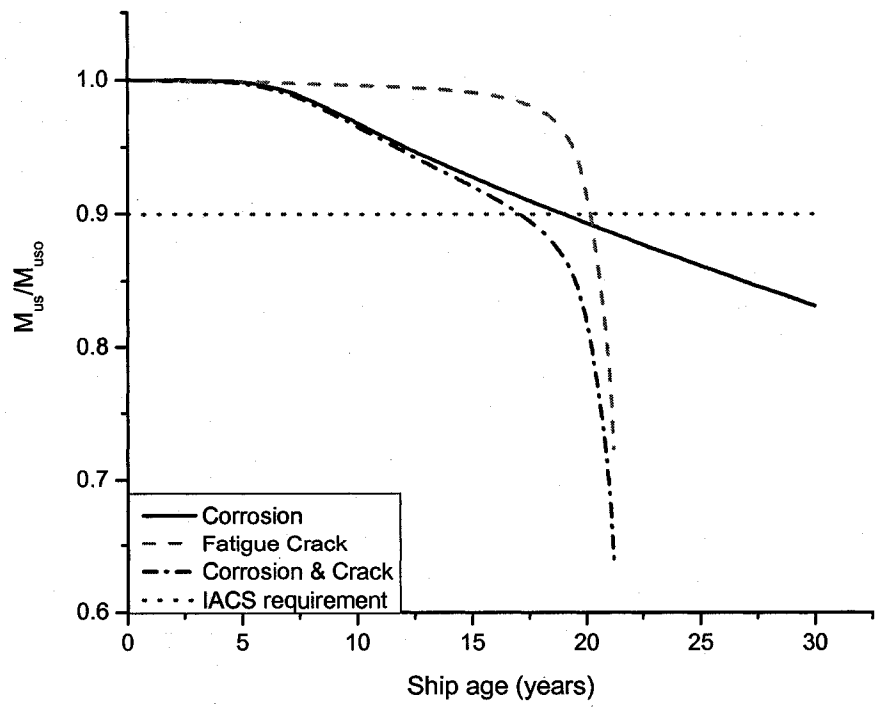

Figure 9.5 Time-dependent ultimate hull girder strength under sagging condition

9.4. REPAIR AND RENEWAL SCHEME

First, the effect of repairing different ship hull portions has been examined. For this tanker, sagging condition is the most dangerous condition. Therefore the sagging condition has been taken as the illustration condition to demonstrate the repair scheme and reliability analysis. Figures 9.6-9.8 show the effect of deck repair, sides repair, and bottom repair alone under sagging condition, respectively.

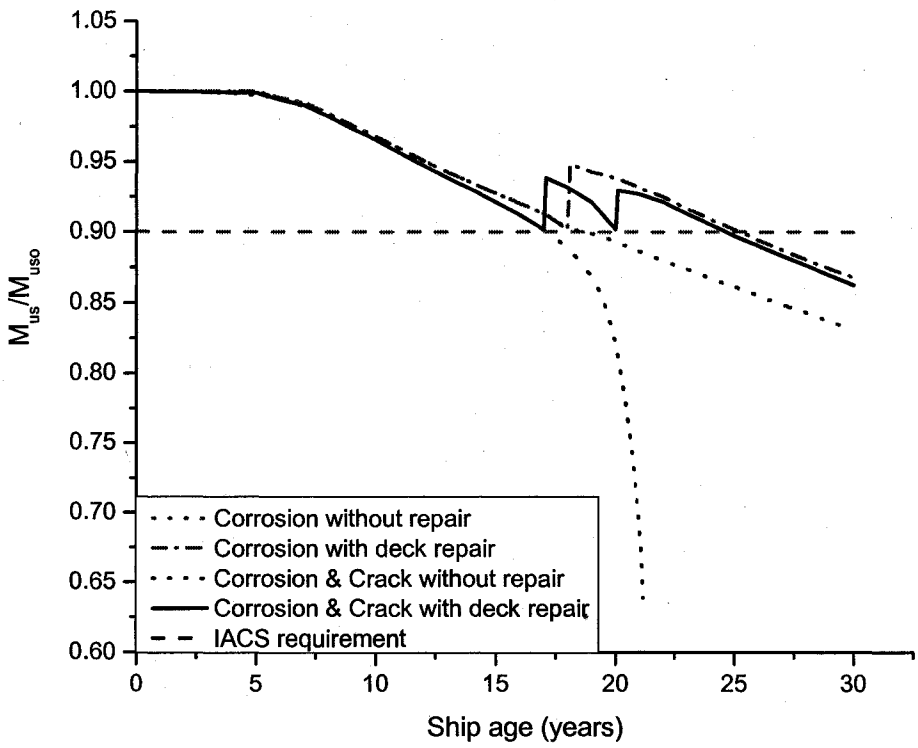

Figure 9.6 Time-dependent ultimate hull girder strength under sagging condition with repair of deck

From Figure 9.6, one can see renewing the deck can effectively approve the ultimate strength. However it is dropped quickly. The reason is that the fatigue cracking damage is dramatic when the cracking approaches the maximum allowable crack size. In this example as the ship age becomes between 21 and 22, the crack size gets close to the critical size. Then the ultimate strength drops quickly. Therefore all the cracks have to be repaired before it gets to the limits. For corrosion only, deck renewal is getting pretty good results, can extend the ship life almost 9 years.

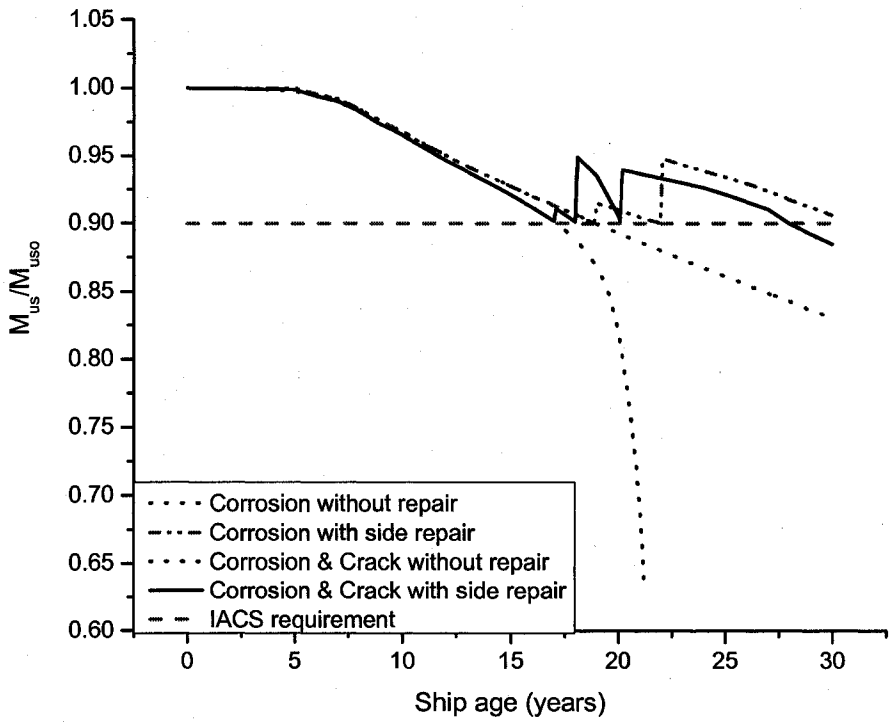

Figure 9.7 Time-dependent ultimate hull girder strength under sagging condition with repair of sides

Figure 9.7 gives the effects of repairing different sides, like inner skin bulkhead, side shell, and longitudinal bulkhead. For considering both corrosion and fatigue cracking

scenario, inner skin bulkhead has been renewed firstly. Obviously it cannot improve the strength well. Longitudinal bulkhead has been renewed subsequently. It improves the strength dramatically, but due to fatigue cracking damage the ultimate strength drops to criterion limit quickly. Therefore, cracks have been repaired and side shell has been renewed. For corrosion alone, again renewing inner skin bulkhead is not a good choice. But longitudinal renewal provides good outcome. 10 more years ship life is expected after the renewal.

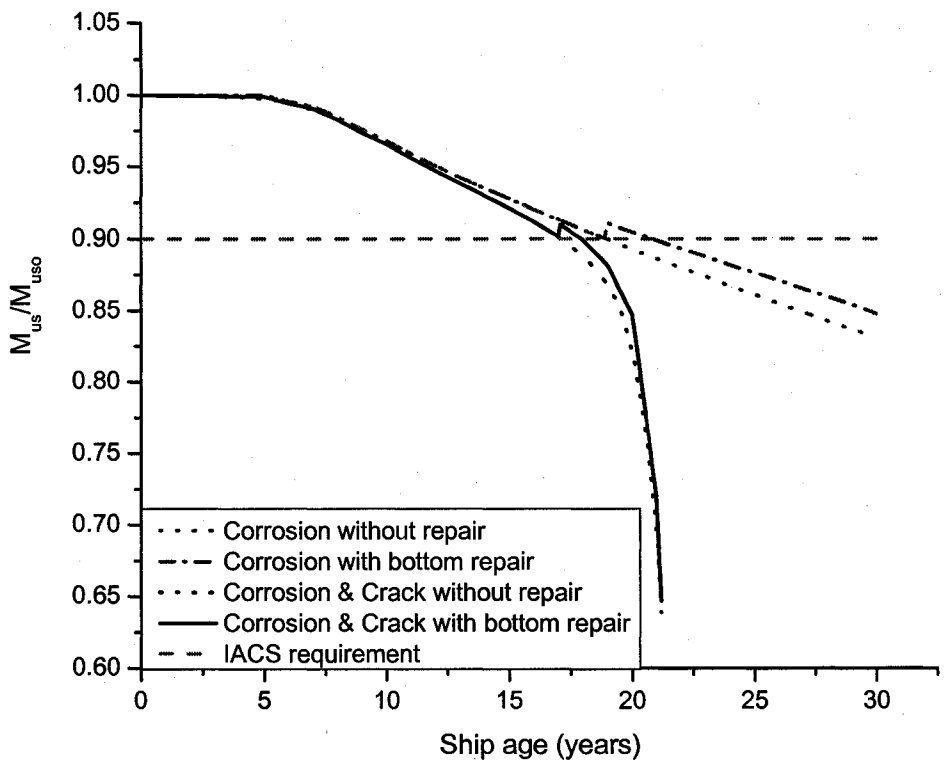

Figure 9.8 Time-dependent ultimate hull girder strength under sagging condition with repair of bottom

From Figure 9.8, renewing bottom seems have very little effect on the ultimate hull girder strength under the sagging condition for not only corrosion alone case but also the corrosion and fatigue cracking scenario.

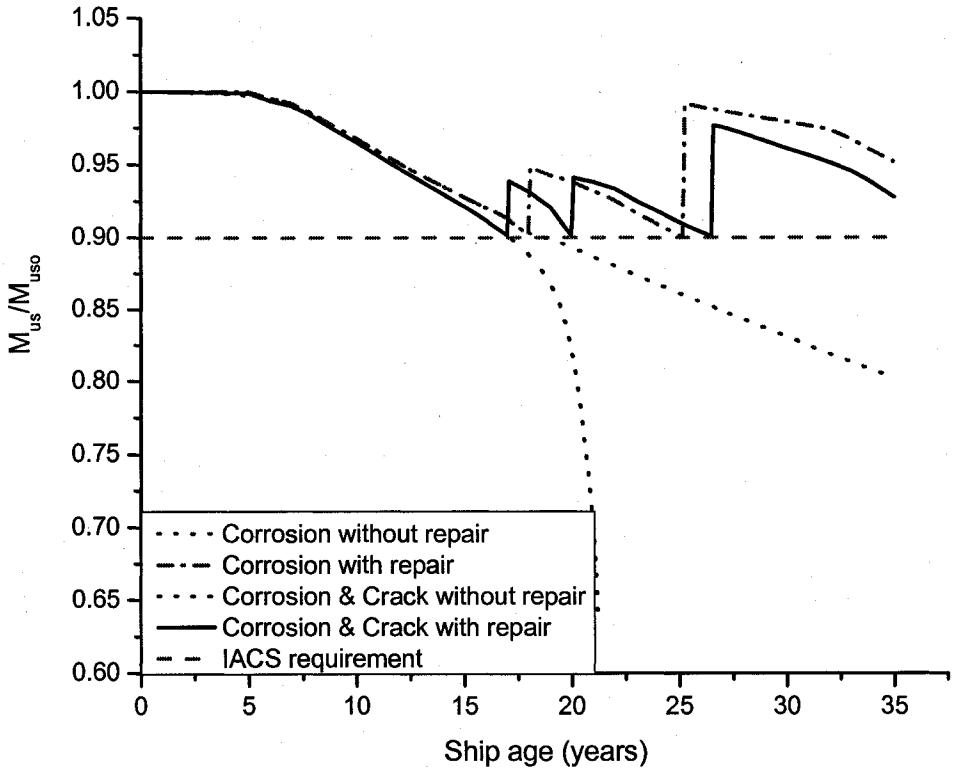

Figure 9.9 Time-dependent ultimate hull girder strength under sagging condition considering repair scheme

After examining the effect of repairing different portions of the ship hull alone, the repair and renewal scheme has been planned for the whole ship hull in order to optimize the repair or/and renewal action. Figure 9.9 shows the repair scheme and the time-dependent ultimate hull girder strength under sagging condition. In order to compare the corrosion and crack effects, corrosion only scenario has also been plotted in Figure 9.9. For both

cases, some members are needed to be renewed according to IACS requirement during ship age of 16-18 years, and 25-27 years, mostly because of corrosion damage. At about ship age of 21-22 years the ship hull is also needed to be repaired for fatigue cracking damage.

9.5. RELIABILITY ANALYSIS

Based on the calculated time-dependent ultimate strength, the time-dependent reliability analysis is performed thereafter. The ultimate limit state was given in Chapter 7 by Equation 7.18. It is given in the following for completeness.

$$g(X) = M_u - [M_{sw} + k_w(M_w + k_d M_d)]$$

Variable	Mu	Msw	Mw	Md	kw	kd
Distribution	Lognormal	Normal	Ext. Value	Ext. Value	Normal	Normal
Mean	198.94	44.38	91.76	18.35	1.00	0.70
Std. Dev.	19.894	6.657	9.176	5.506	0.05	0.105
Note: All bending moment values are in units of 10^8 Nm						

Table 9.4 Statistics of the input variables for the illustration example ship

Table 9.4 gives the statistics of the variables of the illustration example tanker for the reliability analysis. In which stillwater bending moment, M_{sw}, and wave-induced bending moment, M_w, have been computed according to ABS rules (ABS 2005). Dynamic

moment is taken a value of 20 percent of M_w (Mansour et al. 1997). The load combination factors are adopted from Mansour et al. (1997). The mean value of the ultimate hull strength is based on the new-built vessel.

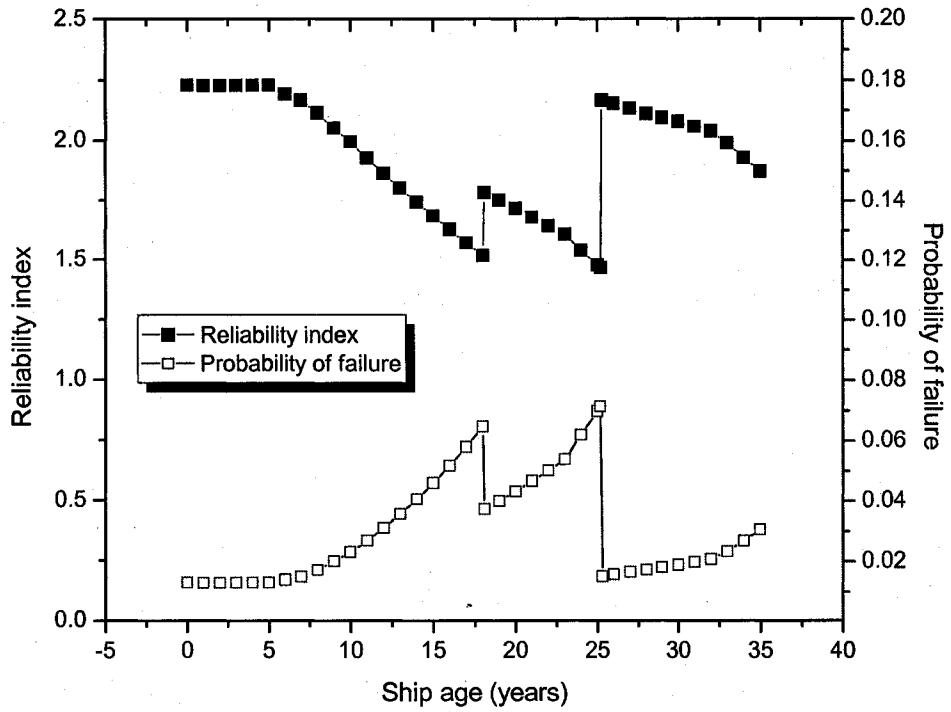

Figure 9.10 Repair scheme and resulting time-dependent reliability index of the example vessel in sagging condition considering corrosion damage

Figure 9.10 gives the repair scheme and resulting time-dependent reliability index and also probability of failure of the example vessel in sagging condition considering corrosion damage. It can be seen that during the ship age of 18 years and 25 years some tankers members much be renewed due to the corrosion damage.

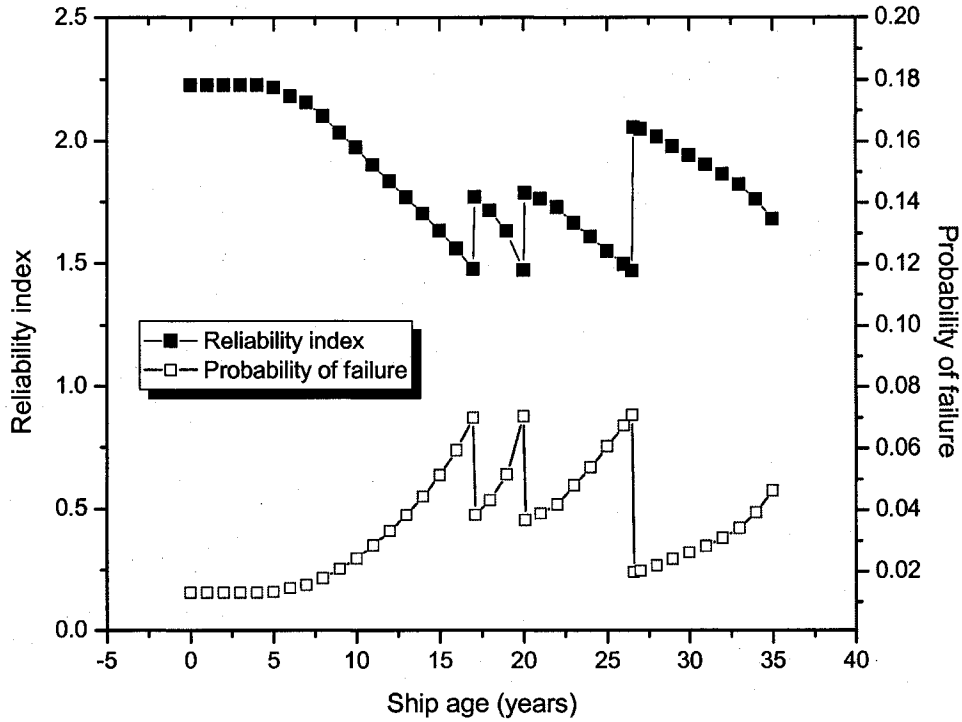

Figure 9.11 Repair scheme and resulting time-dependent reliability index of the example vessel in sagging condition considering corrosion and fatigue cracking damage

Figure 9.11 shows the repair scheme and resulting time-dependent reliability index of the example vessel in sagging condition considering corrosion and fatigue cracking damage. The tanker need to be repaired during the ship age of 17 years first according to the given conditions. Then at ship life of 21 years it is also needed to be repaired mostly because of fatigue cracking damage. Finally at ship age of 26 to 27 years most of members need to be renewed because of critical corrosion damage at that time for most of members.

Further, sensitivity analysis has been performed. Table 9.5 shows the sensitivity data for the illustration tanker when the ship age equals to zero. The absolute values of the

importance factors (α) for each of the different variables determine the relative weight that each one has in determining the final reliability of the structure. For this sample case, the most critical variable is the ultimate strength, Mu, with an important factor $\alpha = 0.709$. Right behind this is the wave-induced bending moment, Mw, with an important factor $\alpha = 0.564$. It is clear that the remaining variables are much less important. Thus, the ultimate strength and the wave loads will dominate this failure mode.

Variable	x*	u*	α	γ	δ	η
M_u	169.00	-1.59	-0.709	-0.709	0.830	-1.191
M_s	48.57	0.63	0.280	0.280	-0.280	-0.176
M_w	103.20	1.24	0.564	0.564	-0.397	-0.495
M_d	19.38	0.40	0.178	0.178	-0.172	-0.038
k_w	1.03	0.55	0.247	0.247	-0.247	-0.136
k_d	0.72	0.20	0.088	0.088	-0.088	-0.017

Table 9.5 Sensitivity measures for the illustration tanker

Another way to look at the relative impact of the different variables is by examining the sensitivity to the coefficient of variation (η). If a variable has a small value of η, then assuming that it is a deterministic constant will have a small impact on the probability of failure estimate. By looking for variables with small values of η, one can determine which, if any, of the random variables in the system can be taken as deterministic. In this way, complexity of the mathematical reliability problem can be greatly simplified. It is especially useful for large system reliability problems. For the illustration example, the dynamic moment has a very small value of η, which implies that no much accuracy would be lost in assuming that it is deterministic.

10. CONCLUDING REMARKS

10.1. SUMMARY AND CONCLUSIONS

Ships in service suffer various types of structural damage, especially age-related degradation, such as corrosion and fatigue cracking damages. In this work, the mathematical models for predicting corrosion as a function of ship age are reviewed and compared based on the sets of real vessel corrosion measurements. In addition, fatigue cracking mechanisms are also analyzed. Crack size prediction model as a function of ship age is developed in this study.

In order to investigate the ultimate strength reduction characteristics of unstiffened plates and stiffened panels due to pit corrosion, extensive numerical studies are carried out. The effects of fatigue cracks on the tensile and compressive ultimate strength of unstiffened plates and stiffened panels are also analyzed by the finite element method. Empirical equations are developed to estimate the ultimate strength of unstiffened plates and stiffened panels with pit corrosion or fatigue cracking damages based on the finite element analysis results. Using these equations, a modified simple formulation is proposed to predict the ultimate strength of ship hull girder considering the age-related degradations.

Structural reliability theory has been reviewed. A procedure is developed to quickly perform the reliability analysis of aging ship hulls. Sensitivity analysis is also included. More rational renewal and repair scheme that not only considers the maximum allowable corrosion wastage and critical crack size criteria, but also takes into account the hull ultimate strength is also developed in this work.

Time-dependent strength-based reliability of a double hull tanker is presented as an example accounting for the effects of corrosion and fatigue crack damage. The procedure developed in this work is illustrated by the example. It is concluded that the methodologies and procedure developed from the present study will be very useful for assessing time-variant ultimate strength reliability of aging ship hulls.

10.2. RECOMMENDATIONS FOR FUTURE WORK

Based on the present study, the following recommendations are made for the future work:

1. There is a need for further research on the effect of pit corrosion. The current corrosion measurement databases usually do not distinguish uniform corrosion from pit corrosion. Pit corrosion database is needed with efforts from the maritime industry and classification societies.

2. Further work is needed on cracking prediction in the ship hull structures. During the course of the current work it is clear that fatigue cracks have catastrophic

effects on ship structures. Predicting crack propagation and building up correct time-variant fatigue crack model are very important.

3. Good repair and maintenance scheme is crucial for extending ship's life. To effectively and efficiently pursue this goal, detailed research on repairing and further research on renewing different categories of ship hull members need

11. REFERENCE

ABS 2002, "ABS database of corrosion wastage for oil tankers", ABS RD 2002-2007

ABS 2005, "Rules for building and classing steel vessels", American Bureau of Shipping, Houston, TX.

ANSYS 2005, "User's manual (version 9.0)", Canonsburg, PA, ANSYS Inc.

Antoniou, A.C. 1980, "On the maximum deflection of plating in newly built ships", *Journal of Ship Research*, Vol. 24, No. 1, pp. 31-39.

Bea, et al. 1997, "Ship's maintenance project", Ship Structure Committee, SSC-395.

Bjerager, P. 1989, "Probabilistic computation methods in structural and mechanical reliability", Mechanics of Probabilistic and Reliability Analysis, Elme Press International, Switzerland.

Bleich, F. 1952, "Buckling strength of metal structures", McGraw-Hill, New York.

Broek, D. 1986, "Elementary engineering fracture mechanics", Martinus Nijhoff Publishers.

Caldwell J.B. 1965, "Ultimate longitudinal strength", RINA Transactions, Vol. 107, pp. 411–430.

Calsen, C.A. and Czujko, J. 1978, "The specification of post-welding distortion tolerance for stiffened plates in compression", *The Structural Engineer*, Vol. 56A, No. 5, pp. 133-141.

Chen, K.Y., Kutt, L.M., Piaszczyk, C.M., and Bieniek, M.P. 1983, "Ultimate strength of ship structures", SNAME Transactions, Vol. 91, pp.149–168.

Cornell, C. A. 1969, "A Probability-based structural code", *Journal of American Concrete Institute*, Vol. 66, pp. 974-985.

Cui, W.C. and Mansour, A.E. 1999, "Generalization of a simplified method for predicting ultimate compressive strength of ship panels", *International Shipbuilding Progress Journal*, Vol. 46, No. 447, pp. 291-303.

De, R.S. 1990, "Offshore structural system reliability: wave-load modeling, system behavior, and analysis", Dissertation submitted to Naval Architecture and Offshore Engineering Department, University of California, Berkeley.

Der Kiureghian, A. and Liu, P.L. 1986, "Structural reliability under incomplete probability information", ASCE, *Journal of Engineering Mechanics*, 112(1), pp.85-104.

Der Kiureghian, A. et al. 1989, "Structural reliability: methods & applications, notes of continuing education in engineering", University Extension, University of California, Berkeley, April 27-29.

Ditlevsen, O. 1979, "Narrow reliability bounds for structural systems", *Journal of Engineering Mechanics*, Vol. 4, pp. 453-472.

Emi, H., Arima, T., and Umino, M. 1994, "A study on developing a rational corrosion protection system of hull structures", NK Tech Bull, 65-79.

Endo H, Tanaka Y, Aoki G, Inoue H, and Yamamoto Y. 1988, "Longitudinal strength of the fore body of ships suffering from slamming", J Soc Naval Arch Jpn, Vol. 163, pp. 322–333.

Faulkner, D. 1975, "A review of effective plating for use in the analysis of stiffened plating in bending and compression", *Journal of Ship Research*, Vol. 19, No. 1, pp. 1-17.

Fontana, M.G. and Greene, N.D. 1967, "Corrosion engineering", McGraw-Hill Book Company, New York, NY.

Garbatov, Y., Guedes Soares, C., and, Wang, G. 2005, "Non-linear time dependent corrosion wastage of deck plates of ballast and cargo tanks of tankers", *Proceedings of the 24nd International conference on Offshore Mechanics and Arctic Engineering*, June 12-17, Halkidiki, Greece.

Guedes Soares, C. and Garbatov, Y. 1996, "Fatigue reliability of the ship hull girder accounting for inspection and repair", *Reliability Engineering and System Safety*, Vol. 51, pp. 341-351.

Guedes Soares, C., and Garbatov, Y., 1998, "Reliability of maintained ship hull girders subjected to corrosion and fatigue", *Structural Safety*, Vol. 20, pp. 201-219.

Guedes Soares, C., and Garbatov, Y., 1999, "Reliability of maintained, corrosion protected plates subjected to non-linear corrosion and compressive loads", *Marine Structures*, Vol. 12, pp. 425-445.

Hogben, N., Dacunha, N., and Olliver, G. F. 1986, "Global wave statistics", Unwin Brothers.

Hogben, N. 1990, "Long term wave statistics", Ocean Engineering Science, Vol. 9, Part A, Section 8, John Wiley & Sons.

John, W.G. 1874, "On the strength of iron ship", Inst Naval Arch Transactions, Vol. 15, pp. 74–93.

Kmiecik, M., Jastrzebski, T., and Kuzniar, J. 1995, "Statistics of ship plating distortions", *Marine Structures*, Vol. 8, pp. 119-132.

Loseth, R., Sekkeseter, G., Valsgard, S. 1994, "economics of high tensile steel in ship hulls", *Marine Structures*, Vol. 7, pp. 31-50.

Liu, P-L., Lin, H-Z. and Der Kiureghian, A. 1989, "CalREL user manual", Report No. UCB/SEMM-89/18, Dept. of Civil Engineering, University of California, Berkeley.

Loukakis, T.A. and Chryssostomidis, C. 1975, "Seakeeping series for cruiser stern ships", SNAME Transactions, Vol. 83, pp. 67-127.

Madsen, H. O., Krenk, S., and Lind, N. C. 1986, "Methods of structural safety", Prentice Hall, Englewood Cliffs, New Jersey.

Maestro, M. and Marino, A. 1988, "An assessment of the structural capacity of damaged ships: the plastic approach in longitudinal unsymmetrical bending and the influence of buckling", *Int Shipbuild Prog*, Vol. 36, No. 408, pp. 255–265.

Mansour, A.E. 1990, "An introduction to structural reliability theory", Ship Structure Committee, SSC-351.

Mansour et al. 1993, "Probability-based ship design procedure: a demonstration", Ship Structure Committee, SSC-368.

Mansour et al. 1997, "Assessment of reliability of ship structures", Ship Structure Committee, SSC-398.

Mansour, A.E. and Elsayed, T. 1999, "Reliability-based allowed unfairness tolerances for unstiffened plates", *Journal of Ship Research*, Vol. 43, No. 4, pp. 255-265.

Mansour, A.E. and Jensen, J.J. 1995, "Slightly non-linear extreme loads and load combinations", *Journal of Ship Research*, Vol. 39, No. 2, pp. 139-149.

Mansour, A.E. and Thayamballi, A. 1994, "Loads and load combinations", Ship Structure Committee, SSC-373.

Mansour, A.E. and Wirsching, P.H. 1995, "Sensitivity factors and their application to marine structures", *Marine Structures* Vol. 8, pp. 229-255.

Mansour, A.E., Yang, J.M., Thayamballi, A. 1990, "An experimental investigation on ship hull ultimate strength", SNAME Transactions, Vol. 98, pp. 411-440.

Masaoka, K. 1996, "Development and application of an efficient ultimate strength analysis method for ship structures", Dr. Eng. Dissertation, Osaka University, Osaka.

Maximadj, A.I., Belenkij, L.M., Briker, A.S., and Neugodov, A.U. 1982, "Technical assessment of ship hull girder", Petersburg: Sudostroenie, (in Russian).

Melchers, R.E. 1995a, "Probabilistic modeling of marine corrosion of steel specimens", Proceedings of the ISOPE'95, June 12-15, the Hague, the Netherlands, pp. 204-210.

Melchers, R.E. 1995b, "Probabilistic modeling of seawater corrosion of steel structures", Proceedings of the International Conference on Applications Statistics and Probability in Structural and Geotechnical Engineering (ICASP), Paris, pp. 265-270.

Melchers, R.E. 1997, "Modeling of marine corrosion of steel specimens", In: Kain, R.M., Young, W.T., editors. Corrosion testing in natural waters, Vol. 2. Philadelphia: ASTM STP 1300, pp. 20-33.

Melchers, R.E. 1998, "Probabilistic modeling of immersion marine corrosion", In: Shiraishi, N., Shinozuka, M., Wen, Y.K., editors. Structural Safety and Reliability, Vol. 3. Rotterdam: Balkema, pp. 1143-1149.

Melchers, R.E. 1999, "Corrosion uncertainty modeling for steel structures", *Journal of Constructional Steel Research*, Vol. 52, pp. 3-19.

Melchers, R.E. 2003a, "Probabilistic models for corrosion in structural reliability assessment – part 1: empirical models", *Journal of Offshore Mechanics and Arctic Engineering*, Vol. 125, pp. 264-271.

Melchers, R.E. 2003b, "Probabilistic models for corrosion in structural reliability assessment – part 2: models based on mechanics", *Journal of Offshore Mechanics and Arctic Engineering*, Vol. 125, pp. 272-280.

Moan, T. et al. 1994, "Applied design – strength limit states formulations", Proceedings of International Ship and Offshore Structures Congress, St. John's Canada, September, Vol. 2, pp. 1-58.

Nishihara S. 1983, "Analysis of ultimate strength of stiffened rectangular plate (4th Report)—on the ultimate bending moment of ship hull girder", *J Soc Naval Arch Jpn* Vol. 154, pp. 367–375.

Nitta, A., Aral, H. and Magaino, A. 1992, "Basis of IACS unified longitudinal strength standard", *Marine Structures*, Vol. 5, pp. 1-21.

Ochi, M.K. and Motter, L.E. 1973, "Predictions of slamming characteristics and hull responses for ship design", SNAME Transactions, Vol. 81, pp. 144-190.

Paik et al. 1998, "Ultimate strength reliability of corroded ship hulls", RINA Transactions, Vol. 140, pp. 1-18

Paik et al. 2003, "Time-dependent risk assessment of aging ships accounting for general/pit corrosion, fatigue cracking and local denting damage", SNAME, San Francisco, CA.

Paik, J.K., Kumar, Y.V.S., and Lee, J.M. 2005, "Ultimate strength of cracked plate elements under axial compression or tension", *Thin-Walled Structures*, Vol. 43, pp. 237-272.

Paik, J.K. and Lee, J.M. 1996, "An empirical formulation for predicting ultimate compressive strength of plates and stiffened plates", Trans Soc Naval Arch Korea, Vol. 33, No. 3, pp. 8-21.

Paik, J.K., Lee, J.M. and Ko, M.J. 2003, "Ultimate compressive strength of plate elements with pit corrosion wastage", *Journal of. Engineering for the Maritime Environment*, Vol. 217, No. M4, pp. 185–200.

Paik, J.K., Lee, J.M., Hwang, J.S. and Park, Y. 2003, "A time-dependent corrosion wastage model for the structures of single- and double-hull tankers and FSOs and FPSOs", *Marine Technology*, Vol. 40, No. 3, pp. 201-217.

Paik, J.K., Lee, J.M, Park, Y., Hwang, J.S. and Kim, C.W. 2003, "Time-variant ultimate longitudinal strength of corroded bulk carriers", *Marine Structures*, Vol. 16, pp. 567-600.

Paik, J.K. and Mansour, A.E. 1995, "A simple formulation for predicting the ultimate strength of ships", *Journal of Marine Science and Technology*, pp. 52-62.

Paik, J.K., Thayamballi, A.K. 1997, "An empirical formulation for predicting ultimate compressive strength of stiffened panels", Proceedings of the Seventh International Offshore and Polar Engineering Conference, Honolulu, USA, May 25-30, pp. 328-338.

Paik, J.K. and Thayamballi, A.K. 2002, "Ultimate strength of ageing ships", *Journal of Engineering Maritime Environments*, Vol. 216, pp.57-77.

Paik, J.K. and Thayamballi, A.K. 2003, "Ultimate limit state design of steel-plated structures", John Wiley & Sons, LTD.

Paik, J.K., Thayamballi, A.K., Chen, J.S. 1996, "Ultimate strength of ship hulls under combined vertical bending, horizontal bending and shearing forces", SNAME Transactions, Vol. 104, pp. 31–59.

Paik, J.K., Thayamballi, A.K., Kim, S.K., and Yang, S.H. 1998, "Ship hull ultimate strength reliability considering corrosion", *Journal of Ship Research*, Vol. 42, No. 2, pp. 154-165.

RINA 1996, "Derbyshire – the search, assessment and survey", The Naval Architect, The Royal Institution of Naval Architects, May, pp. 44-48.

Rubinstein, R. Y. 1981, "Simulations and the Monte Carlo method", John Wiley & Sons, New York.

Rutherford S.E. and Caldwell J.B. 1990, "Ultimate longitudinal strength of ships: a case study", SNAME Transactions, Vol. 98, pp. 441–471.

Smith, C.S. 1977, "Influence of local compressive failure on ultimate longitudinal strength of a ship's hull", Proceedings of the International Symposium on PRADS, Tokyo, Japan, pp. 73–79.

Smith, C.S., Davidson, P.C., Chapman, J.C. and Dowling, P.J. 1988, "Strength and stiffness of ships' plating under in-plane compression and tension", RINA Transactions, Vol. 130, pp. 277-296.

Southwell, C.R., Bultman, J.D., Hummer, C.W. Jr., 1979, "Estimating service life of steel in seawater", In: Schumacher, M., editor, Seawater corrosion handbook. New Jersy: Noyes Data Corporation, pp. 374-387.

Sun, H.H. and Bai, Y. 2003, "Time-variant reliability assessment of FPSO hull girders", *Marine Structures*, Vol. 16, pp. 219-253.

Sundararajan, C. 1995, "Probabilistic structural mechanics handbook", Chapman & Hall, Ltd., New York.

Timoshenko S.P. 1953, "History of strength of materials", New York: McGraw-Hill Book Co.

Timoshenko, S. and Gere, J.M. 1982, "Theory of Elastic Stability", McGraw-Hill, New York.

TSCF 1993, "Guidelines for the inspection and condition assessment of tanker structures", Tanker Structure Co-operative Forum.

TSCF 1997, "Guidance manual for tanker structures", Tanker Structure Co-operative Forum, Witherby & Co. Ltd., London.

Ueda Y., Rashed, S.M.H. 1984, "The idealized structural unit method and its application to deep girder structures", *Computational Structures*, Vol. 18, No. 2, pp. 227–293.

Valsgaard, S., Jorgensen, L., Boe, A.A., and Thorkildsen, H. 1991, "Ultimate hull girder strength margins and present class requirements", Proceedings of the SNAME Symposium on Marine Structural Inspection, Maintenance and Monitoring, Arlington, USA, pp. B.1–19.

Wang, G. Spencer, J., and Sun, H. 2003a, "Assessment of corrosion risks to aging ships using an experience database", *Proceedings of the 22nd International conference on Offshore Mechanics and Arctic Engineering*, ASME, Paper OMAE 2003-37299.

Wang, G. Spencer, J., and Elsayed, T., 2003b, "Estimation of corrosion rates of oil tankers", *Proceedings of the 22nd International conference on Offshore Mechanics and Arctic Engineering*, ASME, Paper OMAE 2003-37361.

Wirsching, P. H. 2003, "Application of reliability methods to fatigue design and analysis", WRC/PVRC Conference on New Approaches to Fatigue Design and Life Prediction, March 12-13.

Wu, Y.T., Millwater, H.R., Cruse, T.A. 1990, "Advanced probabilistic structural analysis method for implicit performance functions", *AIAA Journal*, Vol. 28, No. 9, pp. 1663-1669.

Yamamoto, N., and Ikegami, K. 1998, "A study on the degradation of coating and corrosion of ship's hull based on the probabilistic approach", *Journal of Offshore Mechanics and Arctic Engineering*, Vol. 120, pp. 121-128.

Yao, T. 1999, "Ultimate longitudinal strength of ship hull girder; historical review and state of the art", *Int J Offshore Polar Eng*, Vol. 9, No. 1, pp. 1-9.